TECHNISCHE UNIVERSITÄT MÜNCHEN
Lehrstuhl für Methodik der Fernerkundung

Estimation and Compensation of Ionospheric Propagation Delay in Synthetic Aperture Radar (SAR) Signals

Giorgio Gomba

Vollständiger Abdruck der von der Ingenieurfakultät Bau Geo Umwelt
der Technischen Universität München zur Erlangung des akademischen Grades eines

Doktor-Ingenieurs (Dr.-Ing.)

genehmigten Dissertation.

Vorsitzender:
Prof. Dr.-Ing. Uwe Stilla

Prüfer der Dissertation:
1. Prof. Dr.-Ing. habil. Richard H.G. Bamler
2. Hon.-Prof. Dr. rer. nat. Michael Eineder
3. Prof. Dr. Franz Meyer

Die Dissertation wurde am 27.10.2016 bei der Technischen Universität München eingereicht und durch die Ingenieurfakultät Bau Geo Umwelt am 13.12.2016 angenommen.

Abstract

Synthetic aperture radar (SAR) and interferometric SAR (InSAR) measurements are disturbed by the propagation velocity changes of microwaves that are caused by the high density of free electrons in the ionosphere. Most affected are low-frequency (L- or P-band) radars, as the recently launched L-band ALOS, ALOS-2, and the planned Tandem-L and NISAR, although higher frequency (C- or X-band) systems are not immune. As the ionosphere is an obstacle to increasing the precision of SAR systems needed to remotely measure the Earth's dynamic processes, this thesis aims to develop methods to estimate and compensate ionospheric propagation delays in SAR signals.

The split-spectrum method exploits the dispersive propagation of electromagnetic waves through the ionosphere and can estimate the differential relative ionospheric phase screen that disturbs InSAR measurements; previous works demonstrated its feasibility but a broader analysis was lacking. This method has been improved and thoroughly analyzed in terms of its implementation, accuracy, and noise sources, both random and systematic. Application examples validate its effectiveness by, for the first time, demonstrating correction of interferograms. An extension of the method for TOPS mode SAR, used by wide-swath radars such as the C-band Sentinel-1, has been developed and tested. Finally, some of the estimated ionospheric phase screens have been qualitatively validated by means of global total electron content maps and local GNSS measurements.

The integrated azimuth shifts method is based on the changes in the azimuth impulse response produced by fluctuations of the ionosphere in the along-track direction. The method recovers small-scale azimuth variations of the ionospheric phase screen but is insensitive in the range direction. Experimental results show that integrated azimuth shifts are, on the small-scale, superior to the split-spectrum method, demonstrating the amount of information contained in the impulse response. In order to better understand the use of the impulse response in estimation of the ionosphere, semi-focusing processing proposed in previous works has been analytically derived. It was then used to recover information despite a varying ionospheric height.

Finally, to improve ionospheric estimation, a new method that combines data from various information sources using Bayesian inversion has been developed. To avoid arbitrary smoothing windows, it uses a data-based fractal model of turbulent ionospheric variations, leading to an adaptive anisotropic filtering. While the method could, in general, be used to combine absolute and differential ionospheric information, here it has been applied to the split-spectrum and azimuth shift methods to estimate the differential ionospheric phase screen. It allowed measurement of ground movements over long distances and elevated InSAR methods to be a real alternative to GNSS measurements for large-scale deformation monitoring. The proposed concept also lays the basis for future developments such as estimation of the absolute ionosphere and along-track ground motion.

In conclusion, this dissertation represents a significant advancement to operational correction of ionospheric effects in SAR interferometry by demonstrating its feasibility thus removing a major obstacle to monitoring Earth's dynamic processes.

Zusammenfassung

Messungen mit Synthetic Aperture Radar (SAR) und interferometrischem SAR (InSAR) werden durch Änderungen der Ausbreitungsgeschwindigkeit der Mikrowellen gestört, welche durch die hohe Dichte freier Elektronen in der Ionosphäre verursacht werden. Weil die Ionosphäre ein Hindernis für die Steigerung der Genauigkeit von SAR Systemen darstellt, die zur Messung von dynamischen Vorgängen der Erdoberfläche mittels Fernerkundung notwendig ist, zielt diese Dissertation auf die Entwicklung von Methoden zur Schätzung und Kompensierung von ionosphärischen Ausbreitungsverzögerungen in SAR Signalen.

To my family

Contents

1 Introduction

1.1 Motivation

The capabilities and precision of synthetic aperture radar (SAR) to monitor the Earth's dynamic processes is continuously increasing thanks to newer and more efficient satellite radars and data analysis methods. As an active coherent imaging radar, SAR produces a two-dimensional complex reflectivity map of an illuminated ground scene by transmitting and receiving electromagnetic pulses modulated in the microwave frequency spectrum, usually ranging from P-band (250 MHz) to K_a-band (40 GHz). With some limitation for particularly severe weather or space-weather conditions, microwaves can propagate trough the atmosphere, allowing SAR systems to function also with a covered sky.

The phase of a SAR image depends on the backscatter phase and on the electromagnetic wave propagation time; the phase difference between two images produces interferometric SAR (InSAR) data. InSAR is used to measure the ground scene elevation and create digital elevation models (DEM) of the terrain with meter-level accuracy. Elevation changes, such as surface deformation, can also be monitored, with centimeter to millimeter accuracy. Earthquakes, volcanoes, tectonic deformation, and land subsidence are among the geophysical processes typically monitored by InSAR. The accuracy of InSAR measurements is affected by phase decorrelation, orbital errors, phase-unwrapping errors, and by the extra path delay due to the propagation of the microwave signal through the atmosphere. The selection of the best-suited carrier frequency, revisit time and viewing geometries, as well as the analysis of stacks of images, use of precise orbits, and correction of atmospheric effects are some of the techniques developed to improve the measurement accuracy.

Higher frequency systems, such as the ones employing X-band, usually have better resolution, higher sensitivity to deformation, and might be less susceptible to ionospheric disturbances than lower frequency systems. However, due to the random scattering response of the vegetation, X-band interferograms usually present low coherence levels in vegetated areas, in particular over long temporal spans. On the contrary, L-band microwaves penetrate deeper through vegetation to the ground, which has a more stable scattering response, and interferograms usually show high coherence levels even with a temporal baseline of months or years. Two satellites with an L-band carrier frequency ($\sim$1.27 GHz) were recently launched (ALOS and ALOS-2) with two more planned (Tandem-L and NISAR). Unfortunately, they are less sensitive to deformation, and might be severely disturbed by ionospheric phenomena, which can be the major noise source for L-band interferograms.

Wave propagation in a medium with refractivity index smaller than one is slower than in vacuum since the group velocity is smaller than the one in vacuum. The extra delay introduces an error when measuring the range distance with the wave propagation time and assuming propagation in a vacuum. The term ionosphere distinguishes the ionized upper atmosphere from the background neutral gasses. The refractivity index depends on the density of free electrons in the ionosphere, and

on the temperature, pressure, and humidity in the neutral atmosphere, which mainly includes the troposphere. At X-band the ionospheric delay can reach a few centimeters, at C-band tens of centimeters, and at L-band, a few meters. The spatial scale of the delay variations can be very similar to the ground deformation scale, making the two contributions difficult to distinguish. Ionospheric maps can be produced with navigation satellite system (GNSS) data; however, their resolution and quality are not sufficient to correct interferograms with the desired accuracy. Nevertheless, in contrast to troposphere corrections for single interferograms, which rely on external data, information about the ionosphere can be extracted from SAR data.

1.2 Scope

As the ionosphere is an obstacle to increasing the precision of SAR systems needed to remotely measure dynamic processes of the Earth, this thesis aims to *develop methods to estimate and compensate ionospheric propagation delays in SAR signals in a precise and robust way*.

1.3 Thesis structure

This is a cumulative dissertation. It gathers the findings of the author in the estimation and compensation of the ionospheric propagation delays presented in three peer-reviewed papers and two conference papers (see the Appendix).

Fundamentals and state of the art

Chapter 2 opens with an introduction to the ionosphere and its influence on microwave propagation, then goes on to describe the particular effects produced on SAR images and interferograms; examples are also provided. Interferograms are differential relative measurements, therefore, spatial and temporal variations of the electron content are the effective error source. Particular attention is given to the various phenomena that change the ionosphere, both temporally and spatially.

Information about the ionosphere can be extracted in various ways directly from SAR data. Chapter 2 illustrates the possible information sources and the methods to exploit them, and reviews the current literature on the topic.

The split-spectrum method

Since SAR interferometry is one of the most important products of a SAR system, this thesis focuses more on the estimation and compensation of the differential ionospheric phase screen that disturbs interferograms. With this objective, the split-spectrum method is analyzed in Chapter 3. This method estimates the differential relative ionospheric phase screen and can therefore correct interferograms; previous works demonstrated its feasibility but a broader analysis was lacking. This method has been improved and thoroughly analyzed in terms of its implementation, accuracy and noise sources (both random and systematic) in Chapter 3. Application examples validate its effectiveness by demonstrating, for the first time, correction of the ionospheric phase screen superimposed on SAR interferograms with a precision in the centimeter to millimeter level. Nevertheless, low-coherence, narrow bandwidth, and a rapidly varying ionosphere limit the maximum achievable compensation accuracy, which can in some cases be below expectations.

The split-spectrum method for wide-swath images

Wide-swath images increase the ground coverage permitting better studies of large-scale geophysical phenomena. These imaging modes extend the swath by electronically steering the antenna, acquiring images in a varying squinted geometry. Chapter 4 analyzes the ionospheric effects for images with non-zero Doppler centroid and proposes a correction strategy; the split-spectrum method is adapted for this. This allows for the extraction of ionospheric phase screens from Sentinel-1 data, demonstrating that the influence of the ionosphere is not limited to systems with a low carrier frequency, such as L-band, but that it can also severely disturb C-band interferograms.

Semi-focusing processing and integrated azimuth shifts

Another source of information about the ionospheric electron density fluctuations are the changes in the azimuth SAR impulse response. These are exploited in Chapter 5 to estimate the azimuth variation of the electron density with the integrated azimuth shifts method. The results show that this method is, on the small-scale, superior to the split-spectrum, demonstrating the amount of information contained in the impulse response. To better understand possible implications in the estimation of the ionosphere, semi-focusing processing, proposed in previous works, is here analytically derived. It is then used in a particular test case to recover information despite a varying ionospheric height.

Improved estimation by data combination

To improve ionosphere estimation, the combination of data from different information sources has been suggested several times, and some attempts to implement it have been made. Chapter 6 presents a new method to combine information sources based on a Bayesian inverse problem. With respect to existing techniques, it combines data from different sources based on their expected accuracy and the expected spatial correlation of the result. In this way, it avoids arbitrary smoothing windows with low physical significance by relying on a data-based fractal model of the turbulent ionospheric variations. Therefore, it improves the isotropic filtering used previously in the split-spectrum method, by implementing an anisotropic adapted filter. In general, it could be used to combine absolute and differential ionospheric information, but it is applied here to the split-spectrum method and the azimuth shifts, which estimate the large-scale range and azimuth variations, and the small-scale azimuth variations of the differential ionospheric phase screen respectively. Compared to existing methods it is independent of the interferogram: this allows for the measurement of long distance ground movements, elevating the InSAR method to an alternative or a complement to GNSS measurements.

Validation

Finally, some of the estimated ionospheric phase screens are validated in Chapter 7 by means of GNSS measurements. Global TEC maps can be qualitatively compared to SAR-derived ionosphere estimates, but only over very large distances, because, due to the use of ionospheric models, the sparse GNSS sampling, and the different geometry, small-scale variations are not recovered. Local GNSS data and ad hoc interpolation improve the reconstruction, thereby confirming that the SAR-based results actually estimated the differential ionosphere. A precise validation however, would require developing a method that converts sparse GNSS measurements to a SAR ionospheric phase screen, and provides the accuracy of such a phase screen.

Conclusion

In this thesis, a method that estimates the differential ionospheric phase screen and precisely compensates for it in interferograms is presented. To increase accuracy it aggregates various information sources and automatically adapts its parameters to the characteristics of the ionosphere that is being estimated; moreover, its robustness is tested in various test cases. The proposed concept lays the basis for future developments, leading to the estimation of the absolute ionosphere and along-track ground deformation. The operational correction of ionospheric effects for SAR interferograms now becomes feasible, largely improving the current accuracy limit in monitoring the Earth's dynamic processes.

2 Fundamentals and state of the art

This chapter provides the reader with fundamentals about the ionosphere and its effects on SAR and InSAR. Moreover, the current state of the art in the estimation and correction of ionospheric effects is reviewed, and the improvements developed in this thesis are summarized.

2.1 Ionosphere

The ionosphere is defined as the portion of the Earth's upper atmosphere where ions and electrons are present in sufficient density to significantly affect the propagation of radio waves (Davies, 1990; Yeh and Liu, 1972). The term ionosphere distinguishes the ionized atmosphere from the background neutral gasses. The ionosphere is a weakly ionized gas (plasma) enclosed in the Earth's magnetic field, it contains equal numbers of positive and negative charges and, hence, is electrically neutral. Charged particles are mainly created by the incoming solar radiation that ionizes atmospheric gasses and are carried by the solar wind. The activity level of the ionosphere, therefore, depends on the state of the Sun, the interplanetary medium, the Earth's magnetosphere, and the Earth's neutral atmosphere.

The presence of ionospheric charged particles starts at about 60 km altitude, normally has a peak between 300 and 400 km, and then decreases until about 1000 km (Davies, 1990). During daytime the ionosphere is distinguished in the D, E, F_1 and F_2 layers, whereas during night time only the E layer and one F layer exist. The vertically stratified structure of the ionosphere is often assumed compressed and approximated by an idealized single thin layer positioned at the peak or barycenter of the electron density. Integrating the electron density N along a tube of 1 m^2 cross section gives the total electron content (TEC)

$$TEC = \int_L N \, \mathrm{d}l, \tag{2.1}$$

where L is the integration path. The compressed three-dimensional ionosphere is then represented by the two-dimensional thin layer and by the local vertical TEC. The TEC level is usually measured in TEC units (TECU), where one TECU is equal to 10^{16} electrons/m^2. Unless differently specified, in the following the single layer approximation is used. Due to the longer travel path in the ionosphere, an oblique propagation experiences a different total electron content than a vertical one. Based on the single layer model approximation, a mapping function $M(\theta)$ (Jakowski et al., 2011) can be used to calculate the slant TEC ($sTEC$) from the vertical TEC ($vTEC$):

$$sTEC = vTEC \cdot M(\theta) = vTEC \cdot \left(1 - \left(\frac{R_e \sin(\theta)}{R_e + H_i}\right)\right)^{-1/2}, \tag{2.2}$$

where R_e is the Earth's radius, H_i is the height of the ionospheric layer, and θ is the incidence angle, the angle between the zenith and the propagation axis. Unless differently specified, with TEC is in

the following intended the slant TEC, the total electron content experienced by a signal during its propagation.

The ionization level, i.e. the concentration of charged particles, depends on the amount of received solar radiation. Areas that are differently illuminated present different ionization levels. The *background ionosphere* is usually defined as the ionosphere that varies depending on the relative position to the Sun, and on the solar zenith angle. Additional fluctuations of various magnitude and spatial scale might be produced by localized effects. The intensity and form of global and local horizontal variations of the electron density thus vary greatly with time (sunspot cycle, seasonally and diurnally), with geographical location (polar caps, auroral zones, mid-latitudes and equatorial regions), and with certain solar disturbances.

Differential interferograms only measure temporal and spatial relative changes. Therefore, temporal and spatial variations of the electron density generates relevant ionospheric effects on SAR images and interferograms. For this reason, the most significant variations are summarized in the following.

2.1.1 Electron density temporal variations

The main driver of the ionosphere is the solar radiation; therefore, the rotation of the Earth with respect to the Sun, or changes in the Sun activity influence the maximum electron density. Regular variations that affect the ionization level have different cyclical trends: daily, seasonal, 11 years, and 27 days:

Daily variation The daily electron density variation is a consequence of the 24-hour rotation of the Earth around its axis. Because of the daytime ionization the total electron content is higher during day than during night.

Seasonal variation The seasonal variation results from the yearly orbit of the Earth around the Sun and from the tilt of the Earth's rotational axis. During summer, the hemisphere which is exposed to more direct sunlight generally presents higher ionization levels, whereas the winter hemisphere presents lower levels. However, at middle latitude, due to the higher summer ion loss rate, the electron density is higher during winter than in summer, an effect called the winter anomaly (Davies, 1990).

Solar cycle variations One of the most notable phenomena on the surface of the Sun is the appearance and disappearance of dark, irregularly shaped areas known as sunspots. The occurrence of sunspots follows a cycle that is 11 years long. During periods of maximum sunspot activity, the ionization level of all layers increases. Figure 2.1 shows the smoothed international sunspot number of the last 50 years.

The number of existing sunspots is continually subject to change as some disappear and new ones emerge. However, in addition to the 11 years cycle, there is also a pronounced 27 days periodicity, the approximate period required for the Sun to make one complete rotation.

2.1.2 Electron density spatial variations

Figure 2.2 shows the approximate extent of major geographic regions in the ionosphere. The high-latitudes region is located above about 60° on each side of the geomagnetic equator. It is subdivided between the polar cap and auroral region. The magnetic (or geomagnetic) equator is different from the geographical equator, being about 12° above the geographical equator at African and Asian longitudes, and 12° below at American longitudes. The mid-latitudes region is between 60° and 20° on each side of the magnetic equator. Low-latitudes are defined as the region from -20° to 20°, referring to the magnetic equator.

Electron density spatial variations span all geographical scales, from planetary to meter-level and below. At a global scale, the ionization is higher in equatorial regions and decreases toward the poles,

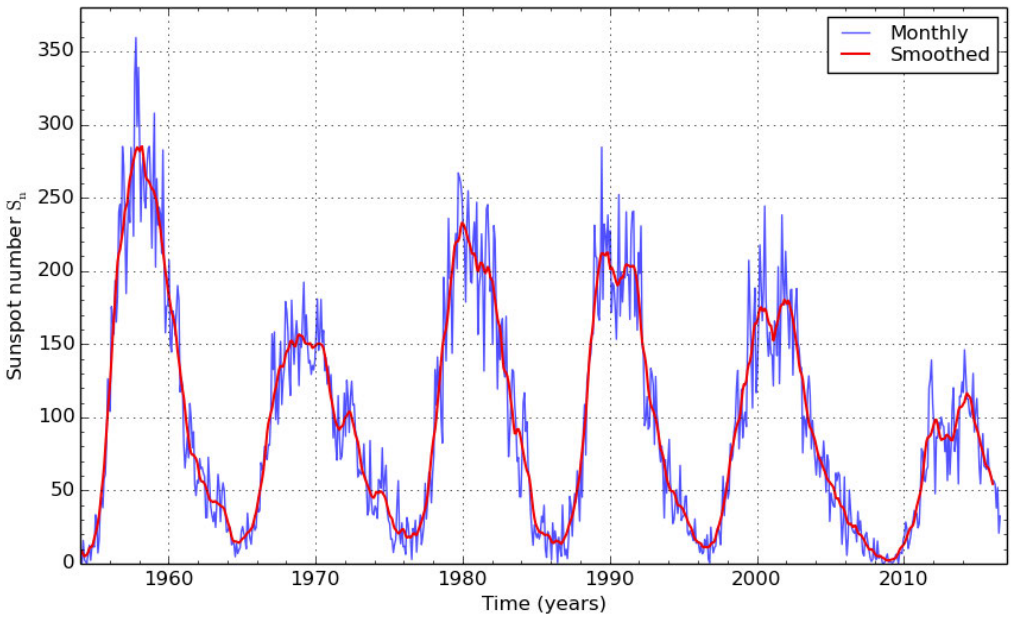

Figure 2.1: International sunspot number S_n: monthly mean and 13-month smoothed number [from (WDC-SILSO, 2016)].

generating the background ionosphere. On an intermediate scale, production, recombination, and electrodynamic transport interact with neutral wind phenomena such as gravity waves to create mid-scale patterns. On a smaller scale, effects as the Rayleigh-Taylor instability and the $\boldsymbol{E} \times \boldsymbol{B}$ instability are the cause of severe localized irregularities.

Background ionosphere The regular spatial variation of the ionosphere, which depends on the solar zenith angle, forms the so-called background ionosphere. The global structure of the background ionosphere moves westwards accordingly with the apparent motion of the Sun around the Earth. Figure 2.3 shows the global distribution of TEC, averaged over the whole year 2015 at a fixed day time, 18:00 UTC. Figure 2.4 shows the global TEC for one day with intervals of two hours. These TEC maps are produced from the international GNSS service (IGS) using GNSS data (Hernández-Pajares et al., 2009). The main geographical variation seen by a SAR satellite with quasi-polar orbit is then a negative gradient, from the equator towards the poles, or a positive one, from the poles toward the equator.

Smooth perturbations of this global pattern are, for example, the equatorial anomaly and the mid-latitude trough. The maximum of the ionization level is located at about ±20° latitude from the magnetic equator, because of the fountain effect. These maxima are referred to as the equatorial anomaly and can also be clearly seen in Figure 2.3. The mid-latitude trough is an effect occurring prevalently at night, characterized by a decrease of the electron concentration equatorward of the auroral region (Moffett and Quegan, 1983).

Traveling ionospheric disturbances Traveling ionospheric disturbances (TID) are large-scale horizontal irregularities of the background ionosphere expressed as wave-like oscillations. TIDs occurrence and direction of travel show significant diurnal, seasonal, and sunspot cycle variations. They are classified into two types: large-scale TIDs and medium-scale TIDs. Large-scale TIDs have a period of 1-2 h, a horizontal wavelength of 1000-2000 km and propagate equatorward at 300-1000 m/s. They are mostly isolated irregularities produced by rare events such as aurora disturbances after magnetic storms, solar flares, volcanic eruptions, earthquakes, rocket launches or nuclear explosions (Davies, 1990; Afraimovich et al., 1992). Medium-scale TIDs occur much more frequently than large scale TIDs, they have shorter periods of 10 min to

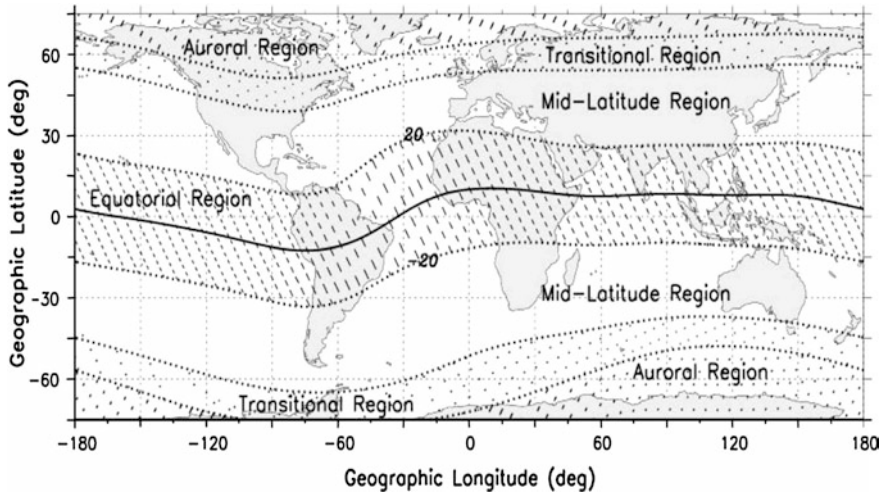

Figure 2.2: Major geographic regions of the ionosphere [from (Zolesi and Cander, 2014)].

1 h, a wavelength of several hundreds of kilometers and move equatorward with speeds of 50-300 m/s. Their origin is not well understood although they are related to acoustic-gravity waves propagating in the neutral atmosphere (Hocke and Schlegel, 1996). Figure 2.5 shows an example of large scale TIDs over North America and medium scale TIDs over Europe, measured by GNSS observations (Ding et al., 2008; Otsuka et al., 2013).

Spread-F Scintillation is the term given to amplitude, phase, polarization, and angle of arrival fluctuations of a radio signal that traversed the ionosphere (Davies, 1990). Equatorial scintillation effects are caused by randomly irregular electron density variations present along the radio wave propagation path. Plasma instability phenomena occurring in the equatorial F layer are usually grouped under the name equatorial spread-F. Various hypotheses exist over the generation of spread-F, large-scale (200 km) variations are thought to be related to gravity waves and electrodynamic uplift, mid-scale variations (20-200 km) to shear effects, and smaller scale (0.1-20 km) to the Rayleigh-Taylor instability (Kelley, 2012). The latter is responsible for the creation of plasma bubbles, which are the source of scintillations. Plasma bubbles form after sunset when the ionization of the atmosphere stops. The ions recombine, forming a lower density layer. This layer can rise through the more ionized layers above, creating plasma bubbles. The bubbles are turbulent with irregular edges in the east-west direction but extend along the magnetic field lines for hundreds of kilometers in a rod-like shape. Plasma bubble occurrence is most prevalent at equinoxes and summers, during quiet magnetic periods, and it is correlated with solar activity level (Xu et al., 2004). Plasma bubbles are most intense and most frequent in two bands surrounding the magnetic equator similarly to the equatorial anomaly crests. The size distribution of the irregularities can be characterized by a power law spectral density function (Rino, 1979).

Magnetic storm Solar disturbances such as solar flares or coronal mass ejection produce an unusually large release of plasma and magnetic field from the solar corona. When the emitted charged particles reach the Earth they cause a geomagnetic storm, a severe disturbance of the Earth's magnetic field. Magnetic storms cause an increase of ionospheric activity, and in particular disturbances of the background ionosphere such as auroras. The planetary K_p index is used to indicate the state of the magnetic field. It is a number ranging from 0 to 9 with 1 being calm and 5 or higher indicating a storm (Davies, 1990).

Aurora The auroral zones may be defined as those regions of the Earth where visible auroras often occur. The solar wind is a stream of charged particles emitted by the Sun. Most of the solar

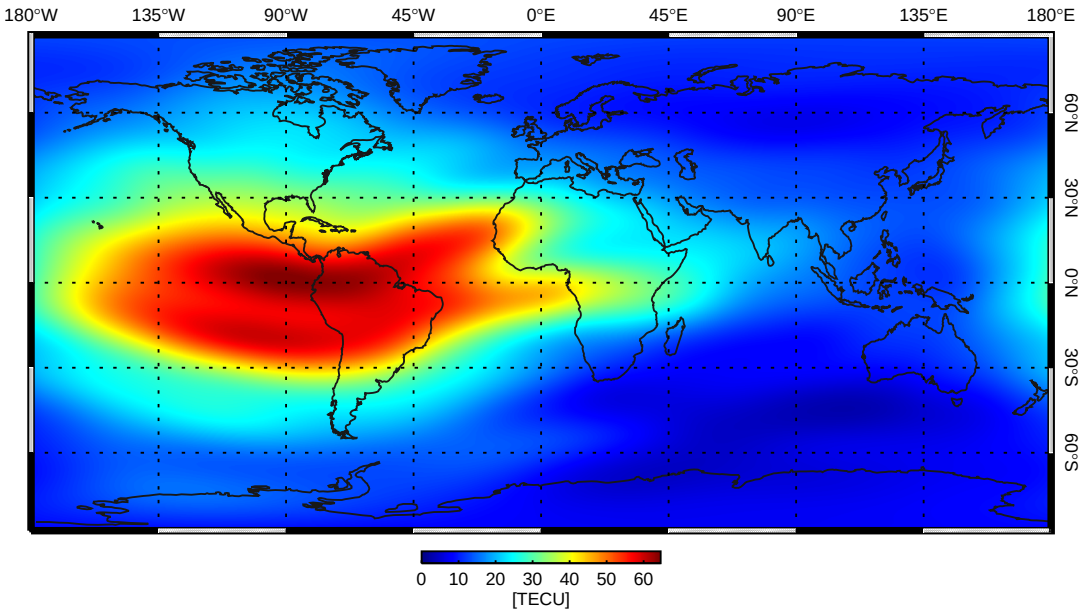

Figure 2.3: Global TEC map, averaged over the year 2015 at 18:00 UTC (data source IGS). The background ionosphere defines the main geographical variation, the electron density is higher in the two crests at ±20° latitude from the geomagnetic equator, the equatorial anomaly crests, and decreases towards the poles.

wind charged particles are deflected by the Earth's magnetosphere, but some are accelerated by the interconnections between the magnetic field of the Earth and that of the Sun. They are conducted downward toward the magnetic poles where they collide with the atmosphere, ionizing oxygen and nitrogen atoms. The ionized atmosphere gasses then return to a less energetic state releasing photons, which cause the visible auroras. Auroras occur in a variety of structures. These range from small-scale sharply defined narrow rays, which are aligned along magnetic field lines, to large-scale structures such as arcs, which are oriented in the magnetic east-west direction. The geographical region enclosed in the auroral ring is the polar cap (Davies, 1990). The presence of visible auroras is connected with severe ionospheric effects on SAR images due to the higher electron density levels (Meyer et al., 2009).

High-latitude irregularities Scintillation effects are also reported at high-latitudes. They are caused by small-scale irregularities in the electron density which derives from the $\boldsymbol{E} \times \boldsymbol{B}$ instability (Tsunoda, 1988; Kelley, 2012).

2.1.3 Ionospheric effects on radio waves

The propagation of electromagnetic waves at radio frequencies in the ionosphere depends on the density of free electrons. The Appleton equation relates the refractive index of the plasma to its ionization (Davies, 1990). Assuming collision and magnetic field effects negligible, the refractive index n for a plane wave with frequency f is

$$n^2 = 1 - \left(\frac{f_N}{f}\right)^2. \tag{2.3}$$

The plasma frequency $f_N^2 = Ne^2/4\pi^2\epsilon_0 m$ depends on the electron number density N (per m^3), its maximum is usually in the order of 10 MHz. The terms e, m and ϵ_0 are respectively the electron

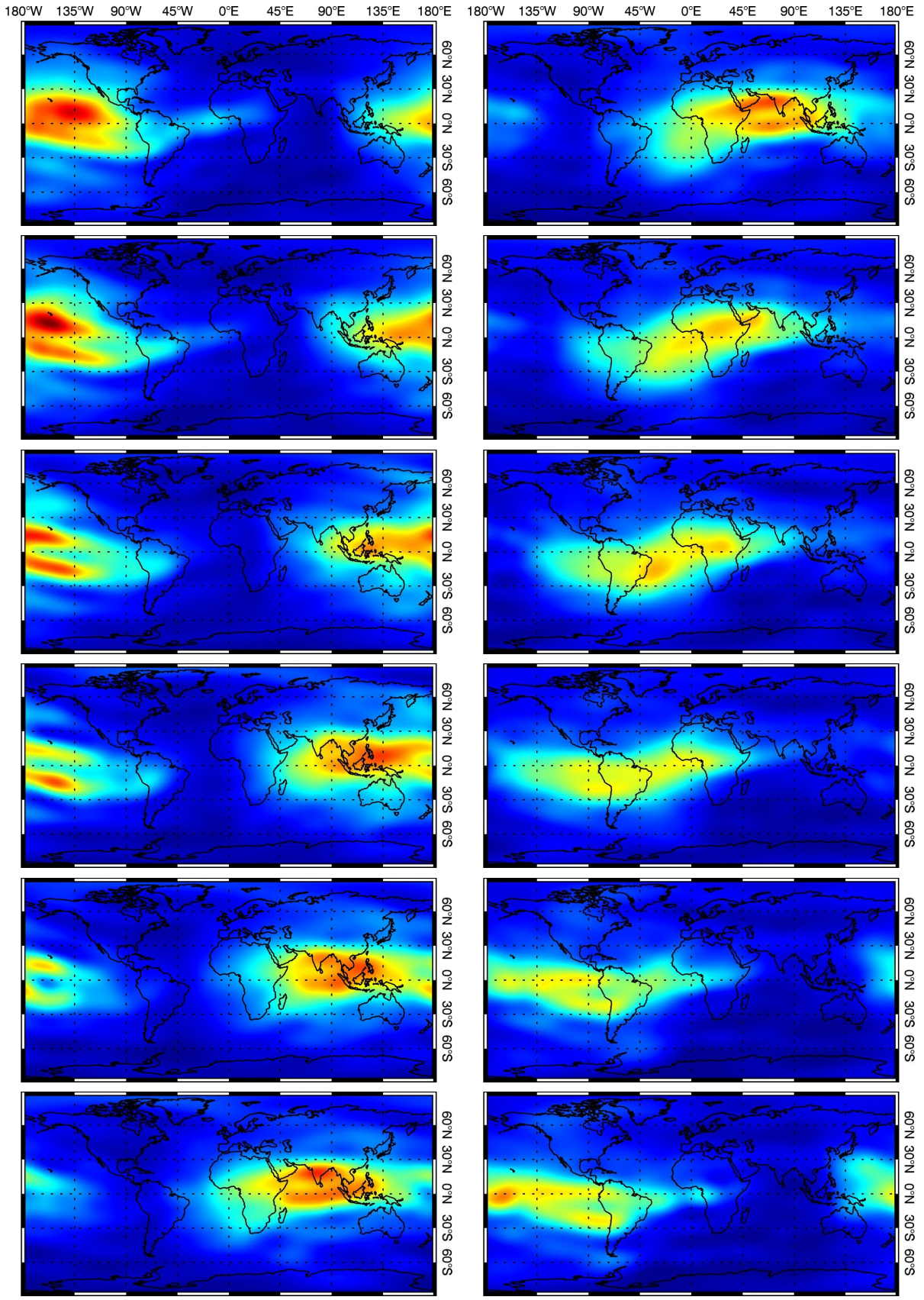

Figure 2.4: Global TEC maps for September 9, 2015 (data source IGS). Left column from top to bottom, from 00:00 to 10:00 UTC every 2 hours; right column, from 12:00 to 22:00. The color scale goes from 0 to 70 TECU.

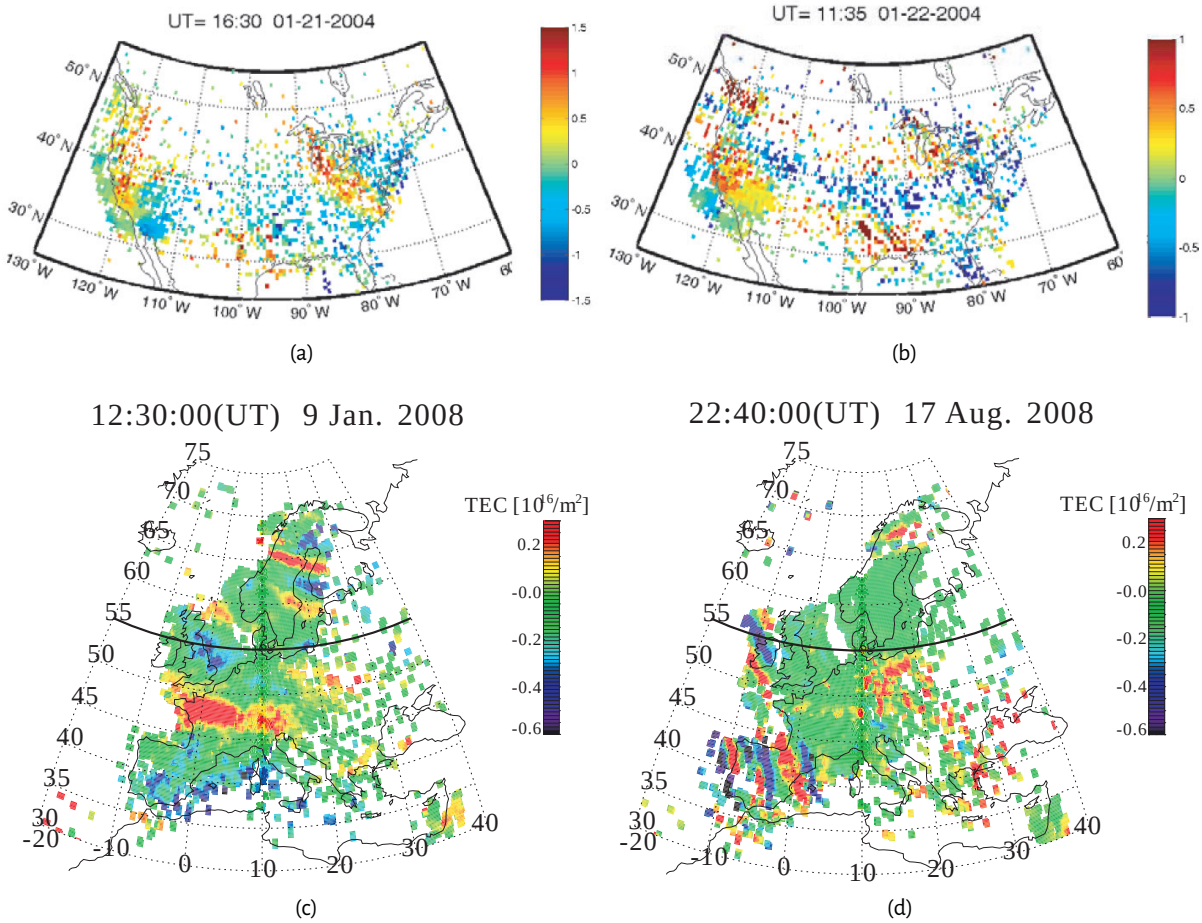

Figure 2.5: (a) and (b) Large scale traveling ionospheric disturbances over North America [from (Ding et al., 2008)]. (c) and (d) Medium scale traveling ionospheric disturbances over Europe [from (Otsuka et al., 2013)].

charge and mass and the permittivity of free space. Equation (2.3) thus becomes

$$n^2 = 1 - \frac{e^2}{4\pi^2 \epsilon_0 m} \frac{N}{f^2} = 1 - 2K\frac{N}{f^2}, \tag{2.4}$$

where $K = e^2/8\pi^2\epsilon_0 m \approx 40.28\,\mathrm{m}^3/\mathrm{s}^2$. Since n must be real for the wave to propagate, the plasma frequency sets a lower boundary below which waves cannot propagate, they will only penetrate the ionosphere when the wave frequency is higher than the plasma frequency. For $f \gg f_N$ the refractive index is

$$n \approx 1 - K\frac{N}{f^2}. \tag{2.5}$$

The refractive index decreases with the increase of electron density and with a decrease of frequency.

2.1.3.1 Dispersive medium

If the speed at which waves propagate through a medium depends on the frequency of the waves the medium is called *dispersive*. The wave speed has then to be distinguished in phase velocity and group velocity. The phase velocity is the speed at which a phase of a given level propagates; it is defined as

$$v_\mathrm{p} = \frac{\omega}{\kappa} = \frac{c}{n} = \frac{c}{1 - KN/f^2}, \tag{2.6}$$

where $\kappa = 2\pi/\lambda$ is the wavenumber, λ the wavelength, and c the speed of light in vacuum. Since the refractive index is always smaller than one, the carrier phase is faster in the ionosphere than in vacuum.

The group velocity is the speed at which the envelope of the wave pulse travels; it is given by

$$v_g = \frac{\partial \omega}{\partial \kappa} = \frac{c}{\frac{\partial n}{\partial \omega}\omega + n} = \frac{c}{1 + \frac{\omega_N^2}{\omega^2}} \approx cn = c\left(1 - K\frac{N}{f^2}\right). \tag{2.7}$$

The wave packet therefore always travels in the ionosphere slower than in free space. The phase and group velocities diverge from the speed in vacuum with opposite directions. Different phase and group velocities are a characteristic of a dispersive medium, such as the plasma.

2.1.3.2 From refractive index to propagation path delay

The wave propagation in the ionosphere takes longer in the ionosphere than in vacuum because the wave is *delayed* by the ionosphere. Integrating the propagation time along the wave path and subtracting the propagation time in vacuum, the propagation path delay for the ionosphere is obtained:

$$\Delta t = \int_L \frac{1}{v_g}\,\mathrm{d}l - \int_L \frac{1}{c}\,\mathrm{d}l \approx \frac{L}{c} + \frac{K}{cf^2}\int_L N\,\mathrm{d}l - \frac{L}{c} = \frac{K}{cf^2}TEC. \tag{2.8}$$

Similarly, the phase offset of a wave that travels through the ionosphere with respect to a wave that traveled in vacuum is

$$\Delta\phi = 2\pi\int_L \frac{\mathrm{d}l}{\lambda} - 2\pi\int_L \frac{\mathrm{d}l}{\lambda_0} = 2\pi f\int_L \left(\frac{1}{v_\mathrm{p}} - \frac{1}{c}\right)\mathrm{d}l = \frac{2\pi f}{c}\int_L (n-1)\,\mathrm{d}l = -\frac{2\pi K}{cf}TEC. \tag{2.9}$$

The offset is as expected negative, with respect to a wave propagating in vacuum the phase is *advanced*.

2.1.3.3 Faraday rotation

When also considering the magnetic field effect, the refractive index for left- and right-handed circularly polarized waves is (Davies, 1990)

$$n_{\mathrm{L,R}}^2 = 1 - \left(\frac{f_N}{f}\right)^2 \frac{1}{1 \pm f_B/f}. \tag{2.10}$$

The electron cyclotron frequency $f_B = e\boldsymbol{B}\cdot\hat{\boldsymbol{\kappa}}/2\pi m$ depends on the magnetic field strength B and on the angle between the magnetic field and propagation versor $\hat{\boldsymbol{\kappa}}$. The propagation velocity depends on the wave polarization, the high frequency approximation of (2.10) is

$$n_{\mathrm{L,R}} \approx 1 - \frac{1}{2}\left(\frac{f_N}{f}\right)^2\left(1 \mp \frac{f_B}{f}\right). \tag{2.11}$$

The differential phase advance between left and right polarized waves is

$$2\Omega = \frac{2\pi f}{c}\int_L (n_\mathrm{L} - n_\mathrm{R})\,\mathrm{d}l = \frac{2\pi f}{c}\int_L \frac{Ke\boldsymbol{B}\cdot\hat{\boldsymbol{\kappa}}}{\pi m f^3} N\,\mathrm{d}l = \frac{2Ke\boldsymbol{B}\cdot\hat{\boldsymbol{\kappa}}}{cmf^2}TEC. \tag{2.12}$$

The polarization angle of a linearly polarized wave propagating in the ionosphere is thus rotated due to the different propagation velocities of left and right polarizations, this effect is called *Faraday rotation*. The rotation angle is

$$\Omega = \frac{Ke\boldsymbol{B}\cdot\hat{\boldsymbol{\kappa}}}{cmf^2}TEC. \tag{2.13}$$

Effect	Ionosphere parameters	L-band	C-band
Range delay	$TEC = 10$ TECU	5 m	0.25 m
Phase advance	$TEC = 10$ TECU	21 cycles	4.8 cycles
Azimuth shift	$\rho_{TEC} = 1$ TECU/100 km $H_i = 350$ km	1.2 m	0.06 m
Range trend differential phase advance	$\Delta TEC = 10$ TECU	1.5 cycles	1.3 cycles

Table 2.1: Numerical examples of ionospheric effects for the L- and C-band systems of Table 2.2. The range delay is calculated with (2.14), the phase advance with (2.16), the azimuth shift with (2.28), and the differential range variation from near range to far range, which is due to the incidence angle change, with (2.40) and (2.14).

Parameter	L-band	C-band
Carrier frequency	1.27 GHz	5.6 GHz
FM rate	-565 Hz/s	-2265 Hz/s
Satellite speed	7650 m/s	7600 m/s
Satellite height	630 km	700 km
Incidence angle near range	37 °	31 °
Incidence angle far range	41 °	46 °

Table 2.2: Parameters of two example L- and C-band systems, based respectively on ALOS-2 and Sentinel-1.

2.2 Ionospheric effects on SAR

SAR is an active radar system, it transmits coherent radio wave pulses and collects the echoes that are reflected by the measurement targets. The received signals are processed to produce complex images of the area of interest. A spaceborne SAR is a satellite-mounted radar, which uses microwaves in a frequency range that can propagate through the atmosphere. However, the atmosphere might not be completely transparent to the traversing waves, and some unwanted effects might arise.

The propagation of radio waves in the neutral atmosphere is affected by the wave speed changes in its lower part, the troposphere. Due to the low height at which the troposphere influences the radar signals (0-100 km) with respect to the satellite orbit (500-700 km), propagation effects can only minimally interfere with the imaging process, but they can significantly change the image phase and change the range pixel position. On the contrary, the propagation in the atmosphere's ionized part, the ionosphere (100-1000 km), can both prevent the generation of good quality high-resolution images and disturb the information that can be extracted from them. The effects of the ionosphere on a SAR system are presented in the following and reviewed in (Quegan and Lamont, 1986; Ishimaru et al., 1999; Liu et al., 2003; Chapin et al., 2006; Xu et al., 2008; Meyer, 2011; Gilman et al., 2013).

In Table 2.1 numerical examples of some of the ionospheric effects illustrated in following sections are reported. The parameters of the two example SAR systems used for the calculations, with L- and C-band carrier frequency and based respectively on ALOS-2 and Sentinel-1, are indicated in Table 2.2.

2.2.1 Range delay and phase advance

Radars use the propagation time of the emitted, reflected, and received pulses to measure the distance between the radar and the scatterer, called range distance. Due to the lower refraction index of ionospheric plasma with respect to one, radio waves propagate in the ionosphere slower

than in vacuum, altering distance measurements and making targets appear more distant than they really are. The extra distance in meters, which is due to the ionospheric propagation path delay for the two-way trip, is, from (2.8),

$$\Delta r = \frac{2K}{f_0^2} TEC, \tag{2.14}$$

where TEC is the total electron content integrated along the propagation path, and f_0 the carrier frequency. The distance along the propagation axis is called slant range and its projection on the Earth ground range. The slant range is altered by Δr, the ground range change also depends on the incidence angle. By knowing the position of the satellite along its orbit, using a DEM and the measured satellite-target distance, it is possible to localize the target in the three-dimensional space; this process is called geolocalization. The ionospheric propagation delay worsens the geolocalization accuracy.

While the pulse envelope is retarded, the pulse phase is advanced, i.e., from (2.9):

$$\Delta\phi = -\frac{4\pi K}{c f_0} TEC. \tag{2.15}$$

If converted to meters the latter is equal to (2.14) but with opposite sign. Equations (2.15) and (2.14) are the signal phase delay and group delay, respectively.

2.2.2 Range impulse response

The ability of a radar to distinguish between two objects in the range direction depends on their distance with respect to the *range resolution*. The resolution depends on the range impulse response, which depends on the transmitted and received waveforms. The range resolution also limits the ability to measure small-scale features in the ionosphere, as it can be seen from the illustration of the system geometry in Figure 2.6. The nonlinear frequency dependence of the ionospheric refraction index causes a distortion of the propagating pulse waveform, altering the impulse response function and therefore worsening the range resolution. The temporal spreading of the received waveform depends on the bandwidth B and is given by (Fitzgerald, 1997; Kim, 2013):

$$\Delta\delta_t = \frac{2K}{c}\left(\frac{1}{(1-B/2f_0)^2} - \frac{1}{(1+B/2f_0)^2}\right) TEC \approx \frac{4KB}{c f_0^3} TEC. \tag{2.16}$$

The phase advance (2.15) can be approximated with a Taylor series expansion around the carrier frequency f_0 of the transmitted signal, obtaining:

$$\Delta\phi(f) \approx -\frac{4\pi K}{c f_0} TEC + \frac{4\pi K}{c f_0^2} TEC(f - f_0) - \frac{4\pi K}{c f_0^3} TEC(f - f_0)^2. \tag{2.17}$$

The first term is the carrier phase advance; the second term varies linearly with the frequency and is, therefore, the time delay caused by the propagation. The third term adds a quadratic phase to the signal waveform. If the latter is a *chirp*, this changes the chirp frequency modulation (FM) rate. The nominal output of the matched filter after the reception of a chirp is a cardinal sine function, a *sinc*. The system range resolution is given by the sinc main lobe width; the change of FM rate blurs the resulting sinc, worsening the resolution. If the extra phase at the edges of the signal spectrum remains under a certain level, e.g. π, then the blurring is limited and the impulse response function is not completely defocused. This holds true until the total electron content is lower than the upper limit set by (Belcher, 2008; Kim, 2013)

$$TEC < \frac{c f_0^3}{2KB^2}, \tag{2.18}$$

which, for L-band, is 120 TECU (with bandwidth 80 MHz).

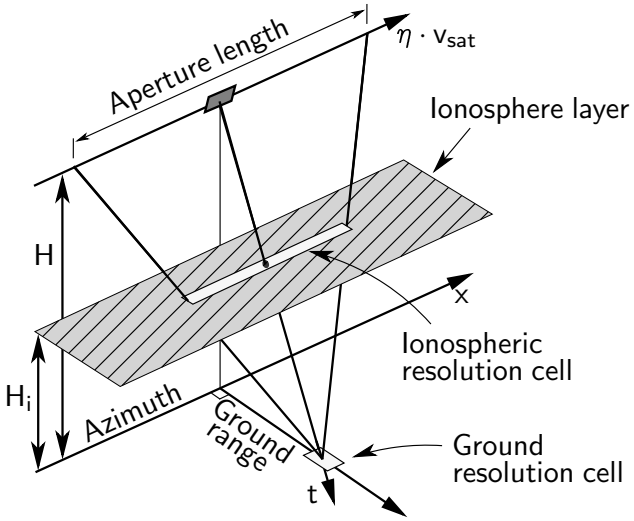

Figure 2.6: Geometry of the system. The ionospheric resolution is limited by the SAR range resolution and by the synthetic aperture length.

2.2.3 Azimuth impulse response

In SAR systems, the azimuth or along-track impulse response is formed by summing coherent pulses acquired from different orbit positions. This creates a long synthetic antenna, which permits to obtain higher azimuth resolutions than what could be obtained with just the real antenna. One of the differences between ionosphere and troposphere is the height at which they influence the radio waves propagation. The ionospheric electron density peak is located more or less halfway between the satellite and the target. Due to the motion of the platform, the ionospheric piercing points of the echoes, which come from a target, also horizontally move. The pulses that are used to synthesize the antenna thus travel through different parts of the ionosphere. If the ionosphere is not constant, a non-nominal phase history, which modifies the azimuth impulse response, is recorded. In general, a constant ionosphere does not have effects on the impulse response, a linear slope of the ionospheric TEC level in the azimuth direction produces a shift (adding an offset error to the geolocalization), and higher order variations can blur the azimuth impulse response.

In (Prats-Iraola et al., 2014) it was shown that the tropospheric path delay could introduce an azimuth defocusing. In the Appendix B it is demonstrated that, on the contrary, a constant ionosphere does not defocus the azimuth impulse response thanks to the particular opposition of the phase and group delay signs. In the following, to derive the ionospheric azimuth shift, the linear orbit approximation is considered. The geometry of the acquisition is sketched in Figure 2.6.

Indicating the slant integrated electron density along the orbit direction with $TEC(x)$, the ionospheric phase screen is

$$\phi(x) = -\frac{4\pi K}{cf_0} TEC(x), \tag{2.19}$$

where x is the azimuth spatial axis. The raw data of a target in $x = 0$, with complex reflectivity $a_0 \exp(j\alpha_0)$, are written as

$$s_r(\eta) = a_0 \exp(j\alpha_0) \operatorname{rect}\left(\frac{\eta}{T_a}\right) \exp\left(j\pi K_a \eta^2\right) \exp\left(j\phi\left(v_{\text{sat}} \eta \frac{H_i}{H}\right)\right) \tag{2.20}$$

where H_i is the height of the ionospheric single layer, H is the satellite orbit height, and η is the orbit slow time. The reflected signals are considered to be received only when the target is within the main lobe of the real antenna, which limits the aperture duration to $T_a = L_a / v_{\text{sat}}$, with L_a being

the synthetic aperture length. The received pulses are modulated in phase by the changing satellite-target distance, which forms the azimuth chirp; K_a is the azimuth chirp FM rate. Azimuth focusing is a convolution with the conjugated chirp:

$$\begin{aligned} s_f(\eta) &= \int s_r(u)\,\mathrm{rect}\left(\frac{\eta-u}{T_a}\right)\exp\left(-j\pi K_a(\eta-u)^2\right)\mathrm{d}u \\ &= a_0\exp(j\alpha_0)\int \mathrm{rect}\left(\frac{u}{T_a}\right)\mathrm{rect}\left(\frac{t-u}{T_a}\right)\exp\left(-j\pi K_a u^2\right)\cdot \\ &\qquad \exp\left(j2\pi K_a\eta u\right)\exp\left(j\phi\left(v_{\mathrm{sat}}u\frac{H_i}{H}\right)\right)\mathrm{d}u. \end{aligned} \tag{2.21}$$

It is convenient to rewrite $\phi(x)$ separating it in a term ϕ_0, which represents the phase average level within the synthetic aperture, a term ρ_ϕ, which is the linear component slope, and $\delta\phi$, which accommodates the residual nonlinear variations:

$$\phi(x) = \phi_0 + x\rho_\phi + \delta\phi(x), \tag{2.22}$$

where

$$\begin{aligned} \phi_0 &= \frac{1}{L_i}\int \mathrm{rect}\left(\frac{u}{L_i}\right)\phi(u)\,\mathrm{d}u, \\ \rho_\phi &= \frac{1}{L_i}\int \mathrm{rect}\left(\frac{u}{L_i}\right)\left.\frac{\mathrm{d}\phi(u')}{\mathrm{d}u'}\right|_{u'=u}\mathrm{d}u. \end{aligned} \tag{2.23}$$

The term L_i is the synthetic aperture length projected at the thin layer height:

$$L_i = L_a\frac{H_i}{H}, \tag{2.24}$$

as illustrated in Figure 2.6. The constant term can be brought outside the integral, and the (2.21) can be rewritten as

$$\begin{aligned} s_f(\eta) = a_0\exp(j\alpha_0)\exp(j\phi_0)\int \mathrm{rect}\left(\frac{u}{T_a}\right)\mathrm{rect}\left(\frac{t-u}{T_a}\right)\exp\left(-j\pi K_a u^2\right)\cdot \\ \exp\left(j2\pi K_a\eta u + jv_{\mathrm{sat}}u\frac{H_i}{H}\rho_\phi + j\delta\phi\left(v_{\mathrm{sat}}u\frac{H_i}{H}\right)\right)\mathrm{d}u. \end{aligned} \tag{2.25}$$

If $\delta\psi(\eta)$ can be assumed negligible, the latter integral can be solved with the stationary phase principle (Cumming and Wong, 1964), the orbit time for which the Doppler frequency is equal to zero is shifted by the ionospheric slope of

$$\Delta\eta_i = \frac{v_{\mathrm{sat}}H_i}{2\pi K_a H}\rho_\phi, \tag{2.26}$$

and the focused data becomes

$$s_f(\eta) = a_0\exp(j\alpha_0)\exp(j\phi_0)\,\mathrm{sinc}\left(K_a T_a(\eta-\Delta\eta_i)\right). \tag{2.27}$$

An ionospheric slope $\rho_{TEC} = cf_0/4\pi K\cdot\rho_\phi$ in TEC per meter thus shifts the target in azimuth of

$$\Delta\eta_i = \frac{2v_{\mathrm{sat}}KH_i}{cf_0K_aH}\rho_{TEC} \tag{2.28}$$

seconds. If the FM rate (for a straight orbit) is

$$K_a = -\frac{2v_{\mathrm{sat}}^2}{\lambda R}, \tag{2.29}$$

where R is the range of closest approach, the shift is

$$\Delta\eta_i = -\frac{KRH_i}{f_0^2 v_{\text{sat}} H}\rho_{TEC}. \tag{2.30}$$

To summarize, the synthetic aperture averages the electron density in the orbit direction acting as a moving window filter, limiting the effect of small-scale variations and the possibility to measure them. The average TEC within the aperture determines the carrier phase advance and group delay. The linear TEC variation shifts the focused data with respect to their true position in azimuth. Residual nonlinear variations blur the azimuth impulse response, defocusing the image.

The phase backscatter of a trihedral corner reflector is constant for reflection angle changes. By analyzing the Doppler phase history of a corner reflector, it should then be possible to obtain a line scan of the ionosphere without the aperture resolution limit.

2.2.3.1 Moving ionosphere and changing ionospheric height

Usually, it is assumed that the ionosphere is stable during the acquisitions, i.e., that the intensity of the TEC does not change with time, and that the ionospheric pattern does not move. This might not always be correct, as horizontal ionospheric drifts exist. They can be originated by diurnal variation in the production and loss of ionization, electromagnetic drift, and neutral winds. Traveling ionospheric disturbances propagate with speed between about 50 to 1000 m/s, generally towards the equator. Equatorial scintillation is generated by plasma irregularities which can move eastwards at speeds between 50 and 150 m/s (Davies, 1990; Kim and Papathanassiou, 2015).

A moving plasma in the ionosphere changes the ionospheric phase experienced by a target. Supposing a constant drift in the orbit direction, the phase screen (2.22) can now be written as

$$\phi(x,\eta) = \phi_0 + (x - v_{\text{az}}\eta)\rho_\phi + \delta\phi(x - v_{\text{az}}\eta), \tag{2.31}$$

where v_{az} is the drift speed. The target shift becomes then

$$\Delta\eta_i = \frac{KR(H_i - v_{\text{az}}/v_{\text{sat}} \cdot H)}{f_0^2 v_{\text{sat}} H}\rho_{TEC}. \tag{2.32}$$

An azimuthal ionospheric motion is thus equivalent to a lower actual ionospheric height.

Other phenomena, that might change the single layer ionospheric height within the geographical size of an image producing particular effects, are auroral arcs (Gomba and De Zan, 2015).

2.2.4 Faraday rotation

Polarimetric SAR measurements are affected by ionospheric Faraday rotation. The measured scattering matrix $\boldsymbol{M}$ is rotated with respect to the true scattering matrix $\boldsymbol{S}$, i.e.,

$$\boldsymbol{M} = \boldsymbol{RSR}, \tag{2.33}$$

with $\boldsymbol{R}$ being the one-way Faraday rotation matrix. The latter depends on the one-way Faraday rotation angle (2.13), i.e.,

$$\boldsymbol{R} = \begin{bmatrix} \cos(\Omega) & \sin(\Omega) \\ -\sin(\Omega) & \cos(\Omega) \end{bmatrix}. \tag{2.34}$$

The Faraday effect depends on the angle between propagation vector and magnetic field. This tends to be small near the geomagnetic equator, limiting the influence of high TEC values at equatorial latitudes. The largest Faraday rotation is expected in mid to high-latitudes, where the magnetic field is more aligned with the imaging direction than at the geomagnetic equator. Examples of Faraday rotation angles for typical scenarios can be found in (Wright et al., 2003).

Figure 2.7(a) and (b) shows an example of Faraday rotation on two L-band ALOS PALSAR images acquired in northern Alaska over the same region. The rotation angle has been estimated with the method described in (Freeman, 2004).

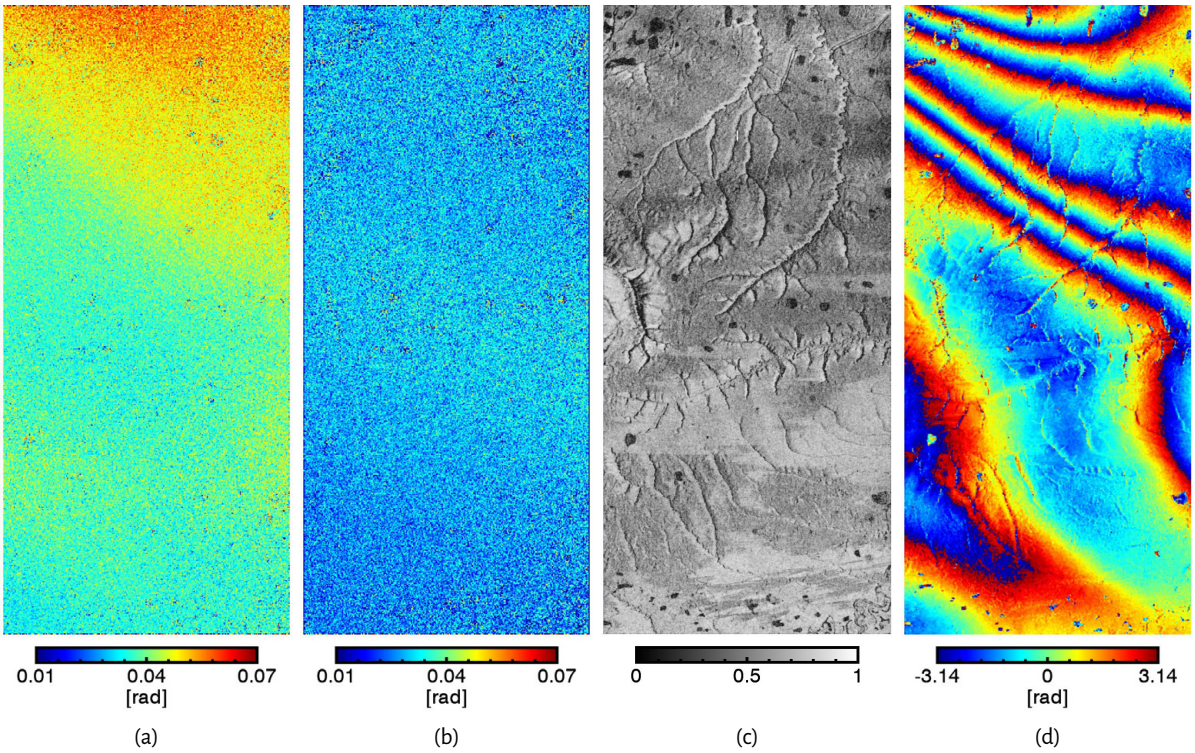

Figure 2.7: (a) and (b) Estimated Faraday rotation for master and slave image, (c) interferometric coherence and (d) interferometric phase. ALOS images acquired (a) April 1, 2006 and (b) May 17, 2006.

2.2.5 Amplitude scintillation

Equatorial plasma bubble phenomena create electron density irregularities elongated in the direction of the magnetic field. Due to ray bending, these irregular tubes of lower electron density can alter the power received along range, changing the amplitude of SAR images and creating undulating bright and dark stripes (Shimada et al., 2008). Figures 2.8(a) and (b) show scintillation effects on the amplitude of two SAR images acquired over the same ground area in the Amazonian region for different dates. These effects can be studied and simulated using a power law model of the irregularities (Rino and Fremouw, 1977; Rino, 1979; Shimada et al., 2008; Bernhardt et al., 2008; Belcher, 2008; Belcher and Rogers, 2009; Carrano et al., 2010; Meyer and Watkins, 2011; Carrano et al., 2012; Belcher and Cannon, 2013, 2014; Rogers et al., 2014; Meyer et al., 2016; Mannix et al., 2016).

2.3 Ionospheric effects on InSAR

The phase component of SAR images can be used to measure the distance between satellite and target with much higher accuracy than when using the pulse envelope. However, by using the phase, it is only possible to make differential temporal and spatial measurements.

Interferograms are used to measure the terrain elevation and its changes, i.e., the line of sight component of eventual ground deformation. They are therefore an important source of information for studying geophysical processes such as earthquakes, landslides, ice motion and subsidence. With a range change Δr the interferometric phase is

$$\Delta\phi = \frac{4\pi f_0}{c}\Delta r. \tag{2.35}$$

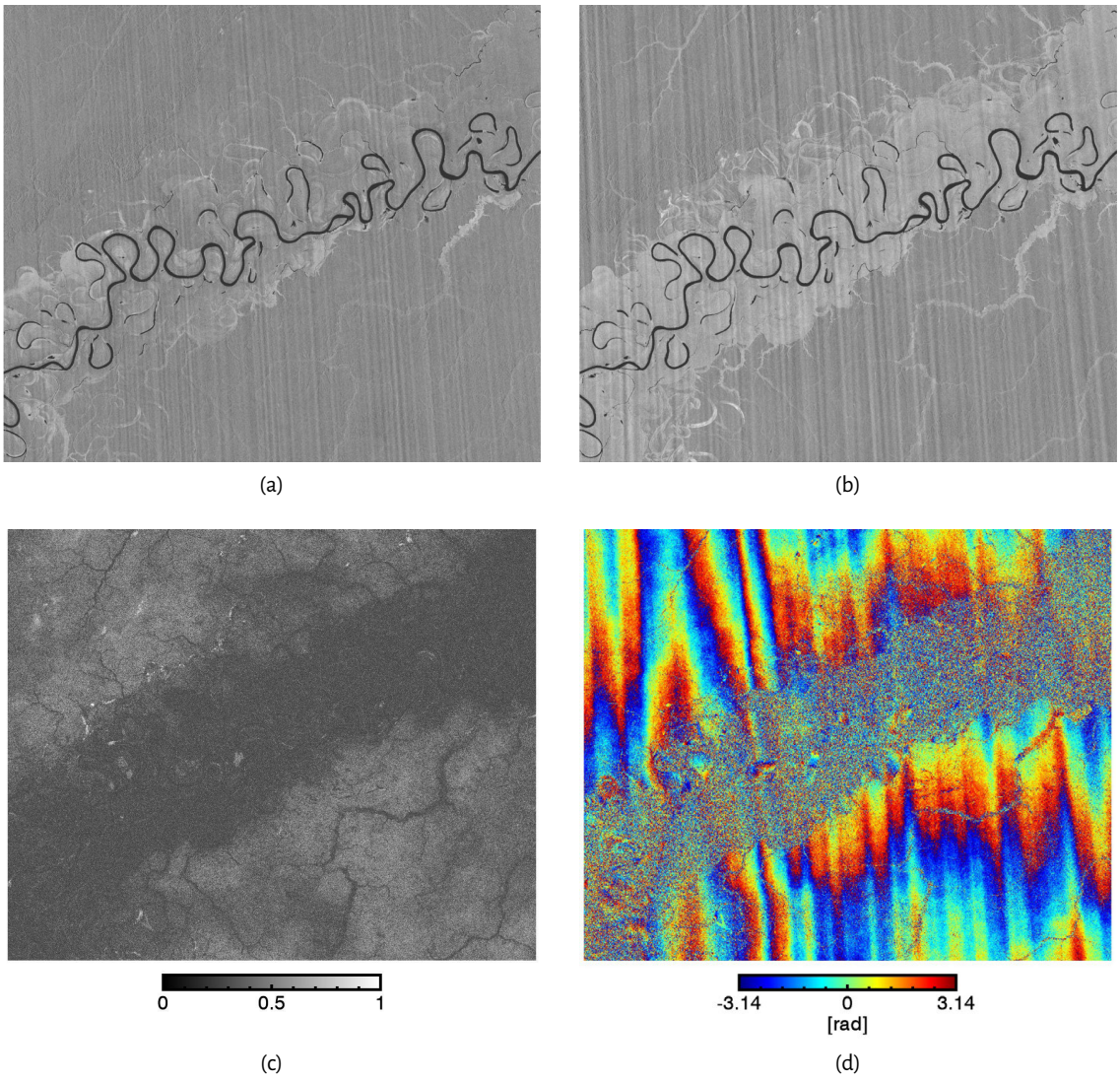

Figure 2.8: (a) and (b) Scintillation effects in master and slave SAR amplitude images, (c) interferometric coherence and (d) interferometric phase. ALOS images acquired (a) December 25, 2007 and (b) March 26, 2008.

The phase is proportional to the deformation and carrier frequency. Higher frequencies (X- or C-band) are more sensitive to ground motion than lower ones (P- or L-band), allowing for better accuracies. Higher frequencies are also less disturbed by the ionosphere, they seem then the optimal choice to measure ground deformations. The accuracy of InSAR measurements, however, is affected by temporal and volumetric decorrelation. Forested areas, which change quite fast in time, often show low levels of coherence, consequently high levels of phase noise and bad displacement measurements. Due to the higher penetration rate, lower frequencies signals can reach, and be reflected from, also the ground and tree trunks, which are more stable than leaves, permitting to obtain higher coherence levels. Moreover, the deeper penetration permits to also study lower vegetation layers. There is then a tradeoff in obtaining a high accuracy thanks to the higher sensitivity of higher frequencies or thanks to the lower phase noise of lower frequencies. Sometimes however, it is more convenient to use lower frequencies and be able to unwrap interferograms, rather than to use higher frequencies but not be able to perform phase unwrapping, as sometimes happens due to the strong phase noise in X- or C-band interferogram.

To conclude, the use of L-band InSAR data for observing surface displacements, for example caused by earthquakes, can be very beneficial. The retrieved signal is generally more stable against temporal phase decorrelation with respect to C-band and X-band InSAR data, such that fault movements in vegetated areas can be observed. In addition, due to the longer wavelength, larger displacement gradients that occur close to the ruptures can be measured. The drawback of L-band data, on the other hand, is that it is more strongly influenced by the inhomogeneity of the ionosphere. The spatial fluctuations of the electron content often cause long trends and small-scale variations in the interferometric phase, which distort the surface deformation signal and therefore affect the geophysical phenomena analysis. It is therefore important to remove or at least mitigate ionospheric effects in interferograms.

2.3.1 Range delay and phase advance

The interferometric phase is the sum of different components, i.e.,

$$\Delta\phi = \frac{4\pi f_0}{c}(\Delta r_{\text{topo}} + \Delta r_{\text{mov}} + \Delta r_{\text{tropo}}) - \frac{4\pi K}{c f_0}\Delta TEC, \tag{2.36}$$

where f_0 is the carrier frequency; and Δr_{topo}, Δr_{mov} and Δr_{tropo} are the topographic path delay (which includes the flat-earth phase and the topography-related phase), the differential path delay associated with a ground movement between acquisitions, and the differential tropospheric path delay, respectively. The nondispersive contributions to the interferometric phase are grouped in

$$\Delta\phi_{\text{non-disp}} = \frac{4\pi f_0}{c}(\Delta r_{\text{topo}} + \Delta r_{\text{mov}} + \Delta r_{\text{tropo}}), \tag{2.37}$$

to distinguish them from the dispersive ionospheric contribution

$$\Delta\phi_{\text{iono}} = -\frac{4\pi K}{c f_0}\Delta TEC, \tag{2.38}$$

where ΔTEC is the differential TEC, i.e., the TEC difference between the two acquisitions. The negative sign in (2.36) and (2.38) indicates that the ionospheric contribution is a phase advance.

Similarly to the phase advance, the range delay that can be measured from the signal envelope is

$$\Delta r = \Delta r_{\text{topo}} + \Delta r_{\text{mov}} + \Delta r_{\text{tropo}} + \frac{2K}{f_0^2}\Delta TEC, \tag{2.39}$$

with respect to (2.36) the ionospheric component has here opposite sign.

Variations of the differential TEC level ΔTEC produce variations in the interferometric phase and in the mutual shifts between images. Figures 2.7(d) and 2.8(d) shows two examples of ionospheric effects on interferograms. All phase fringes are due to differential ionospheric variations. An aurora event was present during the acquisition of the master image in Figure 2.7, whereas scintillation and a gradient are present in the images of Figure 2.8. Figure 2.9(a) shows the differential range shift for the Alaska example, the ionosphere influence can here be clearly seen too.

A variation of the differential TEC within the image is not the only cause of an interferometric phase and group delay variation. For a constant vertical TEC, the incidence angle increase, from near to far range, increases the experienced slant TEC. A range phase variation appears in the interferogram when the two vertical TEC levels are different. The differential slant TEC as a function of the incidence angle is

$$\Delta sTEC(\theta) = (vTEC_m - vTEC_s)\cdot M(\theta), \tag{2.40}$$

where $vTEC_m$ and $vTEC_s$ are, respectively, the constant vertical TEC levels during master and slave acquisition, and $M(\theta)$ is the mapping function.

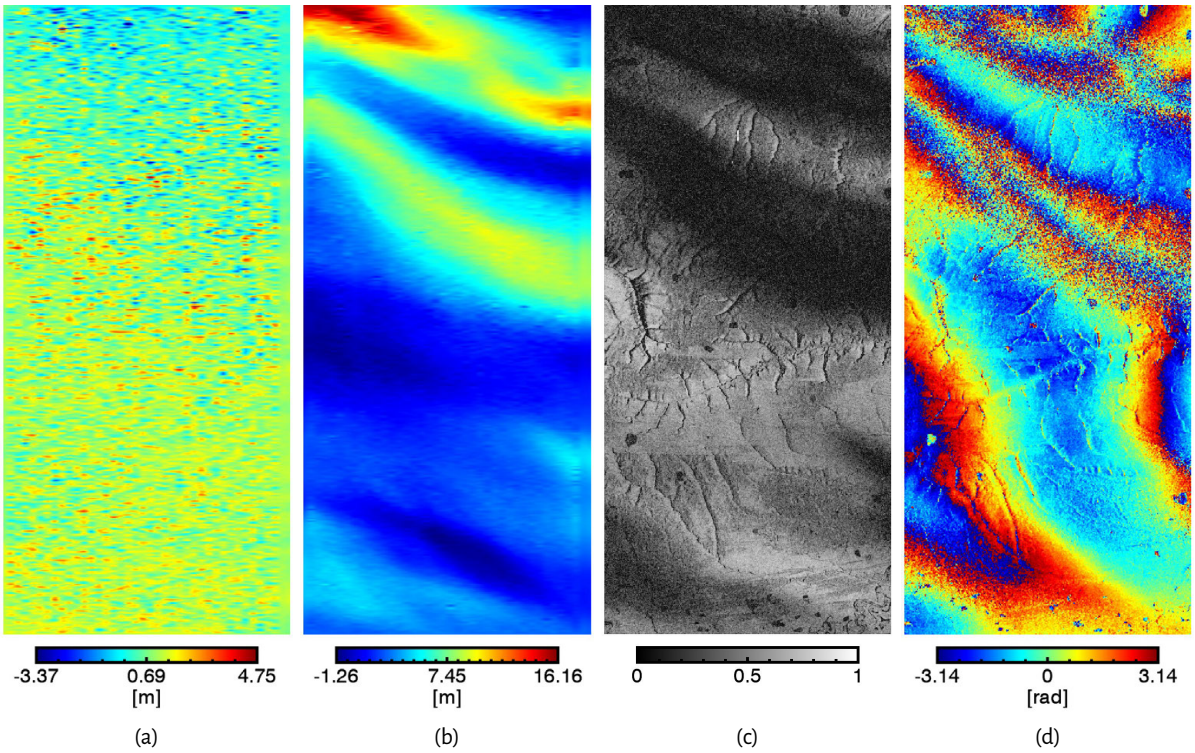

Figure 2.9: Differential (a) range and (b) azimuth shifts of the interferometric pair of Figure 2.7. Interferometric (c) coherence and (d) phase when only orbit information are used to coregister and resample the slave image, not the (a) and (b) shifts.

2.3.2 Azimuth shift

The ionospheric azimuth resolution is limited by the synthetic aperture length projected to the height of the ionosphere layer, as discussed in Section 2.2.3 and illustrated in Figure 2.6. The ionospheric phase screen observed in the interferogram is, therefore, a low-pass version of the *real*, possibly turbulent, ionosphere. Variations of the ionospheric path delay within the ionospheric azimuth resolution produce a non-nominal phase history, which causes azimuth effects like shift and blurring. The magnitude and correlation length of the variations, with respect to the azimuth resolution in the ionosphere, determine type and intensity of the effects. A linear trend of the ionospheric TEC along the flight path of the satellite causes an azimuth shift, while any deviation from a linear trend defocuses the image.

During the interferometric processing, the slave image is coregistered with the master by using patch-based cross correlation. The measured mutual azimuth shifts depend on the difference of ionospheric heights and slopes. From (2.28)

$$\Delta\eta_i = \frac{2v_{\text{sat}}KH_{\text{i}_1}}{cf_0K_aH}\rho_{TEC_1} - \frac{2v_{\text{sat}}KH_{\text{i}_2}}{cf_0K_aH}\rho_{TEC_2}, \tag{2.41}$$

where H_{i_1}, ρ_{TEC_1} and H_{i_2}, ρ_{TEC_2} are respectively the ionospheric height and slope present during the first and second acquisition. If the ionospheric height is the same during both acquisitions, or if ionospheric variations are present during only one acquisition, (2.41) becomes

$$\Delta\eta_i = \frac{2v_{\text{sat}}KH_i}{cf_0K_aH}\Delta\rho_{TEC}, \tag{2.42}$$

where H_i is the ionospheric height and $\Delta\rho_{TEC}$ is the differential ionospheric slope which also affects the interferogram phase.

Figure 2.9(b) shows the measured differential azimuth shifts for the Alaska example. Figure 2.9(c) and 2.9(d) show the coherence and phase of the interferogram, obtained using only orbit information to resample the slave image, and not the measured shifts of Figure 2.9(b) which, on the contrary, were used for the interferogram of Figure 2.7(d). It can be clearly seen how ionospheric shifts, if uncorrected, lower the coherence and bias the phase.

Azimuth shifts can be corrected by the coregistration and resampling steps, while a correction of the defocusing would require additional processing. Sub-apertures or semi-focusing can be used to recover the resolution (Tebaldini et al., 2012; Gomba et al., 2014) and improve those situations where the azimuth variations are so strong that they cause defocusing and loss of interferometric coherence. For all other cases, the coregistration and resampling are normally enough to recover the coherence. To produce an ionosphere-free interferogram, it is sufficient to estimate and remove the low-pass ionosphere that is superimposed to the interferogram (the ionospheric phase). In this sense, if the ionospheric variations, with respect to the aperture length, are moderate enough that they do not cause relevant azimuth defocusing or coherence losses after coregistration, the ionosphere can be considered *smooth* and there is no need to increase the ionospheric resolution using sub-apertures or semi-focusing.

2.4 Discussion

A general view of the possible ionospheric effects that can be expected on a SAR system acquiring images in low- or mid-latitudes can be derived from the description of the typical ionosphere states of Section 2.1. Most important is the acquisition local time and the geographical position. The highest electron density level can, in general, be expected at the equatorial anomaly crests after local noon, and the lowest one before sunrise. Therefore, the acquisition modes of different satellites listed in decreasing order of experienced average electron density are: descending ALOS-2 at 12 AM, ascending ALOS at 10 AM, ascending Sentinel-1, Tandem-L, and NISAR at 6 PM, ascending ALOS at 10 PM, ascending ALOS-2 at 12 PM, and descending Sentinel-1, Tandem-L, and NISAR at 6 AM. Higher electron density levels are possibly associated with steeper gradients and consequently with steeper differential gradients. Interferograms disturbed by ionospheric gradients can then be more often expected in the equatorial region.

The acquisitions that are more likely to encounter equatorial plasma bubbles are, in descending order, at 10 PM, 12 PM, and 6 AM, as also confirmed by simulations in (Meyer et al., 2016). TIDs can be expected in the mid-latitude region starting from the auroral zone, in particular after periods of strong solar activity. Aurora arcs can be expected in images acquired during night in the auroral oval. Scintillation effects are also expected in the high-latitude region.

2.5 Ionosphere correction methods

In this section, the current state of the art in estimating and correcting effects caused by the ionospheric propagation path delay on SAR and InSAR is summarized and reviewed. The lack of precise correction methods for interferograms motivated the development of this thesis.

Differently to what happens with troposphere corrections that have to rely on external data, a lot of information about the ionosphere can be extracted in various ways directly from SAR data. The particular effects that the ionosphere causes on images and interferograms differentiate it from other signals, permitting to estimate it. These effects are essentially the dispersion, the Faraday rotation, and the induced changes to the SAR azimuth impulse response. In Table 2.3 a summary of possible estimation methods is reported. The list is divided in the estimation of the absolute or differential ionosphere; the physical phenomena on which methods are based are reported as well.

Measured ionosphere part		Physical phenomenon	Effect on SAR	Measuring method	
Absolute ionosphere	Full	Dispersion	Range blurring	Single image	Range autofocus
	Azimuth second derivative	TEC azimuth variation	Azimuth blurring		Azimuth autofocus
	Full	Faraday rotation	Polarization angle rotation		Polarization angle rotation estimation
Differential ionosphere	Full	Dispersion	Range blurring	Image pair	Differential range autofocus
	Relative variation	Dispersion	Phase proportional to $1/f$		Split-spectrum method
	Relative variation	Dispersion	Phase proportional to $1/f$		Phase-group delay method
	Azimuth first derivative	ΔTEC azimuth variation	Azimuth shift		Cross correlation or spectral diversity

Table 2.3: Summary of ionospheric effects on SAR images and interferograms with estimation methods.

2.5.1 Absolute ionosphere

2.5.1.1 Dispersion based

The dispersive propagation in the ionosphere blurs the range impulse response, as indicated in (2.16). This can be used to estimate the absolute TEC (Meyer et al., 2006; Meyer, 2010; Belcher, 2008). However, the effect is small and negligible, at least in L-band. Therefore, the estimation accuracy is also too low to permit to correct images or interferograms.

2.5.1.2 Faraday rotation based

The Faraday rotation angle can be measured from the images when quad-pol acquisitions are available. The rotation angle is then converted to a TEC value with (2.13). The accuracy of this method is limited by the signal noise, by the accuracy of the magnetic field model and by the system geometry. These and other aspects have been extensively discussed in (Gail, 1998; Rignot, 2000; Wright et al., 2003; Freeman and Saatchi, 2004; Freeman, 2004; Qi and Jin, 2007; Meyer and Nicoll, 2008; Nicoll and Meyer, 2008; Meyer et al., 2009; Kim and Papathanassiou, 2010; Pi et al., 2011; Kim et al., 2012). It has been shown that TEC estimates derived from Faraday rotation measures are relatively precise, and could possibly be used to correct the ionospheric phase screen in interferograms. The real performance of this method, however, still has to be thoroughly developed and demonstrated.

2.5.1.3 Azimuth impulse response based

Incoherent cross correlation between azimuth subbands of a single image is used in (Wegmüller et al., 2006) to measure the local along-track second derivative of the ionospheric electron density.

2.5.2 Differential ionosphere

The following methods are based on interferometric image pairs. Therefore, they only estimate the differential ionosphere.

2.5.2.1 Dispersion based

Another effect of the dispersive propagation is to delay the signal envelope, and to advance the signal phase, by the same value but opposite sign. The phase-group delay method (Meyer et al., 2006) takes the difference between the phase delay (the interferometric phase) and the group delay (the range mutual shift between the two images) to estimate the TEC. This method has been tested in (Brcic et al., 2010).

Similarly to the procedure used with dual frequency GPS receivers to measure the electron content, the split-spectrum method (Brcic et al., 2010; Rosen et al., 2010; Brcic et al., 2011) takes two range subbands and produces two interferograms, which are then used to estimate the ionospheric TEC. The accuracy of this method is similar to the one of the phase-group delay method.

Both the split-spectrum and the phase-group delay method use interferograms to estimate the differential TEC. They can therefore only recover the relative TEC variation between any two points in the image and are ambiguous with respect to a 2π cyclic constant value over the scene. However, the split-spectrum equations could be applied to the subbands group delay, the cross correlation range shifts between subband images, to recover the number of offset cycles (Brcic et al., 2010, 2011).

2.5.2.2 Azimuth impulse response based

Variations of the electron density generate azimuth shifts in SAR images. The differential shifts between an interferometric pair of images are usually measured during coregistration. The ionospheric phase screen superimposed to the interferogram is related to the differential shifts, which can then be used to estimate the phase screen. This possibility was suggested in (Meyer et al., 2006) and tested in (Raucoules and de Michele, 2010; Kim et al., 2011; Wegmüller et al., 2012; Hu et al., 2012; Jung et al., 2013; Chen and Zebker, 2014; Liu et al., 2014; Kim et al., 2015; Jung and Lee, 2015; Zhang et al., 2016).

Azimuth shifts are extremely sensitive to ionospheric variations. Therefore, they could provide a very good estimate of the electron density azimuth profile. Unfortunately, this method has also some problems: the shifts depend on the local azimuth derivative of the electron content, range variations cannot thus be recovered; secondly, azimuth integration of the shifts amplifies noise over long distances. This method is, therefore, unable to recover large-scale azimuth variations or range variations of the ionospheric phase screen. Finally, along-track ground displacements are mixed with ionospheric shifts and cannot be measured, hence, they disturb the ionosphere estimation. These issues have not been thoroughly solved yet by any of the previously cited works.

2.5.2.3 Combination of methods

Various single methods can estimate different parts of the absolute or differential ionosphere spectrum, with different accuracies. For example, absolute TEC estimates are generally more precise when based on Faraday rotation measurements rather than on the range curvature (due to the relatively small blurring effect at L-, C- or X-band), differential TEC range and azimuth variations can be well estimated by using the split-spectrum method but local azimuth variations can be even more precisely estimated by using azimuth shifts. It is then necessary to develop a strategy to handle these various information sources. In particular, a combination of more sources might improve the overall estimation accuracy and robustness.

Combination of different methods has been proposed and realized in previous works in various ways (Meyer et al., 2006, 2012; Kim et al., 2011; Jung and Lee, 2015; Liu et al., 2014; Jung et al., 2013; Zhang et al., 2016). In (Kim et al., 2011), for example, a least squares inverse problem is used to fuse the TEC estimates derived from Faraday rotation measurements with the azimuth shifts. The smoothness of the result is ensured by Tikhonov regularization with a differential operator oriented in the direction of the Earth's magnetic field, controlled by a weighting coefficient. Apart from the magnetic field orientation, no other physical a priori information about the ionosphere smoothness is used in the model covariance matrix. The spectral characteristics of the solution are then governed by the differential operator, it might thus be difficult to choose an optimum smoothing coefficient and to assess the accuracy and eventual bias of the result.

The procedure used in (Jung and Lee, 2015; Liu et al., 2014; Jung et al., 2013) first integrates the azimuth shifts, then recovers the integration constant and the long-distance errors by fitting the result to the interferometric phase. In this case, the smoothness of the result is governed by filtering windows and low-order polynomials with low physical significance. Furthermore, the polynomial fitting to the interferometric phase cancels long-wavelength signals that may have been caused by

ground motion, tropospheric variations or orbital errors, preventing the possibility to measure geophysical processes with large geographical scales. A slightly different approach is used in (Zhang et al., 2016), here the integrated azimuth shifts are fitted to the phase-group delay method result, not to the interferometric phase, allowing the measurement of slow ground motion.

2.6 Conclusion and organization of the thesis

The influence of the ionosphere on SAR images and interferograms differentiates it from other processes such as standard image formation, troposphere influence, or ground deformation. Its effects on the images can then be used to separate it from other sources, estimate it and possibly correct for it. Different methods produce various estimates of the ionosphere, some of the absolute one, some of the differential one, some only of relative variations, and all with different accuracies. These information sources could be joined, to obtain the best possible estimate of the ionosphere. For these reasons, a new method that combines data from various information sources was developed, and is presented in Chapter 6. It solves some of the problems that existing techniques have. This method can in principle be used to combine data about the absolute ionosphere, or the differential one, and possibly also to improve the estimation accuracy of the absolute one by including differential data. Once the ionospheric state at the time of the acquisitions has been recovered, it can be used to correct the images. One possibility is to only correct the effects, e.g., time delay, phase advance, Faraday rotation, and azimuth shifts. A more advanced solution would be to use the estimated ionospheric state to compensate images during the focusing process, obtaining ionosphere-free images. This possibility is partially evaluated in Chapter 5 with the semi-focusing processing. In this thesis, however, as InSAR measure of ground deformation are among the most important products of spaceborne SAR systems, the focus is put on the estimation of the differential ionospheric phase screen, which is superimposed on interferograms. The combination method is then only used with base methods that estimate the differential ionosphere, and the compensation is realized by simply subtracting the estimated phase screen from the interferogram. Two information sources are here combined, the split-spectrum method, which exploits the dispersive propagation, and the integrated azimuth shifts method, which is based on the azimuth impulse response modifications. The split-spectrum method is thoroughly reviewed and tested in the next chapter. Its extension for wide-swath imaging modes with non-zero squint angles, as the TOPS mode, is presented in Chapter 4. The integrated azimuth shifts method is reviewed in Chapter 5. Finally, the combination method and its experimental results are presented in Chapter 6. A validation of the estimated phase screens is reported in Chapter 7.

3 The split-spectrum method

This chapter demonstrates how the range split-spectrum method is capable of estimating the ionospheric phase screen. To improve the method's robustness, its weaknesses are analyzed together with possible sources of systematic biases; solutions to mitigate these problems are proposed. Finally, examples based on L-band ALOS PALSAR images are provided. The data includes different coherence levels, different environmental conditions such as moving and nonmoving terrain, with and without topography, and different ionospheric conditions. The results show that the method is effectively able to compensate the ionospheric effects in interferograms, that the obtained accuracy is comparable with the expected one, and that the method can be easily applied to new test cases almost without tuning.

This chapter describes the paper in Appendix A: *Gomba, G., Parizzi, A., De Zan, F, Eineder, M., and Bamler, R. (2016). Toward Operational Compensation of Ionospheric Effects in SAR Interferograms: The Split-Spectrum Method. IEEE Transactions on Geoscience and Remote Sensing, 54(3):1446-1461*, (Gomba et al., 2016).

3.1 The range split-spectrum method

The range split-spectrum method (Brcic et al., 2010; Rosen et al., 2010; Brcic et al., 2011) suggests exploiting the different frequency behavior of the dispersive and non-dispersive components of the interferometric phase to separate them. The procedure consists in the generation of two range subbands (indices L for the lower and H for the higher subband) with center frequencies f_L and f_H. The interferograms computed from each subband yield the phases $\Delta\phi_L$ and $\Delta\phi_H$. Rewriting (2.36) for the two interferograms in terms of nondispersive and dispersive effects, one has

$$\begin{aligned}\Delta\phi_L &= \Delta\phi_{\text{nondisp}}\frac{f_L}{f_0} + \Delta\phi_{\text{iono}}\frac{f_0}{f_L},\\ \Delta\phi_H &= \Delta\phi_{\text{nondisp}}\frac{f_H}{f_0} + \Delta\phi_{\text{iono}}\frac{f_0}{f_H}.\end{aligned} \tag{3.1}$$

Inverting these equations, the dispersive $\Delta\phi_{\text{iono}}$ and nondispersive $\Delta\phi_{\text{nondisp}}$ components of the delay can be estimated, i.e.,

$$\begin{aligned}\Delta\hat{\phi}_{\text{iono}} &= \frac{f_L f_H}{f_0\left(f_H^2 - f_L^2\right)}(\Delta\phi_L f_H - \Delta\phi_H f_L),\\ \Delta\hat{\phi}_{\text{nondisp}} &= \frac{f_0}{\left(f_H^2 - f_L^2\right)}(\Delta\phi_H f_H - \Delta\phi_L f_L).\end{aligned} \tag{3.2}$$

This simple mathematical operation requires some care in the practical implementation. The method can, in fact, be realized in different ways, possibly successfully estimating the ionospheric

phase. However, there are some critical steps which could lead to a poor result if not carefully implemented. The interferometric coregistration, for instance, should be able to estimate strong ionospheric azimuth shifts, in order to correct them and recover the coherence. Another issue arises from phase unwrapping: given that the lower and upper interferograms have to be unwrapped prior to the scaling, eventual errors lead to a bias in the estimation. Finally, the interferometric phase noise, which is strongly amplified by the upscaling, has to be reduced. The resulting estimation accuracy will depend on the bandwidth, coherence, multilooking, and noise filtering. In Section 3.2, a possible implementation is proposed, and some critical steps are analyzed to improve the final result.

3.1.1 Split-spectrum method accuracy

In (Bamler and Eineder, 2005; Brcic et al., 2010), it is shown that the accuracy of the ionospheric phase estimate is maximized when the bandwidth of each subband is one third of the total bandwidth. For high coherence and large number of independent samples N, the accuracy is approximated using the interferometric phase variance of the subbands (Seymour and Cumming, 1994), i.e.,

$$\sigma^2_{\Delta\phi_{H,L}} = \frac{1}{2N_{\text{sb}}}\frac{1-\gamma^2_{H,L}}{\gamma^2_{H,L}} = \frac{3}{2N}\frac{1-\gamma^2_{H,L}}{\gamma^2_{H,L}}, \tag{3.3}$$

where γ is the interferometric coherence. The number of independent samples used in each interferogram N_{sb} is one third of the total N, since only one third of the bandwidth is used. Given that the two interferograms are uncorrelated, and supposing that the coherences are equal, from (3.2), the ionospheric phase accuracy is

$$\sigma_{\Delta\hat{\phi}_{\text{iono}}} = \left(\frac{f_L f_H}{f_0(f_H^2 - f_L^2)}\right)\sqrt{f_L^2 + f_H^2}\cdot\sigma_{\Delta\phi_{H,L}} \approx \frac{3f_0}{4B}\sqrt{\frac{3}{N}}\frac{\sqrt{1-\gamma^2}}{\gamma}. \tag{3.4}$$

Which, when converted to TECs, becomes

$$\sigma_{\Delta TEC} = \frac{3cf_0^2}{16\pi KB}\sqrt{\frac{3}{N}}\frac{\sqrt{1-\gamma^2}}{\gamma}, \tag{3.5}$$

and, when converted in meters,

$$\sigma_{\Delta r_{\text{mov}}} = \frac{3c}{16\pi B}\sqrt{\frac{3}{N}}\frac{\sqrt{1-\gamma^2}}{\gamma}. \tag{3.6}$$

The Cramér-Rao bound (CRB) gives the maximum achievable accuracy in estimating the ionospheric path delay, considering the information [which originates from the effect in (2.36)] that can be obtained from range signals. Comparing the CRB (see Appendix A for the derivation)

$$\sigma_{\Delta TEC} \geq \frac{cf_0^2}{4\pi KB}\sqrt{\frac{3}{2N}}\frac{\sqrt{1-\gamma^2}}{\gamma}, \tag{3.7}$$

with (3.5), it can be seen that the split-spectrum method accuracy is just 1.06 times worse than the Cramér-Rao bound.

Equations (3.5) and (3.6) are represented in Figure 3.1. The number of independent samples is calculated for a ground area size of 1 km^2; 1.27-GHz carrier frequency; 14-, 28-, and 85-MHz range bandwidth; 5-m azimuth resolution; and 30° incidence angle. For example, a coherence of 0.6 allows an accuracy of about 1 cm when performing the multilooking on an area of 1 km^2 using images with 28-MHz bandwidth. One centimeter seems already an acceptable accuracy because it is comparable with a typical residual tropospheric influence after compensation. However, the accuracy can be increased by further filtering, as shown in the next section.

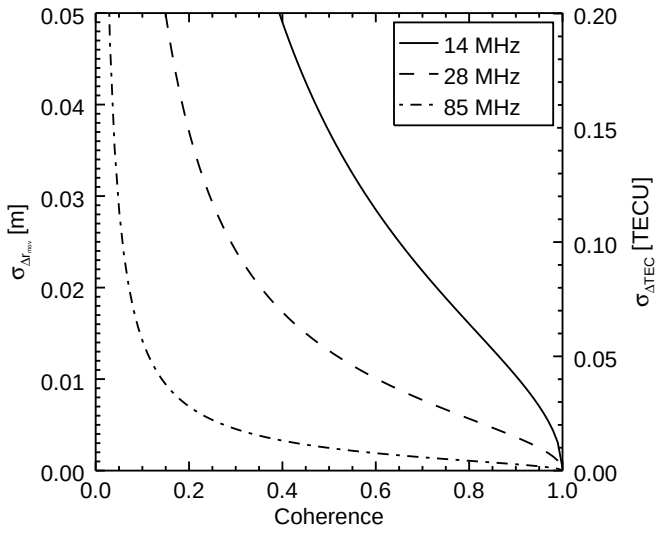

Figure 3.1: Standard deviation of the ground movement (left axis) and ionospheric phase (right axis) estimation, for a ground area of 1 km^2, as a function of the interferometric coherence. Different range bandwidths of (solid line) 14 MHz, (dashed line) 28 MHz, and (dash-dot line) 85 MHz are used. Carrier frequency is 1.27 GHz.

3.2 Implementation and systematic errors

Here follows a description of the proposed implementation of the split-spectrum method. In Figure 3.2 a schematic representation is reported.

First, the images have to be carefully coregistered. In order to ensure that, patch-based cross correlation with no polynomial fitting of the shifts is used. Therefore, in the case of strong ionospheric azimuth variations and/or ground movements, the high-frequency components of the motion field are preserved. Considering the wavenumber shift (Gatelli et al., 1994), in the second step, a common range band filtering is performed; this increases the coherence for pairs with non-zero normal baseline. Two subbands of one third of the total common bandwidth are then generated by bandpass filtering. To avoid phase biases, only after subband filtering the slave images are resampled using the shifts which have been estimated during the coregistration step. Azimuth shifts generated by ionospheric variations are thus corrected and the coherence recovered.

After resampling, an interferogram is calculated from each subband; orbit information and a digital elevation model (DEM) are used to compensate the topographic phase. Interferograms still contain the differential phase due to ground movements between acquisitions, the atmospheric phase, and the ionospheric phase. Both interferograms are unwrapped using a minimum cost flow algorithm. The dispersive and nondispersive components are separated by using (3.2). Differential phase unwrapping errors are then corrected as presented in section 3.2.3.

The ionospheric phase estimates are then filtered to reduce noise. Finally, the ionospheric phase screen is removed from the full-band interferogram obtaining an ionosphere-compensated interferogram.

3.2.1 Multilooking

In this implementation, there are two filtering (averaging) steps: the first is the multilooking performed during the interferogram generation on the complex data whereas the second is the filtering of the estimated ionospheric phase. The amount of multilooking and final filtering can be partly interchanged. However, a minimum initial multilooking has to be done to reach the efficient and asymptotic estimation of the phase (De Zan et al., 2015). Moreover, it has to be, as usual, small enough to obtain high resolution and no coherence losses due to rapid fringes but also big enough

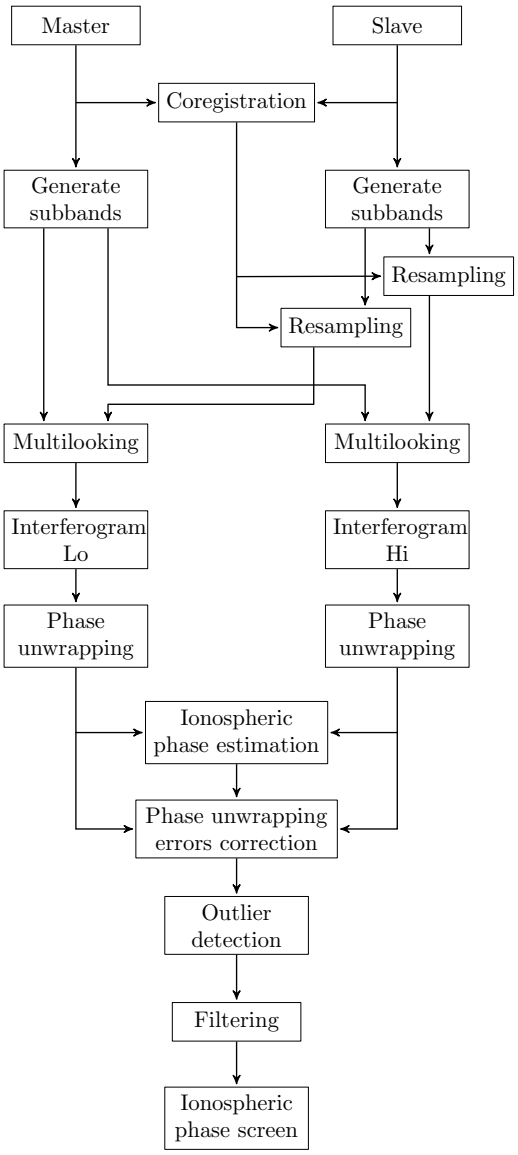

Figure 3.2: Implementation of the split-spectrum method.

such that phase unwrapping is possible. The multilooking factor is then constrained by these pre-requisites. Thereafter, one can decide how to perform the final filtering.

3.2.2 Filtering

With respect to the interferogram spatial sampling, the ionosphere is relatively smooth. The split-spectrum raw data can thus be further filtered, to remove part of the white noise. Here, a 2-D isotropic Gaussian filter is used. It is the normalized product of two identical 1-D Gaussian functions with variance $M^2/4\pi$ in range and azimuth. It reduces the phase variance by a factor equal to the effective number of looks, which is approximately M^2. To optimally combine samples, accordingly to the maximum likelihood principle (Kay, 1993), the split-spectrum estimates are weighted with the inverse of their expected variance (calculated from the interferograms coherence) prior to filtering.

Ionospheric variations with a spatial scale smaller than the filtering window are flattened. An anisotropic and/or adaptive filter could help to increase the accuracy without introducing biases due to excessive smoothing. This is realized in Chapter 6, along with the combination of different estimation methods.

3.2.3 Phase unwrapping errors

Phase unwrapping is performed separately on each subband, and phase unwrapping errors can therefore be different. A phase unwrapping error in the lower and upper subband can be defined with $2\pi m$ and $2\pi(m+d)$, respectively. This way, m is a common phase unwrapping error and d a differential one. Both terms are integers and not necessarily constant within the interferogram. Equation (3.1) becomes

$$\begin{aligned}\Delta\phi_L &= \Delta\phi_{\text{non-disp}}\frac{f_L}{f_0} + \Delta\phi_{\text{iono}}\frac{f_0}{f_L} + 2\pi m,\\ \Delta\phi_H &= \Delta\phi_{\text{non-disp}}\frac{f_H}{f_0} + \Delta\phi_{\text{iono}}\frac{f_0}{f_H} + 2\pi(m+d).\end{aligned} \tag{3.8}$$

The estimated ionospheric phase then yields

$$\Delta\hat{\phi}_{\text{iono}} \approx \Delta\phi_{\text{iono}} + \pi m + \frac{\pi}{2}d - \frac{3\pi f_0}{2B}d. \tag{3.9}$$

3.2.3.1 Differential phase unwrapping error

The term d is scaled by the factor f_0/B, generating a significant bias that should be removed. Taking the difference between the two interferograms, one has

$$\Delta\phi_L - \Delta\phi_H \approx -\frac{2B}{3f_0}\Delta\phi_{\text{non-disp}} + \frac{2B}{3f_0}\Delta\phi_{\text{iono}} - 2\pi d \tag{3.10}$$

whereas their sum yields

$$\Delta\phi_L + \Delta\phi_H \approx 2\Delta\phi_{\text{non-disp}} + 2\Delta\phi_{\text{iono}} + 4\pi c + 2\pi d. \tag{3.11}$$

The term d can be estimated from the phase difference (3.10), i.e,

$$\hat{d} = \left\lfloor \frac{1}{2\pi}\left(\Delta\phi_H - \Delta\phi_L - \frac{2B}{3f_0}\Delta\phi_{\text{non-disp}} + \frac{2B}{3f_0}\Delta\phi_{\text{iono}}\right)\right\rceil \tag{3.12}$$

where $\lfloor\cdot\rceil$ indicates the rounding to the nearest integer. Even if $\Delta\phi_{\text{non-disp}}$ and $\Delta\phi_{\text{iono}}$ are not known with high accuracy, they do not lead to large errors being reduced by the scaling term $2B/(3f_0)$. If needed, an iterative procedure can be implemented to reach the correct values.

3.2.3.2 Common phase unwrapping error

The recovery of the common term m is more delicate; using the phase sum (3.11) one has

$$\hat{m} = \left\lfloor \frac{1}{4\pi}\left(\Delta\phi_L + \Delta\phi_H - 2\Delta\phi_{\text{non-disp}} - 2\Delta\phi_{\text{iono}}\right) - \frac{d}{2}\right\rceil. \tag{3.13}$$

Inaccurate $\Delta\phi_{\text{non-disp}}$ and $\Delta\phi_{\text{iono}}$ are misinterpreted as phase unwrapping errors, leading to an even more inaccurate estimate of $\Delta\phi_{\text{non-disp}}$ and $\Delta\phi_{\text{iono}}$. Larger filtering windows can improve the accuracy of $\Delta\phi_{\text{non-disp}}$ and $\Delta\phi_{\text{iono}}$ but also lower the resolution. This can be unacceptable in particular for the ground-related phase, which is more likely to be spatially variable. The success of this method depends on the scene characteristics (high coherence or smooth signals) and is therefore not robust enough. A common phase unwrapping error, on the other hand, has a small impact, compared with a differential one. Moreover, it can be considered negligible if its magnitude is smaller than the accuracy (3.5), as it usually happens for small error areas.

Wide areas with ambiguous phase unwrapping, e.g., when a river cut an image in two parts, can neither be recovered nor simply ignored. However, this is a general problem for interferometry; radargrammetry or GPS measurements could normally be used to solve it. Unfortunately, the presence of the ionosphere makes the radargrammetry method inapplicable. The expression of the group delay (2.39) is

$$\Delta r = \Delta r_{\text{topo}} + \Delta r_{\text{mov}} + \Delta r_{\text{tropo}} + \frac{2K}{f_0}\Delta TEC, \tag{3.14}$$

which is measured by the range shifts. The difference between the group and phase delay contains both the ionosphere and the absolute phase offset, which cannot be separated.

It is possible to estimate the unambiguous phase by applying the same principle of the split-spectrum method to the radargrammetric shifts of the subbands. Unfortunately, the resulting accuracy is very low, i.e.,

$$\sigma_{\Delta\hat{\phi}_{\text{iono}}} \approx \frac{9f_0^2}{2B^2}\sqrt{\frac{1}{N}}\frac{\sqrt{1-\gamma^2}}{\gamma}, \tag{3.15}$$

making this procedure unlikely applicable.

3.2.4 Asymmetric split-spectrum mode

Here, a special split-spectrum mode for SAR systems with larger bandwidth, such as the Tandem-L, ALOS-2 or NASA-ISRO SAR (NISAR) missions, is evaluated. This mode optimizes the compromise between data rate and accuracy. While wider bandwidths increase the accuracy of ionosphere estimation, the satellite onboard storage and downlink of a great amount of data is not always feasible. The optimum solution to still obtain a high accuracy with a smaller data volume would be to use two subbands of one third each of the allowed bandwidth, separated by one third. However, if the total used bandwidth is further reduced to decrease the data amount, the ionosphere estimation noise grows. The new precision in estimating the ground movement using two subbands of bandwidth B_L and B_H, from (3.6), is

$$\sigma''_{\Delta r_{\text{mov}}} = \frac{c}{4\pi f_0^2}\frac{f_L f_H}{f_H^2 - f_L^2}\sqrt{\frac{f_H^2}{2N_L} + \frac{f_L^2}{2N_H}}\frac{\sqrt{1-\gamma^2}}{\gamma}, \tag{3.16}$$

where $N_L = N \cdot B_L/B$ and $N_H = N \cdot B_H/B$ are the number of independent samples of each subband. For example, supposing to use one subband of 20 MHz and one of 5 MHz, separated by the greatest possible distance inside the 85-MHz allowed L-band spectrum, the accuracy of the split-spectrum method would then be 1.45 times worse than that obtained using an image with the full spectrum. This is anyway better than just using 20-MHz; in that case, the accuracy would be eight times worse. In conclusion, even if the total used bandwidth is reduced due to data constraints, a small second subband, separated by the greatest possible distance inside the allowed spectrum, permits to obtain almost the same accuracy in estimating the ionosphere as when using the full spectrum.

In (Brcic et al., 2009), it was shown that a custom chirp signal that concentrates all energy into the subbands increases the SNR with respect to a nominal chirp where a bandpass filter discards part of the energy to create the subbands. Similarly to what realized in (Brcic et al., 2009), a special mode that uses a modified chirp to increase the SNR, improving the accuracy (3.16), could be investigated in future work.

3.3 Application Examples

The split-spectrum method has been applied to four different ALOS PALSAR data sets to test its robustness and applicability. The first example is an interferogram of the 2008 Kyrgyzstan earthquake; it presents high coherence and smooth ionospheric variations. The excellent results show the correct separation between ground motion and ionospheric delay. The second example is a measure of the aurora in northern Alaska. Due to the narrow 14-MHz bandwidth, the accuracy is low and a big smoothing window is required. Consequently, small-scale variations of the ionosphere cannot be successfully recovered. A more challenging scenario, in the third example, is based on the 2008 Wenchuan earthquake. This dataset is composed of 72 interferograms featuring low and high coherence levels. Phase unwrapping errors and low coherence are the main limitations; the separation between ionospheric and ground phases has been, however, achieved, and phase jumps between adjacent tracks have been reduced. All acquisitions were made during ascending night passages; detailed information about each scene can be found in the Appendix A.

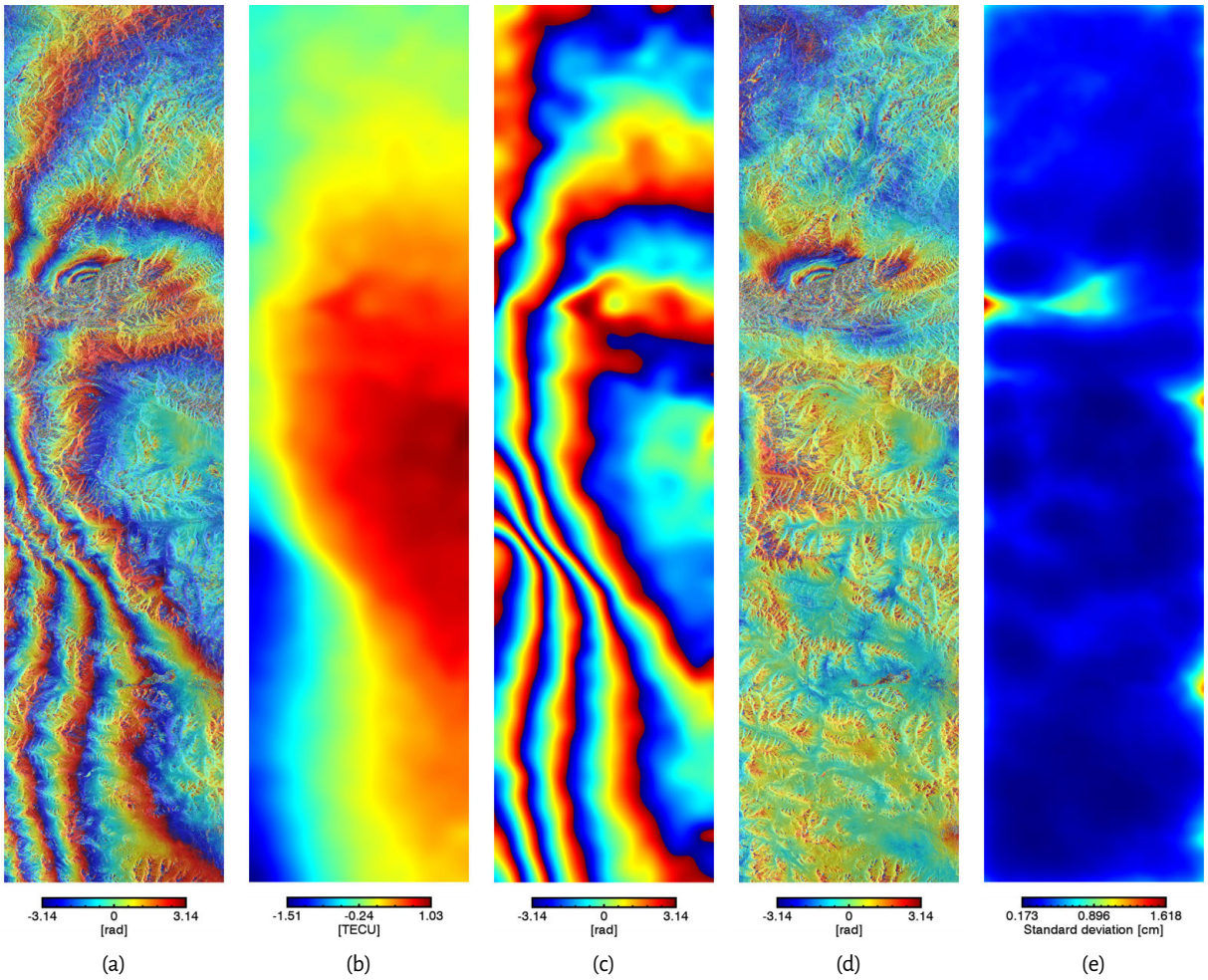

Figure 3.3: (a) Kyrgyzstan 2008 earthquake of October 5 can be recognized in the top part of the interferogram. Five fringes in the bottom part of (a) are supposed to be due to ionosphere changes. (b) The ionospheric TEC map, estimated using the split-spectrum method, converted to (c) a phase screen, is used to produce the (d) ionosphere-compensated interferogram. (e) Expected accuracy of the ionosphere estimation. Azimuth length is 283 km; range length is 68 km.

3.3.1 2008 Kyrgyzstan earthquake

On October 5, 2008, an earthquake struck the Nura region, in southern Kyrgyzstan. SAR data are used to measure the coseismic surface displacements (Teshebaeva et al., 2014). The interferogram is displayed in Figure 3.3(a); the topographic phase was removed from the interferogram using a digital elevation model (DEM). Apart from the earthquake, which is assumed to be localized only in the top part of the image, at least five fringes due to ionospheric variations can be seen in the bottom part of the interferogram. It is difficult to assess the real earthquake motion field since it is superimposed to the ionospheric phase screen.

The split-spectrum method was applied to the dataset. Although the accuracy is limited by the narrow range bandwidth of 14 MHz, the mean coherence is 0.43, and phase unwrapping was performed without problems. The ionosphere is relatively smooth; the point of fastest variation is in the middle of the image where five fringes are visible; this indicates a change of almost 3 TECU in about 45 ground km. The mean expected accuracy of the raw ionospheric estimates, calculated using (3.6), is 25 cm. The Gaussian filtering was used to increase the accuracy to about 2.5 mm, as shown in Figure 3.3(e). The output of the split-spectrum method [see Figure 3.3(b)], converted

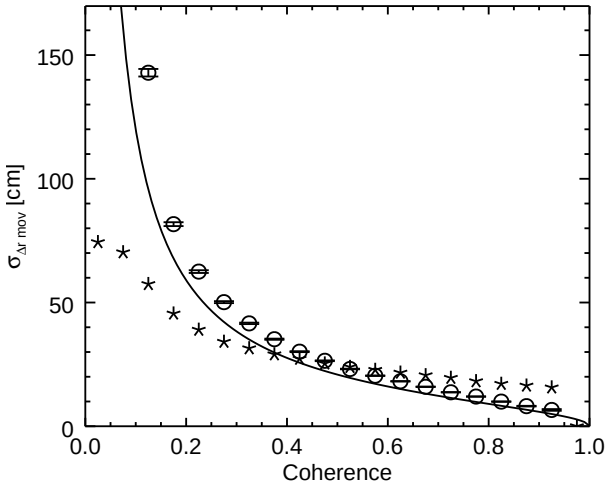

Figure 3.4: Accuracy of the ionosphere estimate before filtering, Kyrgyzstan test case. The line is the theoretical accuracy, and the symbols are the measured standard deviation. Asterisks are calculated using a moving window and the median absolute deviation. Circles are calculated using the smooth ionosphere to remove the mean value and then the sample standard deviation.

to a phase screen [see Figure 3.3(c)], is used to compensate the initial interferogram. The result in Figure 3.3(d) shows how the ionospheric contribution was successfully removed. The earthquake pattern can be easily recognized in the top part of the image, whereas no motion is observed in the bottom part; the 60-cm error that was introduced by five ionospheric fringes is now reduced to a millimeter level. The tropospheric delay is more visible; in particular, a strong correlation of the phase with the topography indicates the presence of stratified tropospheric delay.

To check the performances of the method, the standard deviation of the raw ionosphere estimate has been calculated after the outlier rejection step. Results are shown in Figure 3.4. The solid line represents the theoretical accuracy obtained from (3.6). The asterisks and the circles represent the standard deviation of ionosphere estimates and are calculated in two different ways. The good agreement between theoretical and measured accuracies confirms that the method performs as expected.

3.3.2 Aurora borealis

The same image pair used in Chapter 2 for the Alaska example, is used here to further test the method; the interferogram is shown in Figure 2.7(d). In one half of the image, six fringes are visible; this means that the differential ionosphere varies of almost 3 TECU in about 33 ground km. The total variation is similar to that of the previous example, but this time, it is less regular, and rapid undulations are present. A small smoothing window would then be preferred in order not to bias the output of the method. Unfortunately, the bandwidth is just 14 MHz and the estimated phase is quite noisy.

Figure 3.5 shows the ionospheric phase screen, and the respective compensated interferogram, filtered using a smaller [see Figure 3.5(a)] and a larger [see Figure 3.5(c)] kernel. The larger filtering window ensures a smoother, but unfortunately, biased result. There is a tradeoff between the increase of the accuracy obtained with more smoothing and the bias that too much filtering originates. In any case, the method was able to reduce the error from about 60 cm to some centimeters.

3.3.3 2008 Wenchuan earthquake

On May 12, 2008, an earthquake struck the Wenchuan region in central China. In the set of images typically selected by researchers for studying coseismic deformation patterns (Shen et al.,

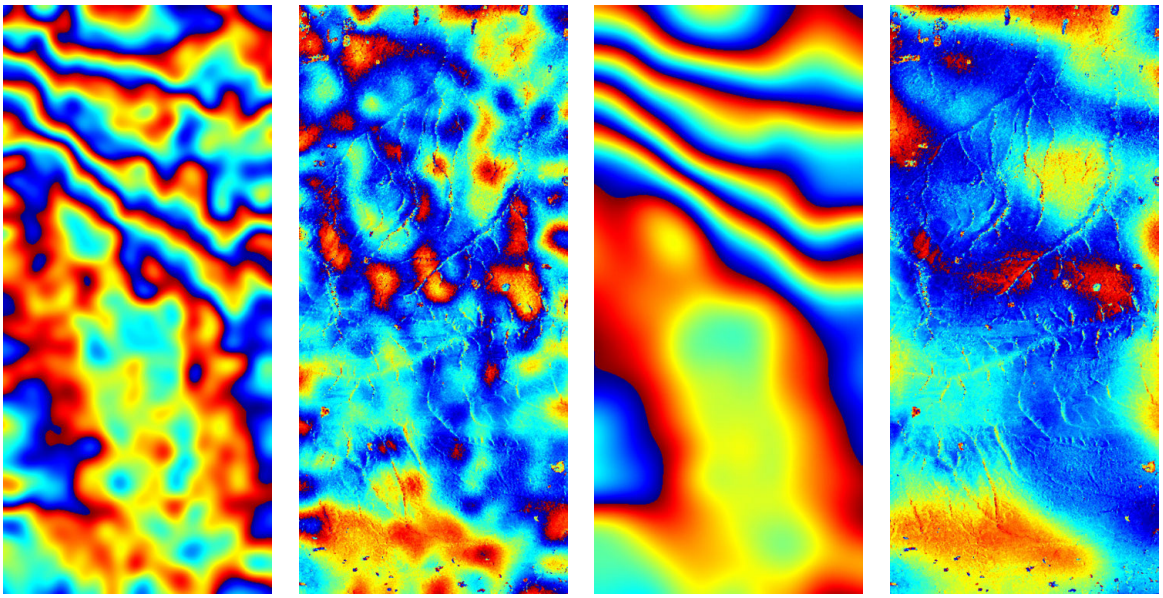

(a) (b) (c) (d)

Figure 3.5: (a) and (c) Estimated ionospheric phase screens. (b) and (d) Compensated interferograms. The larger smoothing window in (c), with respect to (a), ensures smoother but biased results. The colorbar goes from $-\pi$ to π for all images.

2009), the acquisition dates are chosen to reduce the influence of postseismic deformation on the interferograms. Unfortunately, they are heavily influenced by ionospheric distortions and need to be corrected to enable thorough geophysical modeling. To cover the whole earthquake many adjacent tracks have to be joined. Since each track was acquired on a different day, each one experienced a different ionosphere. A discrepancy between adjacent tracks can be expected due to aftershocks motion, different looking angles, and tropospheric delay. However, the strong phase jumps present in the interferogram of Figure 3.6(a), in particular far away from the earthquake, are an indication of ionospheric activity. Moreover, strong residuals between the range deformation predicted by the geophysical model and the InSAR deformation (Shen et al., 2009), are a further indication of the ionosphere presence.

This dataset is composed of 72 interferograms, and the coherence spans from low to high. The bandwidth is 28 MHz for almost all tracks. The differential phase unwrapping errors in the areas of low coherence were corrected as presented in section 3.2.3. The split-spectrum method output is subtracted from the interferogram and the result is shown in Figure 3.6(b). Ionospheric-induced errors in the ground motion estimation, of about 50 cm, have been thus removed. The size of the filtering window has been adapted to the mean coherence of each track to obtain an almost homogeneous accuracy of about 3 mm. It can be seen how the motion is now just localized around the fault and how phase jumps between different tracks are greatly reduced. Remaining discrepancies can be attributed to tropospheric delay and aftershock motion. The linear trend in the first track from the right could be caused by an orbit error or by a frame joining issue.

3.3.3.1 Phase unwrapping errors correction

Here, the effects of the unwrapping errors correction are shown. In Figure 3.7(a) the original interferogram used for this example is displayed. It is one frame of the first track from the left, just beneath the earthquake rupture. Figure 3.7(b) and (c) shows the raw ionospheric phase estimates before and after the correction. Biases, which are due to differential phase unwrapping errors, are present in the uncorrected estimates and are successfully eliminated in the corrected one. Figure 3.7(d) and (e) show the relative filtered phase screens whereas Figure 3.7(f) and (g) shows the

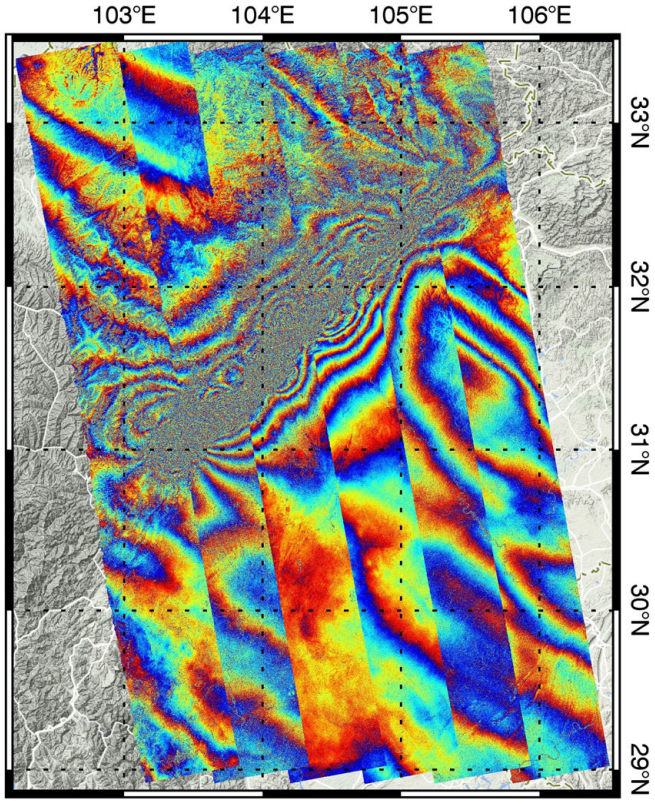

(a)

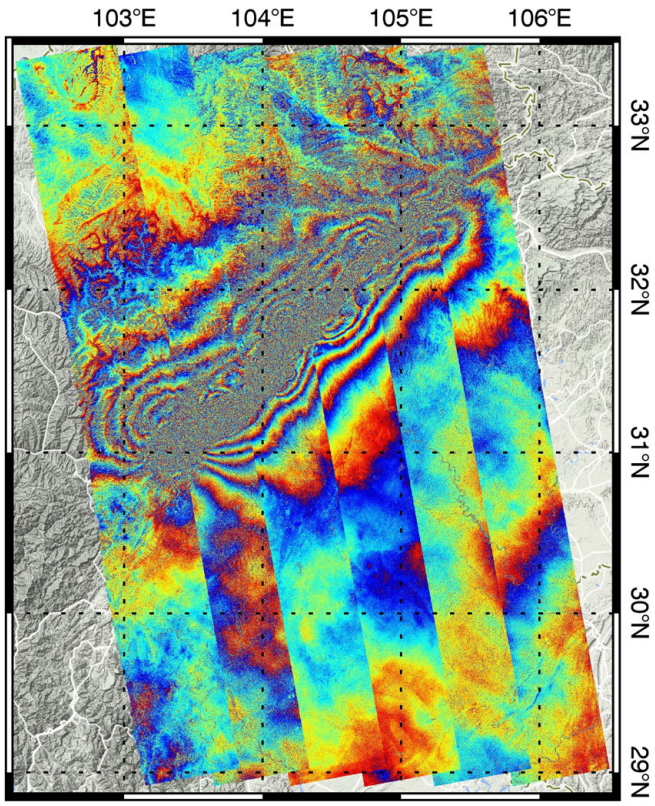

(b)

Figure 3.6: (a) Original 2008 Wenchuan Earthquake interferogram. (b) After ionosphere compensation.

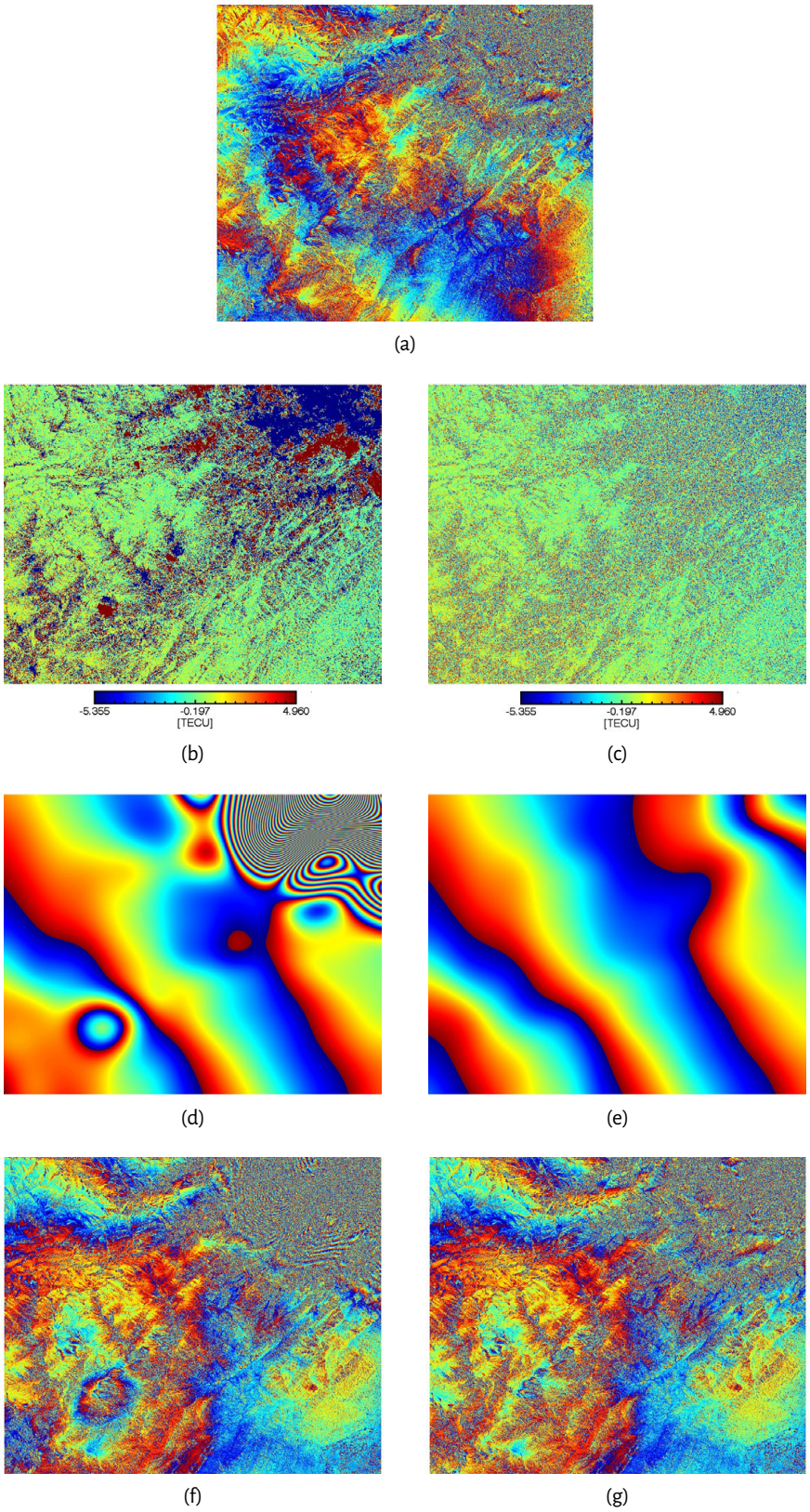

Figure 3.7: Result of the phase unwrapping errors correction. (a) Original interferogram. (b) and (c) Raw ionosphere estimates, (d) and (e) filtered phase screens, (f) and (g) compensated interferograms. The right column shows the improvement brought by the correction; the red an blu areas in (b) are differential phase unwrapping errors which produces biases in (d) and (f), see in particular the bottom left corner.

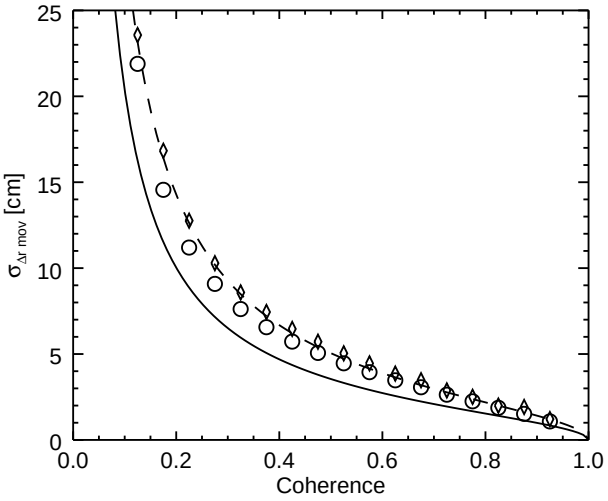

Figure 3.8: The expected accuracy of the 85 MHz acquisition is represented by the black line, while the circles are the measured standard deviation. The dashed line is the expected accuracy for the 20+5 MHz acquisition, diamonds are the measured standard deviation.

ionosphere-compensated interferograms.

3.3.4 Asymmetric split-spectrum mode

To validate the theoretical performance for 20+5 MHz SAR acquisitions that was developed in section 3.2.4, here, two 85-MHz ALOS-2 acquisitions over Alaska are analyzed. The size of the images is 57 km range and 69 km azimuth. This mode is intended to reduce the amount of data but still preserve the ionosphere estimation accuracy. Two subbands of 20 and 5 MHz are produced, at the two ends of the full available spectrum, with band pass filtering.

The split-spectrum method is then applied to the 85-MHz and 20+5 MHz acquisitions. The theoretical and measured standard deviations of the raw ionospheric phase estimate for both implementations are reported in Figure 3.8. The curves of the expected accuracy are calculated from (3.6) and (3.16). The ionosphere estimation accuracy obtained using asymmetrical subbands is close to that obtained with the complete bandwidth. The advantage of using a small second subband at the other end of the available spectrum is demonstrated; it allows a reduction of the bandwidth to save downlink and memory capacity without sacrificing the compensation of ionospheric disturbances. The good agreement between expected and measured accuracies proves again the precision of the assumptions.

The full bandwidth interferogram and the compensated one are presented in Figure 3.9.

3.4 Conclusion

The results in this chapter show that the split-spectrum method can effectively estimate the superimposed differential ionospheric phase screen in interferograms. The estimation accuracy depends on the system carrier frequency, on the range bandwidth, on the interferometric coherence, and on the turbulence level of the differential ionosphere. Ionospheric variations with smaller spatial scales than the isotropic Gaussian filtering window are not recovered, they bias the result lowering the accuracy of the final estimate. To overcome this problem, adapted anisotropic filtering and combination of various information sources will be presented in Chapter 6.

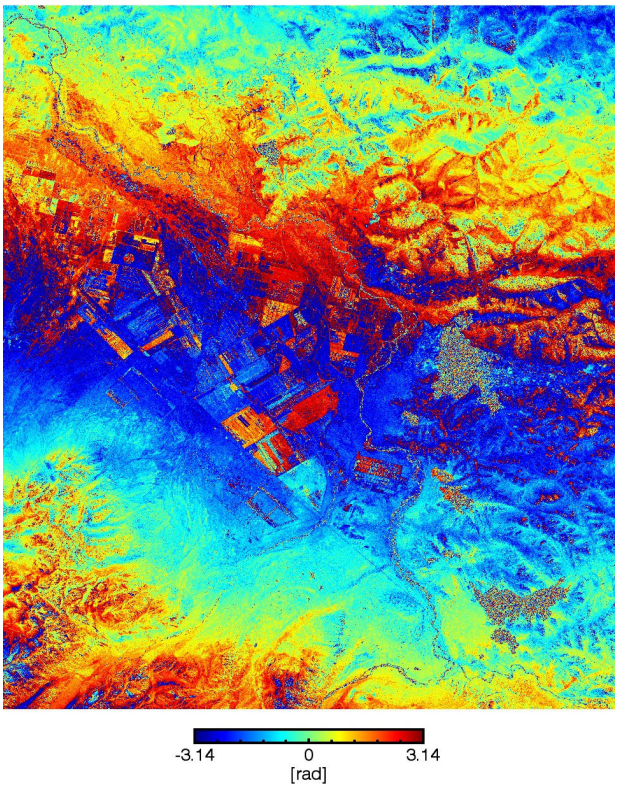

(a)

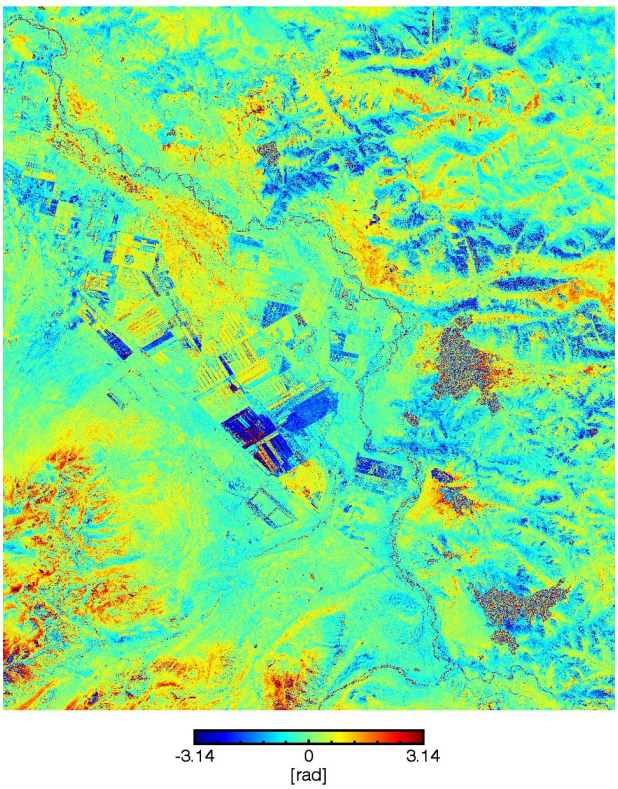

(b)

Figure 3.9: ALOS-2 85 MHz interferogram over Alaska. (a) Original. (b) Ionosphere-compensated version. Azimuth length is 69 km; range length is 57 km.

4 The split-spectrum method for TOPS and ScanSAR

Wide-swath imaging modes extend the ground range coverage, with respect to a Stripmap acquisition, to improve the study of large-scale geophysical phenomena. Terrain observation by progressive scans (TOPS) is the standard operation mode of the Sentinel-1 C-band SAR, and scanning synthetic aperture radar (ScanSAR) is operated by the L-band ALOS-2 satellite. Both modes do not image each subswath continuously, but operate in bursts, and use the time gap between bursts to extend the total imaged swath. As a result, some portions of the image are acquired in a squinted geometry. In this chapter, the split-spectrum method is adapted for squinted acquisitions.

The influence of the ionosphere on radio waves propagation is larger on L-band systems than on C-band systems, because the phase advance grows with the inverse of the carrier frequency. However, ionospheric effects on C-band systems have also been reported, for example, ionospheric strikes can be seen in azimuth displacement maps (Nagler et al., 2015). The examples in this chapter show that the ionospheric phase component can also be extremely relevant in C-band systems. The estimation and removal of ionospheric effects from C- and L-band SAR interferograms is therefore necessary to measure ground deformation over wide swathes.

This chapter describes the paper in Appendix B: *Gomba, G., Rodriguez Gonzalez, F., and De Zan, F. (2017). Ionospheric Phase Screen Compensation for the Sentinel-1 TOPS and ALOS-2 ScanSAR modes. IEEE Transactions on Geoscience and Remote Sensing*, (Gomba et al., 2017).

4.1 Ionospheric effects on squinted acquisitions imaging

Under the assumption of a single-layer model, by using the information about the line of sight (LOS) and the height of the ionospheric layer, it is possible to geometrically determine the ionospheric piercing point position of each target echo. The illustration in Figure 4.1 helps to understand the acquisition geometry and the ionosphere influence on the image formation; it reports the slow time-Doppler spectrum graph for two bursts, the ionospheric TEC level, the ionospheric phase (advance) in the focused image, and the phase spectrum of two targets.

In a TOPS image, the ionosphere is not continuously scanned like in a stripmap image. This happens because the squint angle rotates while the satellite is advancing. These two actions change the ionospheric piercing point position. The final effect is that some portions of the ionosphere are measured while other portions are not (see Figure 4.1). Moreover, at the conjunction between two bursts, the ionospheric piercing point suddenly changes, due to the sudden change of LOS. This means that, for a nonconstant ionosphere, a phase jump is present between bursts.

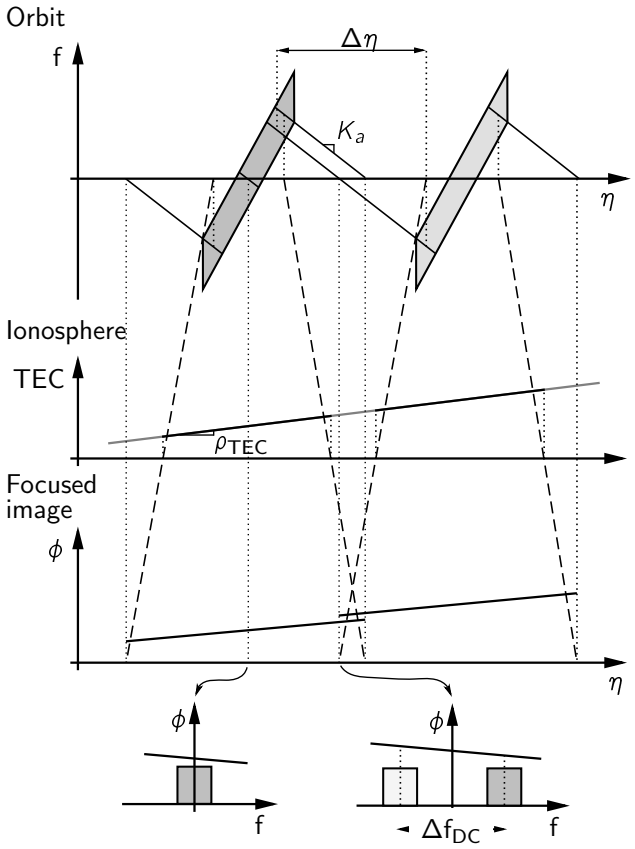

Figure 4.1: Doppler history of the TOPS acquisition. In the top part, the raw data time-Doppler graph of two bursts is plotted at the orbit height. In the middle, at the ionospheric single layer height, the TEC level. In the bottom are reproduced the focused image phase with the ionosphere contribution and the phase spectrum of two targets.

4.1.1 Azimuth shifts

Azimuth shifts that are due to a SAR system azimuth timing error, an orbit error, or a ground movement, generate different effects than azimuth shifts caused by ionospheric variations. The difference is analyzed in the following.

4.1.1.1 Physical Shift

A physical shift originates from an azimuth timing error or ground motion, thus from an actual raw data time shift. A physical shift does not change during the focusing process. A consequence of a physical shift is, after focusing, a phase ramp over the burst. The phase slope is proportional to the shift $\Delta\eta$ and the Doppler centroid frequency f_{DC}. A phase difference arises at the interface between two bursts, that is,

$$\Delta\phi_{\text{az}} = 2\pi\Delta f_{\text{DC}}\Delta\eta, \tag{4.1}$$

where Δf_{DC} is the Doppler centroid difference for the same ground point observed by the two bursts. Considering the maximum Δf_{DC} of 5.2 kHz, in order to limit the phase ramp to, for example, 3.6°, coregistration accuracy of approximately 1.3 cm would be required (Yagüe-Martínez et al., 2016).

4.1.1.2 Ionospheric Shift

An ionospheric shift, on the other hand, is caused by a phase change introduced by a nonconstant ionosphere. Variations of the ionospheric phase within the synthetic aperture produce azimuth shifts and defocusing effects in SAR images. Assuming a linear TEC level trend along azimuth (see Figure 4.1), with physical ionospheric slope indicated by ρ_{TEC} in slant TEC per meter, a target is shifted

by

$$\Delta\eta_i = -\frac{KRH_i}{f_0^2 v_{\text{sat}} H}\rho_{TEC}, \tag{4.2}$$

as described in Chapter 2.

It is important to note that an ionospheric shift does not generate an additional phase ramp over the burst and in the target spectrum (as a physical shift does); it is the ionospheric phase ramp in the target spectrum that generates the ionospheric shift.

4.2 Ionospheric effects on squinted acquisitions processing

In this section, the effects of the ionosphere on the interferometric processing of burst-mode images, which is realized with a standard processor (Yagüe-Martínez et al., 2016), are analyzed.

4.2.1 Azimuth shift estimation

Shift estimation of images with squinted geometry is a delicate step during interferometric processing. If the shift estimation is not accurate, a phase error, proportional to the Doppler centroid frequency, is present in the interferogram. Usually, only a scene offset is measured and corrected, to account for an azimuth timing error. The actual LOS should then be considered when interpreting the InSAR phase (De Zan et al., 2014). In the event that a linear azimuth ionospheric variation is present, it causes an additional shift. The total misregistration measure is then the sum of the azimuth timing error and the ionospheric shift. Measurement of the misregistration can be realized with different techniques (Yagüe-Martínez et al., 2016).

4.2.1.1 Cross-correlation

Coherent (CCC) or incoherent (ICC) patch-based cross correlation (Bamler and Eineder, 2005; De Zan, 2014) measures the mutual shift between two images in the time domain. By averaging all results over the scene, one obtains the timing offset summed up to the mean ionospheric shift. The ionospheric shift which is measured by cross correlation is the actual time shift induced by an ionospheric slope described in (2.30).

4.2.1.2 Enhanced spectral diversity

ESD exploits the Doppler centroid separation in the burst overlap areas to estimate the shift by using the spectral diversity method (Prats et al., 2010). Inverting (4.1), the shift estimator is

$$\Delta\hat{\eta} = \frac{\Delta\phi_{\text{az}}}{2\pi\Delta f_{\text{DC}}}. \tag{4.3}$$

The advantage of ESD over cross correlation is the higher precision due to the large spectral separation of the bursts in the overlap region. Conversely, cross correlation provides unambiguous measurements, whereas ESD cannot retrieve the ambiguity band.

The ionospheric shift that is measured by ESD depends on the ionospheric phase jump at the bursts overlap. Letting the slow time separation between bursts be

$$\Delta\eta = \frac{\Delta f_{\text{DC}}}{K_a}, \tag{4.4}$$

where K_a is the azimuth FM rate. From (2.22), considering a linear ionosphere, the phase jump for a target in the burst overlap is

$$\Delta\phi_{\text{az}} = \frac{4\pi K}{c f_0}\rho_{TEC}\Delta\eta\frac{H_i}{H}v_{\text{sat}}. \tag{4.5}$$

Combining (4.3) and (4.5), the estimated azimuth shift is then

$$\Delta\hat{\eta} = -\frac{KH_iR}{f_0^2 H v_{\text{sat}}}\rho_{TEC}, \tag{4.6}$$

which is equal to (4.2). For a linear ionosphere then, the ionospheric shift estimated either by cross correlation or ESD is the same. In case of a nonlinear ionosphere, the two techniques could yield slightly different results.

4.2.2 Azimuth shift resampling

The sum of the timing error offset and the global ionospheric shift is estimated (either with cross correlation or with ESD) and then corrected by resampling the slave bursts. The correction of the timing error offset removes the Doppler-dependent phase ramp term of (4.1). On the other hand, the correction of the ionospheric shift introduces an additional phase term to the bursts and consequently to the interferogram. In order to understand why this happens, the shift correction mechanisms in the Fourier domain are now recalled.

4.2.2.1 Physical shift

Consider the spectrum of an interferogram as illustrated in Fig 4.2(a). The interferogram is produced with a squinted acquisition that presents an azimuth differential displacement caused by ground motion or a timing error. The phase of the azimuth spectrum is composed of an offset, due to range motion, and a slope, due to the azimuth shift. The interferometric phase is the sum of the across-track motion phase, $\Delta\phi_{\text{rg}}$, and the along-track motion phase, $\Delta\phi_{\text{az}}$, of (4.1). That is,

$$\Delta\phi = \Delta\phi_{\text{rg}} + \Delta\phi_{\text{az}} = 4\pi f_0 \frac{\Delta r}{c} + 2\pi f_{\text{DC}} \Delta\eta, \tag{4.7}$$

where f_0 is the carrier frequency and Δr the cross-track range displacement. Coregistration, both cross correlation or ESD, measures the phase slope (a shift in the time domain) and resampling applies an inverse slope to shift the data. After resampling, the phase spectrum is constant, as shown in Figure 4.2(b). The interferometric phase is now just the range phase and a possible coregistration error multiplied by the Doppler centroid (not represented here).

4.2.2.2 Ionospheric shift

Consider a quadratic ionospheric trend along the azimuth direction, like the one represented in Figure 4.2(c). The interferometric phase is the across-track motion phase $\Delta\phi_{\text{rg}}$ plus the measure of the average ionospheric phase in the target spectrum, i.e.,

$$\Delta\phi = \Delta\phi_{\text{rg}} + \Delta\phi_{\text{iono}}. \tag{4.8}$$

The azimuth shift depends on the local ionospheric slope. Cross correlation or ESD retrieve the shift caused by the global linear trend of the ionosphere. The resampling step applies an inverse slope to shift the data. In Figure 4.2(d), the phase slope is not completely compensated because, here, the local shift is different from the global one.

In the physical shift case, the inverse phase slope cancels the phase that was introduced by the shift. This leaves in the interferogram only the phase related to the across-track motion. On the contrary, in the ionospheric-shift case, the inverse phase slope introduced by the resampling is a bias. The interferometric phase, in fact, is no longer a measure of the ionosphere at the squinted location, but it is approximately the phase that a zero-Doppler acquisition would have measured [see Figure 4.2(d)]. That is,

$$\Delta\phi = \Delta\phi_{\text{rg}} + \Delta\phi_{\text{iono}} - 2\pi f_{\text{DC}} \Delta\hat{\eta}, \tag{4.9}$$

where $\Delta\hat{t}$ is the applied resampling shift, the estimated global offset.

4.2.3 Interferogram

As a consequence of the changing LOS, not all parts of the ionosphere are measured by the interferogram, and phase jumps can be present between bursts. The interferogram that is produced with uncorrected slave bursts presents phase jumps, which are due to the abrupt LOS changes in

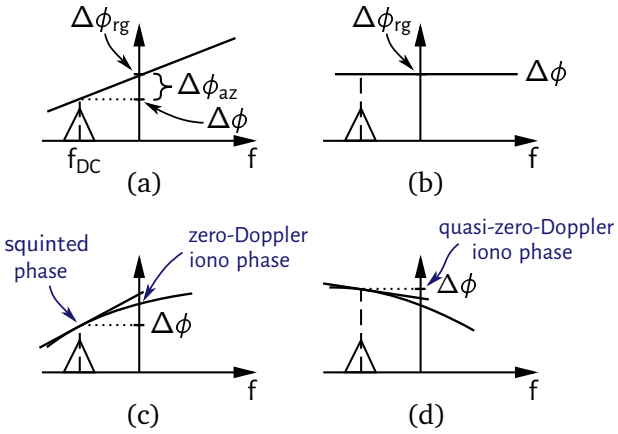

Figure 4.2: (a) Phase spectrum of an interferogram in presence of a physical azimuth shift. (b) After resampling, the azimuth phase is canceled. (c) Phase spectrum of an interferogram in the presence of a varying ionosphere. (d) After resampling, a phase bias which is proportional to the linear component of the ionosphere and to the Doppler centroid has been added. The interferometric phase is similar to what a zero-Doppler acquisition would have measured.

the ionosphere. The effect of the phase bias introduced by the resampling, which converts the ionospheric phase to a quasi-zero-Doppler ionospheric phase, is to greatly reduce these phase jumps or even eliminate them if the ionosphere is a linear slope. The eventual residual jumps in the resampled data interferogram are due to the linear approximation of the azimuth ionospheric phase and to the differences between local and global shift.

Finally, it has to be noted that the ionospheric phase component of the interferogram is dispersive, whereas the phase bias introduced by the resampling is nondispersive. Both these terms have to be estimated and removed by the ionosphere compensation method.

4.3 Ionospheric phase screen compensation

In the following, the split-spectrum method is adapted for estimating and compensating the ionospheric phase screen in Sentinel-1 TOPS images. A coseismic interferogram of the 2016 Taiwan earthquake is used in the following as a processing example. Acquisition parameters are reported in Appendix B.

The interferometric processing of TOPS mode images is realized as described in (Yagüe-Martínez et al., 2016). The azimuth offset estimation is performed using the ESD method. As can be seen from the resulting interferogram in Figure 4.3(a), there is a high number of fringes in the azimuth direction which would indicate a differential LOS displacement of about 50 cm along the Taiwan island. This large motion cannot be realistically attributed to a real displacement or a tropospheric effect; it must, therefore, be due to an orbit error or an ionospheric effect.

Assuming that all fringes are related to an ionospheric gradient, it is possible to calculate the azimuth shift that such a variation would cause by applying (2.30). The result is about 60 cm, which corresponds to the global shift measured by ESD. This excludes a large orbit error and confirms the ionospheric gradient. Furthermore, azimuth shifts (between master and resampled slave) measured at each burst overlap present residuals of several centimeters, much higher than the ESD estimation accuracy. This effect can be explained by a nonlinear ionospheric variation. Figure 4.6 shows the residual measured shift for each burst overlap of the first two beams (blue squares); the last beam is mostly incoherent. These residuals are due to the combined effect of a nonlinear ionospheric azimuth profile, and the phase bias introduced by the resampling of the ionospheric shift.

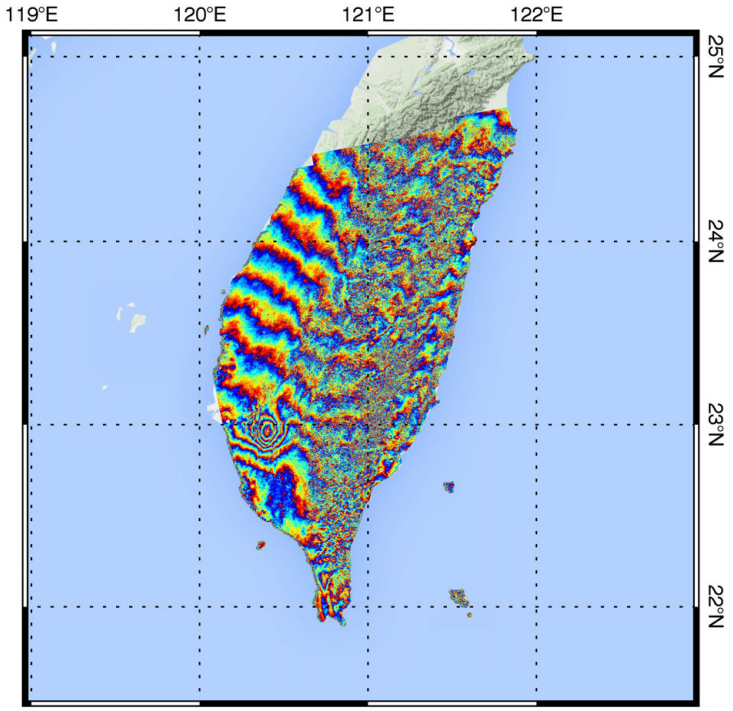

(a)

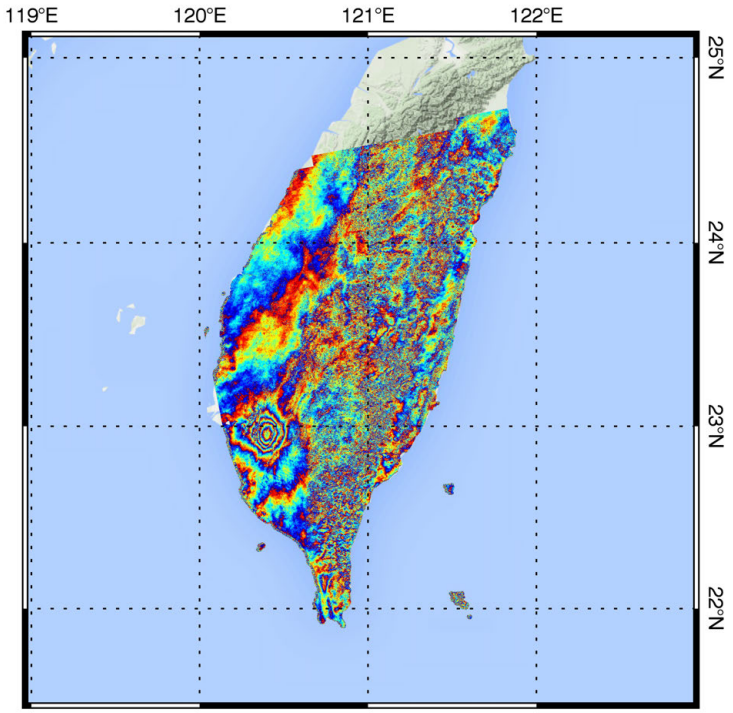

(b)

Figure 4.3: (a) Original Sentinel-1 interferogram of the February 2016 Taiwan Earthquake. (b) After ionospheric compensation.

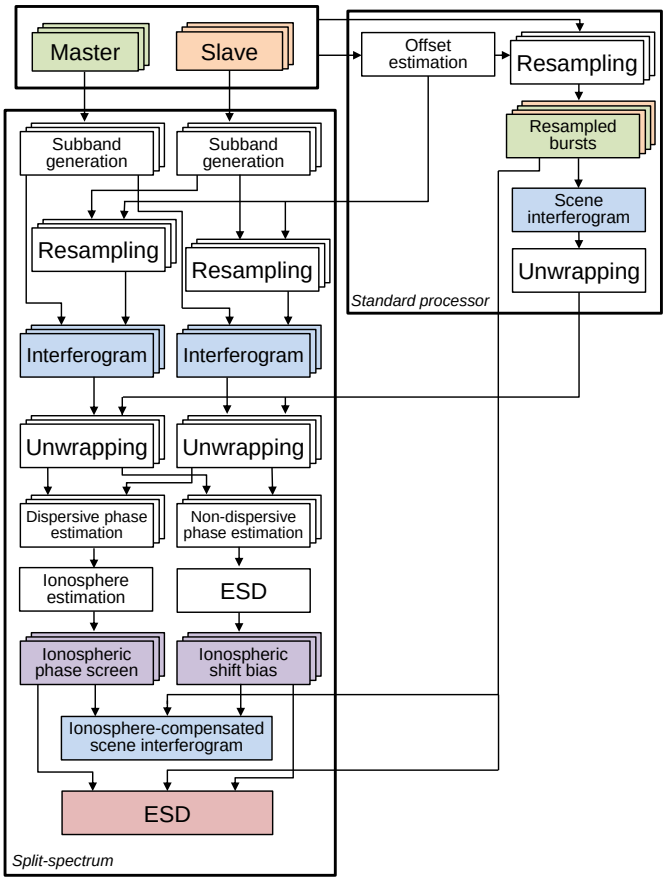

Figure 4.4: Implementation of the split-spectrum method for TOPS mode.

In summary, two correction approaches are possible. The most straightforward uses the split-spectrum method already during coregistration. The steps are the following: resample the bursts and remove the phase which is added by the resampling, apply the split-spectrum to the resampled bursts, apply ESD to the nondispersive phase to estimate the physical shift, remove the Doppler-dependent phase relative to the physical shift, use the dispersive phase to estimate the ionospheric phase screen, remove it from the bursts, and finally, compute the scene ionosphere-free interferogram.

This approach, however, would require modifying the existing processor (Yagüe-Martínez et al., 2016). In order to simplify the adaptations, an ionosphere correction module can be added. This removes the phase bias, which is introduced by the ionospheric shift resampling, by applying ESD to the raw nondispersive phase, estimating the ionospheric shift from the phase bias itself. Thereafter, the processing continues with the ionospheric phase screen compensation as in the previous approach.

4.3.1 Split-spectrum raw estimate

Here follows a description of the proposed modified split-spectrum method. In Figure 4.4, a flow chart is given. The proposed method can be implemented as an extension of a standard TOPS interferometric processor.

First, two range subbands for each burst are generated by bandpass filtering. The slave subbands are then resampled to maximize the coherence, by using the coregistration offset which has been estimated during the standard TOPS processing either with ICC or with ESD.

To accurately estimate the ionospheric phase screen, the split-spectrum method has to be applied at burst level rather than just at scene level; an interferogram is therefore calculated for each burst. Since the unwrapping of a single burst interferogram can be difficult, the unwrapped scene interfer-

ogram is used to unwrap the bursts. Finally, the raw estimates of the nondispersive and dispersive phase are respectively used to estimate the ionospheric azimuth shift and the ionospheric phase screen, as described in the following sections.

4.3.2 Ionospheric shift phase bias compensation

The coregistration and resampling steps measure and compensate a global azimuth offset, which is composed of a physical shift and an ionospheric shift. The linear component of the ionospheric azimuth variation in the scene produces the ionospheric shift. As introduced in Section 4.2.2, the resampling of the physical shift compensates its Doppler-related phase, whereas the resampling of the ionospheric shifts adds a phase bias. This should be removed to obtain the real ionosphere seen in the LOS direction. It is then necessary to estimate and separate the physical shift from the ionospheric shift.

The nondispersive phase is composed of the topography, the ground motion, the troposphere, and the phase bias. For an azimuth position t in a burst overlap area, we write the nondispersive phase of one burst and its adjacent one as $\Delta\phi^0_{\text{nondisp}}(\eta)$ and $\Delta\phi^1_{\text{nondisp}}(\eta)$, i.e.,

$$\begin{aligned}\Delta\phi^0_{\text{nondisp}}(\eta) &= \Delta\phi_{\text{ground}}(\eta) + 2\pi f^0_{\text{DC}}(\eta)\Delta t_i + n^0(\eta),\\ \Delta\phi^1_{\text{nondisp}}(\eta) &= \Delta\phi_{\text{ground}}(\eta) + 2\pi f^1_{\text{DC}}(\eta)\Delta t_i + n^1(\eta),\end{aligned} \tag{4.10}$$

where $\Delta\phi_{\text{ground}}$ is the topographic, motion, and tropospheric phase, f_{DC} is the Doppler centroid frequency and n is the split-spectrum estimation noise. The term $\Delta\eta_i$ is the global ionospheric shift that has to be estimated. The difference of the phases in (4.10) is the ESD phase, i.e.,

$$\Delta\phi^0_{\text{nondisp}}(\eta) - \Delta\phi^1_{\text{nondisp}}(\eta) = 2\pi(f^0_{\text{DC}}(\eta) - f^1_{\text{DC}}(\eta))\Delta t_i + n^0(\eta) - n^1(\eta). \tag{4.11}$$

The ionospheric shift can then be estimated with

$$\Delta\hat{t}_i(\eta) = \frac{\Delta\phi^0_{\text{nondisp}}(\eta) - \Delta\phi^1_{\text{nondisp}}(\eta)}{2\pi(f^0_{\text{DC}}(\eta) - f^1_{\text{DC}}(\eta))}. \tag{4.12}$$

A weighted mean, based on the accuracy of the split-spectrum method, is used to average the ESD phase and obtain a global estimate for the image. Since the estimated nondispersive phase derives from unwrapped interferograms, no cyclicity problems arise.

The accuracy of this estimate depends on the precision of the split-spectrum (3.4). For a Sentinel-1 acquisition with coherence of 0.5, the estimation accuracy of the ionospheric shift is about 1.5 cm (9 cm), if all burst overlaps (or only one burst overlap) are (is) used, and the phase bias correction accuracy is 3° (16°). Due to the low coherence and missing subswath, the expected accuracy for the Taiwan example is 5 cm.

The phase correction, i.e,

$$\Delta\phi_{\text{az-iono}} = 2\pi f_{\text{DC}}\Delta\hat{\eta}_i, \tag{4.13}$$

is then applied to the slave bursts. The ionospheric phase in the scene interferogram is now just a projection of the ionosphere according to the squinted LOS, and, as expected at this stage, strong phase jumps might appear.

4.3.3 Ionospheric phase screen compensation

The dispersive phase component is used to estimate the ionospheric phase screen. First, the ionospheric piercing point position for each interferogram pixel is calculated using the timing information and the ionospheric single layer model. In Figure 4.5(a), the raw dispersive phase estimates are plotted at their piercing point position for a supposed ionospheric height of 350 kilometers. The gaps in the ionosphere measurement can be clearly seen. Second, the raw phase is smoothed by Kriging

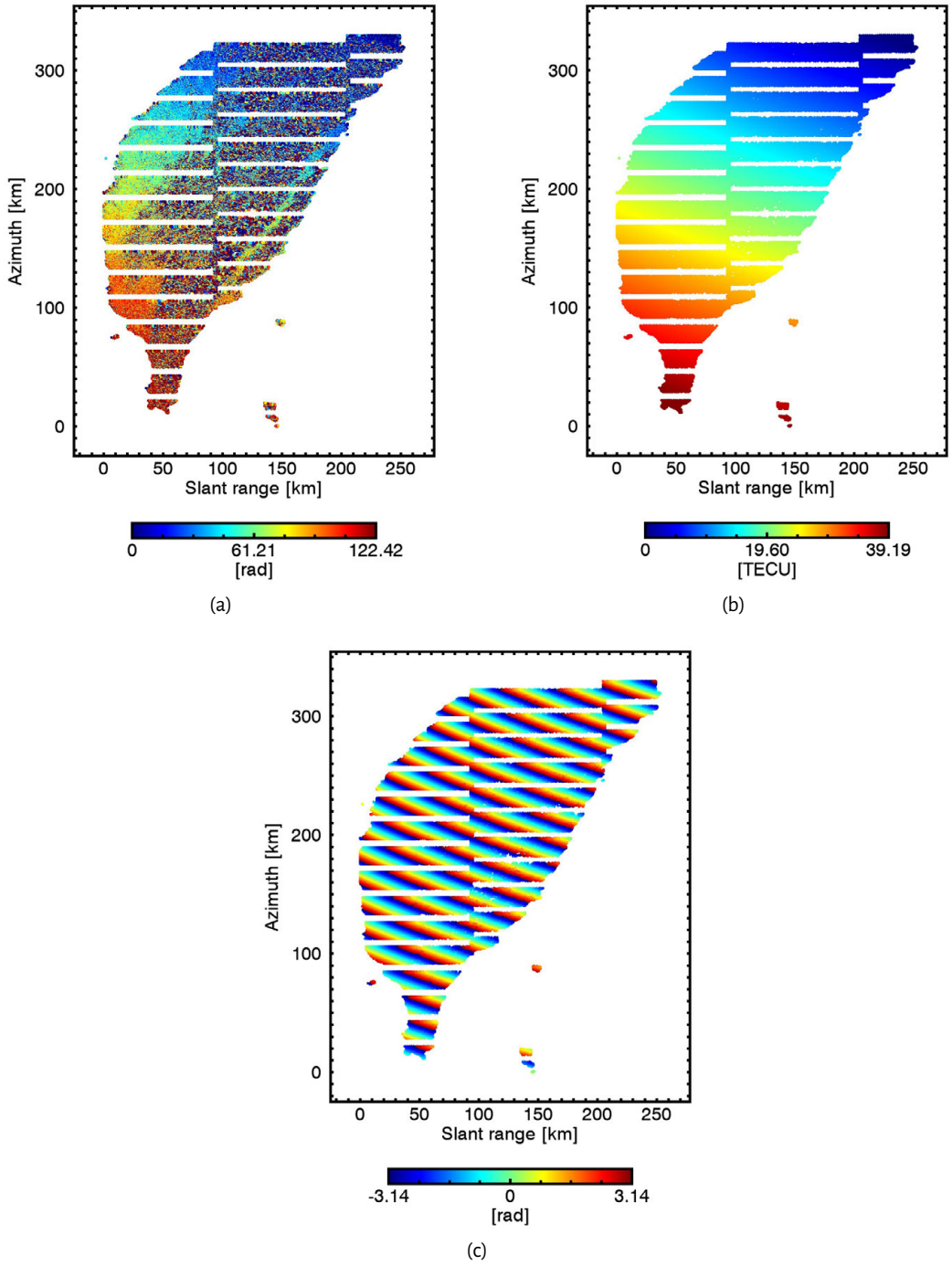

Figure 4.5: (a) Raw, (b) filtered, and (c) wrapped, dispersive phase component of the Taiwan example interferometric phase, plotted at the ionospheric single layer height. The measurements gaps can be noted.

interpolation or by fitting the raw estimates with a model. The resulting ionosphere can be seen in Figure 4.5(b) and, wrapped, in Figure 4.5(c). The differential ionospheric along-track variation is remarkably large, about 25 TECU in 300 kilometers. Finally, the smoothed ionospheric phase is reprojected to the burst geometry and subtracted from the burst interferograms. The mosaicked compensated interferogram can be seen in Fig 4.3(b). A LOS motion error of about 50 cm along the Taiwan island has been removed. Remaining tropospheric path delay could be mitigated by using

numerical weather prediction data and a digital elevation model (Cong, 2014).

It is now also possible to compare the linear component of the smoothed ionosphere with the ionospheric shift which has been estimated in the previous step.

4.3.4 Burst overlap phase check

Finally, ESD can be applied to check whether the ionospheric correction is also able to reduce the residual local shifts and the burst overlap phase differences.

First, the processing steps implemented up to this point are summarized; the master and slave bursts present a mean differential shift of 60 cm due to a strong azimuth ionospheric gradient. The slave bursts are resampled to maximize coherence, and interferograms are produced. The resampling step corrects the Doppler-dependent phase which is due to the timing error but introduces a phase bias that converts the ionospheric phase to approximately what would have been measured by a nonsquinted acquisition. For this reason, no visible phase jumps are present between bursts in the scene interferogram. However, residual small phase jumps and azimuth shifts can still be measured by applying the ESD method. The phase bias and the ionospheric phase screen are estimated and removed by using the split-spectrum method, producing an ionosphere-free interferogram. Finally, ESD is applied again to the compensated bursts to measure eventual remaining shifts.

The results of the final burst overlap phase check are plotted with red diamonds in Figure 4.6. The variation of the new values is considerably reduced. The residual bias, with respect to zero, is comparable with the precision of the global ionospheric shift estimation. Eventual larger errors could be due to the limits of the raw dispersive phase smoothing.

The ESD results of Figure 4.6 and the compensated interferogram of Figure 4.3(b) show how the applied correction method is capable of precisely removing ionospheric effects from Sentinel-1 interferograms.

4.4 Full-aperture ScanSAR mode

Wide-swath images acquired from the L-band PALSAR-2 radar in ScanSAR mode also require ionospheric correction. ScanSAR coseismic interferograms of the 2015 Nepal earthquake are displayed in Figure 4.7, measuring both the main shock, (a) and (c), and the principal aftershock (b). The first analysis of these interferograms presented in (Lindsey et al., 2015) was then used by others (Wang and Fialko, 2015; Grandin et al., 2015; Feng et al., 2015) to model the earthquake.

ALOS-2 ScanSAR acquisitions can be downloaded from the JAXA website in two possible formats: the *SPECAN* mode, where each burst is provided separately, and the *full-aperture* mode, where raw data voids between bursts are filled with zeros, and a stripmap data focusing method is used (Bamler and Eineder, 1996). The advantage of full-aperture data is the possibility to use the standard stripmap interferometric chain. A disadvantage is that the effective Doppler centroid (equivalently, the squint angle) undulates along azimuth around the value imposed by the attitude. Possible consequences of this are that phenomena like azimuth ground deformation or ionospheric variation bias the interferometric phase with a wave effect. Nevertheless, here, for a first analysis of ionospheric phase screens in ALOS-2 ScanSAR images full-aperture processed data are used. Each beam is separately corrected with the standard split-spectrum method of Chapter 3.

The estimated ionospheric phase screens are shown in Fig. 4.7(d)-(f), and the compensated interferograms in Fig. 4.7(g)-(i). All strong phase ramps have been removed; it is then clear that they are due to ionospheric variations and not to an incorrect orbit. The first interferogram presents a differential azimuth TEC variation of about 2.5 TEC units in 300 km, the second 4 TECU, and the third 14 TECU. These gradients are probably caused by the daily difference in the ionization level decrease rate, from low to high latitudes. The range variation, on the other hand, can be caused by the incidence angle change and a difference in the absolute TEC level, or by a differential TEC variation in range. Remaining tropospheric path delay could be mitigated by using numerical weather prediction data and a digital elevation model (Cong, 2014).

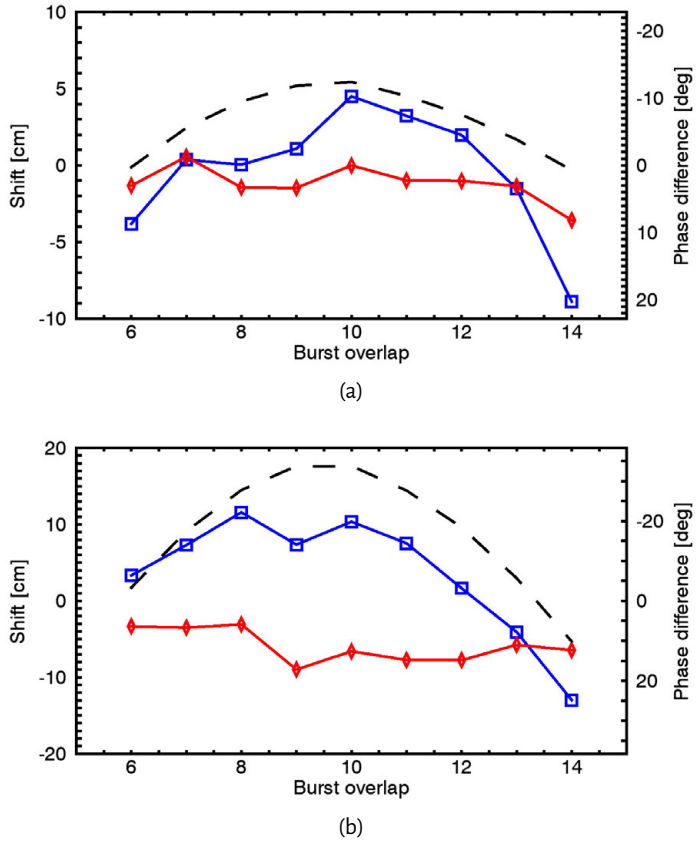

Figure 4.6: Azimuth shifts measured by the ESD method at each burst overlap for beam IW1 (a) and IW2 (b). Blue squares are the residual shifts measured after compensating the global 60 cm offset. The dashed line represents the expected ionospheric shifts, generated with the estimated ionosphere. Red diamonds are the residual shifts, measured after compensating the ionosphere.

As a processing example, the estimated raw nondispersive (a) and dispersive (b) components of the interferometric phase of the interferogram of Fig. 4.7(c) are displayed in Fig. 4.8. Fig. 4.8(c),(e) and (d),(f) shows the filtered and rewrapped phases of the nondispersive and dispersive component, respectively.

4.4.1 Comparison with trend removal

When dealing with localized ground motion, the common procedure to mitigate the ionospheric phase impact is to remove from the interferogram a linear or quadratic trend that may have been caused by ionospheric variations. If the ionosphere does not follow a first- or second-order polynomial variation, this procedure might leave a residual error that later on influences the earthquake source modeling. Moreover, if the measurements objectives are large-scale tectonic motions, this procedure cannot be used or it might also remove the slow motion which has to be measured. Figure 4.9 shows the difference between the fitted trend and the split-spectrum phase screen for the interferogram of Figure 4.7(a). The maximum introduced error is about 25 cm when using a linear slope and 15 cm when using a quadratic function.

4.5 Conclusion

The larger coverage of wide-swath images is helpful for studying large-scale geophysical processes; however, ionospheric distortions become more prominent. The adaptation of the split-spectrum method for the Sentinel-1 TOPS and PALSAR-2 ScanSAR, presented in this chapter, allows the es-

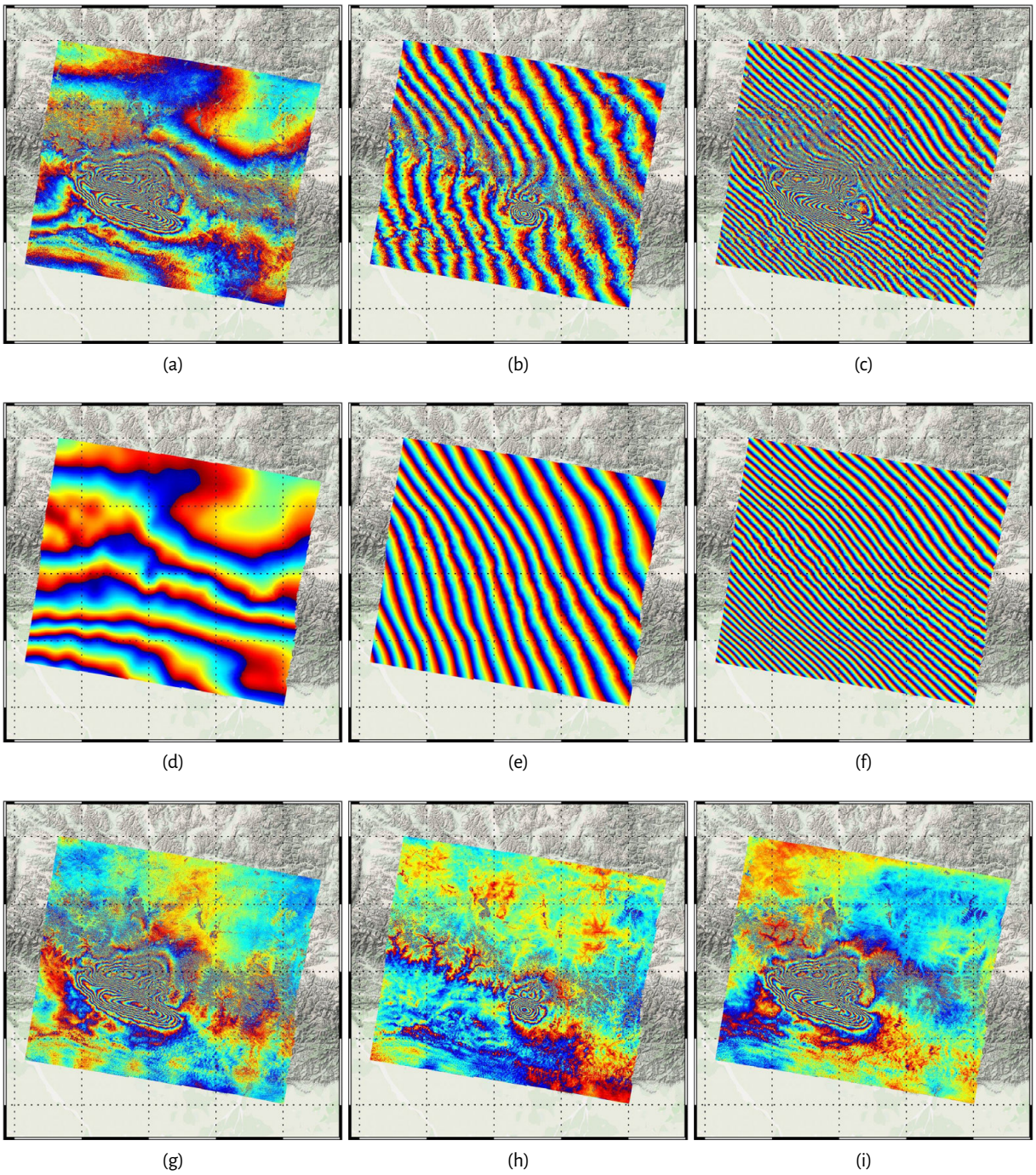

Figure 4.7: (a)-(c) Original ALOS-2 ScanSAR interferograms of the Nepal earthquake. (d)-(f) Estimated ionospheric phase screens. (g)-(i) Ionosphere compensated interferograms.

timation of ionospheric phase screens also with squinted acquisitions. What in the past has often been explained with imprecise orbit information can now be correctly attributed to the influence of the ionosphere. Moreover, it has been shown how C-band deformation measurements can also be severely disrupted by ionospheric variations.

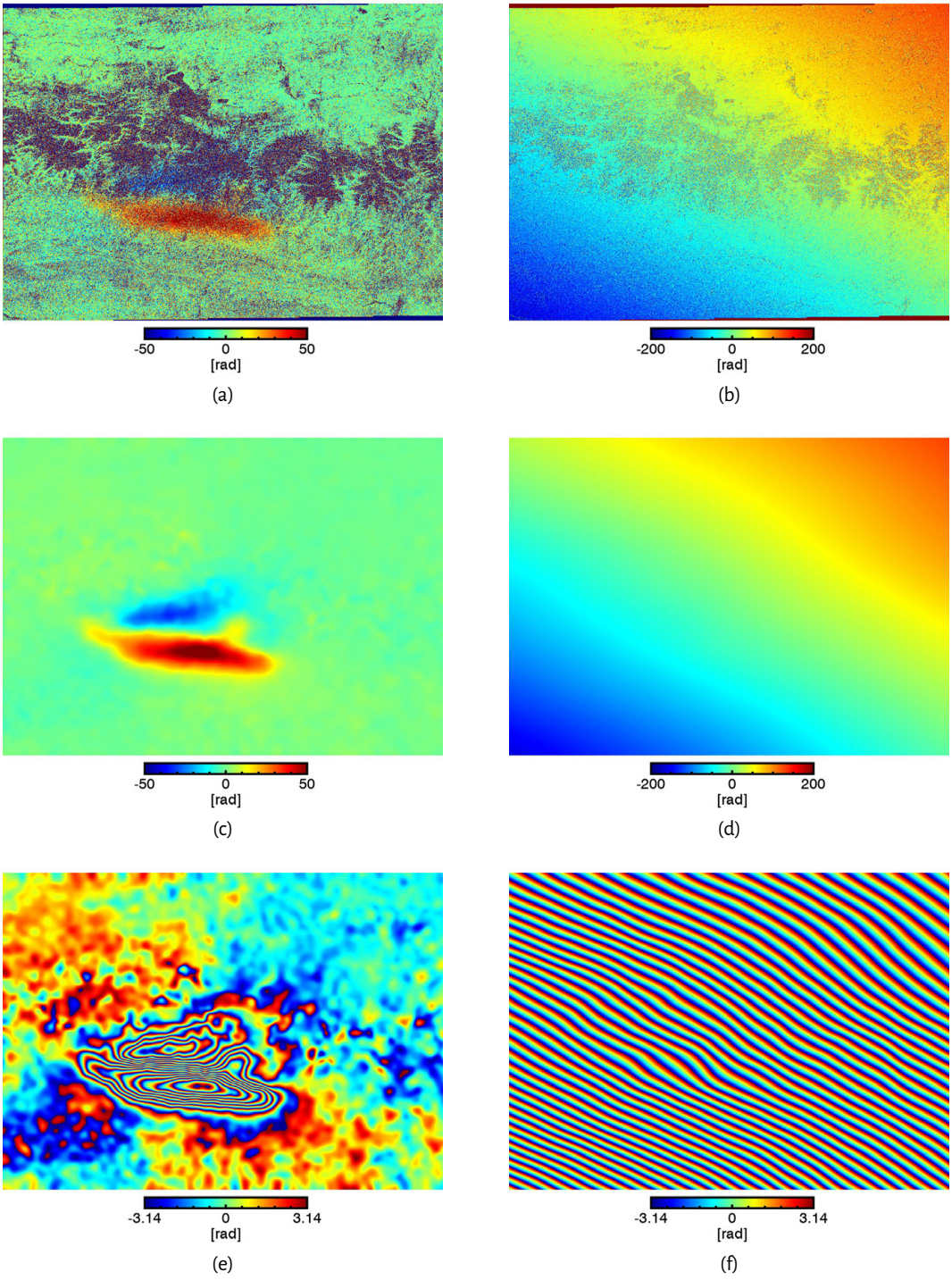

Figure 4.8: Example of the split-spectrum method results for the interferogram of Figure 4.7(c). From top to bottom, raw, filtered, and wrapped components of the interferometric phase: nondispersive (left column) and dispersive (right column). Azimuth length is 300 km, ground range length is 350 km.

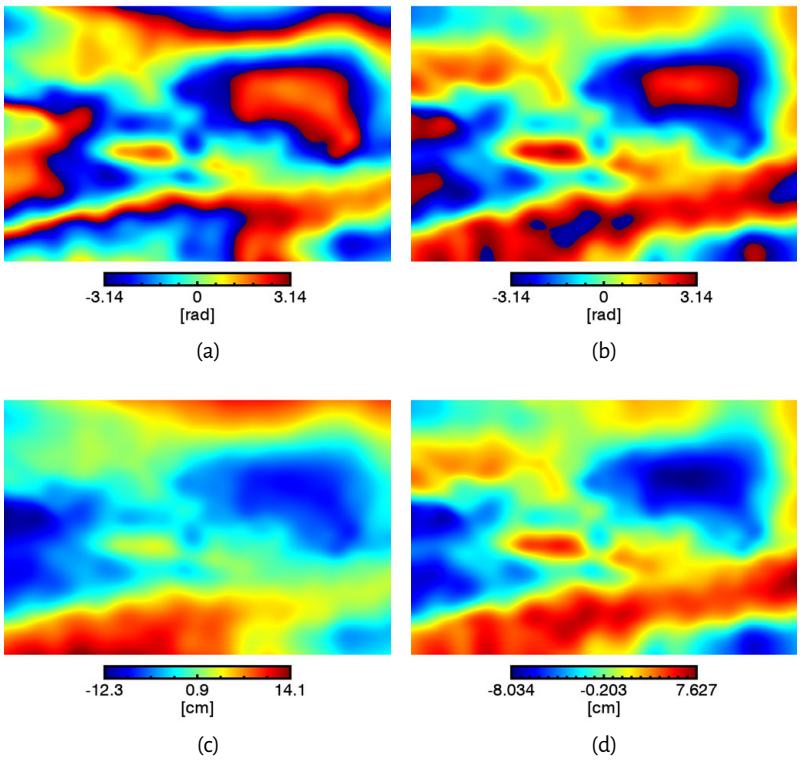

Figure 4.9: Difference between the ionospheric phase screen, estimated with the split-spectrum method, and the linear (left) or quadratic (right) trend fit of the interferogram of Figure 4.7(a) (excluding the earthquake area). Wrapped phase (top) and absolute motion (bottom).

5 Semi-focusing processing and integrated azimuth shifts

The electron density peak is usually at about 350-400 km altitude, whereas a SAR satellite orbits at about 550-800 km altitude. The ionospheric phase screen is assumed to be located at the single layer height, at the peak of the ionosphere influence on radio waves; neither at the ground level, where it would be directly superimposed on the target returns, nor at the orbit level, where it would be directly superimposed on the raw data. The phase screen, hence, never just changes the local phase, it also influences the system azimuth impulse response. As demonstrated in Chapter 2, shift and smearing appear in the focused image. The semi-focusing technique produces an "image" which is focused on the ionosphere, rather than on the ground. The advantage of such an image is that the ionosphere influence is just a phase screen superposition, the azimuth impulse response stays unchanged. Secondly, the ionospheric resolution cell is reduced, and small-scale variations can be better measured.

In this chapter, moreover, the integrated azimuth shifts method is introduced and tested. Modifications to the azimuth impulse response can be very informative about the state of the ionosphere. The integrated azimuth shifts method exploits the azimuth shifts to estimate the azimuth variation of the differential ionospheric phase screen.

This chapter summarizes two conference papers, which can be found in Appendix D and E: *Gomba, G., Eineder, M., Parizzi, A., and Bamler, R. (2014). High-resolution estimation of ionospheric phase screens through semi-focusing processing. In 2014 IEEE International Geoscience and Remote Sensing Symposium (IGARSS), pages 17-20*, and *Gomba, G. and De Zan, F. (2015). Estimation of ionospheric height variations during an aurora event using multiple semi-focusing levels. In 2015 IEEE International Geoscience and Remote Sensing Symposium (IGARSS), pages 4065-4068*, (Gomba et al., 2014; Gomba and De Zan, 2015).

5.1 Method

The system geometry is illustrated again in Figure 5.1, x is the ground space coordinate, and η the orbit timing coordinate. The ionosphere is modeled as a single layer so that $\psi(x)$ is the ionospheric phase screen. An echo, starting from a scatterer in position $\overline{x}$, and arriving at the satellite in $\overline{\eta}$, travels through the ionospheric piercing point at

$$x = v_{\text{sat}}\overline{\eta}\frac{H_i}{H} + \overline{x}\frac{H - H_i}{H}, \tag{5.1}$$

where H is the height of the satellite orbit, and H_i of the single layer model. Raw data can be expressed as the convolution of the ground reflectivity $a(x)$, with the system impulse response function

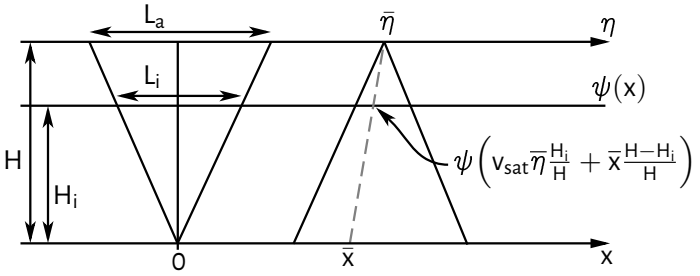

Figure 5.1: System geometry.

$h(\eta)$, i.e.,

$$s_r(\eta) = \int a(x)h(\eta - x/v_{\text{sat}})\,\mathrm{d}x. \tag{5.2}$$

The impulse response function is

$$h(\eta) = \text{rect}\left(\frac{\eta}{T_a}\right)e^{j\pi K_a \eta^2}, \tag{5.3}$$

where K_a is the azimuth FM rate, and $T_a = L_a/v_{\text{sat}}$ is the aperture duration, with L_a being the aperture length and v_{sat} the speed of the platform. The azimuth antenna pattern is approximated by a rectangular function. Including the ionospheric phase screen $\psi(x)$, (5.2) becomes a superposition integral:

$$s_r(\eta) = \int a(x)h(\eta - x/v_{\text{sat}})e^{j\psi\left(v_{\text{sat}}\eta\frac{H_i}{H} + x\frac{H-H_i}{H}\right)}\,\mathrm{d}x. \tag{5.4}$$

For each satellite orbit time η the scatterers reflections, coming from the illuminated ground, are collected and summed together. The ionosphere is not directly superimposed to neither raw nor focused data. The ionosphere seen by each echo depends on both the satellite and ground target position. A constant ionosphere only implies a phase offset in raw and focused data, variations of the TEC value along the azimuth direction generate changes in the raw or focused impulse response function. The severity of these changes, and of the resulting effects, depends on the correlation length of the variations with respect to the synthetic aperture length.

By focusing the raw data with a modified FM rate, it is possible to decouple the ionosphere from the SAR image formation process. The proposed focusing kernel is

$$k_{sf}(\eta) = \text{rect}\left(\frac{\eta}{T_a}\right)e^{-j\pi K_a C \eta^2}, \tag{5.5}$$

which is the conjugate azimuth chirp, the chirp rate is modified by the factor C. The semi-focused data are obtained with a convolution, i.e,

$$\begin{aligned} s_{sf}(\eta) &= \int s_r(u)k_{sf}(\eta - u)\,\mathrm{d}u. \\ &= e^{-j\pi K_a C\eta^2}\int a(x)e^{j\pi K x^2/v_{\text{sat}}^2}\cdot\int \text{rect}\left(\frac{u - x/v_{\text{sat}}}{L_a}\right)\text{rect}\left(\frac{x-u}{L_a}\right)e^{j\phi(u)\eta}\,\mathrm{d}u\;\mathrm{d}x, \end{aligned} \tag{5.6}$$

The term $\phi(u)$ collects all remaining phase terms:

$$\phi(u) = -\pi K_a(C-1)\frac{u^2}{\eta} - 2\pi K_a\frac{ux}{v_{\text{sat}}\eta} + 2\pi K_a C u + \frac{1}{\eta}\psi\left(v_{\text{sat}}u\frac{H_i}{H} + x\frac{H-H_i}{H}\right). \tag{5.7}$$

The integral in (5.6) contains an oscillating phase term $\phi(u)$, it can be solved with the stationary phase method. The stationary phase point u_0 can be found by searching the value of u for which the phase derivative $\phi'(u)$ is zero:

$$\phi'(u) = -2\pi K_a(C-1)\frac{u}{\eta} - 2\pi K_a \frac{x}{\eta} + 2\pi K_a C + \psi'(...)\frac{v_{\text{sat}} H_i}{\eta H}. \tag{5.8}$$

The derivative of the ionospheric phase term ψ' is assumed to be smaller than the other terms, such that it does not change the position of u_0, and is neglected. Following (Cumming and Wong, 1964) the integral (5.6) can be split into two parts, and the stationary phase principle applied to each part. The solution is

$$s_{sf}(\eta) \approx e^{j\frac{\pi}{4}} e^{-j\pi K_a C \eta^2} \int a(x) e^{j\pi K_a x^2 / v_{\text{sat}}^2} \cdot \text{rect}\left(\frac{\eta - x/v_{\text{sat}}}{T_a(C-1)/C}\right) e^{j\phi(u_0)\eta}\, \mathrm{d}x. \tag{5.9}$$

In this result, the length of the rectangular function has been derived considering that the integral is zero when the stationary phase point lays outside the combination of rectangular functions in (5.6). By choosing $C = H/(H - H_i)$, (5.9) yields

$$s_{sf}(\eta) = e^{j\psi(\eta)} e^{j\frac{\pi}{4}} \int a(x)\, \text{rect}\left(\frac{v_{\text{sat}}\eta - x}{L_i}\right) e^{j\pi K_a \frac{H}{H_i}(\eta - x)^2}\, \mathrm{d}x. \tag{5.10}$$

Where L_i is the aperture duration projected at the height of the ionosphere $L_i = L_a H_i / H$. The ionospheric phase screen $\psi(\eta)$ is here superimposed to the semi-focused data without being low-pass filtered, and without interfering with the impulse response function.

Semi-focused data are raw data measured by an imaginary real aperture radar orbiting at the height of the ionosphere single layer. While the resolution cell in the ionosphere is small, the ground one is large, ground phase contributions then shift and defocus the semi-focused data. One application of the semi-focusing method is the compensation of ionospheric effects; if the high-resolution ionospheric phase screen is known, it can be removed from the semi-focused data, this also removes the ionospheric effects such as shifts and blurring from the focused image.

5.2 Integrated azimuth shifts

In this section, the Alaska aurora data set is used to test the semi-focusing method. The motivation is the exploitation of the differential azimuth shifts, obtained by patch-based cross correlation, to estimate the differential ionospheric phase screen. From (2.26) and (2.29), the azimuthal variation of the phase screen is obtained integrating the shifts:

$$\hat{\phi}(\eta) = -\frac{4\pi f_0 v_{\text{sat}} H}{cRH_i} \int_0^{\eta} \Delta\eta_i(u)\, \mathrm{d}u. \tag{5.11}$$

This gives the variation along one azimuth line, the integration constant is unknown, consequently also the range variation is unknown. This problem will be solved in the next Chapter by combining more information sources. In this example, the range variation of the estimated ionospheric phase screens is just taken from the original interferogram.

Figure 5.2 shows some phase screens estimated supposing different constant ionospheric heights. None of them is able to completely recover the variations which disrupt the interferogram, as it can be seen from the relative compensated interferograms. The assumption is that the peak height of the electron density profile changes within the image, due to the particularly severe aurora disturbance. Another possibility would be a motion of the ionosphere in the azimuth direction, which is equivalent to a height change, as demonstrated in Chapter 2. The semi-focusing processing is used here to estimate the azimuth derivative of the ionospheric phase screen, regardless of the changes in the ionospheric height.

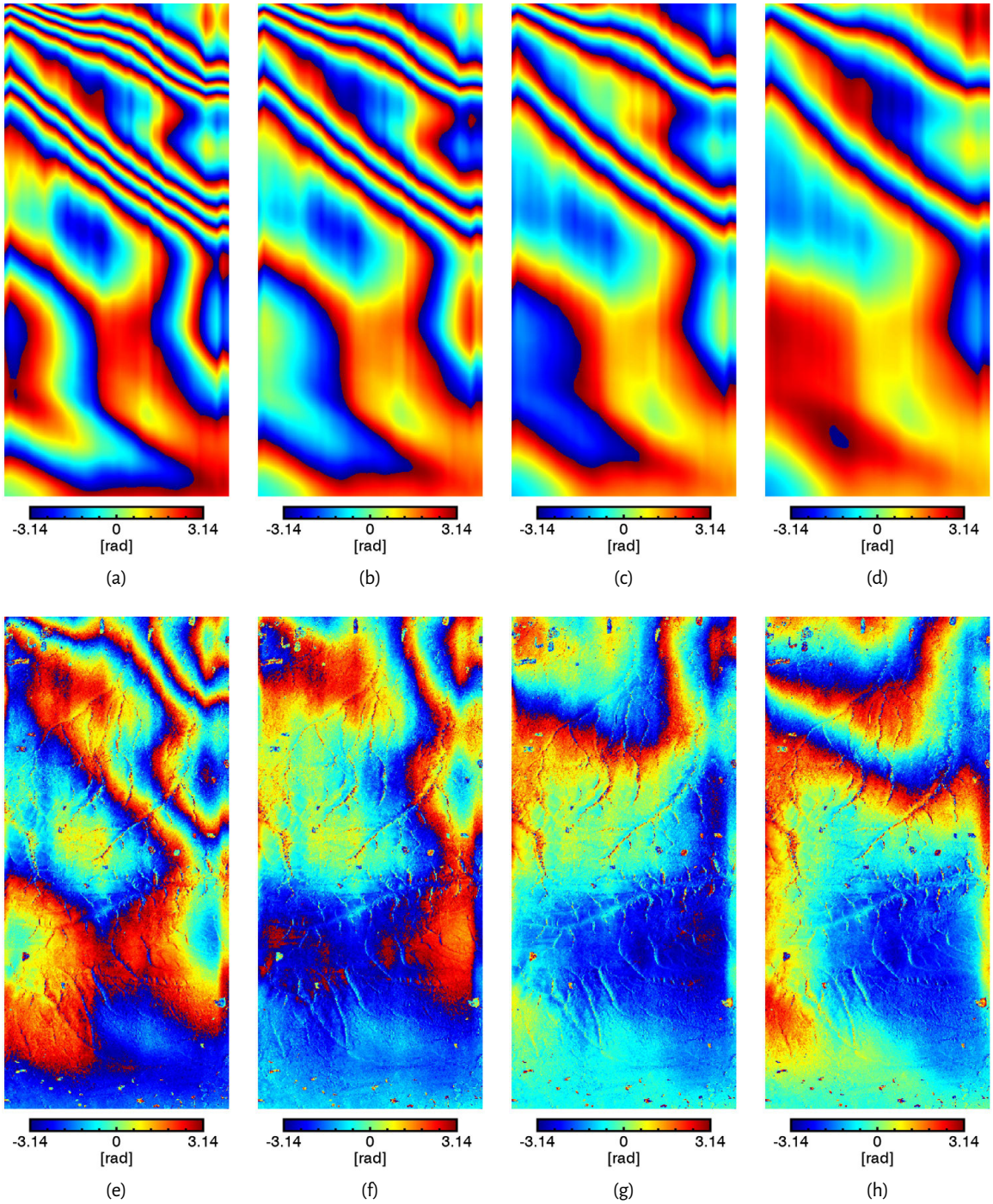

Figure 5.2: (a)-(d) Ionospheric phase screens produced using the integrated azimuth shifts method. (e)-(h) Compensated interferograms. The ionospheric height used in the integration is, from left to right, 150, 200, 250, and 300 km.

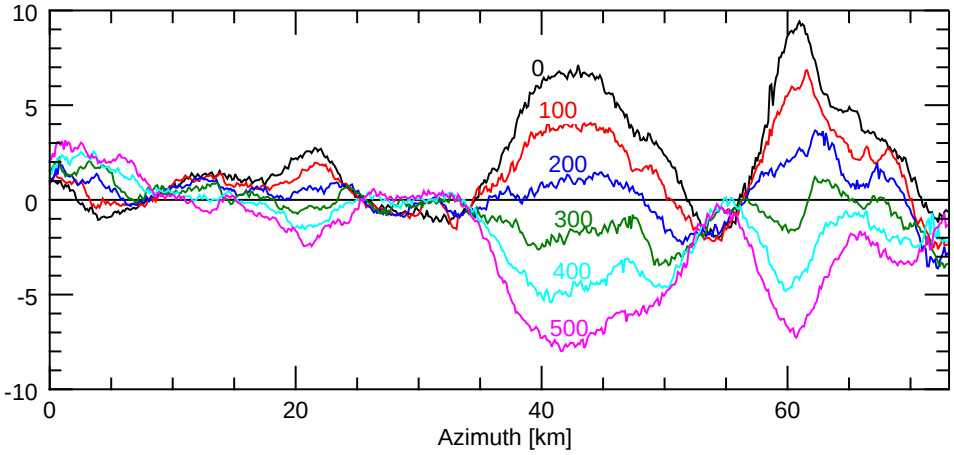

Figure 5.3: Azimuth shifts of one azimuth line, in meter, for different focusing heights (indicated in km). The black line corresponds to the normal focusing.

Figure 5.3 shows the mutual azimuth shifts of one azimuth line for different semi-focusing heights. The relation between the azimuth shift and the local phase screen derivative, as a function of the semi-focusing height H_{sf}, is:

$$\Delta\eta(\eta, H_{sf}) = -\frac{cR(H_i(\eta) - H_{sf})}{4\pi f_0 v_{\text{sat}} H}\rho_\phi(\eta) = \frac{cRH_{sf}}{4\pi f_0 v_{\text{sat}} H}\rho_\phi(\eta) - \frac{cRH_i(\eta)}{4\pi f_0 v_{\text{sat}} H}\rho_\phi(\eta). \tag{5.12}$$

The latter is a linear relation, it is possible to estimate the local ionospheric height $H_i(\eta)$, and the phase screen derivative $\rho_\phi(\eta)$, by repeating the semi-focusing processing and the shifts estimation for different heights, and then fitting a line to the obtained data. For each cross correlation patch, and for varying semi-focusing height, a first order polynomial is fitted to the azimuth shifts $\Delta\eta(\eta, H_{sf})$. Considering (5.12), the ionospheric height and derivative are:

$$\begin{aligned} \hat{\rho}_\phi(\eta) &= b\frac{4\pi f_0 v_{\text{sat}} H}{cR}, \\ \hat{H}_i &= -\frac{a}{b}, \end{aligned} \tag{5.13}$$

where a and b are respectively the zero and first order parameters of the fitted polynomial. This procedure is repeated for each azimuth and range patch.

The estimated phase screen derivative is independent of the ionospheric height. The integration

$$\hat{\phi}(\eta) = \int_0^\eta \hat{\rho}_\phi(u)\,\mathrm{d}u, \tag{5.14}$$

yields the result shown in Figure 5.4. The compensated interferogram is now almost flat, indicating a much better estimation of the ionosphere.

5.3 Conclusion

One possible application of the semi-focusing technique allows the use of the azimuth shifts to estimate the ionospheric phase screen even in a complex situation such as an auroral arc, where the electron density distribution changes rapidly. However, the ionospheric height is usually stable and, in normal situations, it should be possible to directly use the shifts without having to apply the semi-focusing method, as also realized in the next chapter.

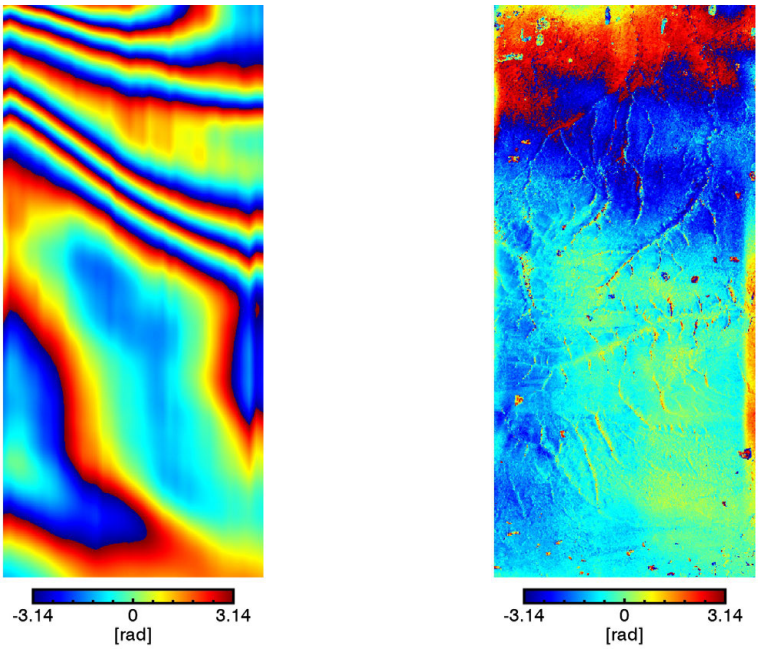

Figure 5.4: (a) Ionospheric phase screen, produced by integrating the estimated ionospheric derivative. (b) Compensated interferogram.

Modifications of the azimuth impulse response carry a lot of information about the ionosphere, as it can be seen from the quality of the reconstructed phase screen. This estimation is, on the small-scale level, superior to the one obtained with the split-spectrum. Two issues, though, are present: the range variation cannot be recovered, and the long distance variation is unreliable. The combination of the split-spectrum with the azimuth shifts, realized in the next chapter, will produce a better result, superior to the current one both in the short- and long-wavelengths level.

6 Improved estimation by data combination

Different effects are produced by the ionosphere on SAR images and interferograms, as discussed in Section 2.6. In this Chapter, a method to combine different information sources and obtain a better final estimate of the ionosphere is presented. Moreover, the filtering step of Chapter 3 is improved: the isotropic Gaussian window with fixed size is no longer used, an adaptive anisotropic filtering is here introduced instead.

A physically realistic model of the ionosphere is used to describe its spatial covariance or, equivalently, its power spectrum. With this approach, non-optimal smoothing windows or coefficients can be avoided. Noise suppression, response function deconvolution and data combination is realized with a single step in a *Wiener* sense, that is, based on the signal to noise ratio (SNR) of each frequency bin (Wiener, 1964). This is done in practice by formulating a Bayesian inverse problem, implemented in the space domain because of the non-constant noise variance.

This concept could in general be applied to combine information about absolute or temporally differential ionosphere. Nevertheless, in this thesis, the focus is put on the estimation of the differential ionospheric phase screen, which is superimposed on interferograms. For the multi-source estimation, the split-spectrum method is combined with the azimuth shifts.

Two application examples using ALOS PALSAR images are presented: the first contains a spatially rapidly varying aurora effect in northern Alaska; the second is based on an equatorial scintillation event over the Amazon region.

This chapter summarizes the paper in Appendix C: *Gomba, G. and De Zan, F. (2016 submitted). Bayesian Data Combination for the Estimation of Ionospheric Effects in SAR Interferograms. IEEE Transactions on Geoscience and Remote Sensing*, (Gomba and De Zan, 2016 submitted).

6.1 Bayesian data combination

The Bayesian approach to inverse problems is used to combine different information sources and improve the final estimation of the ionosphere. In the following, it is again assumed that the ionosphere can be represented by a single thin layer with known height. The general linear model is

$$\boldsymbol{x} = \boldsymbol{G}\boldsymbol{\theta} + \boldsymbol{w}, \tag{6.1}$$

where $\boldsymbol{x}$ is a vector containing the observations, the matrix $\boldsymbol{G}$ transforms the model parameters vector $\boldsymbol{\theta}$ into the observations, and $\boldsymbol{w}$ is the measurement noise vector; $\boldsymbol{\theta}$ and $\boldsymbol{w}$ are modeled as Gaussian distributed. The linear minimum mean square error estimator of $\boldsymbol{\theta}$ is

$$\hat{\boldsymbol{\theta}} = \left(\boldsymbol{G}^T \boldsymbol{C}_{\boldsymbol{ww}}^{-1} \boldsymbol{G} + \boldsymbol{C}_{\boldsymbol{\theta\theta}}^{-1}\right)^{-1} \boldsymbol{G}^T \boldsymbol{C}_{\boldsymbol{ww}}^{-1} (\boldsymbol{x} - \boldsymbol{G}\bar{\boldsymbol{\theta}}) + \bar{\boldsymbol{\theta}}, \tag{6.2}$$

where $\boldsymbol{C_{ww}}$ is the covariance of $\boldsymbol{w}$, $\bar{\boldsymbol{\theta}}$ is the a-priori model of $\boldsymbol{\theta}$ and $\boldsymbol{C_{\theta\theta}}$ its covariance (Kay, 1993).

The proposed combination technique is rather general and could be used to combine information from different sources. The structure of the ionosphere model is presented in the following section. In Section 6.2 the inverse problem is implemented to combine the split-spectrum method with the azimuth shifts, to first apply and test the proposed concept.

6.1.1 Ionosphere model and a-priori information

Large scale TEC variations depend on the global distribution of solar radiation, forming the background ionosphere. In addition, turbulent local irregularities may perturb the smooth trends. The ionospheric phase screen model of the inverse problem consists therefore of two components (Rino, 2011):

$$\phi(t,\eta) = \phi_b(t,\eta) + \delta\phi(t,\eta), \tag{6.3}$$

where t and η are, respectively, range and azimuth axes. The values $\phi(t,\eta)$ are arranged in the vector $\boldsymbol{\theta}$. The component $\phi_b(t,\eta)$ accommodates the background ionosphere trends that cannot be characterized by statistically homogeneous measures, in the inverse problem model it is a low-order polynomial. The component $\delta\phi(t,\eta)$ represents the turbulent irregularities. They are caused by random electron density variations, whose size distribution can be characterized by a power law spectral density function, in particular when considering scintillation effects (Rino, 2011, 1979; Belcher, 2008; Carrano et al., 2012; Rogers et al., 2014; Meyer et al., 2016).

The Bayesian approach to statistical estimation allows the use of a-priori information in the estimator. This possibility is exploited by forcing the autocorrelation function of $\delta\phi(t,\eta)$ to be a physically realistic function, thus also avoiding generic smoothing window or regularization.

In (Rino, 1979), the power spectral density of the 2-D ionospheric phase screen is derived from the 3-D autocorrelation function of the refractive index. The spatial autocovariance of the 2-D phase screen is the Fourier transform of a power law spectral density. The result is a function of the Matérn family (Guttorp and Gneiting, 2006) which can describe turbulence with adjustable smoothness for short distances, and saturating variance for long distances, satisfying physical and statistical requirements (Knospe and Jonsson, 2010). This correlation function models in (Rino, 1979) equatorial irregularities which causes scintillation effects. Here, it is generically used to model the residual variations that are not represented by the trend. Relating phase screen to physical constants is not the main topic of this thesis, for an introduction see Appendix C. Therefore, the formulation of (Rino, 1979) is simplified by using a generic Matérn covariance function:

$$R_{\delta\phi}(\boldsymbol{r}) = P_\phi \frac{2^{3/2-\nu}}{\Gamma(\nu-1/2)} (k_0 r)^{\nu-1/2} K_{\nu-1/2}(k_0 r), \tag{6.4}$$

where $K_\nu(x)$ is the modified Bessel function of the second kind, $\Gamma(x)$ is Euler's gamma function, P_ϕ is a turbulence strength parameter, ν is the spectral index, and the outer scale wavenumber $k_0 = 2\pi/l_0$ is associated with the outer scale l_0 (usually 10 to 50 kilometers), at which the spatial correlation drops. The argument r is

$$r^2 = \frac{C r_t^2 - B r_t r_\eta + A r_\eta^2}{AC - B^2/4}, \tag{6.5}$$

where r_t and r_η are the spatial distances related to the wavenumber k_t and k_η in the range and azimuth direction, respectively. An example of a 2D anisotropic Matérn covariance function is shown in Figure 6.1(d); 1D range and azimuth axis are shown in Figure 6.2(c) and (d). The power spectral density is the two dimensional Fourier transform of (6.4) (Rasmussen, 2006):

$$\Phi_{\delta\phi}(\boldsymbol{k}) = \frac{P_\phi}{G} \frac{\Gamma(\nu+1/2)}{\Gamma(\nu-1/2)} \frac{4\pi k_0^{2\nu-1}}{(k^2+k_0^2)^{\nu+1/2}}, \tag{6.6}$$

where the argument k is

$$k^2 = Ak_t^2 + Bk_t k_\eta + Ck_\eta^2. \tag{6.7}$$

To add anisotropy, the power spectrum axes are scaled and rotated. The parameters A, B, C, and G depend on the scaling and rotation factors (see Appendix C).

As introduced above, the inverse problem model is composed by a polynomial, to account for the background ionosphere trends, and by a function, to represent the turbulent part. The covariance (6.4) is used to model the spatial correlation of the turbulence, by inserting it into the model a-priori covariance matrix $\boldsymbol{C_{\theta\theta}}$. The parameters P_ϕ, ν, k_0, A, B, and C set the magnitude, smoothness, correlation length and anisotropy of the turbulent part of the estimated ionospheric phase screen.

In the examples of this chapter these parameters were manually set, but in principle they could be automatically extracted from the data. To begin with, the background ionosphere trend should be removed from the split-spectrum raw estimates trough polynomial fitting; the fitting residuals would be the turbulent variations, plus the uncorrelated measurement noise of the split-spectrum method. A 2D semi-variogram analysis of the residuals could then be used to estimate the covariance parameters. It might happen that the turbulent variations would be small enough to be masked by the split-spectrum estimation noise, but still large enough to produce visible azimuth shifts: in these cases, also the azimuth shifts should be used to estimate the parameters. Thus, the exploitation of all information sources to characterize the turbulence is also an interesting topic for future investigations.

6.2 Split-spectrum method and azimuth shifts combination

As a first implementation of the inverse problem estimator, the split-spectrum method is combined with the azimuth shifts to improve the estimation of the ionospheric phase screen. These two information sources complement each other: the split-spectrum method can measure long distance range and azimuth variations but is not sensitive enough to estimate turbulence which is small in magnitude and scale. Azimuth shifts, on the contrary, are sensitive to small azimuth changes and can therefore refine the split-spectrum in the short wavelengths level, but wouldn't be able to precisely recover large scale variations if used alone.

The azimuth shifts are ionosphere-induced changes of the SAR impulse response; therefore, they are used here to estimate the ionospheric phase screen, supposing no ground deformation in the along track direction. An eventual ground motion, in fact, would result summed up to the ionosphere-induced azimuth shifts, modifying the reconstruction of the ionospheric phase screen. It is then necessary to find a way to estimate azimuth changes to the impulse response, independently from ground motion. The factor that differentiates these two contributions is the altitude. Azimuth sub-apertures, or the semi-focusing method, are therefore first candidates for developing a method that separates ionosphere- from ground-based shifts.

The observation vector $\boldsymbol{x}$ contains the split-spectrum estimates of the ionospheric phase screen, and the azimuth shifts measured by coherent cross correlation. $\boldsymbol{C_{ww}}$ is the observation noise covariance matrix. It is filled using the covariance of the split-spectrum method and cross correlation:

$$\boldsymbol{C_{ww}} = \begin{bmatrix} \boldsymbol{\sigma}^2_{\Delta\phi_{\text{iono}}} & \boldsymbol{0} \\ \boldsymbol{0} & \boldsymbol{\sigma}^2_{\Delta\eta} \end{bmatrix}. \tag{6.8}$$

The forward problem $\boldsymbol{G}$ describes how to generate the recalculated split-spectrum and azimuth shifts data for a given ionosphere model.

6.2.1 Forward problem

Due to the moving window filtering effect of the synthetic aperture integration, the ionospheric phase screen observed in the interferogram is a smoothed version of the real ionosphere. Unless the

ionosphere turbulence is that strong that it defocusses the images and lowers the coherence, there is no need to increase the ionospheric resolution using techniques as azimuth subbands or semifocusing (Tebaldini et al., 2012; Gomba et al., 2014). Moreover, the objective here is the estimation of the ionospheric phase screen that is superimposed on the ground signals in the interferogram and not the estimation of the *real* ionosphere. For this reason, neither the low-pass effects produced by the synthetic aperture, nor by the interferogram multilooking, are included in the forward problem modeling.

Due to the relatively high sampling frequency of the SAR images with respect to the ionospheric variations, the observation data can be downsampled without loss of information, to reduce matrices size. The subsampling factor, and the resolution cell size of the model are automatically derived from the data with a power spectrum analysis. For each observation data pixel, a raw of the forward problem matrix $\boldsymbol{G}$ is written. The row contains the transfer function that converts the model into the observation pixel.

6.2.1.1 Split-spectrum

The split-spectrum method data are a direct measure of the ionospheric phase screen, filtered by the anti-aliasing filter prior to data subsampling. The transfer function is then relatively simple. It is obtained by interpolating the filtering kernel to the model dimension. This way, the correlation between data pixels is taken into account.

6.2.1.2 Azimuth shifts

The azimuth shift transfer function also contains the anti-aliasing filter, with the addition of the derivative operator. A target's azimuth shift depends on the linear variation of the ionosphere within the synthetic aperture. This is equivalent to low-pass filter the ionosphere with the synthetic aperture size and differentiate the result. As introduced above, the synthetic aperture low-pass filter is neglected and only the derivative is considered. The transfer function is then the azimuth shifts anti-aliasing filtering kernel, interpolated to the model dimensions, and convolved with a derivative operator.

To complete the azimuth shifts forward problem, a coefficient that converts the phase derivative in radians per meter to an azimuth shift in meter is required. The latter is derived from the relationship (2.26). The ionospheric height scales the effect of the ionospheric derivative and is therefore an important parameter. An iterative procedure that minimizes the mean square error between observed and recalculated data is used to find the correct ionospheric height.

An azimuth offset, probably a timing error, is often present between PALSAR images. An additional offset in the azimuth shifts would add an unwanted phase ramp to the inversion result producing an error over long distances. The problem is solved by the split-spectrum data, which constrain large-scale variations. By including an offset for the azimuth shifts in the problem model unknowns and in the direct problem, it is thus possible to recover the timing error and avoid biases. The parameters vector becomes then

$$\boldsymbol{\theta} = \begin{bmatrix} \phi \\ \Delta\eta_{\text{offset}} \end{bmatrix}, \tag{6.9}$$

where the vector ϕ is the ionospheric phase screen and $\Delta\eta_{\text{offset}}$ is the azimuth offset. Consequently, the forward problem is

$$\boldsymbol{G} = \begin{bmatrix} \boldsymbol{G}_{\Delta\phi_{\text{iono}}} & \mathbf{0} \\ \dfrac{v_{\text{sat}} H_i}{2\pi K_a H} \cdot \boldsymbol{G}_{\Delta\eta} & \mathbf{1} \end{bmatrix}, \tag{6.10}$$

where $\boldsymbol{G}_{\Delta\phi_{\text{iono}}}$ and $\boldsymbol{G}_{\Delta\eta}$ are respectively the transfer function of the split-spectrum method and azimuth shift.

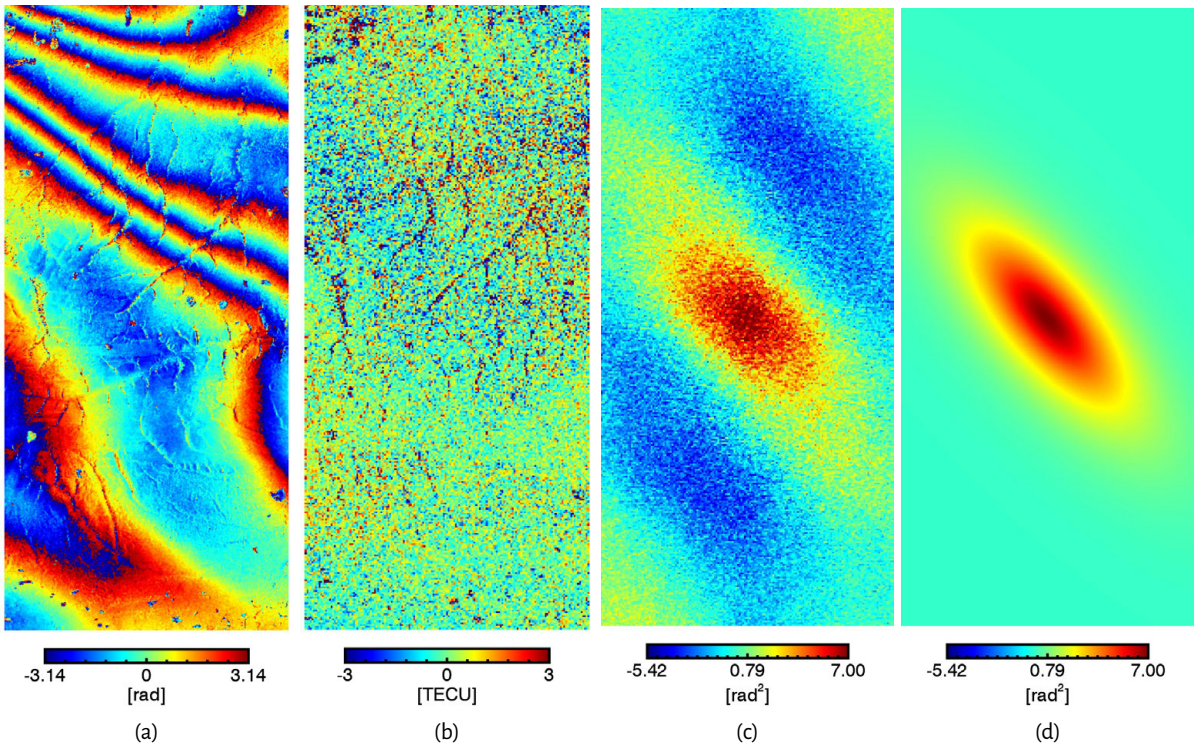

Figure 6.1: Auroral TEC variations produce phase slopes, visible in the (a) interferogram. (b) Detrended raw estimates of the ionospheric phase screen obtained with the split-spectrum method. (c) Sample and (d) modeled covariance of (b). Azimuth length is 66 km, range length is 28 km.

6.3 Application examples

6.3.1 Alaska aurora test case

The Alaska dataset has been already used in Chapter 2 to introduce the ionospheric effects to interferograms, in Chapter 3 to test the split-spectrum method, and in Chapter 5 to test the semifocusing. Here, the improvement obtained with the adapted anisotropic filtering, and with the addition of the azimuth shifts is demonstrated.

With a polynomial fitting, large-scale trends are removed from the raw estimates of the split-spectrum method. The residual variation is shown in Figure 6.1(b). The analysis of the residuals is used to characterize the turbulent ionosphere part and to extract the spectral density parameters. The range and azimuth power spectral density of the residuals is plotted in black in Figure 6.2(a) and (b). Two regimes can be clearly seen: at longer wavelengths the decreasing linear slope indicates a power-law distribution of phase irregularities, at shorter wavelengths the power density becomes flat due to the white estimation noise, masking small-scale ionospheric variations. Figure 6.1(c), 6.2(c) and (d) show the signal covariance. The red line in Figure 6.2 is the fitted power-law model. This is used to fill the model covariance matrix of the inverse problem [see Figure 6.1(d)], regulating the smoothness of the inversion result. The same analysis is also done on the azimuth shifts. The estimated covariance models and noise levels are also used to automatically determine the data downsampling factors.

The inversion results are presented in Figure 6.3, (a) is the estimated ionospheric phase screen, and (b) is the compensated interferogram. Figure 6.3(c) is the turbulent part of the result, the same of Figure 6.1(b). These results can be compared with the reference ones, obtained with the stand-alone split-spectrum data in Chapter 3, which are shown in Figure 6.3(d-f). The new ionospheric phase screen better recovers the irregular variations, it is smoother and more similar to the original

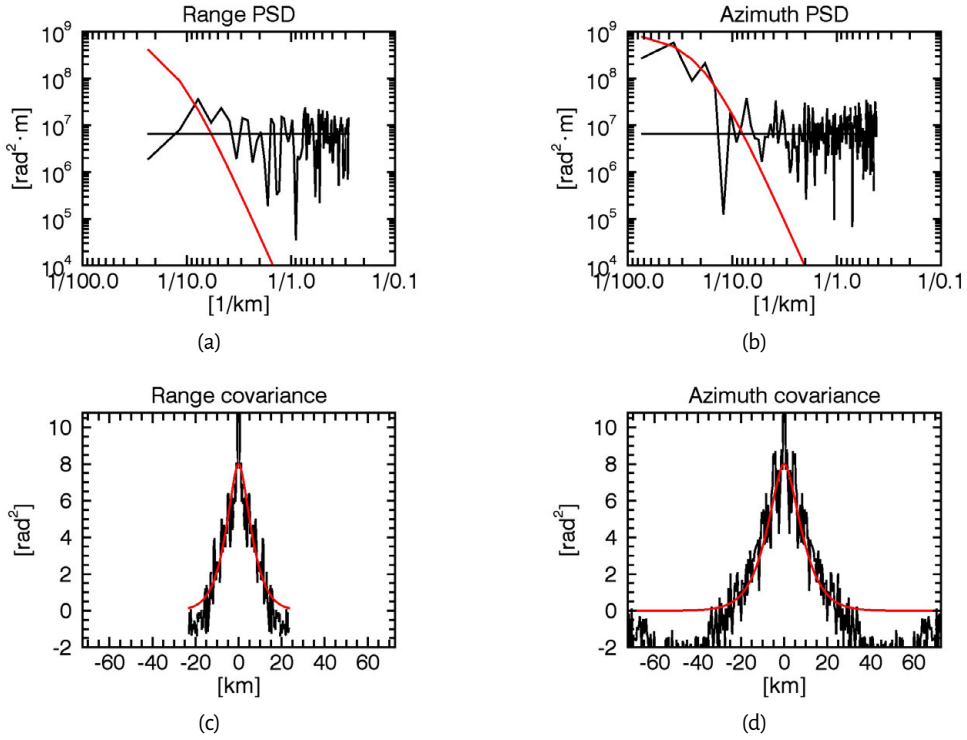

Figure 6.2: Range (left) and azimuth (right) power spectral density (top), and covariance (bottom) of the detrended split-spectrum raw estimates. In red, the fitted covariance model.

interferogram than the reference one. The improvement is considerable, this can be directly seen by comparing the two compensated interferograms.

6.3.2 Amazon scintillation test case

Two ascending ALOS PALSAR images, acquired at around 10 PM local time over the Amazon region, are used in this example. They are part of the same track from which the examples of Figure 2.8 are taken. They also present strong amplitude stripes which are due to the scintillation effect. Figure 6.4(a) shows the interferogram and Figure 6.4(b) the azimuth shifts. The rapid phase fluctuations are due to plasma bubbles, which are elongated in the direction of the local magnetic field vector (Kim and Papathanassiou, 2015). Due to their slight orientation with respect to the along track direction they can also affect the SAR impulse response producing azimuth shifts.

The split-spectrum method estimated ionospheric phase screen and compensated interferogram are presented respectively in Figure 6.4(c) and (f). Here, the estimates are filtered with an isotropic Gaussian window. Figure 6.4(d) and (g) shows respectively the phase screen and the compensated interferogram when using the inverse problem method, but only with the split-spectrum data and not the azimuth shifts. This way, the inverse problem is used as an adapted anisotropic filter for the split-spectrum data. The result considerably improves when also the azimuth shifts are included, as it can be seen in Figure 6.4(e) and (h).

In Figure 6.5 are reported the range and azimuth variograms of the compensated interferogram, the dashed line represent the split-spectrum method, the solid line the combination. It can be seen that the inverse problem result compensation reduces the variance of the compensated interferogram.

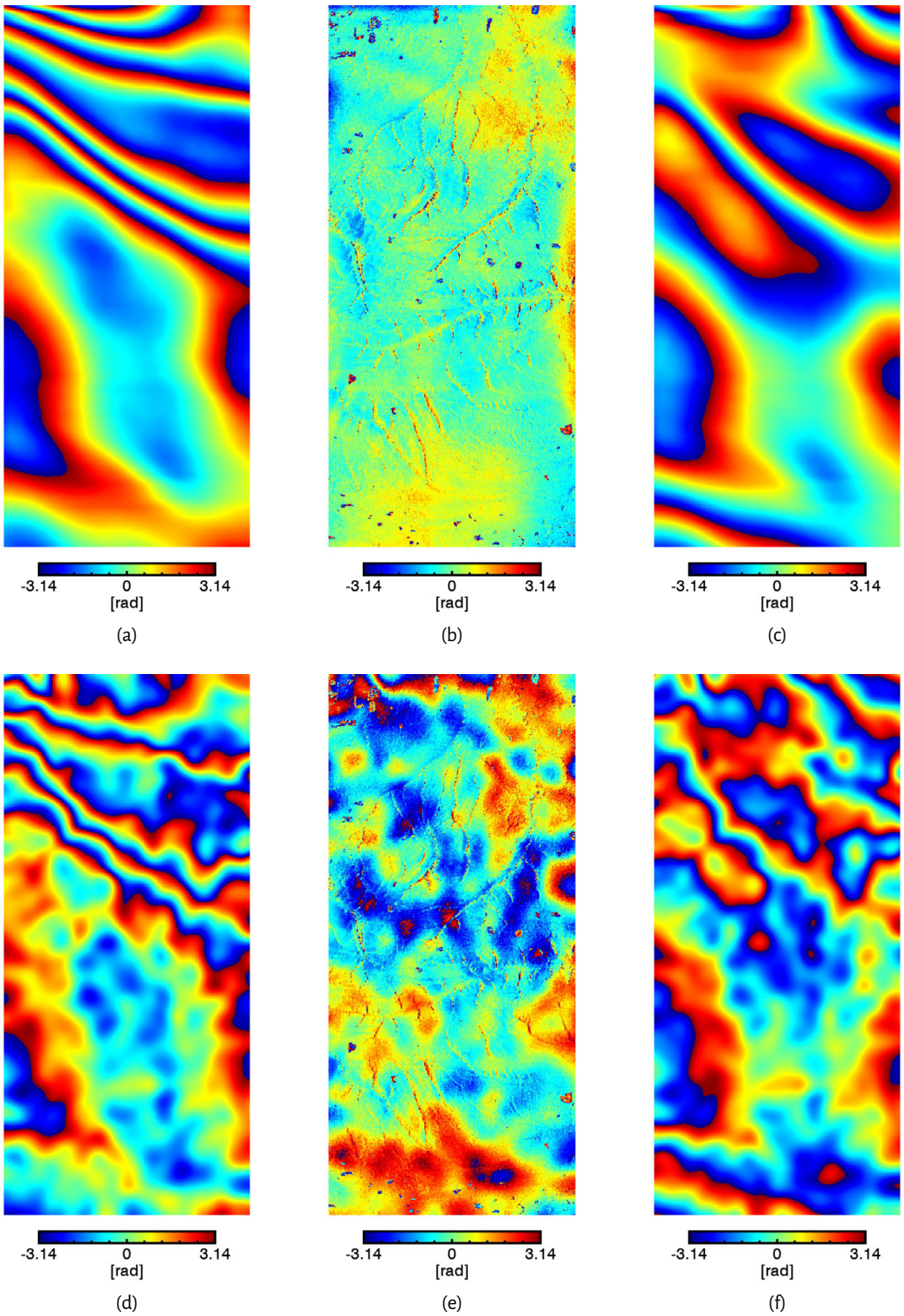

Figure 6.3: From left to right, estimated ionospheric phase screen, compensated interferogram, and turbulent part of the ionospheric phase screen. (a)-(c) Bayesian combination of split-spectrum and azimuth shifts with adapted anisotropic filtering. (d)-(f) Split-spectrum with isotropic Gaussian filtering.

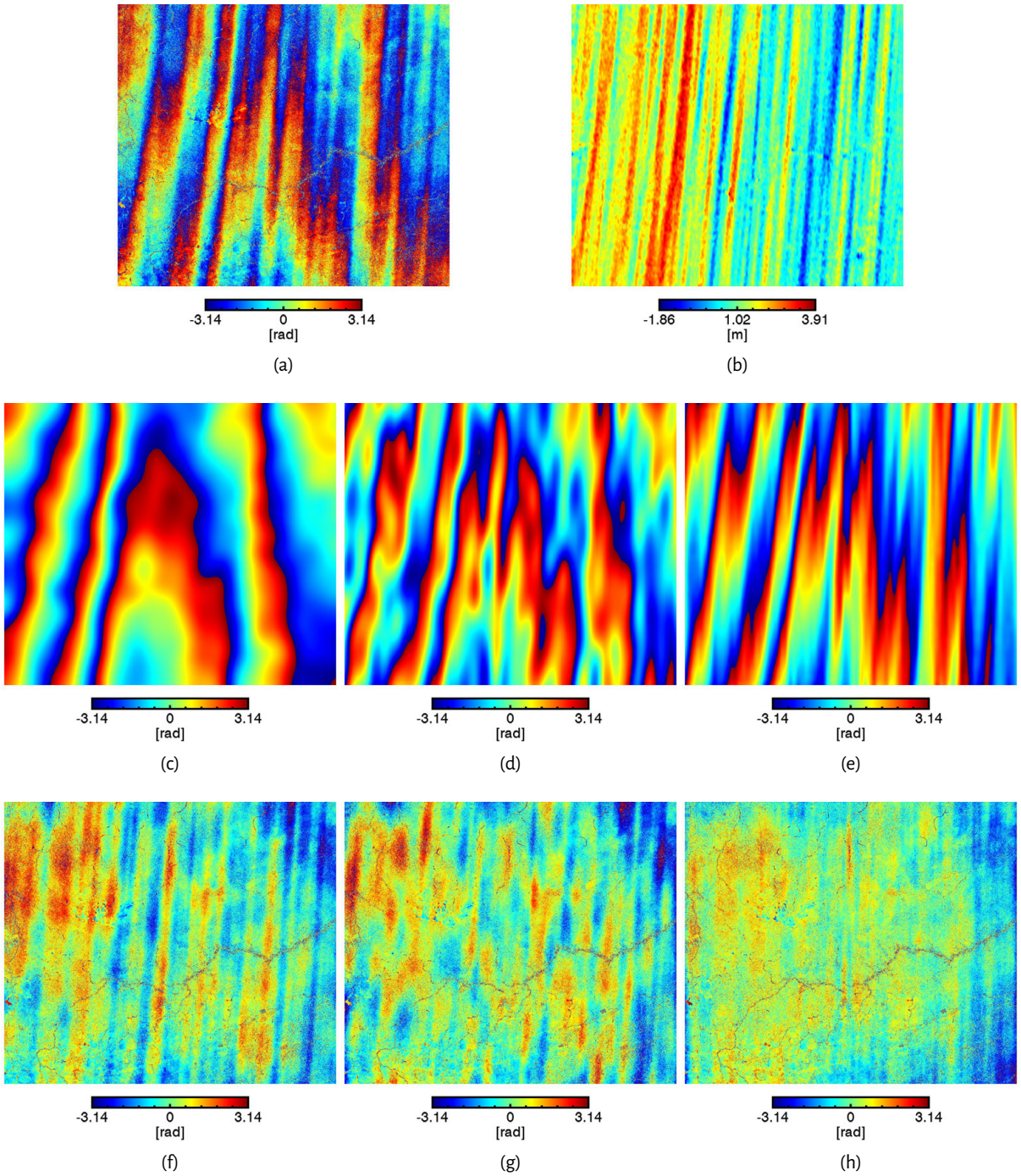

Figure 6.4: (a) Interferogram of the scintillation test case, rapid range phase variations are due to the turbulent ionospheric state. (b) Azimuth shifts, measured by patch-based cross correlation. Estimated ionospheric phase screen using the (c) split-spectrum method with isotropic Gaussian filtering, (d) split-spectrum method with adapted anisotropic filtering and (e) combined split-spectrum and azimuth shifts with adapted anisotropic filtering. (f)-(h) Compensated interferograms. Azimuth length is 59 km, ground range length is 66 km.

6.4 Conclusion

The method presented in this chapter combines information from two sources to improve the estimation of the ionospheric phase screen. The advantages of the new approach are manifold: a

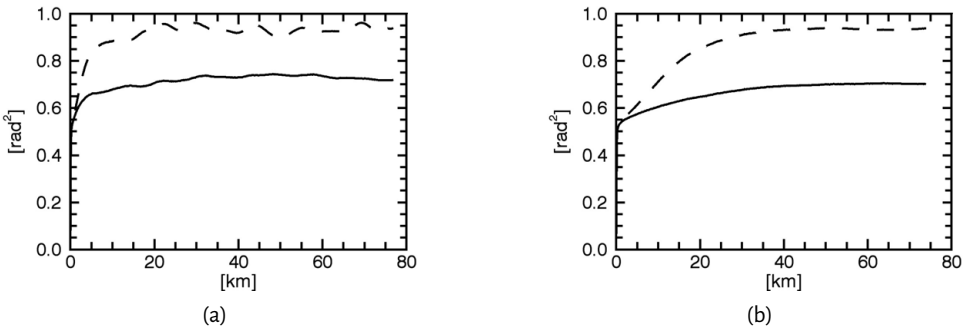

Figure 6.5: (a) Range and (b) azimuth variogram of the compensated interferogram, using the split-spectrum method (dashed line) and the combined method (solid line).

physically realistic function of the ionosphere spatial correlation can be used. Data-based extraction of the model parameters allows one to avoid generic smoothing windows and coefficients. Noise filtering, impulse response deconvolution and signals combination are realized in a Wiener sense.

Nevertheless, the split-spectrum and azimuth shifts combination has its limits, as no azimuth ground motion is allowed. The inclusion of other data, or methods, in the inverse problem, could further increase the accuracy and remove this limitation. This combination is therefore also a first step towards the estimation of north-south ground motion in the presence of ionospheric disturbances. The latter, in fact, requires an accurate estimation of the ionosphere, which is only reachable by combining information from different sources as no existing method, when used singularly, is accurate enough. Other issues that could be addressed by a more complex estimation scheme are for example different ionospheric heights and motion of the ionosphere during SAR acquisitions.

7 Validation

A complete validation of the ionospheric parameters estimated from SAR images by independent measurements is very challenging. In fact, no system is known which would be able to measure the ionosphere with the same resolution of SAR. Nevertheless, a qualitative validation by means of GPS measurements, presented in the Appendix B: *G. Gomba, F. Rodriguez-Gonzalez, and F. De Zan, "Ionospheric Phase Screen Compensation for the Sentinel-1 TOPS and ALOS-2 ScanSAR modes," IEEE Transactions on Geoscience and Remote Sensing, (2017)*. (Gomba et al., 2017), is summarized in this chapter.

7.1 Validation with GNSS measurements

Simulated ionospheric interferograms can be generated using TEC maps, which are derived from GNSS measurements. The international GNSS service (IGS) produces vertical TEC maps on a daily basis with a temporal resolution of two hours, by combining several products independently generated from different ionospheric analysis centers (Hernández-Pajares et al., 2009). These maps use GNSS measurements to adapt the ionospheric models to the current ionosphere state. They are thus only able to capture the large-scale variations of the background ionosphere, localized effects such as TIDs, aurora, spread-F, or local gradients and waves, cannot be seen in global TEC maps. GNSS measurements possibly also have a completely different viewing geometry with respect to SAR, the piercing point positions could be very distant and the elevation angle different. Moreover, they measure the complete ionosphere whereas SAR satellites orbits at about 550-700 km altitude, and thus only experience a part of it. In conclusion, in order to better capture the same ionosphere that a SAR image could have encountered, raw GNSS data should be used to produce regional or local TEC maps, which seems to be better suited to validate SAR measurements.

7.1.1 Comparison with global TEC maps

The global maps have to be interpolated in time and space to obtain the TEC estimation for the ionospheric piercing point associated with every image pixel. A mapping function and the local look angle is used to convert vertical TEC to slant TEC. The expected interferometric phase is calculated by converting the difference between TEC maps to a phase delay using (2.38), creating a simulated interferogram.

Here, simulated ionospheric phase screens of the Nepal earthquake data set, produced using IGS TEC maps, are displayed in Figure 7.1 along with the split-spectrum interferograms. The Nepal simulated interferograms show an azimuth variation of about 1.5, 3 and 9 TECU in 300 kilometers, whereas the split-spectrum measured respectively a variation of about 2.5, 4 and 14 TECU. The smaller TEC maps values could be attributed to the coarse sampling of the GNSS measurements in the considered regions, and to the smooth ionospheric models used during data assimilation.

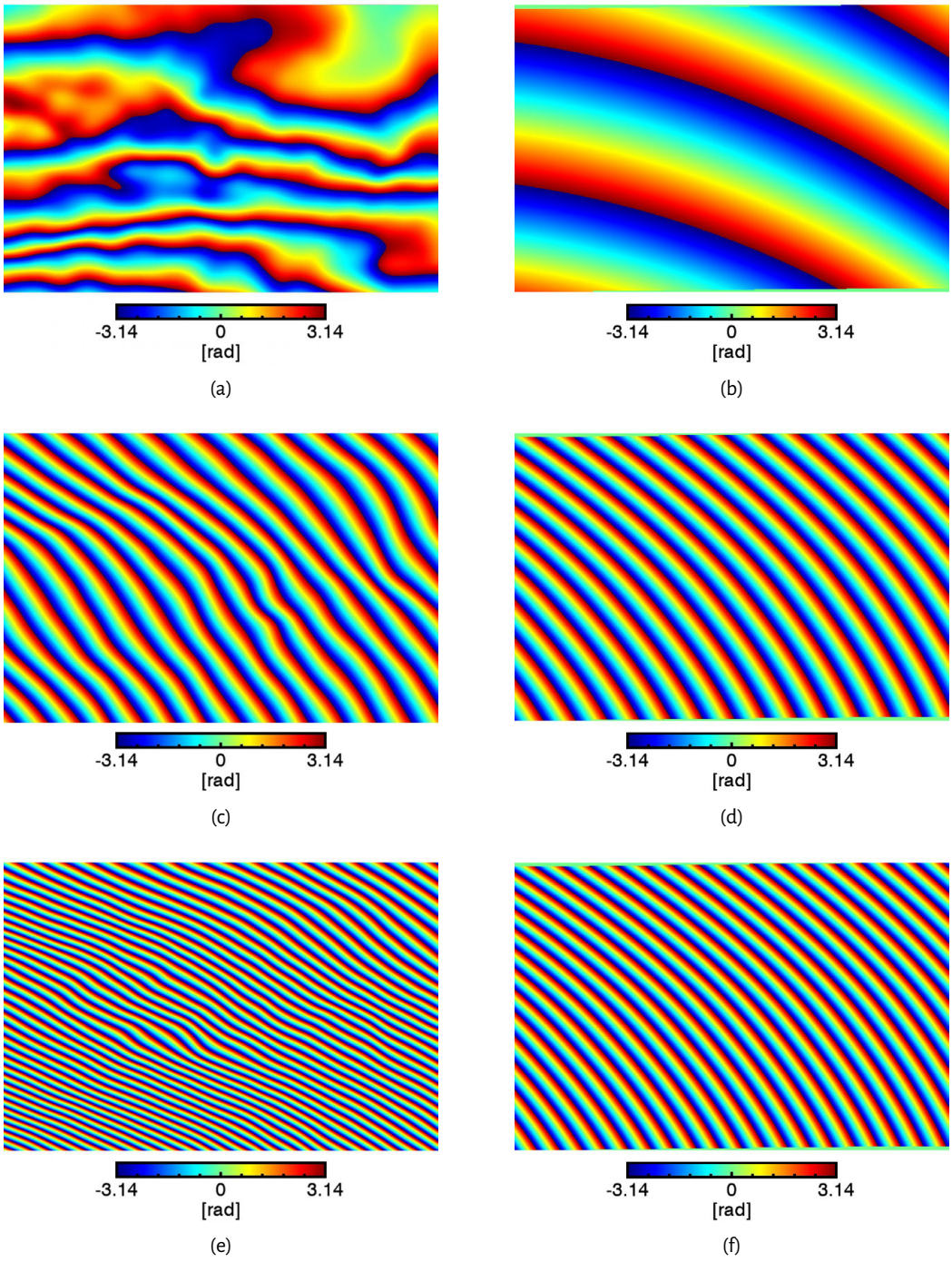

Figure 7.1: Ionospheric phase screens from split-spectrum data (left column) and from IGS TEC maps (right column). Azimuth length is 300 km, ground range length is 350 km.

According to IGS TEC products, the differential vertical TEC levels are about 5, 18 and 24 TECU. The correlation with the spatial variation indicates how higher absolute and differential TEC levels seem to be associated with steeper slopes. The range variation measured by InSAR also depends on the differential constant TEC level (Meyer et al., 2006), as indicated in (2.40). In addition to the eventual TEC range variation, the differential ionospheric level will then produce a variation in the range direction because of the incidence angle change. In the Nepal interferograms, about one range fringe is expected for every six differential TECU. Therefore, one range fringe in the first

interferogram, three in the second and eight in the third are due to the different constant TEC level, and the remaining ones to a ΔTEC range variation.

7.1.2 Comparison with local GPS measurements

IGS TEC maps for the Taiwan test case indicate a north-south variation of only about 2 TECU over 300 kilometers [see Figure 7.2(b)] whereas the split-spectrum measure is of about 25 TECU [see Figure 7.2(a)]. To improve the ionosphere reconstruction, local estimates of the vertical TEC are used. These are obtained from calibrated slant TEC measurements, extracted from GPS data, at the time of the SAR acquisitions. The measurements are overlaid on IGS TEC maps in Figure 7.2(d) and (f), for master and slave, respectively. The black line is the satellite orbit, and the black square is the image ground footprint. The red square is the ionosphere which is seen by the SAR image when assuming a single layer model at the height of 350 kilometers. The black triangles are the GPS receivers, and the colored circles are the ionosphere measurements. Differences between global maps and local measurements demonstrate how the TEC maps are only a smooth approximation of the background ionospheric variation and do not recover small-scale structures, even if they have a large magnitude.

The local ionosphere over Taiwan is then estimated by Kriging interpolation of the GPS TEC measurements. The resulting improved local TEC maps are shown in Figure 7.2(e) and (g). The simulated interferogram [see Figure 7.2(c)], produced using the new interpolated TEC maps, is similar to the original Sentinel-1 interferogram and to the split-spectrum result. The north-south variation is now about 15 TECU in 300 kilometers. The residual difference with respect to the split-spectrum can be due to the lack of piercing points near the ionosphere seen by the SAR images.

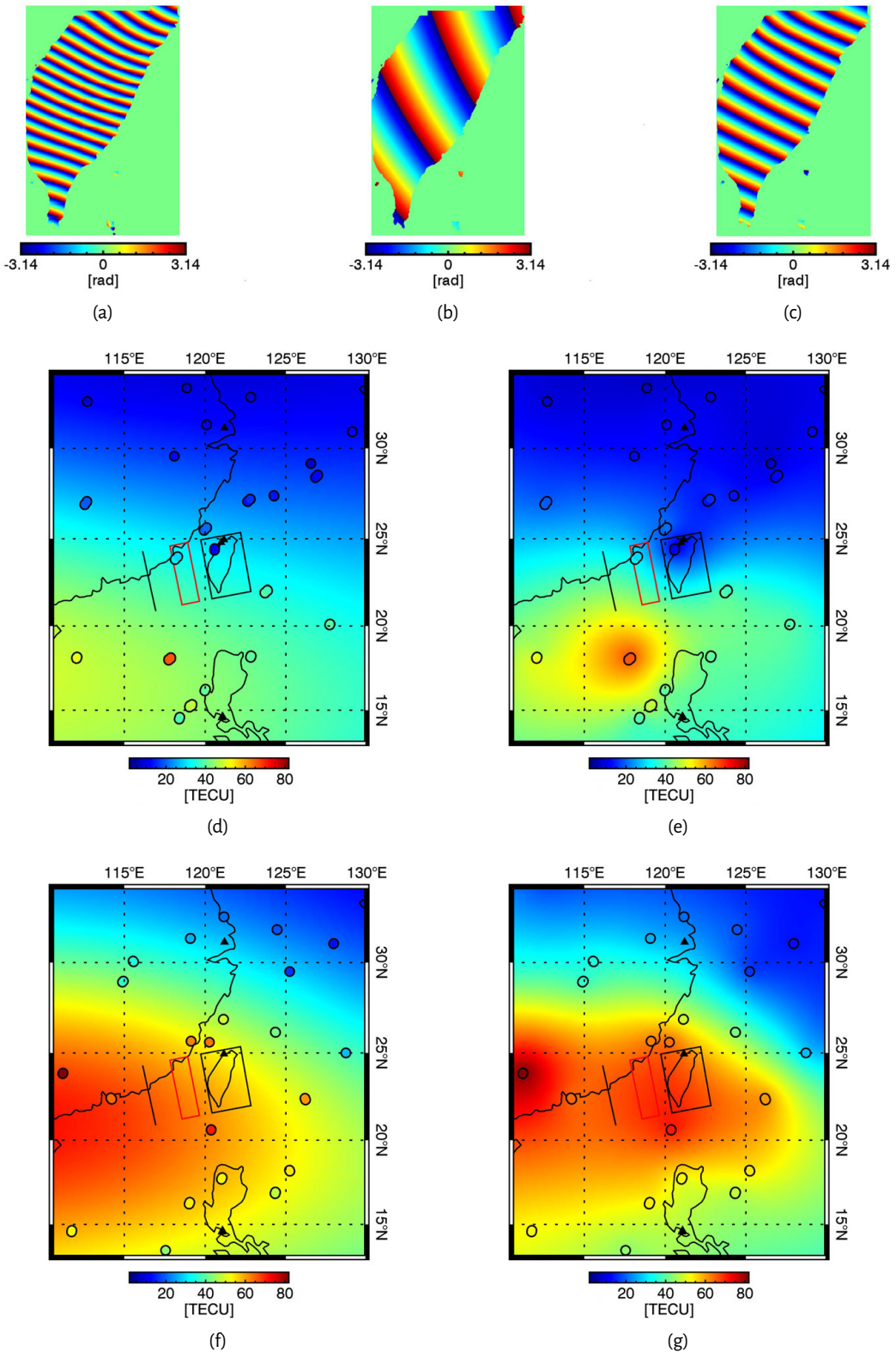

Figure 7.2: Simulated interferograms of the Taiwan ionosphere using (a) the split-spectrum data, (b) the IGS data, and (c) the local TEC maps from GPS data. (d) and (f) GPS TEC measurements overlaid on the IGS TEC maps for master and slave acquisition, respectively. Black line and square indicate the orbit and image ground footprint, red square indicates the crossed ionosphere, triangles indicate the GPS receiver position, colored points are the GPS derived TEC measurements. (e) and (g) Interpolated TEC maps produced with the GPS data.

8 Conclusion

The propagation of electromagnetic waves in the ionosphere introduces errors that limit the quality of satellite radars products. This dissertation aims to develop methods to estimate and compensate ionospheric propagation delays in SAR signals. Correction of ionospheric effects for SAR interferograms, in particular, improves the accuracy in measuring ground deformation thus helping scientists to monitor the Earth's dynamic processes. L-band interferograms benefit most of ionospheric corrections, as low frequencies are more influenced by the ionosphere. Nevertheless, for precise ground deformation measurements, even C-band systems may require ionospheric corrections.

It has been demonstrated with real data tests that the split-spectrum method can estimate and compensate the ionospheric phase screen in interferograms. The method has been applied to Stripmap, ScanSAR, and TOPS data, with L- and C-band carrier frequency. The method estimates the ionospheric phase screen from the SAR data and the result is independent of ionospheric models, external data, and ground-related interferometric phase. This permits to correct interferograms without biases also over long spatial distances. The precision of the compensated interferograms, which depends on coherence, bandwidth, and ionospheric smoothness, is usually in the centimeter to millimeter level.

The semi-focusing processing has been analytically derived. It enables to produce raw images, as acquired from an imaginary satellite with an orbit altitude equal to the ionosphere peak height. This decouples the ionosphere from the image formation, permitting to compensate ionospheric effects by simply removing the ionospheric phase screen estimated with other techniques. Otherwise, in this thesis, the semi-focusing is used to estimate the electron content along-track derivative independently of ionospheric peak height changes.

The mutual azimuth shifts between the images of an interferometric pair have been used to estimate the local along-track derivative of the differential ionospheric phase screen. It has been shown that the azimuth shifts can recover small-scale variations with better accuracy than the split-spectrum method. An improved estimation of the ionospheric phase screen, therefore, has been obtained by developing a method that combines the split-spectrum method with the azimuth shifts. This new method is based on a Bayesian inverse problem formulation and uses, for the spatial autocorrelation of the result, a fractal model. By extracting the model parameters directly from the data, the inverse problem performs an anisotropic filtering, automatically adapted to the characteristics of the ionosphere under estimation.

The method presented in this dissertation could be easily included in an operational processing environment to correct single interferograms. Moreover, it could also be adapted for interferogram stacks. The split-spectrum method would be the core of the interferograms correction. The fractal model would be automatically adapted to the ionosphere characteristics realizing an anisotropic filtering. Other data sources could then be included in the inverse problem. If the assumption of no along-track ground deformation could be made, azimuth shifts could be used, or, if quad-polarized

data should be available, also Faraday rotation measurements.

Future developments include the estimation of along-track ground motion and the estimation of the absolute ionosphere. The former could be achieved by splitting the azimuth bandwidth into subapertures and exploiting the different variation in the Doppler domain of ground- and ionosphere-based azimuth effects. The latter would require using a stack of images to increase the accuracy of the absolute ionosphere estimation. The effects of the ionospheric propagation delay on persistent scatterers processing are also still unknown and would require further studies. The compensation of ionospheric effects has been realized in this thesis by simply subtracting the estimated ionospheric phase screen from the interferogram. However, if a precise estimation of the absolute ionosphere would be available, also single images could be corrected. One possible solution includes the use of the semi-focusing processing. However, for severe turbulence or lower carrier frequency than L-band a more advanced technique that also corrects higher-order effects should be developed. With the increasing number of GNSS systems and more accurate estimation methods, the validation of SAR-based ionosphere estimates and the integration with GNSS-based ones should become feasible. Finally, statistical analysis of ionospheric effects on SAR systems with different carrier frequencies, or mapping of ionospheric TEC distributions with SAR, benefits from the increasing number of available SAR systems and should be put into practice.

A

Gomba, G., Parizzi, A., De Zan, F., Eineder, M., and Bamler, R. (2016). Toward Operational Compensation of Ionospheric Effects in SAR Interferograms: The Split-Spectrum Method. IEEE Transactions on Geoscience and Remote Sensing, 54(3):1446-1461

Toward Operational Compensation of Ionospheric Effects in SAR Interferograms: The Split-Spectrum Method

Giorgio Gomba, Alessandro Parizzi, Francesco De Zan, Michael Eineder, *Senior Member, IEEE*, and Richard Bamler, *Fellow, IEEE*

***Abstract*—The differential ionospheric path delay is a major error source in L-band interferograms. It is superimposed to topography and ground deformation signals, hindering the measurement of geophysical processes. In this paper, we proceed toward the realization of an operational processor to compensate the ionospheric effects in interferograms. The processor should be robust and accurate to meet the scientific requirements for the measurement of geophysical processes, and it should be applicable on a global scale. An implementation of the split-spectrum method, which will be one element of the processor, is presented in detail, and its performance is analyzed. The method is based on the dispersive nature of the ionosphere and separates the ionospheric component of the interferometric phase from the nondispersive component related to topography, ground motion, and tropospheric path delay. We tested the method using various Advanced Land Observing Satellite Phased-Array type L-band synthetic aperture radar interferometric pairs with different characteristics: high to low coherence, moving and nonmoving terrains, with and without topography, and different ionosphere states. Ionospheric errors of almost 1 m have been corrected to a centimeter or a millimeter level. The results show how the method is able to systematically compensate the ionospheric phase in interferograms, with the expected accuracy, and can therefore be a valid element of the operational processor.**

***Index Terms*—Interferometric synthetic aperture radar (InSAR), ionosphere estimation, split spectrum, synthetic aperture radar (SAR) ionospheric effects.**

I. Introduction

IONOSPHERIC propagation delay is one of the most relevant error sources in low-frequency spaceborne synthetic aperture radar (SAR) interferograms. SAR interferometry is a successful technique used to measure the Earth's topography and to study geophysical processes such as earthquakes, volcanoes, landslides, and glacier movements. Unfortunately, the accuracy of these measurements is limited by distortions that the ionosphere causes in the propagation of microwaves. In SAR interferograms, topography and ground deformation signals are mixed with ionospheric disturbances [1]. In order to avoid that the ionospheric propagation delay is confused with ground signals, it has to be estimated and removed [2]. The ionospheric distortions on the propagation of microwaves cause an additional group delay and a phase advance on SAR images, whose magnitude is inversely proportional to the frequency of the system. For this reason, L-band SAR systems such as the Advanced Land Observing Satellite (ALOS) Phased-Array type L-band SAR (PALSAR), its follow-up, i.e., ALOS-2, or the future Tandem-L, due to the lower frequency, experience more severe ionospheric distortions compared with C-band or X-band systems.

The magnitude of ionospheric effects depends on the slant total electron content (TEC), which is the total number of electrons integrated between the satellite and the target, along a tube of 1 m^2 cross section. If the correct TEC at the time of the two acquisitions is known, the TEC difference can be converted to a phase and removed from the interferogram. Global Navigation Satellite Systems (GNSS) dual-frequency systems can be used to estimate the TEC between the GNSS satellite and the ground and produce global or local vertical TEC maps [3]. These measures are unfortunately not detailed enough to be directly used to correct the ionospheric delay in L-band SAR interferograms [2].

Several methods to estimate the ionospheric differential TEC from SAR data, with higher precision compared with the GNSS-based measurements, have been proposed in the past years [4] and are briefly summarized in the following. The range split-spectrum method exploits the dispersive propagation of the ionosphere to separate the ionospheric-related phase term from the nondispersive phase term of an interferogram [5], [6]. The range phase–group delay difference method estimates the ionosphere, taking advantage of the fact that the ionospheric phase and group delays have opposite signs, unlike ground-related phase and group delays, which have the same sign [5], [7]. The azimuth shift method exploits the proportional relation between differential azimuth shift and the azimuth derivative of the differential ionosphere [7]–[9]. Multiple aperture interferometry is sometimes used to estimate the azimuth shifts and can be considered an equivalent method [10]. These two methods cannot recover the ionospheric range variations, being sensitive

Manuscript received May 26, 2015; revised August 25, 2015; accepted September 17, 2015. Date of publication October 27, 2015; date of current version February 24, 2016.

G. Gomba, A. Parizzi, and F. De Zan are with the Remote Sensing Technology Institute, German Aerospace Center (DLR), 82234 Wessling, Germany (e-mail: giorgio.gomba@dlr.de).

M. Eineder is with the Remote Sensing Technology Institute, German Aerospace Center (DLR), 82234 Wessling, Germany, and also with Technische Universität München, 80333 Munich, Germany.

R. Bamler is with the Remote Sensing Technology Institute, German Aerospace Center (DLR), 82234 Wessling, Germany, and also with Lehrstuhl für Methodik der Fernerkundung, Technische Universität München, 80333 Munich, Germany.

Color versions of one or more of the figures in this paper are available online at http://ieeexplore.ieee.org.

Digital Object Identifier 10.1109/TGRS.2015.2481079

just along the azimuth direction. The Faraday rotation method requires quad-polarized measurements to estimate the Faraday rotation angle and TEC from the individual images [11]–[13]. By differencing the derived TEC information, differential TEC maps can be produced and converted to ionospheric phase screens. However, the Faraday rotation depends on the geometry between the radar acquisition and the Earth magnetic field. For this reason, the method's sensitivity is strongly reduced in an area of several hundred kilometers along the magnetic equator. Therefore, in addition to requiring full-pol data sets, this approach has the disadvantage of not being globally applicable.

These techniques have been proven to work, but an evaluation of their performances and suitability for an operational environment on a global scale is still missing. In this paper, we demonstrate how the range split-spectrum method is capable of estimating the differential ionospheric path delay, increasing the performance of interferometric SAR (InSAR) techniques and, hence, improving the measurement accuracy of geophysical processes. To improve the method's robustness, its weaknesses are analyzed together with possible sources of systematic biases; solutions to mitigate these problems are proposed. Finally, to show its wide applicability, the improved method has been tested with a variety of different L-band ALOS PALSAR images. The data include different coherence levels, different environmental conditions such as nonmoving and moving terrains, with and without topography, and different ionospheric conditions. Images with particular ionosphere phenomena such as aurora borealis are also used. The results show that the method is effectively able to compensate the ionospheric effects in interferograms, that the obtained accuracy is comparable with the expected one, and that the method can be easily applied to new test cases almost without tuning and can therefore be included in an operational processor.

In Section II of this paper, the ionospheric effects on the propagation of microwaves are summarized. Their estimation using the range split-spectrum method is presented along with its accuracy. In Section III, an overall scheme of the implementation of the method is presented, and its critical points are analyzed in detail. The method is applied to L-band ALOS PALSAR images; Section IV presents the tests results. In Section V, the findings are summarized, and future work is proposed.

II. Theoretical Background

A. Ionospheric Effects on Interferograms

The ionosphere is the portion of the Earth's upper atmosphere where ions and electrons are present with sufficient density to significantly affect the propagation of radio waves. Charged particles are created by the incoming solar radiation that ionizes atmospheric gases. Their concentration in the ionosphere varies with the altitude but normally has a peak between 300 and 400 km. The 3-D structure of the ionosphere is often approximated by an idealized thin layer, which is positioned at the barycenter of the electron density. Two effects of the ionosphere on a traversing microwave can be derived from the Appelton–Hartree equation [14], which relates the refractive index of the plasma to its ionization. The first effect is

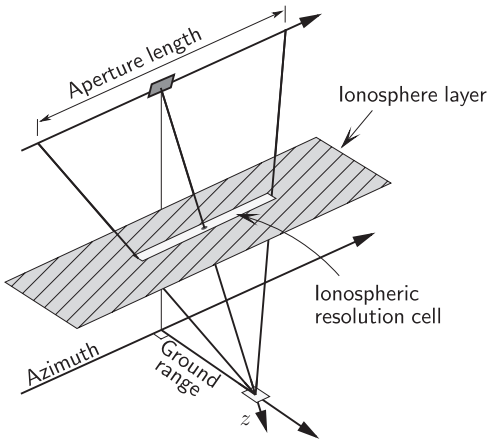

Fig. 1. Geometry of the system. The ionospheric resolution is limited by the SAR range resolution and by the synthetic aperture length.

a phase advance of the carrier. This is calculated by integrating the density of free electrons n_e along the two-way wave path, i.e.,

$$\phi_{\text{iono}}(f) = 2 \cdot \frac{2\pi K}{cf} \int n_e(z)\, dz = \frac{4\pi K}{cf}\text{TEC}. \quad (1)$$

In the latter, f is the carrier frequency, c is the speed of light in vacuum, and $K = 40.28\ \text{m}^3/\text{s}^2$. The slant TEC $= \int n_e(z)\, dz$ is the TEC experienced by the radio wave; it can be converted to a vertical TEC using a mapping function [15].

As the ionosphere is dispersive, different frequencies are differently advanced according to (1). The second effect is a rotation of the polarization angle, a phenomenon known as Faraday rotation. Since its contribution to the interferometric phase is minimal, it will be neglected in the following.

The interferometric phase is the sum of different components, i.e.,

$$\Delta\phi = \frac{4\pi f_0}{c}(\Delta r_{\text{topo}} + \Delta r_{\text{mov}} + \Delta r_{\text{tropo}}) - \frac{4\pi K}{cf_0}\Delta\text{TEC} \quad (2)$$

where f_0 is the carrier frequency; and Δr_{topo}, Δr_{mov}, and Δr_{tropo} are the topographic path delay, which includes the flat-earth phase and the topography-related phase, the differential path delay associated with a ground movement between acquisitions, and the differential tropospheric path delay, respectively. We group the nondispersive contributions to the interferometric phase in

$$\Delta\phi_{\text{non-disp}} = \frac{4\pi f_0}{c}(\Delta r_{\text{topo}} + \Delta r_{\text{mov}} + \Delta r_{\text{tropo}}) \quad (3)$$

to distinguish them from the dispersive ionospheric contribution

$$\Delta\phi_{\text{iono}} = -\frac{4\pi K}{cf_0}\Delta\text{TEC} \quad (4)$$

where ΔTEC is the differential TEC, i.e., the TEC difference between the two acquisitions. The negative sign of (2) and (4) indicates that the ionospheric contribution is a phase advance.

The ionospheric azimuth resolution is limited by the synthetic aperture length projected at the height of the ionosphere layer, as illustrated in Fig. 1. The ionospheric phase screen,

observed in the interferogram, is therefore a low-pass version of the *real*, possibly turbulent, ionosphere. Variations of the ionospheric path delay within the ionospheric azimuth resolution produce a nonnominal phase history which causes azimuth effects such as shift and blurring. These effects reduce the interferometric coherence. The magnitude and correlation length of the variations, with respect to the azimuth resolution in the ionosphere, determine the type and intensity of the effects. A linear trend of the ionospheric TEC along the flight path of the satellite causes an azimuth shift, whereas any deviation from a linear trend defocuses the image. Azimuth shifts are corrected by the coregistration and resampling steps, whereas a correction of the defocusing would require additional processing. Subapertures or a semifocusing processing can be used to increase the resolution [16], [17] and improve those situations where the azimuth variations are so strong that they cause defocusing and loss of interferometric coherence. For all other cases, the coregistration and resampling are normally enough to recover the coherence. To produce an ionosphere-free interferogram, it is sufficient to estimate and remove the low-pass ionosphere which is superimposed to the interferogram (the ionospheric phase). In this sense, if the ionospheric variations, with respect to the aperture length, are moderate enough that they do not cause relevant azimuth defocusing or coherence losses after coregistration, the ionosphere can be considered *smooth*, and there is no need to increase the ionospheric resolution using subapertures or semifocusing.

The dispersive ionospheric contribution $\Delta\phi_{\text{iono}}$ is inversely proportional to the frequency, whereas the nondispersive ground and troposphere contribution $\Delta\phi_{\text{non-disp}}$ is directly proportional to the frequency. This characteristic can be exploited to separate these two phase components: to establish the maximum possible separation accuracy, we calculate the Cramér–Rao bound (CRB).

B. CRB for Ionospheric Path Delay Estimation

We use the CRB to calculate the maximum achievable accuracy of estimating the ionospheric path delay, considering the information [which originates from the effect in (1)] that can be obtained from range signals. To derive the CRB estimate, we assume that the SAR acquisitions are dominated by distributed scatterers, such that the observed SAR signals can be represented by partially correlated complex Gaussian signals. The acquisitions can be modeled without loss of generality in the frequency domain, i.e.,

$$\begin{aligned} S_1(f) &= \sqrt{\gamma}A(f) + \sqrt{1-\gamma}W_1(f) \\ S_2(f) &= \sqrt{\gamma}A(f)\exp\left(-j\Delta\phi_{\text{non-disp}}\frac{f}{f_0} - j\Delta\phi_{\text{iono}}\frac{f_0}{f}\right) \\ &\quad + \sqrt{1-\gamma}W_2(f) \end{aligned} \tag{5}$$

where $A(f)$, $W_1(f)$, and $W_2(f)$ are uncorrelated complex Gaussian signals, with zero mean, unitary variance, and a white spectrum of bandwidth B and central frequency f_0. A represents the coherent scattering, whereas W_1 and W_2 represent the decorrelation noise; γ is the magnitude of the interferometric coherence. The interferometric phase is assigned to the second acquisition.

For each frequency, the two observations are collected in the vector $\boldsymbol{y}(f) = [S_1(f), S_2(f)]$. The elements of the Fisher information matrix, calculated using the covariance $\boldsymbol{C}(f) = E[\boldsymbol{y}(f)\boldsymbol{y}^H(f)]$, are given by [18]

$$[\mathbf{FIM}(f)]_{n,k} = \text{tr}\left\{\boldsymbol{C}^{-1}(f)\frac{\delta\boldsymbol{C}(f)}{\delta\theta_n}\boldsymbol{C}^{-1}(f)\frac{\delta\boldsymbol{C}(f)}{\delta\theta_k}\right\} \tag{6}$$

where $n, k = \{1, 2\}$; and θ_1 and θ_2 are the two unknown parameters $\Delta\phi_{\text{non-disp}}$ and $\Delta\phi_{\text{iono}}$, respectively. The result is

$$\mathbf{FIM}(f) = \frac{2\gamma^2}{1-\gamma^2}\begin{bmatrix} \frac{f^2}{f_0^2} & 1 \\ 1 & \frac{f_0^2}{f^2} \end{bmatrix}. \tag{7}$$

The final Fisher information matrix can be obtained by integrating across the signal spectrum and multiplying by the number of independent samples N [19], [20], i.e.,

$$\mathbf{FIM} = \frac{N}{B}\int_{f_0-B/2}^{f_0+B/2}\mathbf{FIM}(f)df. \tag{8}$$

The CRB for the two parameters $\Delta\phi_{\text{non-disp}}$ and $\Delta\phi_{\text{iono}}$ is the inverse of the Fisher information matrix, i.e.,

$$\text{CRB} = \frac{f_0^2}{B^2}\frac{3}{2N}\frac{1-\gamma^2}{\gamma^2}\begin{bmatrix} 1 & \frac{B^2}{4f_0^2}-1 \\ \frac{B^2}{4f_0^2}-1 & \left(1-\frac{B^2}{4f_0^2}\right)\left(1+\frac{B^2}{12f_0^2}\right) \end{bmatrix}. \tag{9}$$

From the latter, we obtain the standard deviation of the ionospheric phase estimate

$$\sigma_{\Delta\text{TEC}} \geq \frac{cf_0}{4\pi K}\cdot[\text{CRB}]_{2,2} \approx \frac{cf_0^2}{4\pi\text{KB}}\sqrt{\frac{3}{2N}}\frac{\sqrt{1-\gamma^2}}{\gamma}. \tag{10}$$

Expressing this accuracy in meters, we obtain the precision with which the error component of the ground motion estimation, related to the ionospheric noise, can be estimated, i.e.,

$$\sigma_{\Delta r_{\text{mov}}} \geq \frac{c}{4\pi f_0}\cdot[\text{CRB}]_{1,1} = \frac{c}{4\pi B}\sqrt{\frac{3}{2N}}\frac{\sqrt{1-\gamma^2}}{\gamma}. \tag{11}$$

It is interesting to note that the latter is equal to the group delay estimation accuracy [21], divided by two. The additional 0.5 factor is due to the fact that the ionosphere contributes both to the phase and group delays, but with opposite signs. The precision limit, in estimating the ionosphere, is then set by the estimation accuracy of the group delay.

The estimated ionospheric phase and its accuracy are relative to the resolution cell in the ionosphere. This is limited in range by the SAR image resolution and by the multilooking factor and in azimuth by the aperture length projected at the height of the ionosphere. Ionospheric variations with a finer spatial scale than the resolution are neither measured by the interferogram nor can they be estimated (unless using other techniques, such as subapertures or semifocusing).

C. Range Split-Spectrum Method

The range split-spectrum method [5], [6] suggests to exploit the different frequency behavior of the two components of (2) to separate them. The procedure consists in the generation of two range subbands (indices L for the lower subband and H for the higher subband) with center frequencies f_L and f_H. The interferograms computed from each subband yield the phases $\Delta\phi_L$ and $\Delta\phi_H$. Rewriting (2) for the two interferograms in terms of nondispersive and dispersive effects, we have

$$\begin{aligned}\Delta\phi_L &= \Delta\phi_{\text{non-disp}}\frac{f_L}{f_0} + \Delta\phi_{\text{iono}}\frac{f_0}{f_L}\\ \Delta\phi_H &= \Delta\phi_{\text{non-disp}}\frac{f_H}{f_0} + \Delta\phi_{\text{iono}}\frac{f_0}{f_H}.\end{aligned} \tag{12}$$

Inverting these equations, the dispersive $\Delta\phi_{\text{iono}}$ and nondispersive $\Delta\phi_{\text{non-disp}}$ components of the delay can be estimated, i.e.,

$$\begin{aligned}\Delta\hat{\phi}_{\text{iono}} &= \frac{f_L f_H}{f_0\,(f_H^2 - f_L^2)}(\Delta\phi_L f_H - \Delta\phi_H f_L)\\ \Delta\hat{\phi}_{\text{non-disp}} &= \frac{f_0}{(f_H^2 - f_L^2)}(\Delta\phi_H f_H - \Delta\phi_L f_L).\end{aligned} \tag{13}$$

This simple mathematical operation requires some care in the practical implementation. The method can in fact be realized in different ways, possibly reaching the correct estimation of the ionospheric phase. However, there are some critical steps which could lead to a poor result if not carefully implemented. The interferometric coregistration, for instance, should be able to estimate strong ionospheric azimuth shifts, in order to correct them and recover the coherence. Another issue arises from phase unwrapping: given that the lower and upper interferograms have to be unwrapped prior to the scaling, eventual errors lead to a bias in the estimation. Finally, the interferometric phase noise, which is strongly amplified by the upscaling, has to be reduced. The resulting estimation accuracy will depend on the bandwidth, coherence, multilooking, and noise filtering. In Section III, we propose an implementation, and we focus on some critical steps which were carefully analyzed to improve the final result.

D. Split-Spectrum Method Accuracy

In [5], it is shown that the accuracy of the ionospheric phase estimate is maximized when the bandwidth of each subband is one third of the total bandwidth. For high coherence and large N, the accuracy is approximated using the interferometric phase variance of the subbands [22], i.e.,

$$\sigma^2_{\Delta\phi_{H,L}} = \frac{1}{2N_{sb}}\frac{1-\gamma^2}{\gamma^2} = \frac{3}{2N}\frac{1-\gamma^2}{\gamma^2} \tag{14}$$

where γ is the interferometric coherence. The number of independent samples used in each interferogram N_{sb} is one third of the total N, since only one third of the bandwidth is used. Given that the two interferograms are uncorrelated, from (13) we can write

$$\sigma^2_{\Delta\hat{\phi}_{\text{iono}}} = \left(\frac{f_L f_H}{f_0\,(f_H^2 - f_L^2)}\right)^2 \left(f_H^2\sigma^2_{\Delta\phi_L} + f_L^2\sigma^2_{\Delta\phi_H}\right). \tag{15}$$

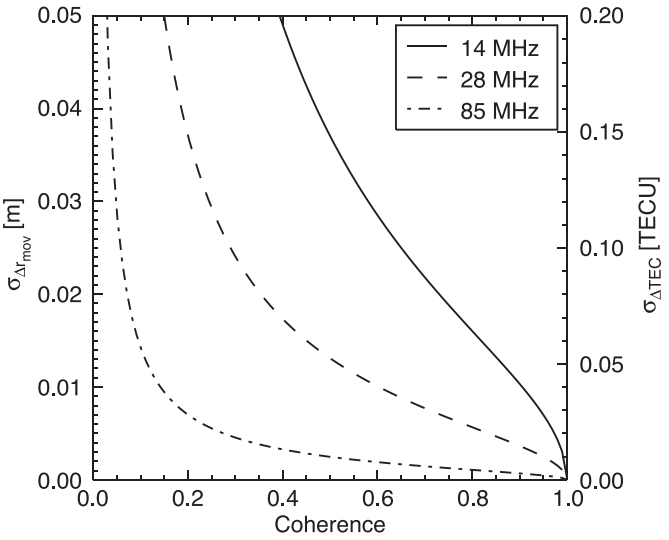

Fig. 2. Standard deviation of the ground movement (left axis) and ionospheric phase (right axis) estimation, for a ground area of 1 km^2, as a function of the interferometric coherence. Different range bandwidths of (solid line) 14 MHz, (dashed line) 28 MHz, and (dash–dot line) 85 MHz are used. Carrier frequency is 1.27 GHz.

Supposing that the coherences of both interferograms are equal, the ionospheric phase accuracy, from (14) and (15), is

$$\begin{aligned}\sigma_{\Delta\hat{\phi}_{\text{iono}}} &= \left(\frac{f_L f_H}{f_0\,(f_H^2 - f_L^2)}\right)\sqrt{f_L^2 + f_H^2}\cdot\sigma_{\Delta\phi_{H,L}}\\ &\approx \frac{3f_0}{4B}\sqrt{\frac{3}{N}}\frac{\sqrt{1-\gamma^2}}{\gamma}\end{aligned} \tag{16}$$

which, when converted to TECs, becomes

$$\sigma_{\Delta\text{TEC}} = \frac{3cf_0^2}{16\pi\text{KB}}\sqrt{\frac{3}{N}}\frac{\sqrt{1-\gamma^2}}{\gamma}. \tag{17}$$

In reality, the coherences of the interferograms can differ; the exact accuracy is then just a bit more complex than (16). It includes both coherences, as well as the range and azimuth oversampling factors. To simplify the discussion, in the following, we will use the shorter (16). As it can be seen, comparing (17) and (10), the split-band method accuracy is only 1.06 times worse than the CRB. The estimation accuracy converted in meters is

$$\sigma_{\Delta r_{\text{mov}}} = \frac{3c}{16\pi B}\sqrt{\frac{3}{N}}\frac{\sqrt{1-\gamma^2}}{\gamma}. \tag{18}$$

Equations (17) and (18) are represented in Fig. 2. The number of independent samples is calculated for a ground area size of 1 km^2; 1.27-GHz carrier frequency; 14-, 28-, and 85-MHz range bandwidths; 5-m azimuth resolution; and 30° incidence angle. For example, a coherence of 0.6 allows an accuracy of about 1 cm when performing the multilooking on an area of 1 km^2 using images with 28-MHz bandwidth. One centimeter seems already an acceptable accuracy because it is comparable with a typical residual tropospheric influence after compensation. However, the accuracy can be increased by further filtering: a discussion about multilooking and filtering can be found in Section III.

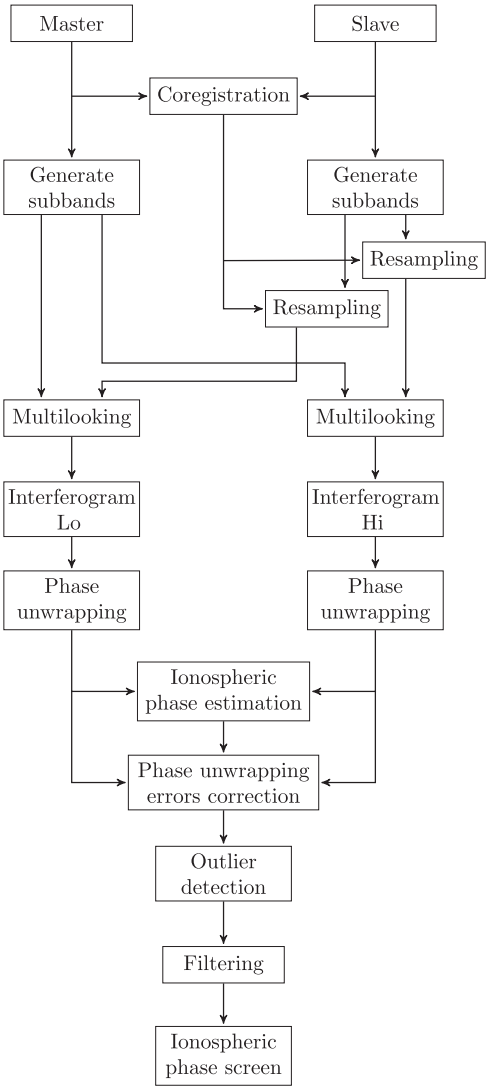

Fig. 3. Implementation of the split-spectrum method.

III. Implementation and Systematic Errors

Here follows a description of the proposed implementation of the split-spectrum method. In Fig. 3, a schematic representation is reported.

First, the images have to be carefully coregistered; to improve robustness, in our implementation, we use a mixture of coherent patch-based cross correlation for high-coherence areas and incoherent cross correlation for low-coherence areas. In order to ensure that, in case of strong ionospheric azimuth variations and/or ground movements, the high-frequency components of the motion field are preserved, no polynomial fitting of the shifts is performed.

Considering the wavenumber shift [23], in the second step, common range band filtering is performed; this increases the coherence for pairs with nonzero normal baseline. In Section III-E, wavenumber-shift-related aspects are further discussed. Two subbands of one third of the total common bandwidth are then generated by bandpass filtering. The slave images are resampled using the shifts which have been estimated during the coregistration step. Azimuth shifts generated by ionospheric variations are thus corrected and the coherence recovered.

After resampling, an interferogram is calculated from each subband; orbit information and a digital elevation model (DEM) are used to compensate the topographic phase. The amount of multilooking is discussed in Section III-A. Interferograms still contain the differential phase due to ground movements between acquisitions, the atmospheric phase, and the ionospheric phase. Both interferograms are unwrapped using a minimum cost flow algorithm. The effect of possible phase unwrapping errors is discussed in Section III-C. The dispersive and nondispersive components are separated by using (13). Differential phase unwrapping errors are then corrected as presented in Section III-C.

An outlier detection step is necessary to eliminate those pixels that do not follow a Gaussian distribution. This is performed using a robust median moving filter and the theoretical standard deviation (16), calculated using the interferograms coherences.

The ionospheric phase estimates are then filtered, to reach, if possible, the desired accuracy. The filtering step is described in Section III-B. Finally, the ionospheric phase screen is removed from the full-band interferogram obtaining an ionosphere-compensated interferogram.

A. Multilooking

In this implementation, there are two filtering (averaging) steps: the first one is the multilooking performed during the interferogram generation on the complex data, and the second one is the filtering of the estimated ionospheric phase. The amount of multilooking and final filtering can be partly interchanged. However, a minimum initial multilooking has to be done to reach the efficient and asymptotic estimation of the phase [24]. Moreover, it has, as usual, to be realized such that the number of looks is small enough to obtain high resolution and no coherence losses due to rapid fringes but also big enough such that phase unwrapping is possible. The multilooking factor is then constrained by these requisites. Thereafter, one can decide how to perform the final filtering.

B. Filtering

Since the ionosphere is usually relatively smooth, the estimates are often spatially correlated. This suggests that a filtering step, which removes the high-frequency noise components, could help to increase the accuracy. It is then more convenient to filter the ionosphere estimate rather than the ground component estimate, because the former is usually spatially smoother than the latter. The filtered phase screen is then subtracted from the full-band interferogram to obtain an ionosphere-compensated interferogram. The final precision is related to the phase screen accuracy. The amount of filtering depends on the desired final precision with respect to the variance of the initial estimate and needs to be decided after some careful considerations.

In our implementation, a 2-D Gaussian weighted filter is used to smooth the ionospheric phase. The filter is the normalized product of two identical 1-D Gaussian functions with variance $M^2/4\pi$ in range and azimuth. It reduces the phase variance

by a factor equal to the effective number of looks, which is approximately M^2. The precise effective number of looks N_{eff} can be obtained by numerical integration. The parameter M, which is needed to reach a desired accuracy $\sigma_{\Delta r_{\text{mov}}}$, can be calculated with respect to the initial accuracy. From (18), we obtain the relationship

$$M = \frac{3c}{16\pi B}\sqrt{\frac{3}{N}}\frac{\sqrt{1-\gamma^2}}{\gamma}\frac{1}{\sigma^2_{\Delta r_{\text{mov}}}} \tag{19}$$

where N is, as before, the multilooking factor.

Apart from the Gaussian window, the optimum approach to filter the ionosphere estimates is based on the maximum-likelihood principle [18]. We use a weighted mean, where the weights are the inverse of the expected variance, calculated from the interferograms coherence. Outliers, which have been detected in the previous step, are not used by giving them a weight equal to zero. The coefficients of the weighted mean, which are used to calculate the filtered ionosphere $\overline{\Delta\phi_{\text{iono}}}(i,k)$, combine the Gaussian filter g (having its peak at $\{i,k\}$) and the expected variance

$$w(i,k) = K\frac{g(i,k)}{\sigma^2_{\Delta\hat{\phi}_{\text{iono}}}(i,k)} \tag{20}$$

where K is a normalization factor such that $\sum w(i,k) = 1$. The variance of the result can be calculated as

$$\begin{aligned}\sigma^2_{\overline{\Delta\phi_{\text{iono}}}}(i,k) &= \sum w_i^2(i,k)\sigma^2_{\Delta\hat{\phi}_{\text{iono}}}(i,k)\\ &= K^2\sum\frac{g^2(i,k)}{\sigma^2_{\Delta\hat{\phi}_{\text{iono}}}(i,k)}.\end{aligned} \tag{21}$$

In practice, the filtering can be realized with convolutions (indicated by $*$), i.e.,

$$\overline{\Delta\phi_{\text{iono}}} = \frac{\Delta\phi_{\text{iono}}/\sigma^2_{\Delta\hat{\phi}_{\text{iono}}} * g}{1/\sigma^2_{\Delta\hat{\phi}_{\text{iono}}} * g} \tag{22}$$

$$\sigma^2_{\overline{\Delta\phi_{\text{iono}}}} = \frac{1/\sigma^2_{\Delta\hat{\phi}_{\text{iono}}} * g^2}{\left(1/\sigma^2_{\Delta\hat{\phi}_{\text{iono}}} * g\right)^2}. \tag{23}$$

Ionospheric variations with a spatial scale smaller than the smoothing window are smoothed out and not recovered. Then a tradeoff exists between reducing the estimation noise and reducing the bias due to excessive smoothing, and it could be difficult to decide the size of the filter window, i.e., the parameter M. Anisotropic filters or adaptive filters could help to increase the accuracy without introducing biases. The combination of different ionosphere estimation methods is also a possibility that is being studied [4], [9].

C. Phase Unwrapping Errors

Here, we analyze the effect of phase unwrapping errors on the estimation of the ionospheric phase. In particular, if the coherence is low, phase unwrapping errors can occur and introduce biases in the ionosphere estimation. Phase unwrapping is performed separately on each subband, and phase unwrapping errors can therefore be different. Let us define phase unwrapping errors in the lower and upper subbands with $2\pi m$ and $2\pi(m+d)$, respectively. This way, m is a common phase unwrapping error, and d is a differential one. Both terms are integers and not necessarily constant within the interferogram. Equation (12) becomes

$$\begin{aligned}\Delta\phi_L &= \Delta\phi_{\text{non-disp}}\frac{f_L}{f_0} + \Delta\phi_{\text{iono}}\frac{f_0}{f_L} + 2\pi m\\ \Delta\phi_H &= \Delta\phi_{\text{non-disp}}\frac{f_H}{f_0} + \Delta\phi_{\text{iono}}\frac{f_0}{f_H} + 2\pi(m+d).\end{aligned} \tag{24}$$

The estimated ionospheric phase thus yields

$$\Delta\hat{\phi}_{\text{iono}} \approx \Delta\phi_{\text{iono}} + \pi m + \frac{\pi}{2}d - \frac{3\pi f_0}{2B}d. \tag{25}$$

The latter shows the different behavior of common phase unwrapping errors and differential ones.

1) Differential Phase Unwrapping Error: The term d is scaled by the factor f_0/B, generating a significant bias that should be removed. Taking the difference between the two interferograms, one has

$$\Delta\phi_L - \Delta\phi_H \approx -\frac{2B}{3f_0}\Delta\phi_{\text{non-disp}} + \frac{2B}{3f_0}\Delta\phi_{\text{iono}} - 2\pi d \tag{26}$$

whereas their sum yields

$$\Delta\phi_L + \Delta\phi_H \approx 2\Delta\phi_{\text{non-disp}} + 2\Delta\phi_{\text{iono}} + 4\pi c + 2\pi d. \tag{27}$$

The term d can be then estimated from the phase difference (26), i.e.,

$$\hat{d} = \left\lfloor \frac{1}{2\pi}\left(\Delta\phi_H - \Delta\phi_L - \frac{2B}{3f_0}\Delta\phi_{\text{non-disp}} + \frac{2B}{3f_0}\Delta\phi_{\text{iono}}\right)\right\rceil \tag{28}$$

where $\lfloor\cdot\rceil$ indicates the rounding to the nearest integer. Even if $\Delta\phi_{\text{non-disp}}$ and $\Delta\phi_{\text{iono}}$ are not known with high accuracy, they do not lead to large biases in the measure of d since they are reduced by the scaling term $2B/(3f_0)$. If needed, an iterative procedure can be implemented to reach the correct values.

An example of the results obtained by applying this correction is reported in Section IV-C2.

2) Common Phase Unwrapping Error: The recovery of the common term m is more delicate; using the phase sum (27), one has

$$\hat{m} = \left\lfloor \frac{1}{4\pi}(\Delta\phi_L + \Delta\phi_H - 2\Delta\phi_{\text{non-disp}} - 2\Delta\phi_{\text{iono}}) - \frac{d}{2}\right\rceil. \tag{29}$$

Inaccurate $\Delta\phi_{\text{non-disp}}$ and $\Delta\phi_{\text{iono}}$ are misinterpreted as phase unwrapping errors, leading to an even more inaccurate estimate of $\Delta\phi_{\text{non-disp}}$ and $\Delta\phi_{\text{iono}}$. Larger filtering windows can improve the accuracy of $\Delta\phi_{\text{non-disp}}$ and $\Delta\phi_{\text{iono}}$ but also lower the resolution. This can be unacceptable, particularly for the ground-related phase, which is more likely to be spatially variable. The success of this method depends on the scene characteristics (high coherence or smooth signals) and is therefore not robust enough. A common phase unwrapping error, on the

other hand, has a small impact, compared with a differential one. Moreover, it can be considered negligible if its magnitude is smaller than the accuracy (17), as it usually happens for small error areas.

Wide areas with ambiguous phase unwrapping, e.g., when a river cut an image in two parts, can neither be recovered nor simply ignored. This is a general problem for interferometry; radargrammetry or GPS measurements could be normally used to solve it. Unfortunately, the presence of the ionosphere makes the radargrammetry method inapplicable, as discussed in the next session.

D. Unambiguous Ionospheric Phase

The estimated differential ionospheric phase can be only known to within a constant offset, since both interferograms are not absolute phases. The split-spectrum estimate is then only a relative differential phase, not an absolute differential phase. Radargrammetry is also subject to the ionospheric influence; in fact, the group delay $\Delta\tau$ is increased by the presence of the ionosphere, i.e.,

$$2f_0\Delta\tau = \frac{4\pi f_0}{c}(\Delta\tau_{\text{topo}} + \Delta\tau_{\text{mov}} + \Delta\tau_{\text{tropo}}) + \frac{4\pi K}{cf_0}\Delta\text{TEC}. \tag{30}$$

With respect to (2), the ionospheric term has, in the latter, the opposite sign. This property is used in the phase–group delay difference method [5], [7] to estimate the ionospheric contribution by subtracting the unwrapped phase from the radargrammetry. The difference contains both the ionosphere and the absolute phase offset, which cannot be separated.

It is possible to estimate the unambiguous phase by applying the same principle of the split-spectrum method to the radargrammetric shifts of the subbands. Unfortunately, the resulting accuracy is very low, i.e.,

$$\sigma_{\Delta\hat{\phi}_{\text{iono}}} \approx \frac{9f_0^2}{2B^2}\sqrt{\frac{1}{N}}\frac{\sqrt{1-\gamma^2}}{\gamma} \tag{31}$$

making this procedure unlikely applicable.

E. Wavenumber Shift

The wavenumber shift effect [23] has to be considered, while generating the subbands, to only take the common band and thus increase the coherence. However, since different parts of the ground reflectivity spectrum are linked to different signal frequencies, the matching of differently shifted ground spectra (between two images) aligns bands with different central frequencies. In [25], it is suggested that, due to this effect, each image has a different carrier frequency and therefore experiences a different ionospheric phase advance. Let us reformulate (4) as follows:

$$\Delta\phi_{\text{iono}} = \frac{4\pi K}{c}\left(\frac{\text{TEC}_1}{f_0 - \Delta f/2} - \frac{\text{TEC}_2}{f_0 + \Delta f/2}\right) \tag{32}$$

where TEC_1 and TEC_2 are the TEC levels during the first and second acquisitions, respectively; and Δf is the spectral shift [23]. Considering that $\Delta f \ll f_0$, the latter can be reduced to

$$\Delta\phi_{\text{iono}} \approx \frac{4\pi K}{cf_0}\Delta\text{TEC} + \frac{4\pi K}{cf_0}\frac{\Delta f}{2f_0}\Sigma\text{TEC} \tag{33}$$

where ΔTEC is, as in (4), the differential TEC between acquisitions, and $\Sigma\text{TEC} = \text{TEC}_1 + \text{TEC}_2$, i.e., the sum of the two TEC levels. We rewrite (12) to take into account also the last term of (33), i.e.,

$$\begin{aligned}\Delta\phi_L &= \Delta\phi_{\text{non-disp}}\frac{f_L}{f_0} + \Delta\phi_{\Delta\text{iono}}\frac{f_0}{f_L} + \Delta\phi_{\Sigma\text{iono}}\frac{f_0}{f_L}\frac{\Delta f}{2f_L}\\ \Delta\phi_H &= \Delta\phi_{\text{non-disp}}\frac{f_H}{f_0} + \Delta\phi_{\Delta\text{iono}}\frac{f_0}{f_H} + \Delta\phi_{\Sigma\text{iono}}\frac{f_0}{f_H}\frac{\Delta f}{2f_H}\end{aligned} \tag{34}$$

where $\Delta\phi_{\Delta\text{iono}} = (4\pi K/cf_0)\Delta\text{TEC}$, and $\Delta\phi_{\Sigma\text{iono}} = (4\pi K/cf_0)\Sigma\text{TEC}$. The estimated ionospheric phase becomes thus

$$\Delta\hat{\phi}_{\text{iono}} \approx \Delta\phi_{\Delta\text{iono}} + \frac{3\Delta f}{4f_0}\Delta\phi_{\Sigma\text{iono}} \tag{35}$$

this shows that the absolute ionosphere biases the differential ionosphere estimate. A compensation of the absolute ionosphere bias could be done using data from different sources, such as GNSS-based TEC maps. On the other hand, an estimation of the absolute ionosphere could be possible if the spectral shift varies within the same ionospheric level.

Relative variations of the terms of (35) generate biases in the estimated phase. To get an idea of the order of magnitude of the possible biases, we analyze two examples.

Consider an ionospheric spatial gradient in midlatitude regions; a long acquisition spanning some hundreds of kilometers could encounter a relative spatial change of ΣTEC on the order of some tens of TECU, and, supposing similar ionospheric conditions in different days, a relative spatial change of ΔTEC on the order of some TECU [26]. A spectral shift of 200 kHz, corresponding to a baseline of 100 m and an incidence angle of 35°, is used. The relative spatial change of $\Delta\phi_{\Delta\text{iono}}$ is on the order of some cycles, whereas for $\Delta\phi_{\Sigma\text{iono}}$, it is on the order of some hundreds of cycle. A terrain slope of 30° corresponds to a spectral shift of 1.7 MHz, which yields a phase difference between flat and oblique surfaces of one tenth of cycle. In this case, the second term of (35) can be then mostly ignored.

As second scenario, we consider a small acquisition in a low-latitude region; $\Sigma\text{TEC} = 80$ TECU is constant within the image, and $\Delta\text{TEC} = 0$ TECU. The baseline is 1 km, and the incidence angle is 35°. A terrain slope of 30° generates a bias of almost two cycles with respect to flat zones. In this case, the final effect on ionosphere estimation after filtering should be considered, and countermeasures could be needed.

F. Asymmetric Split-Spectrum Mode

Here, a special split-spectrum mode for SAR systems with larger bandwidth, such as the Tandem-L, ALOS-2, or NASA-ISRO SAR (NISAR) missions, is evaluated. This mode optimizes the compromise between data rate and accuracy. While wider bandwidths increase the accuracy of ionosphere estimation, the satellite onboard storage and downlink of a great amount of data is not always feasible. The optimum solution to still obtain a high accuracy with a smaller data volume would be to use two subbands of one third each of the allowed bandwidth, separated by one third. However, if the total used bandwidth is further reduced, to decrease the data amount, the ionosphere estimation noise grows. The new precision in estimating the ground movement using two subbands of bandwidth B_L and B_H, from (18), is

$$\sigma''_{\Delta r_{\mathrm{mov}}} = \frac{c}{4\pi f_0^2}\frac{f_L f_H}{f_H^2 - f_L^2}\sqrt{\frac{f_H^2}{2N_L} + \frac{f_L^2}{2N_H}}\frac{\sqrt{1-\gamma^2}}{\gamma} \quad (36)$$

where $N_L = N \cdot B_L/B$ and $N_H = N \cdot B_H/B$ are the numbers of independent samples of each subband. The ratio between this accuracy and the one obtained using the full bandwidth B is

$$\frac{\sigma''_{\Delta r_{\mathrm{mov}}}}{\sigma_{\Delta r_{\mathrm{mov}}}} \approx \frac{2f_0 B}{9}\sqrt{6B\frac{B_H + B_L}{B_H B_L}}\frac{1}{f_0(2B - B_H - B_L)} \cdot \frac{1}{B(B_L - B_H)/2 + (B_H^2 - B_L^2)/4}. \quad (37)$$

For example, if we suppose to use one subband of 20 MHz and one of 5 MHz, separated by the greatest possible distance inside the 85-MHz allowed L-band spectrum, the accuracy of the split-spectrum method would be then 1.45 times worse than that obtained using an image with the full spectrum. This is anyway much better than only using 20 MHz; in that case, the accuracy would be eight times worse. In conclusion, even if the total used bandwidth is reduced due to data constraints, a small second subband, separated by the greatest possible distance inside the allowed spectrum, permits to obtain almost the same accuracy in estimating the ionosphere as when using the full spectrum.

This mode is tested in Section IV-D using high-resolution 85-MHz ALOS-2 data to simulate a $20 + 5$ MHz acquisition.

In [27], it was shown that a custom chirp signal that concentrates all energy into the subbands increases the SNR with respect to a nominal chirp where a bandpass filter discards part of the energy to create the subbands. A special mode, which uses a modified chirp to increase the SNR, improving the accuracy (36), could be investigated in future work.

IV. Application Examples

The split-spectrum method has been applied to four different ALOS PALSAR data sets to test its robustness and applicability. The first example is an interferogram of the 2008 Kyrgyzstan earthquake; it presents high coherence and smooth ionospheric variations. The excellent results show the correct separation between ground motion and ionospheric delay. The second example is a measure of the aurora in northern Alaska. Due to the narrow 14-MHz bandwidth, the accuracy is low, and a big smoothing window is required. Consequently, small-scale variations of the ionosphere cannot be successfully recovered. A more challenging scenario, in the third example, is based on the 2008 Wenchuan earthquake. This data set is composed of 72 interferograms featuring low and high coherence levels. Phase unwrapping errors and low coherence are the main limitations; the separation between ionospheric and ground phases has been, however, achieved, and phase jumps between adjacent tracks have been reduced. All acquisitions were made during ascending passes; Table I reports detailed information about each scene.

TABLE I
Scenes Acquisition Information

Example	Track(s)	Frame(s)	Master	Slave	N.
Aurora	243	1410	01/04/06	17/05/06	2
Kyrgyzstan	527	750-790	02/06/08	20/08/09	10
Wenchuan	471	570-650	29/02/08	31/05/08	18
	472	570-650	28/01/07	17/06/08	18
	473	570-650	17/02/08	19/05/08	18
	474	570-650	05/03/08	05/06/08	18
	475	570-650	20/06/07	22/06/08	18
	476	570-650	08/04/08	24/05/08	18
ALOS-2	76	1280	10/09/14	05/10/14	2

Fig. 4. Ground coverage of the PALSAR acquisitions for the Kyrgyzstan data set.

A. Kyrgyzstan 2008 Earthquake

1) Data Set: On October 5, 2008, an earthquake struck the Nura region, in southern Kyrgyzstan [28]. We use SAR data to measure the coseismic surface displacements. The ALOS PALSAR images ground coverage is illustrated in the map in Fig. 4. With five pairs of ALOS PALSAR images, we generate an L-band interferogram, which is displayed in Fig. 5(a). The topographic phase was removed from the interferogram using a DEM. Apart from the earthquake, which is assumed to be localized only in the top part of the image, at least five fringes due to ionospheric variations can be seen in the bottom part of the interferogram. It is difficult to assess the real earthquake motion field since it is superimposed to the ionospheric phase screen.

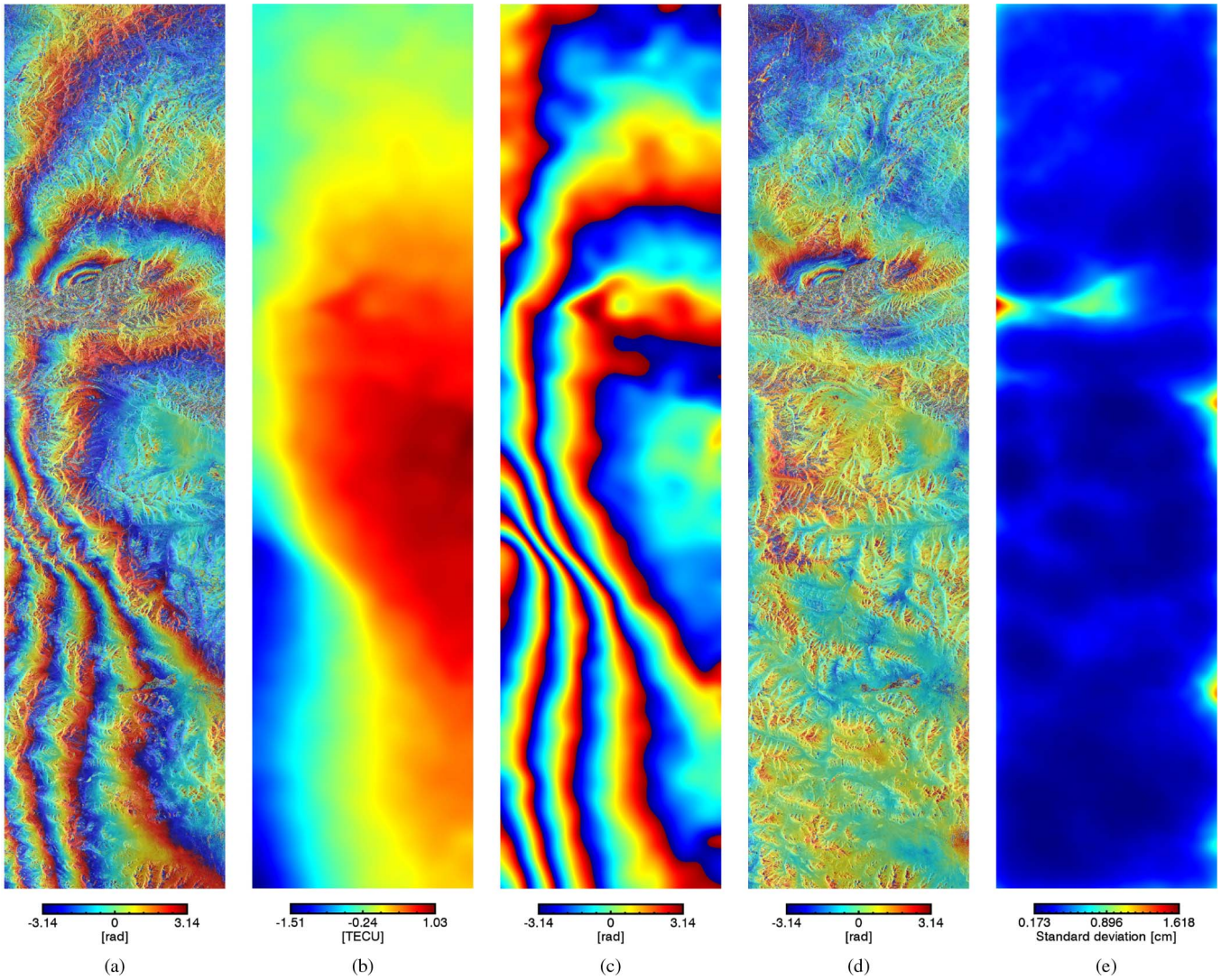

Fig. 5. (a) Kyrgyzstan 2008 earthquake of October 5 can be recognized in the top part of the interferogram. Five fringes in the bottom part of (a) are supposed to be due to ionosphere changes. (b) The ionospheric TEC map, estimated using the split-spectrum method, converted to a (c) phase screen, is used to produce the (d) ionosphere-compensated interferogram. (e) Expected accuracy of the ionosphere estimation. Azimuth length is 283 km; range length is 68 km.

The split-spectrum method was applied to the data set. Although the accuracy is limited by the narrow range bandwidth of 14 MHz, the mean coherence is 0.43, and phase unwrapping was performed without problems. The ionosphere is relatively smooth; the point of fastest variation is in the middle of the image where five fringes are visible; this indicates a change of almost 3 TECU in about 45 ground km. The images are oversampled by a factor 2 in both directions. The resulting oversampling is then 2.29 in range and 2.83 in azimuth. The applied multilooking is 23 pixels in range and 95 in azimuth; the resulting mean expected accuracy of the raw ionospheric estimates, which is calculated using (18), is 25 cm. A Gaussian filtering with an M parameter of 100 was used to increase the accuracy to about 2.5 mm, as shown in Fig. 5(e). The output of the split-spectrum method [see Fig. 5(b)], converted to a phase screen [see Fig. 5(c)], is used to compensate the initial interferogram. The result [see Fig. 5(d)] shows how the ionospheric contribution was successfully removed. The earthquake pattern can be easily recognized in the top part of the image, whereas no motion is observed in the bottom part; the 60-cm error that was introduced by five ionospheric fringes is now reduced to a millimeter level. Tropospheric delay is now more visible; in particular, a strong correlation of the phase with the topography indicates the presence of stratified tropospheric delay.

2) Performance Assessment: To check the performances of the method, the standard deviation of the raw ionosphere estimate has been calculated after the outlier rejection step. Results are shown in Fig. 6. The solid line represents the theoretical accuracy obtained from (18) considering the multilooking factor 23×95 and the oversampling. The asterisks and the circles represent the standard deviation of ionosphere estimates and are calculated in two different ways. For the asterisks, we used a moving window and the median absolute deviation, which is a robust estimator of the standard deviation. For the circles, we used the smooth ionosphere, which we suppose to be equal to the real ionospheric screen, to remove the mean value. We then take the squared error and average within different coherence intervals. The square root of the results is then displayed with their error bars. The good agreement between theoretical and measured accuracies confirm that the method performs as expected.

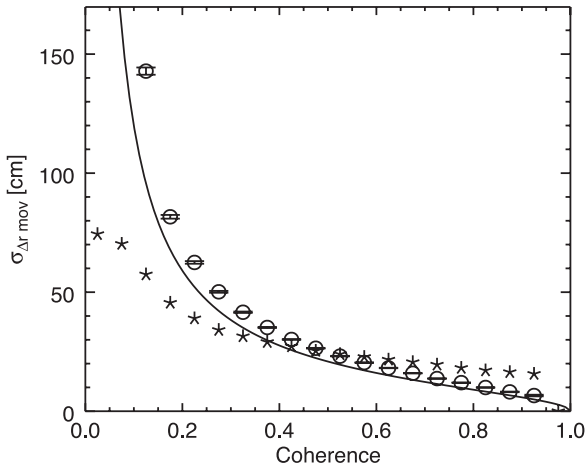

Fig. 6. Accuracy of the ionosphere estimate before filtering, Kyrgyzstan test case. The line is the theoretical accuracy, and the symbols are the measured standard deviation. Asterisks are calculated using a moving window and the median absolute deviation. Circles are calculated using the smooth ionosphere to remove the mean value and then the sample standard deviation.

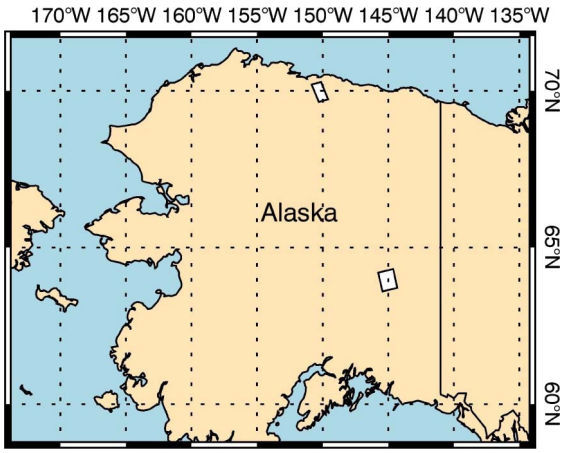

Fig. 7. In northern Alaska, the ground coverage of the PALSAR acquisition for the aurora data set; in eastern Alaska, the ALOS-2 acquisition.

B. Aurora Borealis

1) Data Set: The aurora borealis is caused by interactions between the solar wind and the Earth's atmosphere. Charged particles, which are carried by the solar wind and accelerated by the interconnections between the magnetic field of the Earth and that of the Sun, are conducted downward toward the magnetic poles where they collide with the atmosphere, ionizing oxygen and nitrogen atoms. A solar wind stream hit the Earth on March 31, 2006, causing visible auroras all around the north polar region for almost three days. L-band ALOS PALSAR images were acquired above Alaska during April 1, capturing the change of electron density in the ionosphere. The shape of the acquisition's ground coverage is represented in the map in Fig. 7. With a second acquisition in May 17, we produce an interferogram; the topographic phase was removed using a DEM.

The auroral activity generated strong and turbulent fluctuations in the ionospheric phase, as shown in the interferogram in Fig. 8. Coregistration is used to correct the azimuth shifts, which are caused by variations of the ionosphere along the flight path, recovering most of the coherence losses. In the left top corner, there is still a residual effect due to uncorrected

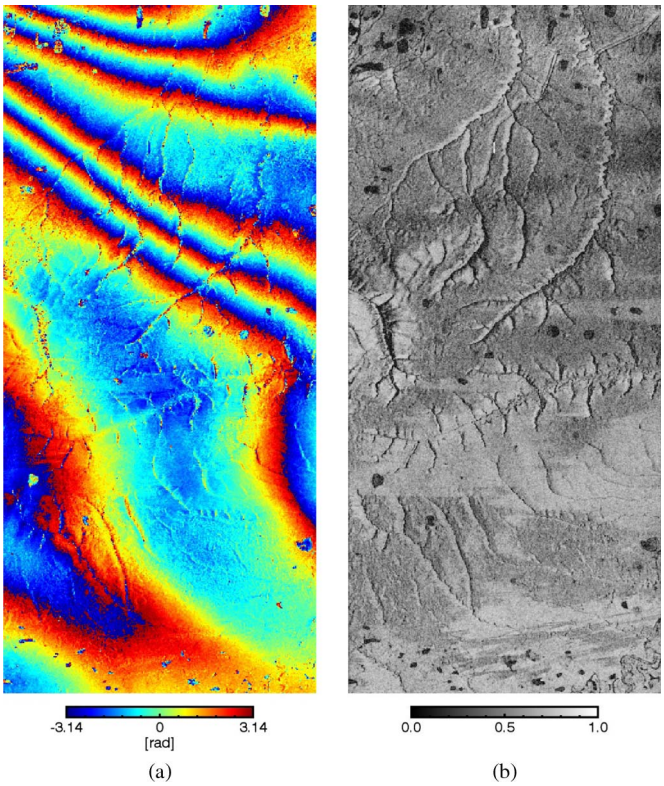

Fig. 8. Aurora activity generates rapid spatial variations in the ionospheric TEC; these variations are mapped in the (a) interferogram as phase changes. The (b) coherence shows almost no losses correlated with the ionosphere variations. Azimuth length is 66 km; range length is 28 km.

shift and/or blurring. The coherence features visible in the bottom half of the image are most probably related to changes in the ground backscatter. The along-track azimuth scale of these features is much smaller than the ionospheric azimuth resolution, which is some kilometers long. For this reason, we can exclude an ionospheric effect.

With a mean coherence of 0.5, phase unwrapping is performed without problems. The size of this image is 66 km in azimuth and 28 km in range. In one half of the image, six fringes are visible; this means that the differential ionosphere varies of almost 3 TECU in about 33 ground km. The total variation is similar to that of the previous example, but this time, it is less regular, and rapid undulations are present. Due to the relatively fine scale spatial variations of the phase screen, a small smoothing window would be preferred in order not to bias the output of the method. Unfortunately, the bandwidth is only 14 MHz, and the estimated phase is quite noisy.

2) Performance Assessment: To test this aspect, we calculate the root-mean-square deviation for increasing smoothing windows. The error is calculated between the output of the filter and the real ionospheric phase screen. Supposing no significant tropospheric contribution, the interferogram is used as real ionospheric phase screen. It is shown in Fig. 9 that the measured errors diverge from the theoretical ones when the filter size increases. The theoretical curve is the expected accuracy calculated with (18) considering the increasing effective number of looks N_{eff}. The measured error is composed of the estimation noise, which reduces for increasing filter sizes, and of the bias (the uncompensated high-frequency components), which, on the contrary, grows.

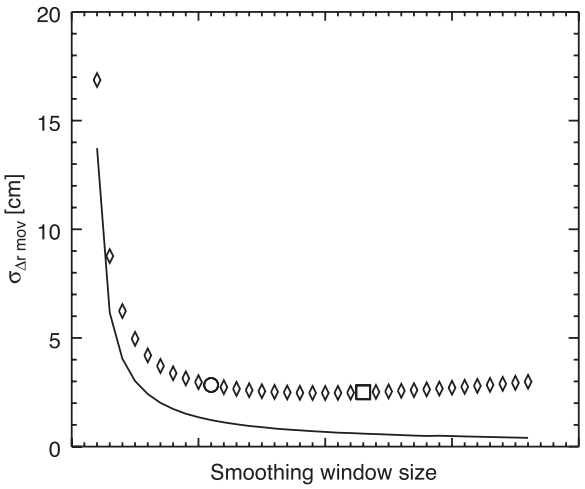

Fig. 9. Accuracy of filtered ionosphere estimate, aurora test case. Larger smoothing windows should theoretically give (solid line) lower errors; on the contrary, since small-scale ionospheric variations are not recovered, the (diamonds) measured error increases for larger smoothing windows.

Fig. 10 shows two examples of the filtered ionospheric phase screen and the respective compensated interferogram. Fig. 10(a) is produced using the filter size correspondent to the circle in Fig. 9. The result is very similar to the interferogram in Fig. 8, but a lot of irregularities, which can be also seen in the compensated interferogram in Fig. 10(b), are still present. They derive from the estimation noise, being unlikely due to atmospheric delay. A larger filtering window, correspondent to the square in Fig. 9, is used to produce Fig. 10(c). This ensures a smoother result, but the compensated interferogram still show residuals, which are the cause of the higher error, with respect to the expected, in Fig. 9. The residuals can be attributed to a bias between the real and estimated ionospheric phase screens. There is a tradeoff between the increase of the accuracy obtained with more smoothing and the biases that too much smoothing can originate. An adaptive filter, which should reduce the noise variance but also respect the high-frequency components of the phase screen, could be used to improve the result. Another possibility, to make the phase screen more precise, is the combination of more ionosphere estimation methods. Anyway, despite this issue, the method was able to reduce the error from approximately 60 cm to some centimeters.

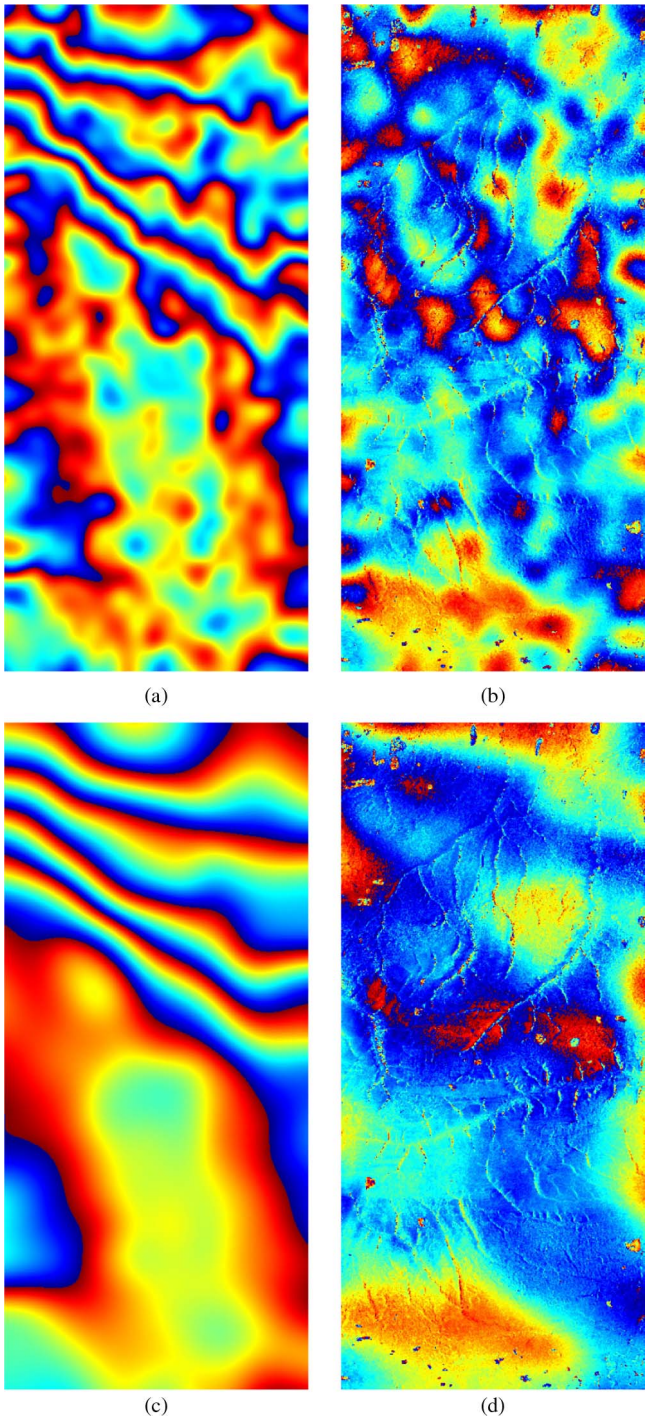

Fig. 10. (a) and (c) Estimated ionospheric phase screens. (b) and (d) Compensated interferograms. The larger smoothing window in (c), with respect to (a), ensures smoother but biased results. The color bar goes from $-\pi$ to π for all images.

C. Wenchuan 2008 Earthquake

1) Data Set: On May 12, 2008, an earthquake struck the Wenchuan region in central China. The set of images shown in Fig. 11 is what is typically selected by researchers for studying coseismic deformation patterns [29].

This is because the acquisition dates of these images reduce the influence of postseismic deformation on the interferograms. Unfortunately, this image set is heavily influenced by ionospheric distortions and needs to be corrected to enable thorough geophysical modeling. The ionospheric disturbances are superimposed on the ground motion signal and are clearly visible in the set of interferograms in Fig. 12(a). To cover the whole earthquake, many adjacent tracks have to be joined. Since each track was acquired on a different day, each one experienced a different ionosphere. A discrepancy between adjacent tracks can be expected due to aftershocks motion, different looking angles, and tropospheric delay. However, the strong phase jumps present in the interferogram in Fig. 12(a), particularly far away from the earthquake, are an indication of ionospheric activity. Moreover, strong residuals between the range deformation predicted by the geophysical model and the InSAR deformation [29] are a further indication of the ionosphere presence.

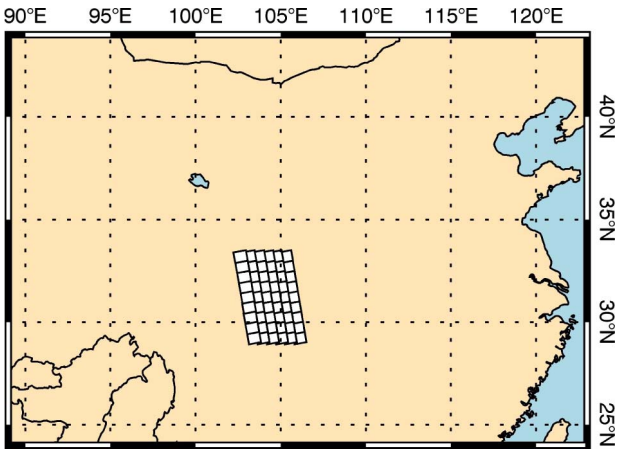

Fig. 11. Ground coverage of the PALSAR acquisitions for the Wenchuan data set. The azimuth length of nine consequent images is 510 km; the range length of six adjacent tracks is 480 km.

This data set is composed of 72 interferograms, and the coherence spans from low to high. The bandwidth is 28 MHz for all tracks, except one (475). The differential phase unwrapping errors in the areas of low coherence were corrected as presented in Section III-C. An example of this correction is presented in the next paragraph. The split-spectrum method output is subtracted from the interferogram, and the result is shown in Fig. 12(b). Ionospheric-induced errors in the ground motion estimation, of about 50 centimeters, have been thus removed. The size of the filtering window has been adapted to the mean coherence of each track to obtain an almost homogeneous accuracy of about 3 mm. It can be seen how the motion is now only localized around the fault and how phase jumps between different tracks are greatly reduced. Remaining discrepancies can be attributed to tropospheric delay and aftershock motion. The linear trend in the first track from the right could be caused by an orbit error.

2) Phase Unwrapping Errors Correction: Here, we show the effects of the unwrapping errors correction. In Fig. 13(a), the original interferogram used for this example is displayed. It is one frame of the first track from the left, just beneath the earthquake rupture. Fig. 13(d) and (e) shows the raw ionospheric phase estimates before and after the correction. Biases, which are due to differential phase unwrapping error, are present in the uncorrected estimates and are successfully eliminated in the corrected one. Fig. 13(f) and (g) shows the relative filtered phase screens, whereas Fig. 13(b) and (c) shows the ionosphere-compensated interferograms.

D. Asymmetric Split-Spectrum Mode

To validate the theoretical performance for $20 + 5$ MHz SAR acquisitions that was developed in Section III-F, here, we analyze two 85-MHz ALOS-2 acquisitions over Alaska. The ground coverage is displayed in Fig. 7; the size of the images is 57 km range and 69 km azimuth. This mode is intended to reduce the amount of data but still preserve the ionosphere estimation accuracy. Two subbands of 20 and 5 MHz are produced, at the two ends of the full available spectrum, with bandpass filtering.

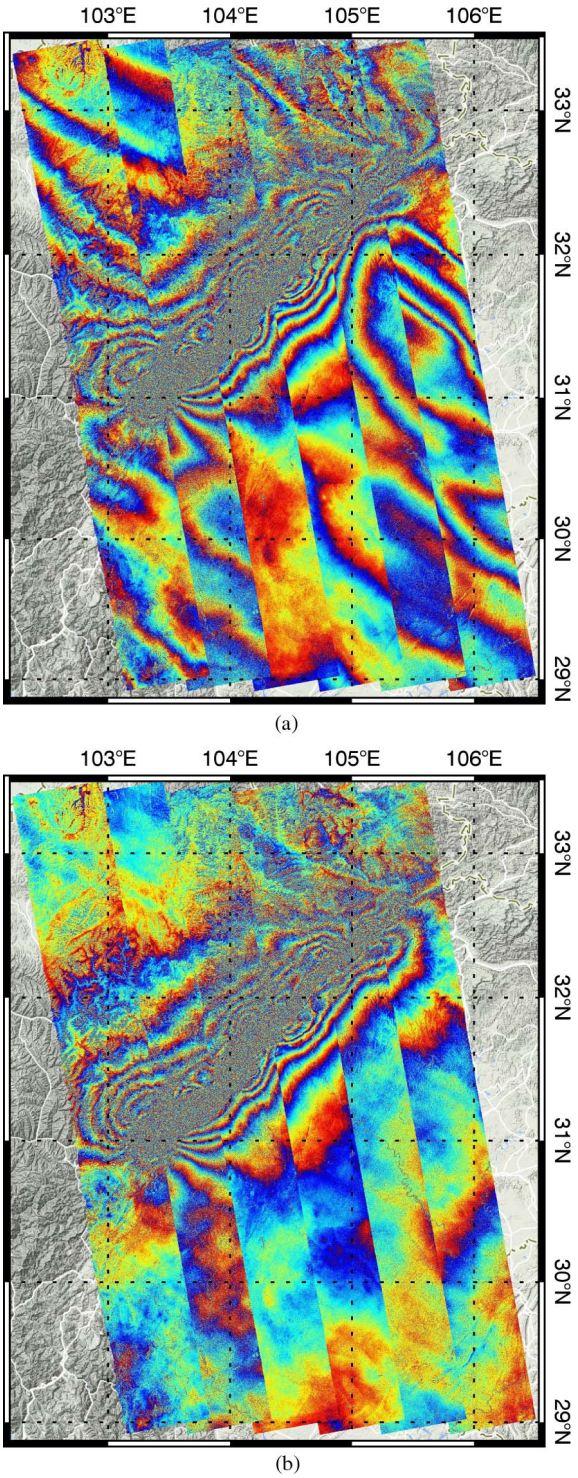

Fig. 12. (a) Original 2008 Wenchuan Earthquake interferogram. (b) After ionosphere compensation.

The split-spectrum method is then applied to the 85-MHz and $20 + 5$ MHz acquisitions. The theoretical and measured standard deviations of the raw ionospheric phase estimate for both implementations are reported in Fig. 14. The curves of the expected accuracy are calculated from (18) and (36), considering the multilooking factor 11×16. The ionosphere estimation accuracy obtained using asymmetrical subbands is close to that obtained with the complete bandwidth. The advantage of using

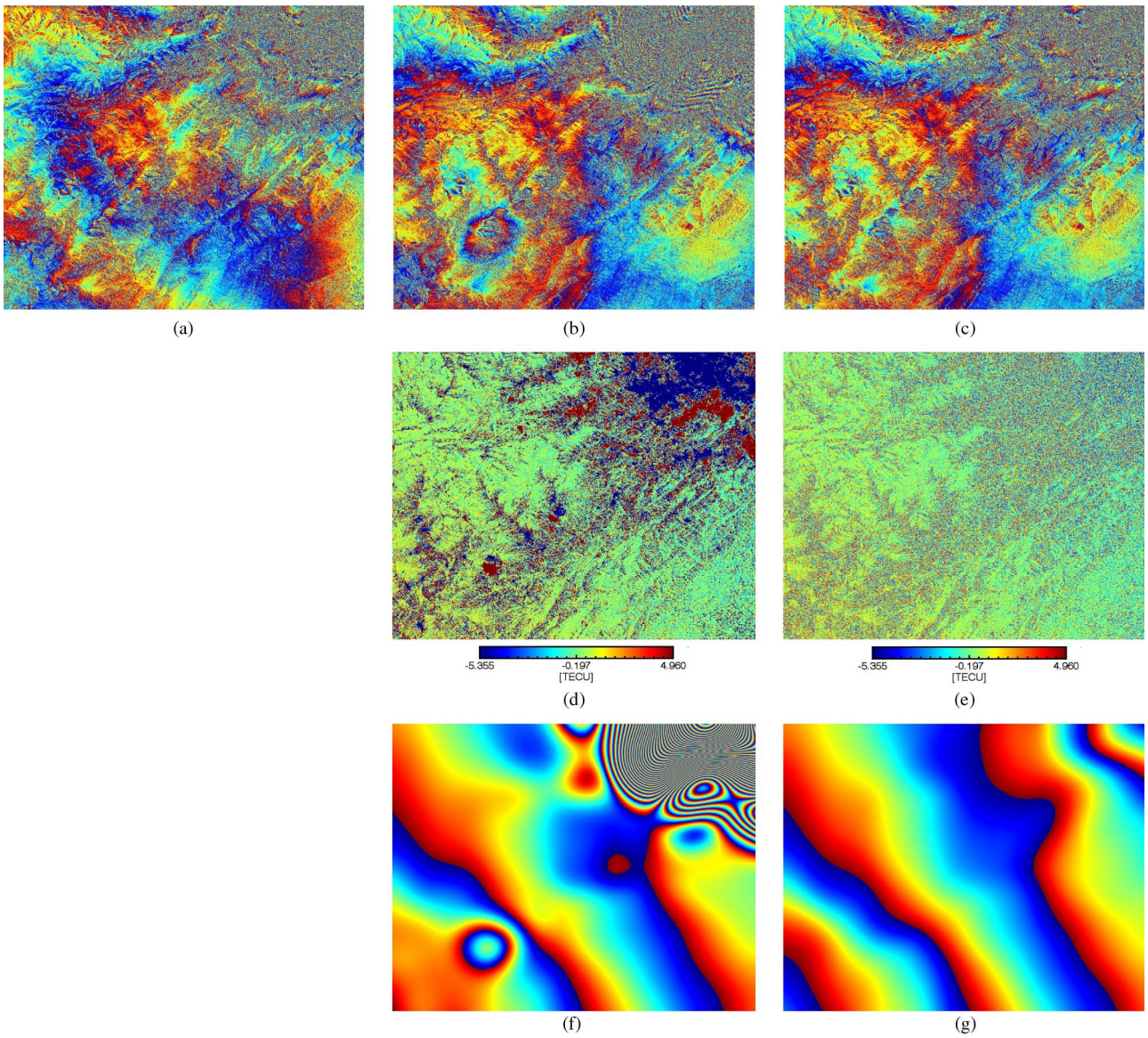

Fig. 13. Effect of the phase unwrapping errors correction. (a) Original interferogram. (b) and (c) Corrected interferograms without and with correction. (d) and (e) Raw ionosphere estimates without and with correction. (f) and (g) Respective filtered phase screens.

a small second subband at the other end of the available spectrum is demonstrated; it allows a reduction of the bandwidth to save downlink and memory capacity without sacrificing the compensation of ionospheric disturbances. The good agreement between expected and measured accuracies proves again the precision of the assumptions.

The full bandwidth interferogram and the compensated one are presented in Fig. 15.

V. Conclusion

The split-spectrum method is an important element toward the realization of an operational processor for compensation of ionospheric effects in SAR interferograms. In this paper, we presented and tested an implementation of the method, which estimates the ionospheric phase. The final estimation accuracy depends on the carrier frequency and bandwidth of the images, on the interferometric coherence, and on the correlation length of the differential ionosphere. For example, using typical L-band images with 28-MHz bandwidth and coherence 0.6, it is necessary to average over a ground area of about 1 km^2 to reach the accuracy of 1 cm. To increase the accuracy up to 1 mm, it is necessary to use a ground area of about 100 km^2.

We applied the method to four data sets of ALOS and ALOS-2 images, each with different characteristics. The Kyrgyzstan earthquake example (see Section IV-A) shows the correct separation between the ground movements and troposphere and the ionospheric phase. Despite the narrow 14-MHz bandwidth, it was possible to reach millimeter accuracy. The aurora borealis example (see Section IV-B), on the other hand, shows how small-scale ionospheric variations limit the amount of allowable filtering and, hence, the estimation and correction performance that can be achieved by the algorithm. The Wenchuan earthquake example (see Section IV-C) demonstrates the

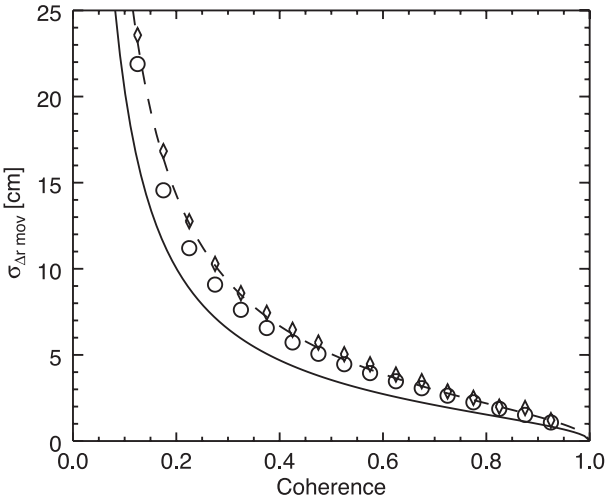

Fig. 14. Expected accuracy of the 85-MHz acquisition is represented by the black line, whereas the circles are the measured standard deviation. The dashed line is the expected accuracy for the 20+5 MHz acquisition; diamonds are the measured standard deviation.

robustness of the method, being applied to 72 interferograms with different characteristics. In these examples, an ionospheric error of almost 1 m has been reduced to millimeter or centimeter level. The asymmetric split-spectrum mode, tested using ALOS-2 images in Section IV-D, shows how it is possible to reduce the bandwidth and thus the data amount but still estimate the ionospheric phase with almost the same accuracy as when using full-band images.

It is conceivable to extend this work in various directions; possible future works are discussed in the following paragraphs. The combination of precise differential ionosphere variations, which are obtained from SAR images, and absolute measurements can lead to the development of an ionospheric mapping system with high spatial resolution and accuracy. Absolute TEC values can be obtained from GNSS measurements or from the SAR images, e.g., by exploiting the quadratic behavior of the ionospheric phase or the wavenumber shift effect reported in Section III-E. These methods have been already proposed, but they still have to be developed and demonstrated.

SAR systems working with different frequencies other than L-band can benefit from the split-spectrum correction method, too. Spatial phase undulations generated by ionospheric variations are often attributed to troposphere or orbit errors and removed with polynomial fitting of uncertain accuracy. The split-spectrum processing can be now used to precisely correct the ionospheric contribution. More testing is required to prove the importance of ionospheric effects in C-band or X-band images.

An extension of the split-spectrum method to point scatterers and stacks of images is a topic worthy of further investigations.

Regarding the improvement of the processor, we know that ionospheric variations with smaller spatial scales than the filtering window are not recovered and bias the result, lowering the accuracy of the final estimate. Adaptive filtering of the raw ionosphere estimate can improve the final phase screen. Alternatively, we propose to use the azimuth shifts, which are estimated by cross correlation or spectral diversity, to increase

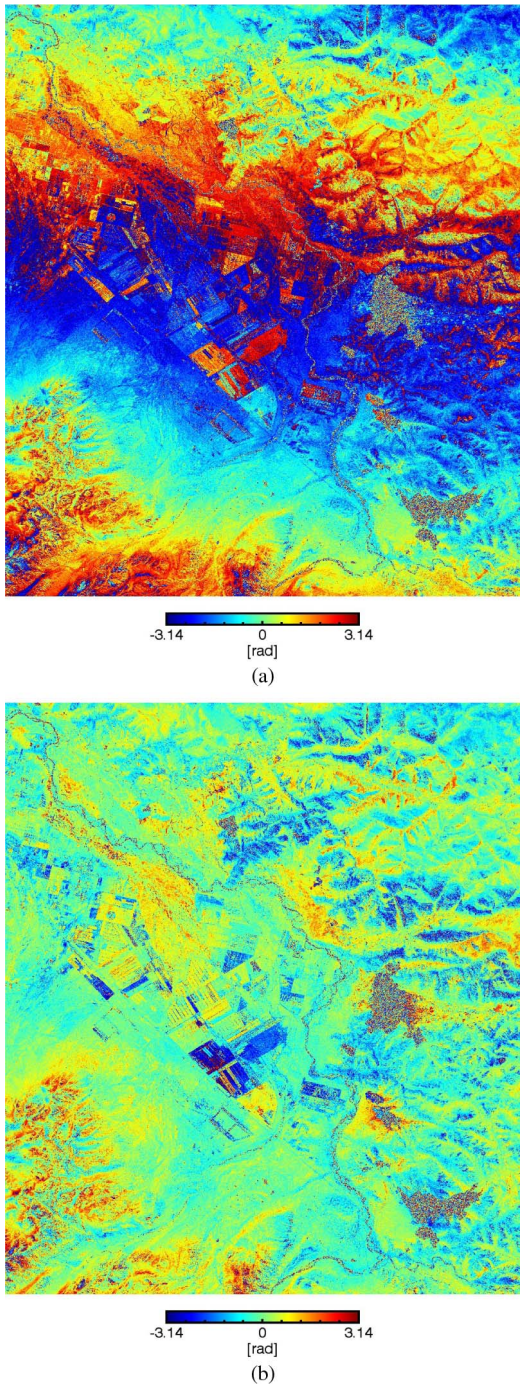

Fig. 15. ALOS-2 85-MHz interferogram over Alaska. (a) Original. (b) Ionosphere-compensated version. Azimuth length is 69 km; range length is 57 km.

the accuracy of the ionospheric phase estimate. Subapertures will be used to separate the ionosphere-induced azimuth shifts from the ground movements. Being sensitive to local azimuth variations of the ionosphere, the azimuth shifts can estimate the high-frequency components of the ionosphere spectrum but are prone to an increasing error in the long distance and are insensitive to range variations. The split-spectrum method ensures accurate estimation over long wavelengths and can recover range variations. The two techniques will therefore complement each other in the realization of an operational processor.

ACKNOWLEDGMENT

The authors would like to thank Dr. R. Brcic for his previous work on the split-spectrum method, the anonymous reviewers who helped to improve the quality of this paper, and the Japanese Aerospace Exploration Agency for providing the PALSAR data for this study (in part under the ALOS RA-4 proposal PI1118). The authors also acknowledge the support of the "Helmholtz Alliance *Remote Sensing and Earth System Dynamics*."

REFERENCES

[1] Z.-W. Xu, J. Wu, and Z.-S. Wu, "A survey of ionospheric effects on space-based radar," *Waves Random Media*, vol. 14, no. 2, pp. S189–S273, Apr. 2004.
[2] F. Meyer, "Performance requirements for ionospheric correction of low-frequency SAR data," *IEEE Trans. Geosci. Remote Sens.*, vol. 49, no. 10, pp. 3694–3702, Oct. 2011.
[3] N. Jakowski, C. Mayer, M. M. Hoque, and V. Wilken, "Total electron content models and their use in ionosphere monitoring," *Radio Sci.*, vol. 46, no. 6, 2011, Art ID. RS0D18.
[4] F. Meyer, "A review of ionospheric effects in low-frequency SAR—Signals, correction methods, and performance requirements," in *Proc. IEEE IGARSS*, Jul. 2010, pp. 29–32.
[5] R. Brcic, A. Parizzi, M. Eineder, R. Bamler, and F. Meyer, "Estimation and compensation of ionospheric delay for SAR interferometry," in *Proc. IEEE IGARSS*, 2010, pp. 2908–2911.
[6] P. Rosen, S. Hensley, and C. Chen, "Measurement and mitigation of the ionosphere in L-band interferometric SAR data," in *Proc. IEEE Radar Conf.*, May 2010, pp. 1459–1463.
[7] F. Meyer, R. Bamler, N. Jakowski, and T. Fritz, "The potential of low-frequency SAR systems for mapping ionospheric TEC distributions," *IEEE Geosci. Remote Sens. Lett.*, vol. 3, no. 4, pp. 560–564, Oct. 2006.
[8] D. Raucoules and M. de Michele, "Assessing ionospheric influence on L-band SAR data: Implications on coseismic displacement measurements of the 2008 Sichuan earthquake," *IEEE Geosci. Remote Sens. Lett.*, vol. 7, no. 2, pp. 286–290, Apr. 2010.
[9] J. S. Kim, A. Danklmayer, and K. Papathanassiou, "Correction of ionospheric distortions in low frequency interferometric SAR data," in *Proc. IEEE IGARSS*, Jul. 2011, pp. 1505–1508.
[10] H.-S. Jung, D.-T. Lee, Z. Lu, and J.-S. Won, "Ionospheric correction of SAR interferograms by multiple-aperture interferometry," *IEEE Trans. Geosci. Remote Sens.*, vol. 51, no. 5, pp. 3191–3199, May 2013.
[11] A. Freeman and S. Saatchi, "On the detection of Faraday rotation in linearly polarized L-band SAR backscatter signatures," *IEEE Trans. Geosci. Remote Sens.*, vol. 42, no. 8, pp. 1607–1616, Aug. 2004.
[12] A. Freeman, "Calibration of linearly polarized polarimetric SAR data subject to Faraday rotation," *IEEE Trans. Geosci. Remote Sens.*, vol. 42, no. 8, pp. 1617–1624, Aug. 2004.
[13] F. Meyer and J. Nicoll, "Prediction, detection, and correction of Faraday rotation in full-polarimetric L-band SAR data," *IEEE Trans. Geosci. Remote Sens.*, vol. 46, no. 10, pp. 3076–3086, Oct. 2008.
[14] D. Belcher, "Theoretical limits on SAR imposed by the ionosphere," *Radar, Sonar Navigat., IET*, vol. 2, no. 6, pp. 435–448, Dec. 2008.
[15] R. Hanssen, *Radar Interferometry: Data Interpretation and Error Analysis*. Boston, MA, USA: Kluwer, 2001.
[16] S. Tebaldini, A. M. Guarnieri, and F. Rocca, "Recovering time and space varying phase screens through SAR multi-squint differential interferometry," in *Proc. 9th EUSAR*, Apr. 2012, pp. 16–19.
[17] G. Gomba, M. Eineder, A. Parizzi, and R. Bamler, "High-resolution estimation of ionospheric phase screens through semi-focusing processing," in *Proc. IEEE IGARSS*, Jul. 2014, pp. 17–20.
[18] S. Kay, *Fundamentals of Statistical Signal Processing: Estimation Theory*, ser. Fundamentals of Statistical Signal Processing. Englewood Cliffs, NJ, USA: Prentice-Hall, 1993.
[19] F. De Zan, "Coherent shift estimation for stacks of SAR images," *IEEE Geosci. Remote Sens. Lett.*, vol. 8, no. 6, pp. 1095–1099, Nov. 2011.
[20] B. Friedlander, "On the Cramer–Rao bound for time delay and Doppler estimation," *IEEE Trans. Inf. Theory*, vol. IT-30, no. 3, pp. 575–580, May 1984.
[21] R. Bamler and M. Eineder, "Accuracy of differential shift estimation by correlation and split-bandwidth interferometry for wideband and delta-k SAR systems," *IEEE Geosci. Remote Sens. Lett.*, vol. 2, no. 2, pp. 151–155, Apr. 2005.
[22] M. Seymour and I. Cumming, "Maximum likelihood estimation for SAR interferometry," in *Proc. IGARSS, Surface and Atmospheric Remote Sensing: Technologies, Data Analysis and Interpretation*, 1994, vol. 4, pp. 2272–2275.
[23] F. Gatelli *et al.*, "The wavenumber shift in SAR interferometry," *IEEE Trans. Geosci. Remote Sens.*, vol. 32, no. 4, pp. 855–865, Jul. 1994.
[24] F. De Zan, P. Prats-Iraola, and M. Rodriguez-Cassola, "On the dependence of delta-k efficiency on multilooking," *IEEE Geosci. Remote Sens. Lett.*, vol. 12, no. 8, pp. 1745–1749, Aug. 2015.
[25] G. Krieger *et al.*, "Tropospheric and ionospheric effects in spaceborne single-pass SAR interferometry and radargrammetry," in *Proc. 10th EUSAR*, Jun. 2014, pp. 1–4.
[26] K. Davies, *Ionospheric Radio*. Stevenage, U.K.: IET, 1990, no. 31.
[27] R. Brcic, M. Eineder, and R. Bamler, "Interferometric absolute phase determination with TerraSAR-X wideband SAR data," in *Proc. IEEE Radar Conf.*, May 2009, pp. 1–6.
[28] K. Teshebaeva, H. Sudhaus, H. Echtler, B. Schurr, and S. Roessner, "Strain partitioning at the eastern Pamir-Alai revealed through SAR data analysis of the 2008 Nura earthquake," *Geophys. J. Int.*, vol. 198, no. 2, pp. 760–774, Jun. 2014.
[29] Z.-K. Shen *et al.*, "Slip maxima at fault junctions and rupturing of barriers during the 2008 Wenchuan earthquake," *Nature Geosci.*, vol. 2, no. 10, pp. 718–724, 2009.

Giorgio Gomba received the Bachelor's and Master's degrees in telecommunication engineering from Politecnico di Milano, Milano, Italy, in 2009 and 2011, respectively. He is currently working toward the Ph.D. degree at the Technical University of Munich (TUM), Munich, Germany.

Since 2012, he has been with the Remote Sensing Technology Institute, German Aerospace Center (DLR), Wessling, Germany. His current research interests are the estimation and compensation of ionospheric propagation delay in synthetic aperture radar signals.

Alessandro Parizzi received the Master's degree in telecommunications engineering from Politecnico di Milano, Milano, Italy, in 2004.

From 2004 to 2006, he was with the Department of Electronics, Politecnico di Milano, working in the field of SAR interferometry. Since 2006, he has been with the Remote Sensing Technology Institute, German Aerospace Center (DLR), Wessling, Germany, working on interferometric SAR processing. His main research interest is related to the study of atmospheric and decorrelation disturbances in differential SAR interferometry.

Francesco De Zan received the Master's degree in telecommunication engineering and the Ph.D. degree from Politecnico di Milano, Milano, Italy, in 2004 and 2008, respectively.

During his Ph.D. studies, he worked on extending permanent scatter interferometry to decorrelating targets and contributed to European Space Agency studies in preparation for Sentinel-1. Since 2008, he has been with the German Aerospace Center (DLR), Wessling, Germany, initially at the Microwaves and Radar Institute and then at the Remote Sensing Technology Institute. He has been involved in studies for numerous future interferometric SAR missions and in calibration activities of the TanDEM-X interferometer. His research interests include algorithms and theoretical bounds for shift estimation and SAR interferometry and interpretation of phase and coherence signatures.

Michael Eineder (SM'01) received the Diploma degree in electrical engineering from Technische Universität München (TUM), München, Germany, in 1990 and the Dr. rer. nat. degree from the University of Innsbruck, Innsbruck, Austria, in 2004.

Since 2013, he has been an honorary Professor with TUM, where he is also currently a part-time Lecturer of remote sensing. He is also currently the Head of the SAR signal processing department of the Remote Sensing Technology Institute, German Aerospace Center (DLR), Wessling, Germany. His responsibilities encompass the development of SAR and interferometric SAR processing systems for current and future radar missions. Since 1990, he has been with DLR, where he has worked on a variety of international missions, including SIR-C/X-SAR, SRTM/X-SAR in cooperation with the National Aeronautics and Space Administration, ERS-1 (European Space Agency), and TerraSAR-X and TanDEM-X (Germany). His current research interest is focused on future SAR missions and on imaging geodesy, an absolute positioning technique exploiting high-resolution SAR.

Richard Bamler (M'95–SM'00–F'05) received the Diploma degree in electrical engineering, the Doctorate degree in engineering, and the Habilitation degree in the field of signal and systems theory from Technische Universität München (TUM), München, Germany, in 1980, 1986, and 1988, respectively.

From 1981 to 1989, he worked on optical signal processing, holography, wave propagation, and tomography at the university. In 1989, he joined the German Aerospace Center (DLR), Wessling, Germany, where he is currently the Director of the Remote Sensing Technology Institute. In early 1994, he was a Visiting Scientist with the Jet Propulsion Laboratory in preparation of the SIC-C/X-SAR missions. In 1996, he was a Guest Professor with the University of Innsbruck, Innsbruck, Austria. Since 2003, he has also held a full professorship in remote sensing technology at TUM as a double appointment with his DLR position. His teaching activities include university lectures and courses on signal processing, estimation theory, and SAR. He, his team, and his institute have been working on SAR and optical remote sensing, image analysis and understanding, stereo reconstruction, computer vision, ocean color, passive and active atmospheric sounding, and laboratory spectrometry. They were and are responsible for the development of the operational processors for SIR-C/X-SAR, SRTM, TerraSAR-X, TanDEM-X, Tandem-L, ERS-2/GOME, ENVISAT/SCIAMACHY, MetOp/GOME-2, Sentinel 5p, EnMAP, etc. His research interests are in algorithms for optimum information extraction from remote sensing data with emphasis on SAR. This involves new estimation algorithms, such as sparse reconstruction and compressive sensing. He has devised several high-precision algorithms for monostatic and bistatic SAR processing, SAR calibration and product validation, Ground Moving Target Indicator (GMTI) for traffic monitoring, SAR interferometry, phase unwrapping, persistent scatterer interferometry, and differential SAR tomography and data fusion.

B

Gomba, G., Rodriguez Gonzalez, F., and De Zan, F. (2017). Ionospheric Phase Screen Compensation for the Sentinel-1 TOPS and ALOS-2 ScanSAR modes. IEEE Transactions on Geoscience and Remote Sensing

Ionospheric Phase Screen Compensation for the Sentinel-1 TOPS and ALOS-2 ScanSAR Modes

Giorgio Gomba, Fernando Rodríguez González, and Francesco De Zan

***Abstract*—Variations of the ionosphere can significantly disrupt synthetic aperture radar (SAR) acquisitions and interferometric measurements of ground deformation. In this paper, we show how the ionosphere can also strongly modify C-band interferograms despite its smaller influence at higher frequencies. Thus, ionospheric phase screens should not be neglected: their compensation improves the estimation of ground deformation maps. The split-spectrum method is able to estimate the dispersive ionospheric component of the interferometric phase; we describe the implementation of this method for the burst modes TOPS and ScanSAR to estimate and remove ionospheric phase screens. We present Sentinel-1 interferograms of the 2016 Taiwan earthquake and ALOS-2 interferograms of the 2015 Nepal earthquake, which show strong ionospheric phase gradients, and their corrected versions. Finally, to validate the results and better understand the origin of these ionospheric variations, we compare the estimated differential ionosphere with global Total Electron Content maps and local Global Positioning System measurements.**

***Index Terms*—InSAR, ionosphere estimation, SAR ionospheric effects, split-spectrum.**

I. Introduction

WIDE-swath imaging modes extend the ground range coverage, with respect to a Stripmap acquisition, to reduce the revisit time and improve the study of large-scale geophysical phenomena. Terrain observation by progressive scans (TOPS) is the standard operation mode of the Sentinel-1 C-band SAR, and scanning synthetic aperture radar (ScanSAR) is operated by the L-band ALOS-2 satellite. Both modes do not image each subswath continuously, but operate in bursts, and use the time gap between bursts to extend the total imaged swath. As a result, some portions of the image are acquired in a squinted geometry.

The ionosphere is the ionized portion of the atmosphere that affects the transmission of microwaves. Because of the ionospheric dispersive propagation, the radio signal is subject to a phase advance, rather than to a delay [1], which modifies synthetic aperture radar (SAR) interferograms, disrupting ground motion measurements.

The influence of the ionosphere on radio wave propagation is larger on L-band systems than that on C-band systems, because the phase advance grows with the inverse of the carrier frequency. However, ionospheric effects on the C-band systems have been also reported. In particular, ionospheric strikes can be seen in azimuth displacement maps generated with Sentinel-1 and Radarsat images [2]. We will show that the ionospheric phase component can also be extremely relevant in C-band interferograms and, thus, should not be neglected. The estimation and removal of ionospheric effects from C- and L-band SAR interferograms is therefore necessary to measure ground deformation over wide swaths.

The range split-spectrum method, which was extensively presented in [3]–[5], is able to compensate the ionospheric phase screen in SAR interferograms. In this paper, we describe the implementation of the split-spectrum method for the burst modes TOPS and ScanSAR.

In Sections II and III, we describe the effects of the ionosphere on squinted image acquisition and on their processing, respectively. In Section IV, we propose a modified implementation of the split-spectrum method for burst-mode images and apply it to a Sentinel-1 interferogram of the February 6, 2016 Taiwan earthquake. The interferogram presents a strong phase gradient in the along-track direction, which is too strong to be interpreted as a tropospheric contribution or an orbit error. We show that it is, in fact, caused by a differential ionospheric phase variation and, using the split-spectrum method, compensate for it.

In Section V, we apply the split-spectrum method to ALOS-2 ScanSAR interferograms of the 2015 Nepal earthquake, which also show unexpected strong azimuth phase gradients. We present the compensated interferograms of the earthquake and demonstrate how a proper correction of the ionospheric phase can improve the ground deformation measurement with respect to the more common practice of removing linear or quadratic trends.

In Section VI, we use global Total Electron Content (TEC) maps and local Global Positioning System (GPS) measurements to validate our results with independent measurements and to understand the origin of such strong phase gradients.

II. Ionospheric Effects on Squinted Acquisition Imaging

The ionospheric path delay, experienced by a traveling microwave, increments the group delay of the wave packet. On the other hand, due to dispersive ionospheric propagation, the wave phase is advanced rather than delayed. The phase advance has the same magnitude as the group delay, that is [1]

$$\phi_{\text{iono}} = \frac{4\pi K}{c f_0}\text{TEC} \tag{1}$$

Manuscript received June 17, 2016; revised August 18, 2016; accepted August 24, 2016. This work was supported by "Helmholtz Alliance *Remote Sensing and Earth System Dynamics*."

The authors are with the Remote Sensing Technology Institute, German Aerospace Center (DLR), 82234 Wessling, Germany (e-mail: giorgio.gomba@dlr.de).

Color versions of one or more of the figures in this paper are available online at http://ieeexplore.ieee.org.

Digital Object Identifier 10.1109/TGRS.2016.2604461

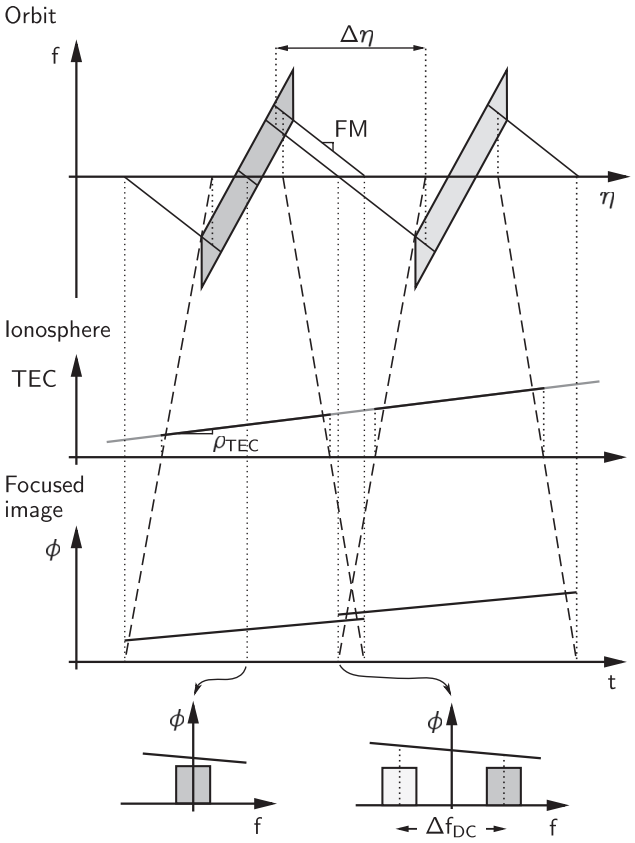

Fig. 1. Geometry of the TOPS acquisition. (Top) Raw data time–Doppler graph of two bursts plotted at the orbit height. (Middle) TEC level at the ionospheric single layer height. (Bottom) Focused image phase with the ionosphere contribution and the phase spectrum of two targets.

with f_0 being the carrier frequency, c being the speed of light in vacuum, and $K = 40.28\ \mathrm{m}^3/\mathrm{s}^2$. The term "TEC" in (1) is the slant TEC that is experienced by the radio wave while traveling through the ionosphere.

The interferometric processing of burst-mode acquisitions is different with respect to the processing of stripmap images due to the presence of the squint. Consequently, the correction of ionospheric effects needs to be adapted. Below, we analyze the effects of the ionosphere on the imaging of squinted acquisitions.

In [6], it was shown that the tropospheric path delay can lower the focusing quality by introducing azimuth defocusing. In the Appendix, we demonstrate that on the contrary, a constant ionosphere does not defocus the system impulse response due to the particular opposition of the phase and group delay signs.

On the other hand, if the TEC level changes along the azimuth, this does produce effects during the focusing process. In the following, the simple linear orbit approximation is used. Under the assumption of a single-layer model, by using the information on the line of sight (LOS) and the height of the ionospheric layer, it is possible to geometrically determine the ionospheric piercing-point position of each target echo. The illustration in Fig. 1 helps in understanding the acquisition geometry and the ionosphere influence on the image formation; it reports the slow time–Doppler spectrum graph for two bursts, the ionospheric TEC level, the ionospheric phase (advance) in the focused image, and the phase spectrum of two targets.

In a TOPS image, the ionosphere is not continuously scanned as in a stripmap image. This happens because the squint angle rotates while the satellite is advancing. These two actions change the ionospheric piercing-point position. The final effect is that some portions of the ionosphere are measured while other portions are not (see Fig. 1). Moreover, at the conjunction between two bursts, the ionospheric piercing point suddenly changes, due to the sudden change in LOS. This means that, for a nonconstant ionosphere, a phase jump is present between bursts.

A target's ionospheric phase depends on the average ionospheric TEC level present within the aperture that was used to imagine that target. The ionosphere, which is measured by the interferogram, is then a low-pass version of the real differential ionosphere [7].

A. Azimuth Shifts

Azimuth shifts that are due to a SAR system timing error, an orbit error, or a ground movement generate different effects with respect to azimuth shifts caused by ionospheric variations. We analyze the difference in the following.

1) Physical Shift: A physical shift originates from a timing error or ground motion, thus from an actual raw data time shift. A physical shift does not change during the focusing process.

A consequence of a physical shift is, after focusing, a phase ramp over the burst. The phase slope is proportional to the shift Δt and to the Doppler centroid frequency f_{DC}. A phase difference arises at the interface between two bursts, that is

$$\Delta\phi_{\mathrm{az}} = 2\pi\Delta f_{\mathrm{DC}}\Delta t \tag{2}$$

where Δf_{DC} is the Doppler centroid difference for the same ground point observed by the two bursts [8].

2) Ionospheric Shift: An ionospheric shift, on the other hand, is caused by a phase change introduced by a nonconstant ionosphere. Variations of the ionospheric phase within the synthetic aperture produce azimuth shifts and defocusing effects in SAR images. In general, linear phase trends result in shifts, and curvatures or higher-order terms result in defocusing. The shift produced by a nonconstant ionosphere changes during focusing.

Let us assume a static ionosphere during the acquisition and a linear TEC level trend along azimuth, as illustrated in Fig. 1. The physical ionospheric slope is indicated by ρ_{TEC} in slant TEC per meter. For a target in $t = 0$, the TEC variation observed from the satellite in η is

$$\mathrm{TEC}(\eta) = \rho_{\mathrm{TEC}} \cdot \eta \frac{H_i}{H} v \tag{3}$$

where H_i is the height of the ionospheric single layer, H is the satellite orbit height, and v is the satellite speed. The target extra phase linearly varies within the synthetic aperture, i.e.,

$$\varphi(\eta) = -\frac{4\pi K}{cf_0}\mathrm{TEC}(\eta) = -\frac{4\pi K}{cf_0}\rho_{\mathrm{TEC}}\eta\frac{H_i}{H}v. \tag{4}$$

The Doppler frequency increase is proportional to the change rate of the target extra phase, i.e.,

$$\Delta f_D = -\frac{1}{2\pi}\frac{d\varphi(\eta)}{d\eta} = \frac{2KH_i v}{cf_0 H}\rho_{\mathrm{TEC}}. \tag{5}$$

The frequency modulation (FM) rate, which is due to the relative satellite motion to the target, is

$$\mathrm{FM} = -\frac{2v^2}{\lambda R}. \tag{6}$$

The target is focused in the zero Doppler position. The latter has a shift of

$$\Delta t_i = \frac{\Delta f_D}{\mathrm{FM}} = -\frac{KH_i R}{f_0^2 H v}\rho_{\mathrm{TEC}} \tag{7}$$

by the ionospheric phase ramp.

It is important to note that an ionospheric shift does not generate an additional phase ramp over the burst and to the target spectrum (similar to what a physical shift does); it is the ionospheric phase ramp in the target spectrum that generates the ionospheric shift.

III. Ionospheric Effects on Squinted Acquisition Processing

In this section, we analyze the effects of the ionosphere on the interferometric processing of burst-mode images, which is realized with a standard processor, as, for example, in [8].

A. Azimuth Shift Estimation

Shift estimation of images with squinted geometry is a delicate step during interferometric processing. A phase error, proportional to the Doppler centroid frequency, is present in the interferogram if the shift estimation is not accurate. Only a scene offset is measured and corrected to account for timing error. Correction of local shifts due to ground motion can be avoided if the coherence is not considerably reduced by the shift. The actual LOS should then be considered when interpreting the InSAR phase [9].

In the event that a linear azimuth ionospheric variation is present, it causes an additional shift. The total misregistration measure is then the sum of the timing error and the ionospheric shift. Similarly to local ground shifts, the correction of local ionospheric shifts can also be avoided if the coherence is not reduced.

Measurement of the azimuth offset can be realized with different techniques [8].

1) Cross-Correlation: Coherent (CCC) or incoherent (ICC) patch-based cross correlation [10] measures the mutual shift between two images in the time domain. Averaging all results over the scene, one obtains the timing offset summed up to the mean ionospheric shift. The ionospheric shift, which is measured by cross correlation, is the actual time shift induced by an ionospheric slope described in (7).

2) Enhanced Spectral Diversity: Another possible technique is the enhanced spectral diversity (ESD) [11]. ESD exploits the Doppler centroid separation in the burst overlap areas to estimate the shift by using the spectral diversity method. Inverting (2), we obtain the shift estimator as

$$\Delta\hat{t} = \frac{\Delta\phi_{\mathrm{az}}}{2\pi\Delta f_{\mathrm{DC}}}. \tag{8}$$

The advantage of ESD over cross correlation is the higher precision due to the large spectral separation of the bursts in the overlap region. Conversely, cross correlation provides unambiguous measurements, whereas ESD cannot retrieve the ambiguity band.

The ionospheric shift, which is measured by ESD, depends on the ionospheric phase jump at the burst overlap. Let the slow-time separation between bursts be

$$\Delta\eta = \frac{\Delta f_{\mathrm{DC}}}{\mathrm{FM}}. \tag{9}$$

From (4), considering a linear ionosphere, the phase jump for a target in the burst overlap is

$$\Delta\phi_{\mathrm{az}} = \frac{4\pi K}{cf_0}\rho_{\mathrm{TEC}}\Delta\eta\frac{H_i}{H}v. \tag{10}$$

Combining (8) and (10), the estimated azimuth shift is then

$$\Delta\hat{t} = -\frac{KH_i R}{f_0^2 H v}\rho_{\mathrm{TEC}} \tag{11}$$

which is equal to (7). For a linear ionosphere then, the ionospheric shift estimated either by cross correlation or ESD is the same. In case of a nonlinear ionosphere, the two techniques could yield slightly different results.

B. Azimuth Shift Resampling

The sum of the timing error offset and the global ionospheric shift is estimated (either with cross correlation or with ESD) and then corrected by resampling the slave bursts. The correction of the timing error offset removes the Doppler-dependent phase ramp term of (2). On the other hand, the correction of the ionospheric shift introduces an additional phase term to the bursts and, consequently, to the interferogram. To understand why, we recall the shift correction mechanisms in the Fourier domain.

1) Physical Shift: Consider the spectrum of an interferogram as illustrated in Fig. 2(a). The interferogram is produced with a squinted acquisition that presents an azimuth differential displacement caused by ground motion or timing error. The phase of the azimuth spectrum is composed of an offset, due to range motion, and a slope, due to the azimuth shift. The interferometric phase is the sum of the across-track motion phase, i.e., $\Delta\phi_{\mathrm{rg}}$, and the along-track motion phase, i.e., $\Delta\phi_{\mathrm{az}}$, of (2). That is

$$\Delta\phi = \Delta\phi_{\mathrm{rg}} + \Delta\phi_{\mathrm{az}} = 4\pi f_c\frac{\Delta r}{c} + 2\pi f_{\mathrm{DC}}\Delta t \tag{12}$$

where f_c is the carrier frequency, and Δr is the cross-track range displacement. Coregistration, both cross correlation or ESD, measures the phase slope (a shift in the time domain), and resampling applies an inverse slope to shift the data. After resampling, the phase spectrum is constant, as shown in Fig. 2(b). The interferometric phase is now just the range phase

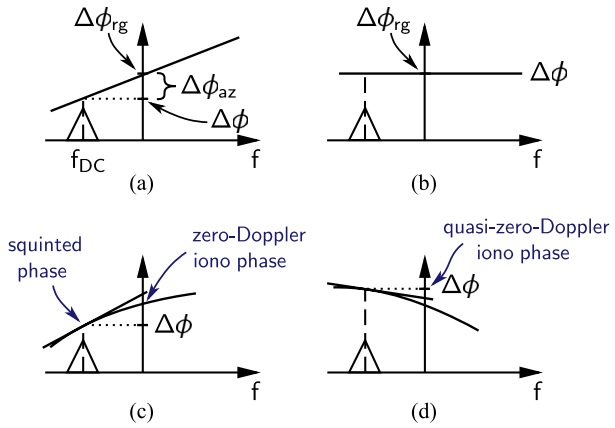

Fig. 2. (a) Phase spectrum of an interferogram in the presence of an azimuth shift. (b) After resampling, the azimuth phase is canceled. (c) Phase spectrum of an interferogram in the presence of a varying ionosphere. (d) After resampling, a phase bias that is proportional to the linear component of the ionosphere and to the Doppler centroid has been added. The interferometric phase is similar to what a zero-Doppler acquisition would have measured.

plus a possible coregistration error multiplied by the Doppler centroid (not represented here).

2) Ionospheric Shift: Let us consider a quadratic ionospheric trend along the azimuth direction, similar to that represented in Fig. 2(c). The interferometric phase is the across-track motion phase $\Delta\phi_{\rm rg}$ plus the measure of the average ionospheric phase in the target spectrum, i.e.,

$$\Delta\phi = \Delta\phi_{\rm rg} + \Delta\phi_{\rm iono}. \tag{13}$$

The azimuth shift depends on the local ionospheric slope. Cross correlation or ESD retrieves the shift caused by the global linear trend of the ionosphere. The resampling step applies an inverse slope to shift the data. In Fig. 2(d), the phase slope is not completely compensated because, here, the local shift is different from the global shift.

In the physical-shift case, the inverse phase slope cancels the phase that was introduced by the shift. This leaves, in the interferogram, only the phase related to the across-track motion. On the contrary, in the ionospheric-shift case, the inverse phase slope introduced by the resampling is a bias. The interferometric phase, in fact, is no longer a measure of the ionosphere at the squinted location, but it is approximately the phase that a zero-Doppler acquisition would have measured [see Fig. 2(d)]. That is

$$\Delta\phi = \Delta\phi_{\rm rg} + \Delta\phi_{\rm iono} - 2\pi f_{\rm DC}\Delta\hat{t} \tag{14}$$

where $\Delta\hat{t}$ is the applied resampling shift, the estimated global offset.

C. Interferogram

As a consequence of the changing LOS, not all parts of the ionosphere are measured by the interferogram, and phase jumps can be present between bursts. The interferogram that is produced with uncorrected slave bursts presents phase jumps that are due to the abrupt LOS changes in the ionosphere. The effect of the phase bias introduced by the resampling, which converts the ionospheric phase to a quasi-zero-Doppler ionospheric phase, is to greatly reduce these phase jumps or even eliminate them if the ionosphere is a linear slope. The eventual residual jumps in the resampled data interferogram are due to the linear approximation of the azimuth ionospheric phase and to the differences between local and global shifts.

Finally, it has to be noted that the ionospheric phase component of the interferogram is dispersive, whereas the phase bias introduced by the resampling is nondispersive. Both these terms have to be estimated and removed by the ionosphere compensation method.

TABLE I
SCENE ACQUISITION INFORMATION

Satellite		Master	Slave	Path	Frame
Sentinel-1		02/02/16	14/02/16		
ALOS-2	(a)	22/02/15	03/05/15	48	3050
	(b)	03/05/15	17/05/15	48	3050
	(c)	05/04/15	03/05/15	48	3050

IV. IONOSPHERIC PHASE SCREEN COMPENSATION

In the following, we propose a modified split-spectrum method to estimate and compensate the ionospheric phase screen in Sentinel-1 TOPS images. The ionosphere compensation for burst-mode images requires additional processing steps with respect to the compensation of stripmap images described in [3]. A coseismic interferogram of the 2016 Taiwan earthquake is used in the following as a processing example. Acquisition parameters are reported in Table I.

The interferometric processing of TOPS mode images is realized as described in [8]. The azimuth offset estimation is performed using the ESD method. As can be seen from the resulting interferogram in Fig. 5(a), there is a high number of fringes in the azimuth direction, which would indicate a differential LOS displacement of about 50 cm along the Taiwan island. This large motion cannot be realistically attributed to a real displacement or to a tropospheric effect; it must therefore be due to an orbit error or an ionospheric effect.

Assuming that all fringes are related to an ionospheric gradient, it is possible to calculate the azimuth shift that such a gradient would cause by applying (7). The result is about 60 cm, which correspond to the global shift measured by ESD. This therefore confirms the presence of a strong ionospheric azimuth variation.

Furthermore, azimuth shifts measured at each burst overlap present variations of several centimeters, much higher than the ESD estimation accuracy. This effect can be explained by a nonlinear ionospheric gradient along the azimuth. Fig. 6 reports the residual measured shift for each burst overlap of the first two beams (blue squares); the last beam is mostly incoherent. These residuals are due to the combined effect of a nonlinear ionospheric azimuth profile, and the phase bias introduced by the resampling of the ionospheric shift.

Broadly speaking, two correction approaches are possible. The most straightforward uses the split-spectrum method already during coregistration. The steps are the following: resample the bursts and remove the phase that is added by resampling, apply the split-spectrum to the resampled bursts,

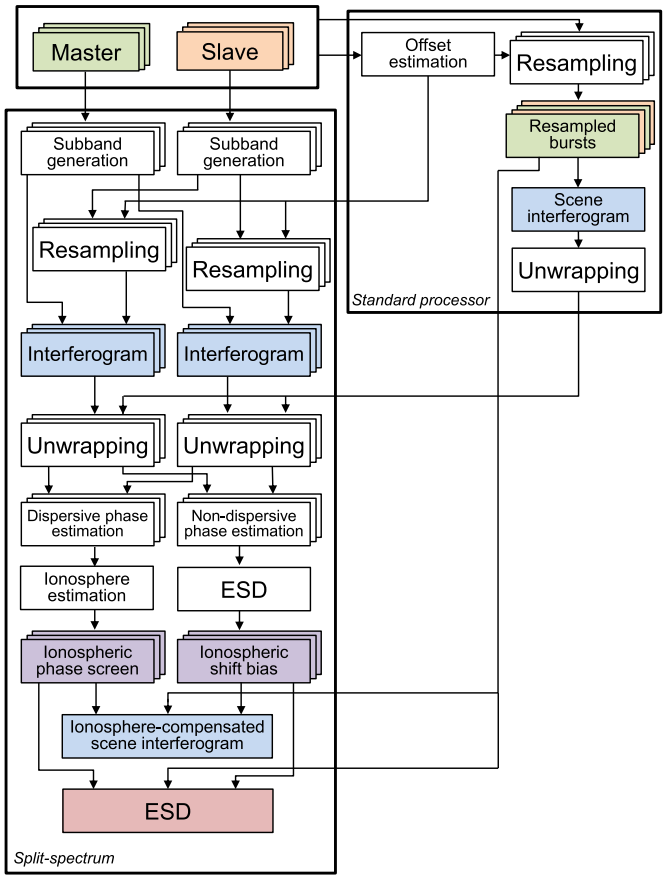

Fig. 3. Implementation of the split-spectrum method for TOPS mode.

apply ESD to the nondispersive phase to estimate the physical shift, remove the Doppler-dependent phase relative to the physical shift, use the dispersive phase to estimate the ionospheric phase screen and remove it from the bursts, and finally, compute the scene ionosphere-free interferogram.

This approach, however, would require modifying the existing processor. To simplify the adaptations, we propose using a standard TOPS interferometric processor and adding an ionosphere correction module. We suggest removing the phase bias, which is introduced by the ionospheric shift resampling, by applying ESD to the raw nondispersive phase, estimating the ionospheric shift from the phase bias itself. Thereafter, the processing continues with the ionospheric phase screen compensation as in the previous approach.

A. Split-Spectrum Raw Estimate

Here follows a description of the proposed modified split-spectrum method. In Fig. 3, a schematic representation is reported. The proposed method can be implemented as an extension of a standard TOPS interferometric processor.

First, two range subbands for each burst are generated by bandpass filtering. The subbands are demodulated for their carrier frequency, with respect to the fullband carrier frequency, to obtain a symmetric spectrum. Eventual spectral weighting is also eliminated. The slave subbands are then resampled. This ensures that no phase bias is added to the interferograms by the resampling in the range direction. Resampling is performed to maximize the coherence by using the coregistration offset, which was estimated during the standard TOPS processing either with ICC or with ESD.

To obtain a first approximate estimation of the ionospheric phase screen, it is possible to apply the split-spectrum method on the mosaicked scene-level interferograms. After unwrapping both subband interferograms, the scene-level nondispersive and dispersive phases can be obtained [3]. The dispersive phase can be smoothed, and the result subtracted from the original interferogram, producing an approximate ionosphere-compensated interferogram. Nevertheless, precise processing should consider the voids in the ionosphere measurements, described in Section III-C, and the phase bias, which is due to the azimuth resampling, described in Section III-B.

To accurately estimate the ionospheric phase screen, the split-spectrum has to be applied at the burst level rather than just at the scene level; an interferogram is therefore calculated for each burst. To exploit the maximum coherence, the resampled bursts are used. Since the unwrapping of a single burst interferogram can be difficult, the unwrapped scene interferogram is used to unwrap the bursts. The correspondent part of the scene interferogram is compared with the burst interferogram, and the difference is added to the burst interferogram. The unwrapped burst interferograms are then used to estimate the nondispersive and dispersive components of the phase. The phase unwrapping error correction module of the split-spectrum method requires a smooth estimate of the dispersive and nondispersive phases. With stripmap images, this is usually realized by iterating the smoothing of the raw estimate with the unwrapping error correction. However, due to the small size of the burst, the smoothing can now be problematic. Hence, the scene-level smooth estimates are used instead.

Finally, the raw estimates of the nondispersive and dispersive phases are, respectively, used to estimate the ionospheric azimuth shift and the ionospheric phase screen, as described in the following sections.

B. Ionospheric Shift Phase Bias Compensation

The coregistration and resampling steps measure and compensate an azimuth global offset, which is composed of a physical shift and an ionospheric shift. The linear component of the ionospheric azimuth variation in the scene produces the ionospheric shift. As introduced in Section III-B, the resampling of the physical shift compensates its Doppler-related phase, whereas the resampling of the ionospheric shifts adds a phase bias. This should be removed to obtain the real ionosphere seen in the LOS direction. It is then necessary to estimate and separate the physical shift from the ionospheric shift.

The nondispersive phase is composed of the topography, the ground motion, the troposphere, and the phase bias. For an azimuth position t in a burst overlap area, we write the nondispersive phase of one burst and its adjacent one as $\Delta\phi^0_{\mathrm{nondisp}}(t)$ and $\Delta\phi^1_{\mathrm{nondisp}}(t)$, i.e.,

$$\begin{aligned}\Delta\phi^0_{\mathrm{nondisp}}(t) &= \Delta\phi_{\mathrm{ground}}(t) + 2\pi f^0_{\mathrm{DC}}(t)\Delta t_i + n^0(t)\\ \Delta\phi^1_{\mathrm{nondisp}}(t) &= \Delta\phi_{\mathrm{ground}}(t) + 2\pi f^1_{\mathrm{DC}}(t)\Delta t_i + n^1(t)\end{aligned} \quad (15)$$

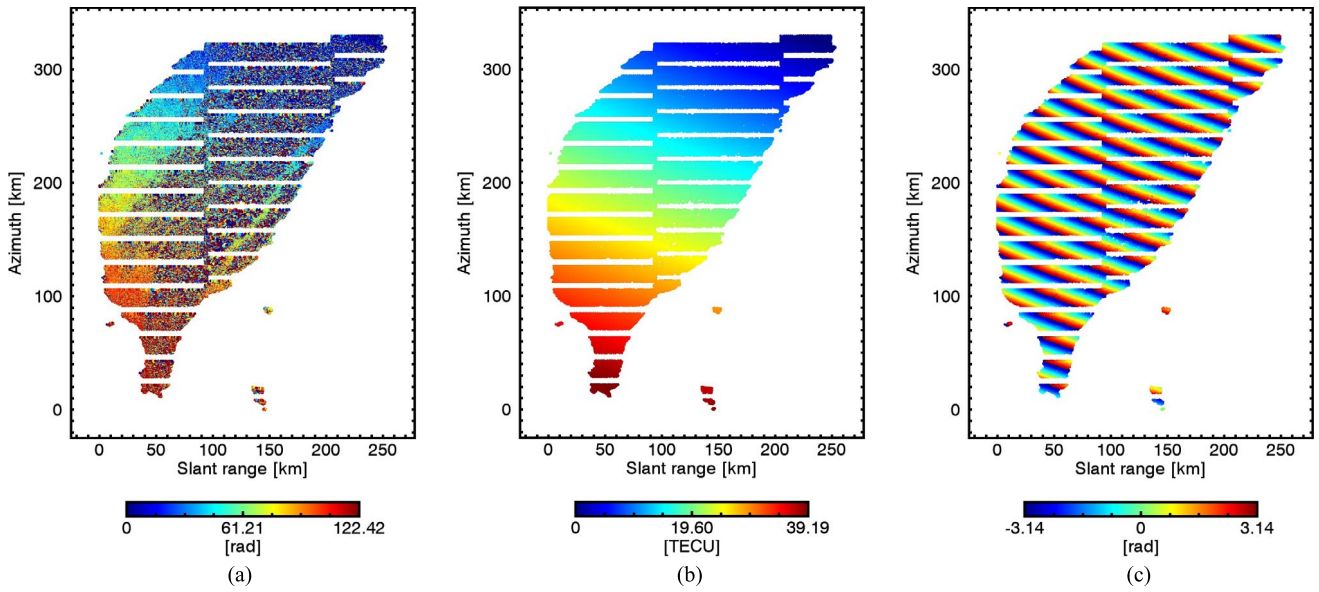

Fig. 4. (a) Raw, (b) filtered, and (c) wrapped dispersive phase components of the Taiwan example interferometric phase, plotted at the ionospheric single-layer height. The measurements gaps can be noted.

where $\Delta\phi_{\text{ground}}$ is the topographic, motion, and tropospheric phase, f_{DC} is the Doppler centroid frequency, and n is the split-spectrum estimation noise. The term Δt_i is the global ionospheric shift that has to be estimated. The difference of the phases in (15) is the ESD phase, i.e.,

$$\Delta\phi^0_{\text{nondisp}}(t) - \Delta\phi^1_{\text{nondisp}}(t) = 2\pi\left(f^0_{\text{DC}}(t) - f^1_{\text{DC}}(t)\right)\Delta t_i + n^0(t) - n^1(t). \quad (16)$$

The ionospheric shift can be estimated by rewriting the latter equation as

$$\Delta\hat{t}_i(t) = \frac{\Delta\phi^0_{\text{nondisp}}(t) - \Delta\phi^1_{\text{nondisp}}(t)}{2\pi\left(f^0_{\text{DC}}(t) - f^1_{\text{DC}}(t)\right)}. \quad (17)$$

A weighted mean, based on the accuracy of the split-spectrum, can be used to average the ESD phase and obtain a global estimate for the image. Since the estimated nondispersive phase derives from unwrapped interferograms, no cyclicity problems arise.

The accuracy of this estimate depends on the precision of the split-spectrum, which is [3]

$$\sigma_{\Delta\phi_{\text{nondisp}}} = \frac{3f_0}{4B}\sqrt{\frac{3}{2N}}\frac{\sqrt{1-\gamma^2}}{\gamma} \quad (18)$$

where f_0 is the carrier frequency, B is the full bandwidth, N is the number of independent samples, and γ is the interferometric coherence. For a Sentinel-1 acquisition with coherence of 0.5, the estimation accuracy of the ionospheric shift is about 1.5 cm (9 cm), if all burst overlaps (or only one burst overlap) are (is) used, and the phase bias correction accuracy is 3° (16°).

The phase correction, i.e.,

$$\Delta\phi_{\text{az-iono}} = 2\pi f_{\text{DC}}\Delta\hat{t}_i \quad (19)$$

is then applied to the slave bursts. The ionospheric phase in the scene interferogram is now just a projection of the ionosphere according to the squinted LOS, and, as expected at this stage, strong phase jumps might appear.

C. Ionospheric Phase Screen Compensation

The dispersive phase component is used to estimate the ionospheric phase screen. First, the ionospheric piercing-point position for each interferogram pixel is calculated using the timing information and the ionospheric single-layer model. In Fig. 4(a), the raw dispersive phase estimates are plotted at their piercing-point position for a supposed ionospheric height of 350 km. The gaps in the ionosphere measurement can be clearly seen. Second, the raw phase is smoothed by Kriging interpolation or by fitting the raw estimates with a model. The resulting ionosphere can be seen in Fig. 4(b) and, wrapped, in Fig. 4(c). The differential ionospheric along-track variation is remarkably large, i.e., about 25 TECU in 300 km. Finally, the smoothed ionospheric phase is reprojected to the burst geometry and subtracted from the burst interferograms. The mosaicked compensated interferogram can be seen in Fig. 5(b). A LOS motion error of about 50 cm along the Taiwan island has been removed. Remaining tropospheric path delay could be mitigated by using numerical weather prediction data and a digital elevation model [12].

It is now also possible to compare the linear component of the smoothed ionosphere with the ionospheric shift, which has been estimated in the previous step.

D. Burst Overlap Phase Check

Finally, ESD can be applied to check whether the ionospheric correction is also able to reduce the residual local shifts and the burst overlap phase differences.

First, we summarize the implemented processing steps; the master and slave bursts present a mean differential shift of 60 cm due to a strong azimuth ionospheric gradient. The slave

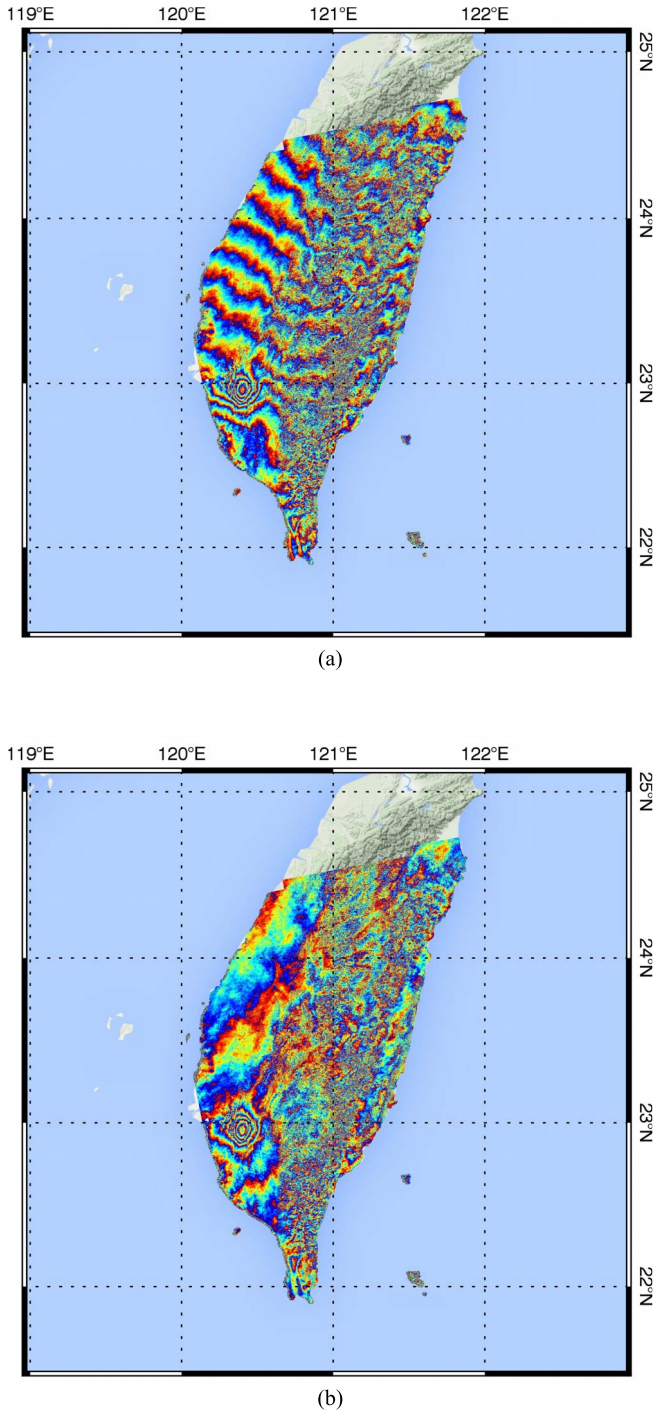

Fig. 5. (a) Original Sentinel-1 interferogram of the February 2016 Taiwan earthquake. (b) After ionospheric compensation.

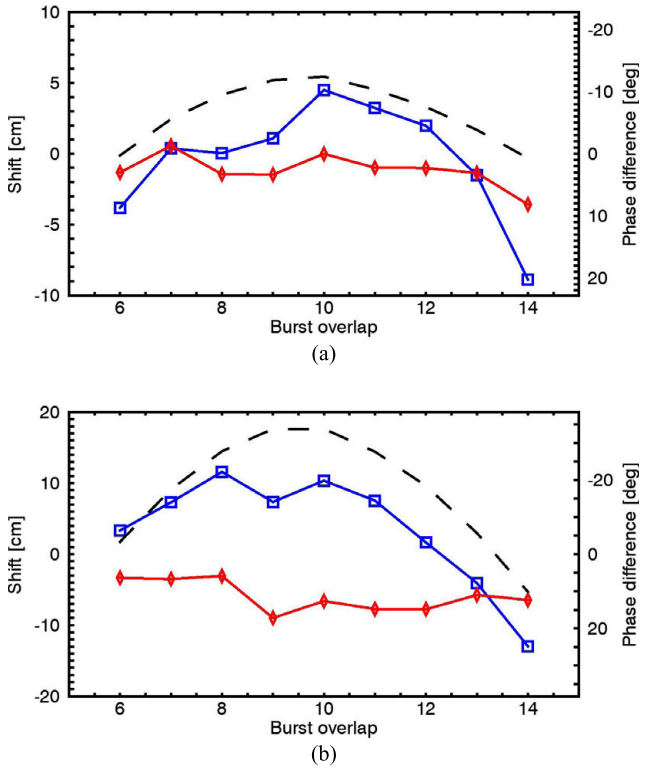

Fig. 6. Azimuth shifts measured by the ESD method at each burst overlap for beam (a) IW1 and (b) IW2. Blue squares are the residual shifts measured after compensating the global 60-cm offset. The dashed line represents the expected ionospheric shifts, generated with the estimated ionosphere. Red diamonds are the residual shifts measured after compensating the ionosphere.

bursts are resampled to maximize coherence, and interferograms are produced. The resampling step corrects the Doppler-dependent phase that is due to the timing error, but introduces a phase bias that converts the ionospheric phase to approximately what would have been measured by a nonsquinted acquisition. For this reason, no visible phase jumps are present between bursts in the scene interferogram. However, residual small phase jumps and azimuth shifts can still be measured by applying the ESD method. The phase bias and the ionospheric phase screen are estimated and removed by using the split-spectrum method, producing an ionosphere-free interferogram. Finally, ESD is applied again to the compensated bursts to measure eventual remaining shifts.

The results of the final burst overlap phase check are plotted with red diamonds in Fig. 6. The variation of the new values is considerably reduced. The residual bias, with respect to zero, is comparable with the precision of the global ionospheric shift estimation. Eventual larger residual errors could be due to the limits of the raw dispersive phase smoothing.

The ESD results in Fig. 6 and the compensated interferogram in Fig. 5(b) show how the applied correction method is capable of precisely removing ionospheric effects from Sentinel-1 interferograms.

V. Full-Aperture ScanSAR Mode

Wide-swath images acquired from the L-band PALSAR-2 radar in ScanSAR mode might also require ionospheric correction.

The Nepal 2015 earthquake region was imaged several times, allowing the generation of multiple interferograms spanning different dates. We concentrate in particular on ScanSAR coseismic interferograms, measuring both the main shock and the principal aftershock. The results of the first analysis of these interferograms presented in [13] were then used by others [14]–[16] to model the earthquake. We select three of these interferograms, displayed in Fig. 7(a)–(c), acquired during descending passes. We demonstrate that the phase ramps present

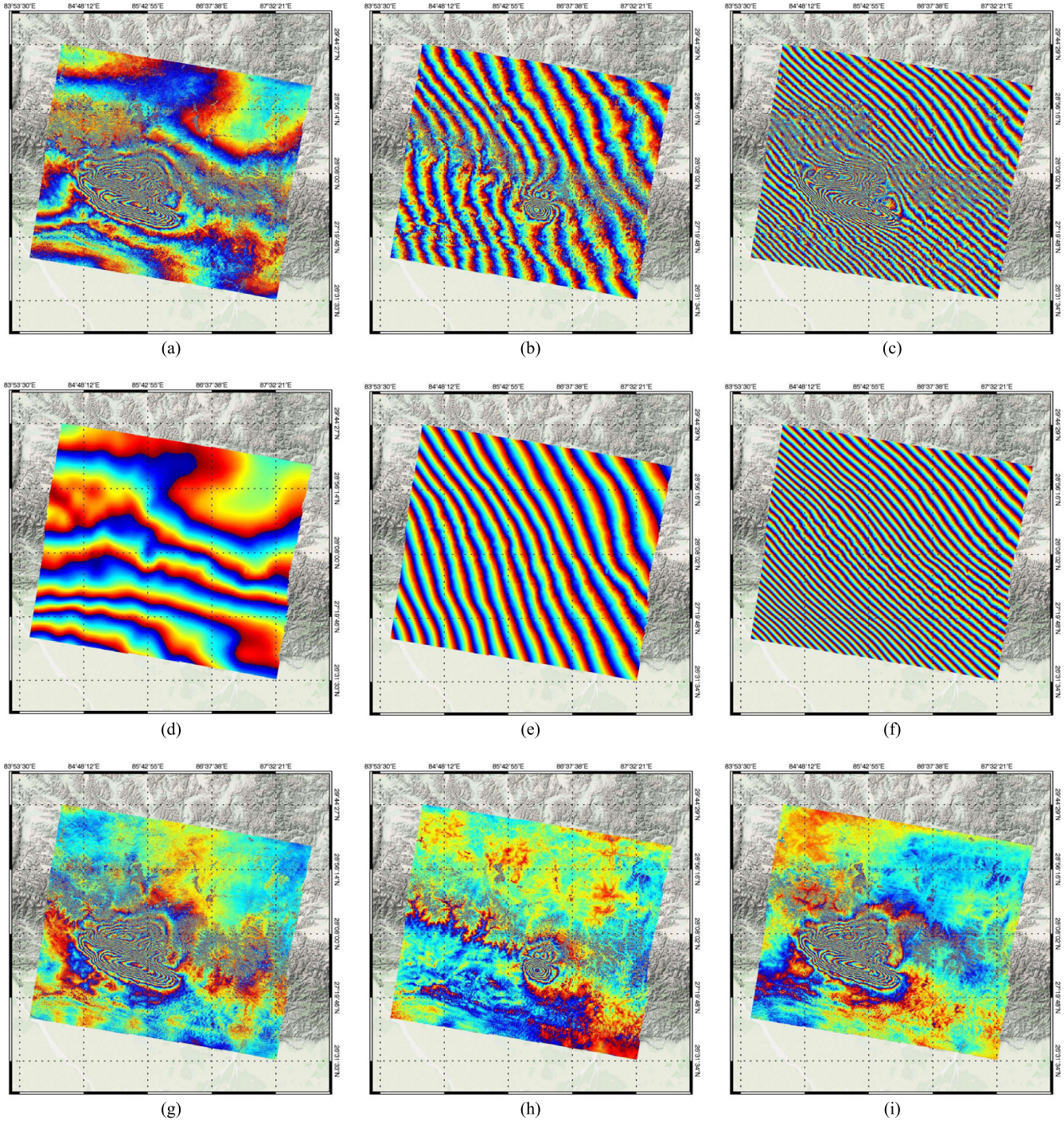

Fig. 7. (a)–(c) Original ALOS-2 interferograms. (d)–(f) Estimated ionospheric phase screens. (g)–(i) Interferograms after ionospheric compensation.

in the interferograms are due to ionospheric variations and that a compensation based on trend removal only approximates the real ionospheric phase screen. Acquisition parameters are reported in Table I.

A. Processing Description

ALOS-2 ScanSAR acquisitions can be downloaded from the JAXA website in two possible formats: the *SPECAN* mode and the *full-aperture* mode. Images of the latter method are produced by filling the raw data voids between bursts with zeros and focused as stripmap data [17]. The advantage of using full-aperture data is that they can be processed in a standard stripmap interferometric chain. A disadvantage is that the effective Doppler centroid (equivalently, the squint angle) undulates along azimuth around the value imposed by the attitude. Possible consequences of this are that phenomena such as azimuth ground deformation or ionospheric variation bias the interferometric phase with a wave effect.

More precise results can be obtained by using the SPECAN mode data, in which bursts are provided separately, and a burst-mode interferometric processor. The same effects described in

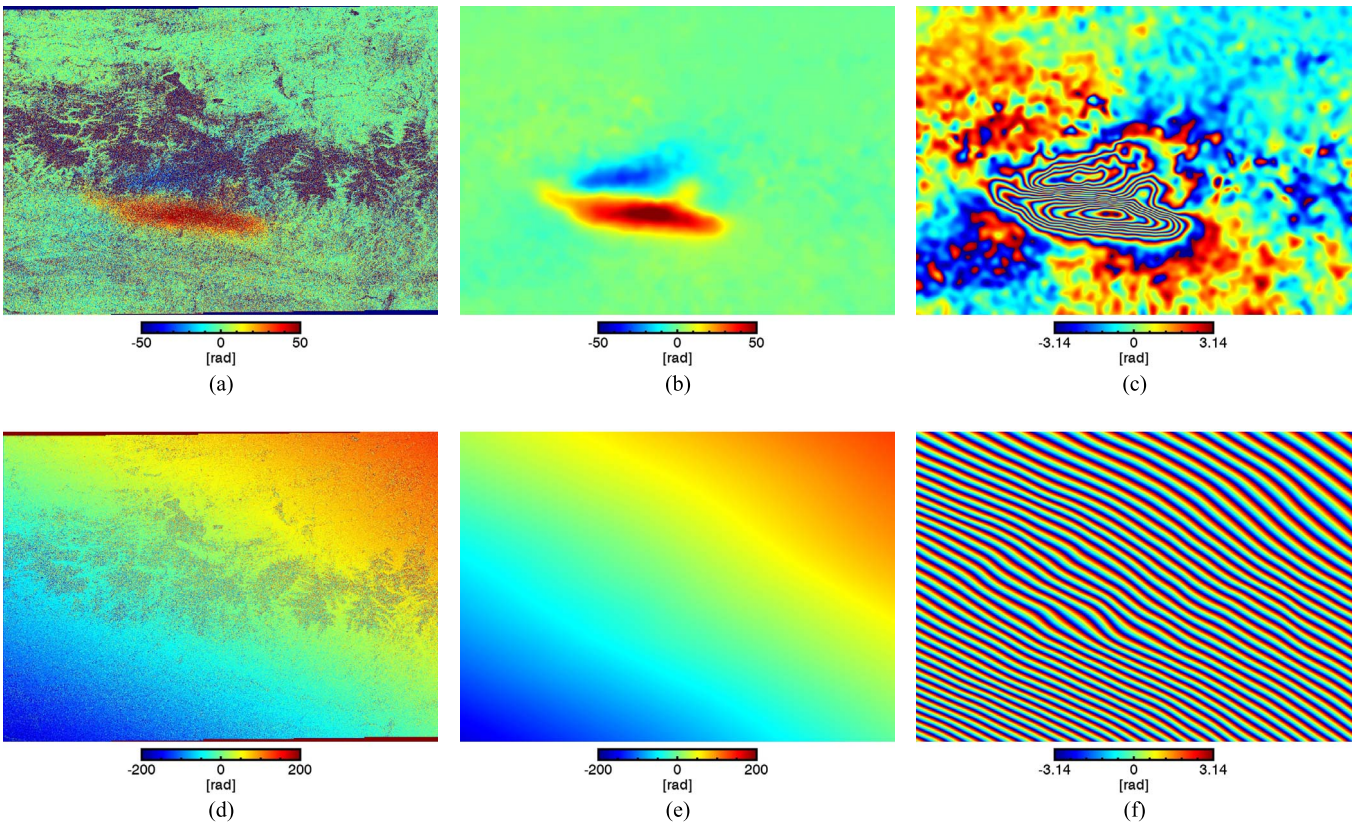

Fig. 8. Raw, filtered, and wrapped (a)–(c) nondispersive and (d)–(f) dispersive phase components of the interferometric phase.

Section II for TOPS data apply here for these ScanSAR images. Similarly, the correction method proposed in Section IV could be employed. A difference between Sentinel-1 TOPS and PALSAR-2 ScanSAR modes is that in the latter, a single target is imaged by multiple bursts. A study of what consequences this fact has on ionospheric effects and their estimation is an interesting subject of possible future work.

Nevertheless, for a first analysis of ionospheric phase screens in ALOS-2 ScanSAR images, in this paper, we use full-aperture processed data. We correct each beam separately using the split-spectrum method described in [3]. Each slave beam is independently coregistered with its own master by using patch-based cross correlation. Afterward, the beams are mosaicked in the radar coordinate system using the timing information. Finally, interferograms are formed. No relevant phase jumps can be seen between beams, at least by visual inspection.

B. Processing Example

The original ScanSAR interferograms of the Nepal earthquake are shown in Fig. 7(a)–(c). Fig. 7(a) and (c) presents the main shock and Fig. 7(b) the aftershock. To apply the split-spectrum technique, high- and low-frequency range subbands were generated for each beam. After mosaicking the beams, the interferograms were calculated and unwrapped.

The final estimated ionospheric phase screens are shown in Fig. 7(d)–(f) and the compensated interferograms in Fig. 7(g)–(i). All strong phase ramps have been removed; it is then clear that they are due to ionospheric variations and not to an incorrect orbit. The first interferogram presents a differential azimuth TEC variation of about 2.5 TEC units in 300 km, the second 4 TECU, and the third 14 TECU. In Section VI, it is shown that these gradients are caused by the daily difference in the ionization level decrease rate, from low to high latitudes. The range variation, on the other hand, can be caused by the incidence angle change and a difference in the absolute TEC level, or by a differential TEC variation in range. Remaining tropospheric path delay could be mitigated by using numerical weather prediction data and a digital elevation model [12].

As a processing example, the estimated raw nondispersive (a) and dispersive (d) components of the interferometric phase of the interferogram in Fig. 7(c) are displayed in Fig. 8. Fig. 8(b), (c) and (e), (f) shows the filtered and rewrapped phases of the nondispersive and dispersive components, respectively.

C. Comparison With Trend Removal

When dealing with localized ground motion, the common procedure to mitigate the ionospheric phase impact is to remove from the interferogram a linear or quadratic trend that may have been caused by ionospheric variations. If the ionosphere does not follow a first- or second-order polynomial variation, this procedure might leave a residual error that later on influences the earthquake source modeling. Moreover, if the measurement objectives are large-scale tectonic motions, this procedure cannot be used, or it might also remove the slow motion that has to be measured. The split-spectrum method is therefore important to precisely remove ionospheric phase screens.

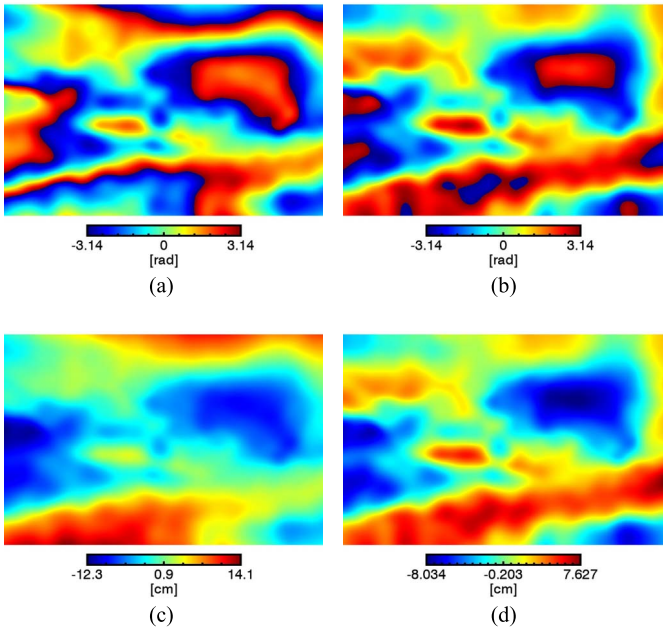

Fig. 9. Residuals between split-spectrum results and estimates of the ionospheric phase by (a) and (c) linear and (b) and (d) quadratic trend fitting, for the interferogram in Fig. 7(a). (a) and (b) Wrapped phase. (c) and (d) Absolute motion.

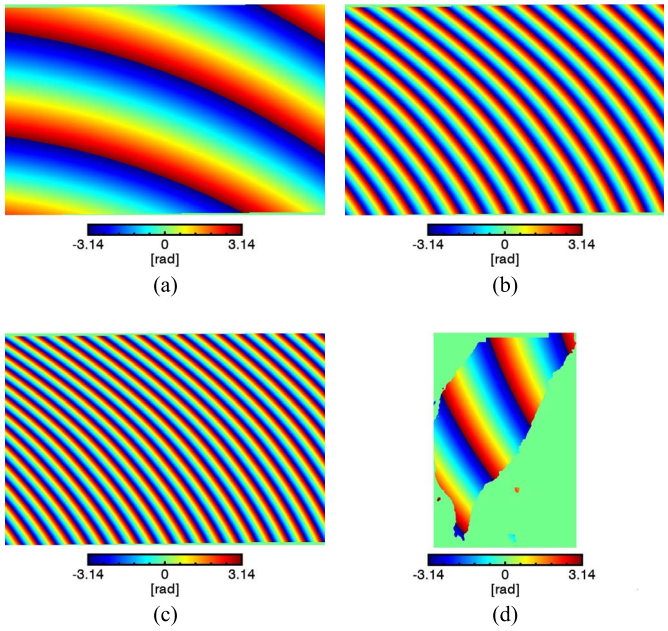

Fig. 10. Estimated ionospheric phase screens using the IGS TEC maps. (a)–(c) Nepal examples. (d) Taiwan example.

To evaluate the error that a trend removal causes on the interferograms analyzed here, we calculate the difference between the estimated trend and the split-spectrum phase screen for the interferogram in Fig. 7(a). Fig. 9 reports the resulting simulated interferograms and the absolute motion. The maximum introduced error is about 25 cm when using a linear trend and 15 cm when using a quadratic trend.

VI. Comparison With TEC Maps

In this section, we compare our estimated ionospheric phase screens with simulated interferograms produced with TEC maps derived from GNSS measurements. We would like to check whether our results are plausible and can be validated by an independent method. Moreover, we would like to understand the origin of such strong ionospheric gradients and be able to predict such effects in future interferograms.

The solar radiation is a main driver for the ionization. This varies during the day and year, generating diurnal and seasonal effects. Morning and midnight acquisitions encounter lower ionization levels, whereas noon and early evening acquisitions encounter higher levels. Moreover, radiation varies with the geographical location: due to the changing solar zenith angle, we observe, in general, an increasing ionization level from higher to lower latitudes. On the other hand, geographically localized effects are, for example, the aurora phenomenon, the fountain effect and equatorial anomaly, and equatorial and high-latitude scintillation [18].

A higher TEC level influences the SAR absolute localization accuracy, but only spatial variations of the differential TEC disrupt interferograms. However, higher TEC levels are possibly associated with stronger spatial variations and, consequently, higher differential TEC levels with stronger differential spatial variations. It is then more probable to detect strongly affected interferograms when the difference in the TEC level is higher, for example, in equatorial regions during the afternoon and evening, because of the strong solar radiation, or in polar regions, because of the aurora effect. Descending ALOS-2 images, being acquired around noon local time, are therefore more likely to be disrupted by ionospheric variations than ascending acquisitions. For the same reason, it is more likely to expect stronger ionospheric variations in ascending Sentinel-1 images acquired in the late afternoon, rather than in descending ones, acquired during early morning.

The International GNSS Service (IGS) produces vertical TEC maps on a daily basis with a temporal resolution of 2 h by combining several products, independently generated by different Ionospheric Associate Analysis Centers [19]. The maps have to be interpolated in time and space to obtain the TEC estimation for the ionospheric piercing point associated with every image pixel. A mapping function and the local look angle are used to convert vertical TEC to slant. The expected interferometric phase is calculated by converting the difference between TEC maps to a phase delay using (1).

A. Nepal Test Case

The simulated ionospheric phase screens obtained using IGS TEC maps are displayed in Fig. 10. The Nepal interferograms, in Fig. 10(a)–(c), show a variation of about 1.5, 3, and 9 TECU in 300 km, whereas the split-spectrum measured, respectively, a variation of about 2.5, 4, and 14 TECU. The smaller variation measured by the TEC maps could be attributed to the coarse sampling of the GNSS measurements in the considered regions and to the smooth ionospheric models used during data assimilation.

According to IGS TEC products, the differential vertical TEC levels are about 5, 18, and 24 TECU. The correlation with the spatial variation indicates how higher absolute and differential TEC levels seem to be associated with steeper slopes.

The range variation measured by InSAR also depends on the differential TEC level [20]. This is clarified by writing the differential slant TEC as a function of the look angle θ, i.e.,

$$\Delta\text{STEC}(\theta) = (\text{TEC}_m - \text{TEC}_s)\frac{1}{\cos(\theta)} \tag{20}$$

where TEC_m and TEC_s are, respectively, the vertical TEC levels during master and slave acquisitions. In addition to the eventual TEC range variation, the differential ionospheric level will then produce a variation in the range direction because of the look angle change. In the Nepal ALOS-2 ScanSAR images, about one range fringe is expected for every six differential TECU. Therefore, one range fringe in the first interferogram, three in the second, and eight in the third are due to the differential TEC level, and the remaining ones are due to the TEC range variation.

B. Taiwan Test Case

IGS TEC maps for the Taiwan test case indicate a north–south variation of only about 2 TECU over 300 km [see Fig. 10(d)], whereas the split-spectrum measure is of about 25 TECU. To gain a better understanding of the real ionospheric conditions, we use local estimates of the vertical TEC obtained from calibrated slant TEC measurements, extracted from GPS data, at the time of the SAR acquisitions.

These measurements are overlaid on IGS TEC maps in Fig. 11(a) and (c) for master and slave, respectively. In Fig. 11, the black line is the satellite orbit, and the black square is the image ground footprint. The red square is the ionosphere that is seen by the SAR image when assuming a single-layer model at a height of 350 km. The black triangles are the GPS receivers, and the colored circles are the ionosphere measurements. Residuals between maps and local measurements indicate how the TEC maps are only a smooth approximation of the background ionospheric variation and do not show small-scale structures, even if they are of large magnitude. Therefore, we estimate the local ionosphere over Taiwan by Kriging interpolation of the GPS TEC measurements. The resulting improved TEC maps are shown in Fig. 11(b) and (d). The simulated interferogram [see Fig. 11(e)], produced using the new interpolated TEC maps, is similar to the original Sentinel-1 interferogram and to the ionospheric phase screen that was estimated with the split-spectrum method. The north–south variation is now about 15 TECU in 300 km. The residual difference with respect to the split-spectrum estimate can be due to the lack of piercing points in the vicinity of the ionosphere seen by the SAR images.

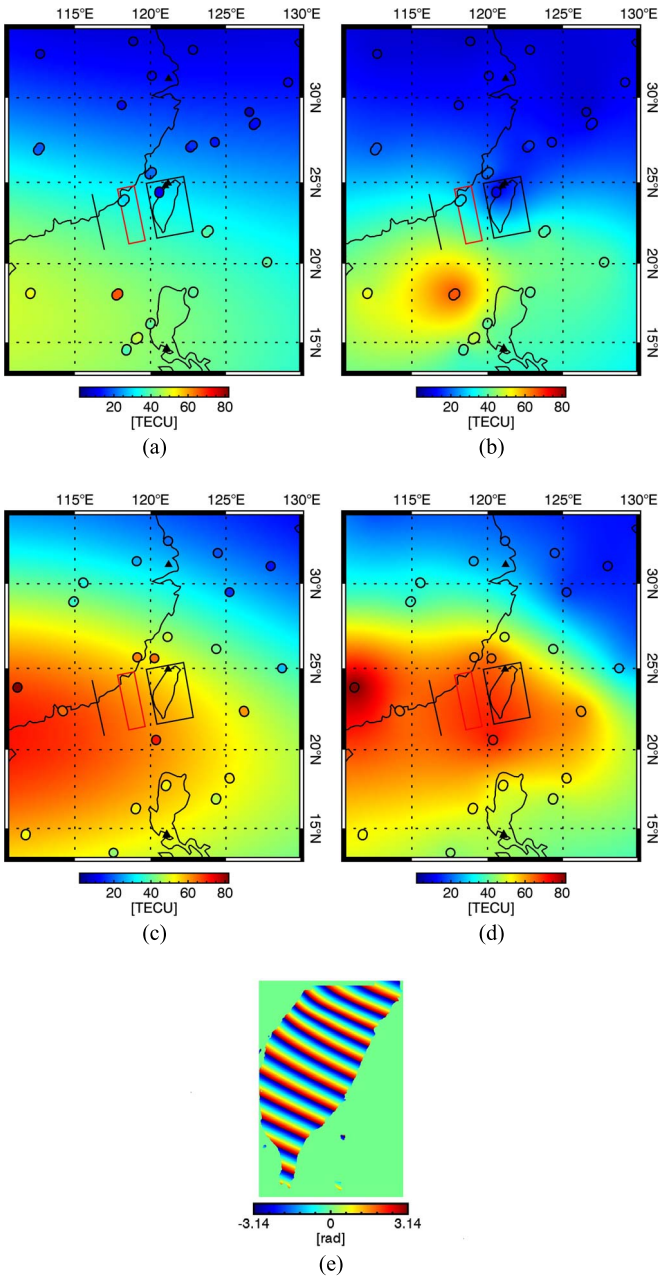

Fig. 11. (a) and (c) GPS TEC measurements overlaid on the IGS TEC maps for master and slave acquisition, respectively. Black line and square indicate the orbit and image ground footprint; red square indicates the crossed ionosphere; triangles indicate the GPS receiver position; colored points are the GPS derived TEC measurements. (b) and (d) Interpolated TEC maps, by using the GPS measurements. (e) Simulated interferogram, by using the new interpolated TEC maps.

VII. Conclusion

The larger coverage of wide-swath images is helpful for studying large-scale geophysical processes. Ionospheric variations can also be better revealed by wider images. What in the past has been often explained with imprecise orbit information can now be correctly attributed to the influence of the ionosphere.

In this paper, we have presented an adaptation of the split-spectrum method for the Sentinel-1 TOPS and PALSAR-2 ScanSAR modes. The method allows us to estimate ionospheric phase screens and remove them from interferograms, increasing the ground deformation estimation accuracy.

This paper has also shown how C-band deformation measurements can also be severely disrupted by ionospheric variations. A Sentinel-1 Taiwan earthquake interferogram from

February 2016 presents an extreme differential ionospheric ramp of 25 TECU in 300 km, which introduces a LOS deformation error of 50 cm. The ionospheric variation has been estimated with the split-spectrum method and removed. Three ScanSAR interferograms of the 2015 Nepal earthquake, which also show relevant ionospheric variations, have been successfully compensated by using the split-spectrum method.

The origin of these strong variations can be explained by the global gradient in the electron density, which decreases from lower to higher latitudes. For the Nepal data set, IGS TEC maps show similar variations to the split-spectrum estimate, validating the results. At the same time, it is demonstrated that global GNSS-based TEC maps cannot be directly used to compensate interferograms. For the Taiwan case, the TEC maps are smoother than expected. Using local GNSS measurements, it was possible to obtain a better estimate of the real ionosphere conditions and also validate the results. However, a method that converts GNSS measurements to precise regional TEC maps still needs to be developed, and its capability to correct interferograms verified.

Ionospheric gradients might be present in almost every image of a stack of SAR images, even at higher carrier frequencies. Then, it becomes clearer that the correction of ionospheric effects is extremely important when one aims to measure ground deformations with high precision. The compensation of ionospheric as well as tropospheric large-scale variations allows for avoiding the use of GNSS measurements to calibrate interferograms. This would permit the measurement of even small movements over large distances such as tectonic motions, in a precise and independent way.

APPENDIX

Contrary to what happens for the troposphere [6], due to the peculiarity of the ionospheric delay mechanism, a constant ionosphere level does not produce azimuth defocusing, at least to a first level of approximation. This happens because there are two mechanisms at play that influence the FM rate in opposite directions: the change in the traveled path within the aperture and the error in the reference azimuth chirp because of the group delay. As we will see, the two effects have roughly the same magnitude and, thus, will have a combined result close to zero.

Let us first analyze the effect of the squint angle. The target will have an extra phase, i.e.,

$$\varphi(\vartheta) = -\phi_{\text{iono}} \frac{1}{\cos(\vartheta)} \approx -\phi_{\text{iono}}(1 + \vartheta^2/2) \tag{21}$$

with ϑ being the azimuth squint angle, approximately $\vartheta = v \cdot \eta / R$. Here, v is the platform velocity, η is the slow time, and R is the range of closest approach. The quadratic term is

$$\varphi(\eta) = -\phi_{\text{iono}} \frac{v^2}{2R^2} \eta^2 \tag{22}$$

from which one can easily derive an FM rate error of

$$\Delta\text{FM}_{\text{phase}} = -\phi_{\text{iono}} \frac{v^2}{2\pi R^2} \tag{23}$$

where ϕ_{iono} is fixed at the value of the closest approach.

We then discuss the effect of group delay. The propagation in the ionosphere delays the signals that, due to the curved orbit, are then focused with a wrong FM rate. If the FM rate is

$$\text{FM} = -\frac{2v^2}{\lambda R} \tag{24}$$

with the usual conventions, the variation with range will be

$$\begin{aligned} \Delta\text{FM}_{\text{group}} &= \frac{2v^2}{\lambda R^2} \Delta R = \frac{2v^2}{\lambda R^2} \phi_{\text{iono}} \frac{\lambda}{4\pi} \\ &= \phi_{\text{iono}} \frac{v^2}{2\pi R^2} \end{aligned} \tag{25}$$

where $\Delta R = \phi_{\text{iono}} \cdot \lambda / 4\pi$ is the ionospheric group delay at the range of closest approach. The combined effect on the FM rate will be

$$\Delta\text{FM} = \Delta\text{FM}_{\text{phase}} + \Delta\text{FM}_{\text{group}} \approx 0. \tag{26}$$

This unexpected compensation occurs only because for the ionosphere, a phase advance corresponds to a group delay; for tropospheric delays, the two variations of the FM rate share the same sign and add up [6].

ACKNOWLEDGMENT

The authors would like to thank their colleagues D. Minkwitz and M. Kriegel of the German Aerospace Center for the provision of calibrated VTEC measurements and the IGS for making available high-rate GNSS data. The PALSAR-2 data are provided by the Japanese Aerospace Exploration Agency under the ALOS RA-4 proposal PI1118.

REFERENCES

[1] D. Belcher, "Theoretical limits on SAR imposed by the ionosphere," *IET Radar, Sonar Navigat.*, vol. 2, no. 6, pp. 435–448, Dec. 2008.
[2] T. Nagler, H. Rott, M. Hetzenecker, J. Wuite, and P. Potin, "The Sentinel-1 mission: New opportunities for ice sheet observations," *Remote Sens.*, vol. 7, no. 7, pp. 9371–9389, 2015.
[3] G. Gomba, A. Parizzi, F. D. Zan, M. Eineder, and R. Bamler, "Toward operational compensation of ionospheric effects in SAR interferograms: The split-spectrum method," *IEEE Trans. Geosci. Remote Sens.*, vol. 54, no. 3, pp. 1446–1461, Mar. 2016.
[4] P. Rosen, S. Hensley, and C. Chen, "Measurement and mitigation of the ionosphere in L-band interferometric SAR data," in *Proc. IEEE Radar Conf.*, May 2010, pp. 1459–1463.
[5] R. Brcic, A. Parizzi, M. Eineder, R. Bamler, and F. Meyer, "Estimation and compensation of ionospheric delay for SAR interferometry," in *Proc. IEEE IGARSS*, Jul. 2010, pp. 2908–2911.
[6] P. Prats-Iraola *et al.*, "On the processing of very high resolution spaceborne SAR data," *IEEE Trans. Geosci. Remote Sens.*, vol. 52, no. 10, pp. 6003–6016, Oct. 2014.
[7] G. Gomba, M. Eineder, A. Parizzi, and R. Bamler, "High-resolution estimation of ionospheric phase screens through semi-focusing processing," in *Proc. IEEE IGARSS*, Jul. 2014, pp. 17–20.
[8] N. Yage-Martnez *et al.*, "Interferometric processing of Sentinel-1 TOPS data," *IEEE Trans. Geosci. Remote Sens.*, vol. 54, no. 4, pp. 2220–2234, Apr. 2016.
[9] F. D. Zan, P. Prats-Iraola, R. Scheiber, and A. Rucci, "Interferometry with TOPS: Coregistration and azimuth shifts," in *Proc. 10th EUSAR*, Jun. 2014, pp. 1–4.
[10] R. Bamler and M. Eineder, "Accuracy of differential shift estimation by correlation and split-bandwidth interferometry for wideband and delta-k SAR systems," *IEEE Geosci. Remote Sens. Lett.*, vol. 2, no. 2, pp. 151–155, Apr. 2005.
[11] P. Prats, L. Marotti, S. Wollstadt, and R. Scheiber, "TOPS Interferometry with TerraSAR-X," in *Proc. 8th EUSAR*, Jun. 2010, pp. 1–4.

[12] X. Cong, "SAR interferometry for volcano monitoring: 3D-PSI analysis and mitigation of atmospheric refractivity," Ph.D. dissertation, Lehrstuhl für Methodik der Fernerkundung, Technische Univ. München, Munich, Germany, 2014.
[13] E. O. Lindsey *et al.*, "Line-of-sight displacement from ALOS-2 interferometry: Mw 7.8 Gorkha Earthquake and Mw 7.3 aftershock," *Geophys. Res. Lett.*, vol. 42, no. 16, pp. 6655–6661, 2015.
[14] K. Wang and Y. Fialko, "Slip model of the 2015 M w 7.8 Gorkha (Nepal) earthquake from inversions of ALOS-2 and GPS data," *Geophys. Res. Lett.*, vol. 42, no. 18, pp. 7452–7458, Sep. 2015. [Online]. Available: http://doi.wiley.com/10.1002/2015GL065201
[15] R. Grandin *et al.*, "Rupture process of the $Mw = 7.9$ 2015 Gorkha earthquake (Nepal): Insights into Himalayan megathrust segmentation," *Geophys. Res. Lett.*, vol. 42, no. 20, pp. 8373–8382, 2015.
[16] G. Feng, Z. Li, X. Shan, L. Zhang, G. Zhang, and J. Zhu, "Geodetic model of the 2015 April 25 M w 7.8 Gorkha Nepal Earthquake and M w 7.3 aftershock estimated from InSAR and GPS data," *Geophys. J. Int.*, vol. 203, no. 2, pp. 896–900, 2015. [Online]. Available: http://gji.oxfordjournals.org/content/203/2/896.short?rss=1
[17] R. Bamler and M. Eineder, "ScanSAR processing using standard high precision SAR algorithms," *IEEE Trans. Geosci. Remote Sens.*, vol. 34, no. 1, pp. 212–218, Jan. 1996.
[18] K. Davies, *Ionospheric Radio*, vol. 31. New York, NY, USA: IET, 1990.
[19] M. Hernández-Pajares *et al.*, "The IGS VTEC maps: A reliable source of ionospheric information since 1998," *J. Geodesy*, vol. 83, no. 3/4, pp. 263–275, 2009.
[20] F. Meyer, R. Bamler, N. Jakowski, and T. Fritz, "The potential of low-frequency SAR systems for mapping ionospheric TEC distributions," *IEEE Geosci. Remote Sens. Lett.*, vol. 3, no. 4, pp. 560–564, Oct. 2006.

Giorgio Gomba received the Bachelor's and Master's degrees in telecommunication engineering from Politecnico di Milano, Milan, Italy, in 2010 and 2012, respectively. He is currently working toward the Ph.D. degree at the Technical University of Munich, Munich, Germany.

Since 2013, he has been with the Remote Sensing Technology Institute, German Aerospace Center (DLR), Wessling, Germany. His current research interests include the estimation and compensation of ionospheric propagation delay in synthetic aperture radar signals.

Fernando Rodríguez González received the Ingeniero degree in telecommunications engineering from the Universidad Politécnica de Madrid (UPM), Madrid, Spain, and the Diplôme de l'École Polytechnique from the École Polytechnique, Palaiseau, France, in 2009.

From 2009 to 2010, he was the Chair of Remote Sensing Technology with Technische Universität München, Munich, Germany. In 2010, he joined the Department of SAR Signal Processing, Remote Sensing Technology Institute, German Aerospace Center (DLR), Wessling, Germany. He has worked in the development of the operational interferometric processor of the TanDEM-X mission. His research interests include synthetic aperture radar (SAR) interferometry, persistent scatterer interferometry, and SAR stereo radargrammetry.

Francesco De Zan received the Master's degree in telecommunication engineering and the Ph.D. degree from Politecnico di Milano, Milan, Italy, in 2004 and 2008, respectively. During his Ph.D. study, he worked on extending Permanent Scatter Interferometry to decorrelating targets and contributed to European Space Agency studies in preparation for Sentinel-1.

Since 2008, he has been with the German Aerospace Center (DLR), Wessling, Germany, first at the Microwaves and Radar Institute and then at the Remote Sensing Technology Institute. He has been involved in studies for numerous future interferometric SAR missions and in calibration activities of the TanDEM-X interferometer. His research interests include algorithms and theoretical bounds for shift estimation and SAR interferometry and interpretation of phase and coherence signatures.

C

Gomba, G. and De Zan, F. (2016, submitted). Bayesian Data Combination for the Estimation of Ionospheric Effects in SAR Interferograms. IEEE Transactions on Geoscience and Remote Sensing

Bayesian Data Combination for the Estimation of Ionospheric Effects in SAR Interferograms

Giorgio Gomba, Francesco De Zan

***Abstract*—The ionospheric propagation path delay is a major error source in synthetic aperture radar interferograms and therefore, has to be estimated and corrected. Various methods can be used to extract different kinds of information about the ionosphere from SAR images, with different accuracies. This paper presents a general technique, based on a Bayesian inverse problem, that combines various information sources in order to increase the estimation accuracy, and thus the correction. A physically realistic fractal modeling of the ionosphere turbulence and a data-based estimation of the model parameters allows the avoidance of arbitrary filtering windows and coefficients. To test the technique, the differential ionospheric phase screen was estimated by combining the split-spectrum method with the azimuth mutual shifts between interferometric pair images. This combination is convenient since it can benefit from the strengths of both sources; range and azimuth variations from the split-spectrum and small-scale azimuth variations from the more sensitive mutual azimuth shifts. Therefore, the two methods can recover the long and short wavelength components of the ionospheric phase screen, respectively. ALOS PALSAR L-band images are used to show how the combined result is more accurate than the simple split-spectrum method.**

***Index Terms*—InSAR, SAR ionospheric effects, ionosphere estimation, methods combination**

I. Introduction

THE propagation speed of radio waves traveling through the ionosphere is influenced by the presence of free electrons and ions. The different propagation in the ionosphere, with respect to vacuum, can cause various effects on SAR images and interferograms [1]. These particular effects differentiate the ionosphere from other signals, allowing their estimation and possible compensation. The geolocalization accuracy of a SAR image depends on the absolute level of ionospheric electron density. Differences between the electron density present during two SAR acquisitions modifies the interferometric phase, which is used to measure ground deformation. Spatial variations of the electron density level in the orbit direction produce shifts and blurring in the images. Different propagation velocities for left and right circularly polarized waves cause a change of the polarization angle, called Faraday rotation.

The 3D ionospheric electron density is often approximated by collapsing it into a single thin layer with fixed height. This is realized by integrating the electron density along vertical lines, thus obtaining the total electron content (TEC).

Table I summarizes possible ionosphere estimation methods. The list is divided into the estimation of the absolute ionosphere and the differential one. The latter is the difference between the absolute ionosphere present during the two acquisitions of an interferogram. The differential ionosphere generates the ionospheric phase screen superimposed to the interferogram.

The dispersive propagation in the ionosphere blurs the range impulse response and autofocus techniques can then be used to estimate the absolute TEC [1]–[3]. Incoherent cross correlation between azimuth subbands of a single image is used in [4] to measure the local along-track second derivative of the absolute TEC. When full-polarimetric acquisitions are available, the Faraday rotation angle can be measured and then converted to a TEC value [5]–[16].

The dispersive propagation causes a delay of the signal envelope, and an advance of the signal phase. The group-phase delay difference method takes the difference between the group delay (the range mutual shift between the two images) and the phase delay (the interferometric phase) to estimate the ionospheric phase screen [1], [17]. Similarly to the procedure used with dual frequency GPS receivers to measure the electron content, the split-spectrum method [17]–[20] takes two range subbands and produces two interferograms, which are then used to estimate the phase screen. Using phase measurements these methods are ambiguous with respect to a 2π cyclic constant value over the scene, which could be recovered by using the mutual range shifts between subband images [17], [19], [20]. Finally, local azimuth variations (first derivative) of the differential ionospheric phase screen can be estimated from the mutual azimuth shifts between images [1], [21]–[30].

These methods estimate different parts of the absolute or differential ionosphere spectrum, with different accuracies. For example, due to the relatively small blurring effect, autofocus techniques are not able to estimate the TEC with sufficient accuracy to correct images or interferograms. On the contrary, the split-spectrum, group-phase delay difference, and Faraday rotation methods are accurate enough to estimate large-scale variations of the ionosphere, and remove the ionospheric phase screen from interferograms. However, they are still limited by the estimation noise in accurately measuring short distances variations. Finally, methods which are based on the azimuth shifts are sensitive enough to also recover small-scale effects, but they only measure local variations in the orbit direction. It is then necessary to develop a strategy to handle these various information sources. In particular, a combination of more sources should improve the overall estimation accuracy and robustness.

The combination of different methods has been proposed

G. Gomba and F. De Zan are with the Remote Sensing Technology Institute, German Aerospace Center (DLR), Münchener Strasse 20, 82234 Wessling, Germany (e-mail: giorgio.gomba@dlr.de)

TABLE I
SUMMARY OF IONOSPHERIC EFFECTS ON SAR IMAGES AND INTERFEROGRAMS WITH ESTIMATION METHODS.

Measured ionosphere part		Physical phenomenon	Effect on SAR	Measuring method	
Absolute ionosphere	Full	Dispersion	Range blurring	Single image	Range autofocus
	Azimuth second derivative	TEC azimuth variation	Azimuth blurring		Azimuth autofocus
	Full	Faraday rotation	Polarization angle rotation		Polarization angle rotation estimation
Differential ionosphere	Full	Dispersion	Range blurring	Image pair	Differential range autofocus
	Relative variation	Dispersion	Phase proportional to $1/f$		Split-spectrum method
	Relative variation	Dispersion	Phase proportional to $1/f$		Group-phase delay difference method
	Azimuth first derivative	ΔTEC azimuth variation	Azimuth shift		Cross correlation or spectral diversity

and realized in previous works in various ways [1], [22], [25], [27], [29]–[31]. In [22], for example, a least squares inverse problem is used to fuse the TEC estimates derived from Faraday rotation measurements with the azimuth shifts. The smoothness of the result is ensured by Tikhonov regularization with a differential operator oriented in the direction of the Earth's magnetic field, controlled by a weighting coefficient. Apart from the magnetic field orientation, no other physical a priori information about the ionosphere smoothness is used in the model covariance matrix. The spectral characteristics of the solution are then governed by the differential operator, it might thus be difficult to choose an optimum smoothing coefficient, and to assess the accuracy and eventual bias of the result.

The procedure used in [25], [27], [29] first integrates the azimuth shifts, then recovers the integration constant and the long-distance errors by fitting the result to the interferometric phase. In this case, the smoothness of the result is governed by filtering windows and low-order polynomials with limited physical significance. Furthermore, the polynomial fitting to the interferometric phase cancels long-wavelength signals that may have been caused by ground motion, tropospheric variations or orbital errors, preventing the possibility to measure geophysical processes with large geographical scales. A slightly different approach is used in [30], here, the integrated azimuth shifts are fitted to the group-phase delay difference method result, not to the interferometric phase, allowing the measurement of large-scale motion.

To overcome the problems of existing methods we propose to use a physically realistic model of the ionosphere to describe its spatial covariance or, equivalently, power spectrum. With this approach, arbitrary smoothing windows or coefficients can be avoided. Noise suppression, response function deconvolution and data combination are then realized with a single step in a *Wiener* sense, that is, based on the signal to noise ratio of each frequency bin [32]. This is done in practice by using a Bayesian inverse problem, presented in Section II, implemented in the space domain because of the nonconstant noise variance.

The proposed method could, in general, be applied to combine methods which estimate the absolute or differential ionosphere. Nevertheless, in this paper, we concentrate on the recovery of the ionospheric phase screen, superimposed to the interferogram, which is caused by the differential ionosphere. An accurate compensation of the ionospheric phase produces better measurements of ground deformation.

Possible combination candidates for the estimation of the ionospheric phase screen are: the split-spectrum method, the group-phase delay method, the Faraday rotation method, and the azimuth shifts method. The first two are roughly equivalent, in that they can directly measure the ionospheric phase, their precision and possible biases have been analyzed in [20]. The precision depends on the ratio between the carrier frequency and the bandwidth, wider bandwidths ensure higher precisions. However, it has been shown in [20] that the smallest available bandwidth for PALSAR data, 14 MHz, is already sufficient to allow the estimation and compensation of at least large-scale ionospheric effects. The Faraday rotation method, whose precision has been derived in [33], measures the Faraday rotation angle and converts it to a TEC value, or interferometric phase, by using a model of the geomagnetic field and approximating the vertical ionospheric profile to a thin layer. It has been shown in [33] that this method can also be used to compensate interferograms at high latitudes. However, estimates of the Faraday rotation method are susceptible to biases, caused by the unknown true conditions of the 3D ionosphere and magnetic field. Moreover, its sensitivity decreases significantly in regions closer to the magnetic equator, lowering the precision. Finally, this technique can only be used if full-polarimetric data are available, which considerably limits its applicability to only a part of existing and future SAR images.

In the Appendix A we demonstrate that, for an L-band system with 14 MHz bandwidth, the Faraday rotation method is in polar regions 1.5 times more precise than the split-spectrum method, and that the split-spectrum becomes the precisest method for latitudes lower than about 40 degrees. For systems with bandwidths of 28 MHz or more, the split-spectrum methods is always the precisest technique. Since the advantages brought by the Faraday rotation seem to be less than its possible issues, we decided to select the split-spectrum method as the principal technique to estimate the ionospheric phase screen. In this paper, we therefore apply

the Bayesian combination to the split-spectrum method and azimuth shifts. The latter are extremely sensitive to ionospheric gradients in the along-track direction, and can thus support the split-spectrum method measuring also small-scale effects, improving the estimation of the phase screen. The details of the combination are presented in Section III. A required assumption is that no azimuthal ground motion is present. An improvement of the method that will use multiple azimuth subbands to remove this limitation is left for future work. In any case, if quad-polarized acquisitions should be available, the Faraday rotation measurements could also be included to further improve the final result.

In Section IV two application examples, using ALOS PALSAR images, are presented. The first is the estimation of a fast spatially varying aurora effect in northern Alaska. The second is based on an equatorial scintillation event over the Amazon region caused by plasma bubbles. Phase screen corrections, based on the split-spectrum alone and on the proposed method, are then compared to assess the accuracy improvement.

II. Bayesian Data Combination

We use the Bayesian approach to inverse problems to combine different information sources and improve the final estimation of the ionosphere, i.e., the absolute TEC or the differential ionospheric phase screen. Assuming that the ionosphere can be represented by a single thin layer with known height the linear model with additive noise is

$$\boldsymbol{x} = \boldsymbol{G\theta} + \boldsymbol{w}, \tag{1}$$

where $\boldsymbol{x}$ is a vector containing the observations, the matrix $\boldsymbol{G}$ transforms $\boldsymbol{\theta}$, the ionosphere vector, into the observations; $\boldsymbol{w}$ is the measurement noise vector. The signal $\boldsymbol{\theta}$ and noise $\boldsymbol{w}$ are modeled as Gaussian distributed. The linear minimum mean square error estimator of $\boldsymbol{\theta}$ is

$$\hat{\boldsymbol{\theta}} = \left(\boldsymbol{G}^T\boldsymbol{C}_{\boldsymbol{ww}}^{-1}\boldsymbol{G} + \boldsymbol{C}_{\boldsymbol{\theta\theta}}^{-1}\right)^{-1}\boldsymbol{G}^T\boldsymbol{C}_{\boldsymbol{ww}}^{-1}(\boldsymbol{x} - \boldsymbol{G}\bar{\boldsymbol{\theta}}) + \bar{\boldsymbol{\theta}}, \tag{2}$$

where $\boldsymbol{C}_{\boldsymbol{ww}}$ is the covariance of $\boldsymbol{w}$, $\bar{\boldsymbol{\theta}}$ is the a-priori model of $\boldsymbol{\theta}$ and $\boldsymbol{C}_{\boldsymbol{\theta\theta}}$ the covariance of $\left(\boldsymbol{\theta} - \bar{\boldsymbol{\theta}}\right)$ [34, p. 391].

The proposed combination technique is rather general and could be used to combine information from different sources. The ionosphere model is also general and is presented in the following section. In Section III we will implement the inverse problem to combine the split-spectrum method with the azimuth shifts, to first apply and test the proposed concept.

A. Ionosphere Model and A-Priori Information

Large-scale TEC variations depend on the global distribution of solar radiation, forming the background ionosphere. In addition, local turbulent irregularities may perturb the smooth trends. The ionosphere in the inverse problem consist therefore of two components [35]:

$$\theta(t,\eta) = \theta_b(t,\eta) + \delta\theta(t,\eta), \tag{3}$$

where t and η are, respectively, range and azimuth axes. The values $\theta(t,\eta)$ are arranged in the vector $\boldsymbol{\theta}$. The component $\theta_b(t,\eta)$ accommodates the background ionosphere trend that cannot be characterized by statistically homogeneous measures, in the inverse problem model it is a low-order polynomial. The component $\delta\theta(t,\eta)$ represents the turbulent irregularities. They are caused by random electron density variations, whose size distribution can be characterized by a power law spectral density function, in particular when considering scintillation effects [2], [35]–[39].

The Bayesian approach to statistical estimation allows the use of a-priori information in the estimator. This possibility is exploited by forcing the autocorrelation function of $\delta\theta(t,\eta)$ to be a physically realistic function, thus also avoiding generic smoothing window or regularization.

In [36] the power spectral density of the 2-D ionospheric phase screen is derived from the 3-D autocorrelation function of the refractive index, obtaining a power law with outer scale function:

$$\Phi_{\delta\theta}(\boldsymbol{k}) = \frac{r_e^2\lambda^2 L\sec^2(\beta)\cdot ab\cdot C_s}{\left(k^2 + k_0^2\right)^{\nu+1/2}}, \tag{4}$$

where r_e is the classical electron radius, λ is the carrier wavelength, L is the ionospheric layer thickness, β is the SAR look nadir angle, C_s is the strength of turbulence. The product C_sL is related to C_kL, the vertically integrated turbulence strength at 1-km scale. The quadratic form

$$k^2 = Ak_x^2 + Bk_xk_y + Ck_y^2 \tag{5}$$

depends on the along and transverse wavenumber to the geomagnetic north k_x and k_y, respectively. The outer scale wavenumber $k_0 = 2\pi/l_0$ is associated with the outer scale l_0 (usually 10 to 50 kilometers) at which the spatial correlation drops. The factors A, B and C are functions of a, b and the propagation angles, where a and b are the principal and secondary axial ratios, which regulate anisotropy [37], [40]. Finally, ν is the spectral index parameter.

The parameters a, b, C_kL, l_0 and ν can be generated by global ionospheric scintillation models for different geophysical conditions, dates, locations and geometries. They can represent different ionospheric states, from scintillation events to quieter mid-latitude variations [2]. By applying these parameters to the phase power spectrum in (4) it is possible to simulate ionospheric phase screens, which are then used to test the effects that different turbulence levels have on SAR image formation [37]–[39].

The spatial autocovariance function of a 2-D phase screen with power law power spectrum is the Fourier transform of (4)

$$R_{\delta\theta}(\boldsymbol{r}) = r_e^2\lambda^2 L\sec(\beta)GC_s\left|\frac{r}{2k_0}\right|^{\nu-1/2}\frac{K_{\nu-1/2}(k_0r)}{2\pi\Gamma(\nu+1/2)}, \tag{6}$$

where G is a geometrical factor, $K_\nu(x)$ is the modified Bessel function of the second kind and $\Gamma(x)$ is Euler's gamma function [36]. The argument r is

$$r^2 = \frac{Cr_x^2 - Br_xr_y + Ar_y^2}{AC - B^2/4}, \tag{7}$$

where r_x and r_y are the spatial distances related to the wavenumbers k_x and k_y. The expression in (6) is a function of the Matérn family [41] which can describe turbulence with adjustable smoothness for short distances, and saturating

variance for long distances, satisfying physical and statistical requirements [42].

The correlation function (6) models in [36] equatorial irregularities which causes scintillation effects. In this paper, it is generically used to model the residual variations that are not represented by a trend. Relating phase screens to physical constants is not the main topic of this paper, therefore, the formulation of [36] is simplified by using a generic Matérn covariance function:

$$R_{\delta\theta}(\boldsymbol{r}) = P_{\delta\theta}\frac{2^{3/2-\nu}}{\Gamma(\nu-1/2)}(k_0 r)^{\nu-1/2}K_{\nu-1/2}(k_0 r). \quad (8)$$

The axes refer now to the range and azimuth directions. The maximum of the function, $P_{\delta\theta}$, and ν, are respectively generic turbulence strength and spectral index parameters. The power spectral density is the two dimensional Fourier transform of (8)

$$\Phi_{\delta\theta}(\boldsymbol{k}) = \frac{P_{\delta\theta}}{G}\frac{\Gamma(\nu+1/2)}{\Gamma(\nu-1/2)}\frac{4\pi k_0^{2\nu-1}}{(k^2+k_0^2)^{\nu+1/2}}. \quad (9)$$

The derivation of (9) and factor G for the anisotropic case is reported in the Appendix B.

As introduced above, the inverse problem model is composed by a polynomial, to account for the background ionosphere trends, and by a function, to represent the turbulent part. The covariance (8) is used to model the spatial correlation of the turbulence, by inserting it into the model a-priori covariance matrix $\boldsymbol{C_{\theta\theta}}$. The parameters $P_{\delta\theta}$, ν, k_0, A, B, and C set the magnitude, smoothness, correlation length and anisotropy of the turbulent part of the estimated ionospheric phase screen. They can be determined by analyzing the data. After a trend removal, the split-spectrum estimates represent the turbulent ionospheric variations. The theoretical covariance (8) can be fitted to the sample covariance of the detrended split-spectrum estimates. The resulting parameters are used in the inverse problem.

If the turbulent variations are small, and masked by the split-spectrum estimation noise but still large enough to produce azimuth shifts, the measured azimuth shifts should also be used to estimate the covariance parameters. The exploitation of all information sources to characterize the turbulence is thus also an interesting topic for future investigations.

The resolution in the ionosphere along azimuth is limited by the synthetic aperture integration. If the shortest measurable ionospheric wavelength is bigger than the wavelength related to the ionospheric resolution, then the low-pass effect can be neglected. Otherwise, it might be necessary to add the synthetic aperture azimuth low-pass filter to the model (8).

B. Data Downsampling

Due to the relative smoothness of the ionosphere, with respect to the dense spatial sampling of SAR, the observation data can be pre-filtered and downsampled without loss of information. The objective is to reduce the data size and consequently computation time. This operation can be performed automatically by analyzing the data power spectra. The logarithmic power spectrum of the turbulent data part should show two regimes, the power law linear behavior at lower frequencies and the estimation noise floor at higher frequencies. Low-pass filtering and downsampling should retain the signal and remove the unnecessary noise and oversample. The relative data noise variance is recalculated to account for the lower noise after low-pass filtering. Also the spatial sampling of the model, that is the size of the model matrix $\boldsymbol{\theta}$, is selected to cover the whole measurable ionosphere spectrum.

III. Split-Spectrum Method and Azimuth Shifts Combination

As a first implementation of the inverse problem, in this Section, we combine the split-spectrum method with the azimuth shifts. These two information sources complement each other: the split-spectrum method can measure long distance range and azimuth variations but is not sensitive enough to estimate small-scale turbulence due to its relatively high noise, as experience shows [17], [20]. Azimuth shifts are very sensitive to local azimuth variations, therefore, they can refine the split-spectrum at the short wavelengths level, but wouldn't be able to recover large-scale variations, and range ones, if used alone.

The observations vector $\boldsymbol{x}$, then, contains the split-spectrum estimates of the ionospheric phase screen and the azimuth shifts, measured by coherent cross-correlation. $\boldsymbol{C_{ww}}$ is the observation noise covariance matrix, it is filled using the accuracy of the split-spectrum method $\boldsymbol{C}_{\Delta\phi_{\text{iono}}}$ and cross correlation $\boldsymbol{C}_{\Delta\eta}$:

$$\boldsymbol{C_{ww}} = \begin{bmatrix} \boldsymbol{C}_{\Delta\phi_{\text{iono}}} & \boldsymbol{0} \\ \boldsymbol{0} & \boldsymbol{C}_{\Delta\eta} \end{bmatrix}. \quad (10)$$

Eventual correlation between samples noise is consequently described by the covariances in $\boldsymbol{C}_{\Delta\phi_{\text{iono}}}$ and $\boldsymbol{C}_{\Delta\eta}$, which are therefore not necessarily diagonal.

A. Split-Spectrum Method

The split-spectrum method exploits the dispersive propagation of the ionosphere to estimate the ionospheric phase screen [17], [18], [20]. It uses two range subband interferograms to separate the non-dispersive phase component of the interferogram from the dispersive ionospheric component. Being $\Delta\phi_L$ and $\Delta\phi_H$, respectively, the low and high subband interferograms with center frequency f_L and f_H, and f_0 the carrier frequency, the ionospheric phase screen is obtained with:

$$\Delta\phi_{iono} = \frac{f_L f_H}{f_0\,(f_H^2 - f_L^2)}(\Delta\phi_L f_H - \Delta\phi_H f_L). \quad (11)$$

The practical implementation of this formula is reported in [20].

B. Azimuth Shifts

One of the differences between ionosphere and troposphere is the height at which they influence the radio waves propagation. The peak of the ionosphere electron density is usually at about 300 to 400 kilometers altitude, more or less halfway between the satellite and the target. For this reason, the ionosphere can strongly modify the SAR impulse response function: a linear slope of the ionospheric TEC level in the

azimuth direction produces a shift, higher order variations can defocus the image.

Let us calculate the azimuth shift produced on a target by an ionospheric slope in the along-track direction of ρ_{TEC} slant TEC per meter. Ignoring the constant TEC level, the TEC variation experienced by a target's echoes which are received by the satellite at the slow time η can be written as

$$\frac{dTEC(\eta)}{d\eta} = \rho_{TEC}\frac{H_i}{H}v, \tag{12}$$

where H_i is the height of the ionospheric single layer, H is the satellite orbit height and v is the platform velocity. The target extra phase varies linearly within the synthetic aperture:

$$\frac{d\varphi(\eta)}{d\eta} = -\frac{4\pi K}{cf_0}\frac{dTEC(\eta)}{d\eta}, \tag{13}$$

where c is the light speed in vacuum, f_0 is the carrier frequency and $K = 40.28\,\mathrm{m}^3/\mathrm{s}^2$. The Doppler frequency increase is proportional to the change rate of the phase:

$$\Delta f_D = -\frac{1}{2\pi}\frac{d\varphi(\eta)}{d\eta} = \frac{2vKH_i}{cf_0H}\rho_{TEC}. \tag{14}$$

The target is focused at the zero Doppler position which is shifted of

$$\Delta\eta_i = \frac{\Delta f_D}{K_a} = \frac{2vKH_i}{cf_0K_aH}\rho_{TEC}, \tag{15}$$

where K_a is the azimuth frequency modulation rate.

During the interferometric processing, the slave image is coregistered with the master by using a patch-based cross correlation. The measured mutual azimuth shifts depend on the difference of ionospheric heights and slopes. From (15)

$$\Delta\eta_i = \frac{2vKH_{i_1}}{cf_0K_aH}\rho_{TEC_1} - \frac{2vKH_{i_2}}{cf_0K_aH}\rho_{TEC_2}, \tag{16}$$

where H_{i_1}, ρ_{TEC_1} and H_{i_2}, ρ_{TEC_2} are respectively the ionospheric height and slope present during the first and second acquisition. In the following we assume that the ionospheric height during both acquisitions is the same, or that ionospheric variations are present during only one acquisition. Consequently (16) becomes

$$\Delta\eta_i = \frac{2vKH_i}{cf_0K_aH}\Delta\rho_{TEC}, \tag{17}$$

where H_i is the ionospheric height and $\Delta\rho_{TEC}$ is the differential ionospheric slope which also affects the interferogram phase. The measured shifts carry information about the local derivative of the ionospheric phase screen, and can therefore be used to improve its estimation.

Usually, it is assumed that the ionosphere is stable during the acquisitions, i.e., that the intensity of the TEC does not change with time, and that the ionospheric pattern does not move. This might not always be correct, as horizontal ionospheric drifts exist. They can be originated by diurnal variation in the production and loss of ionization, electromagnetic drift, and neutral winds [43]. Traveling ionospheric disturbances are large-scale structures with horizontal wavelengths of 100 to 1000 kilometers that travel with speed between about 50 to 1000 m/s, generally towards the equator [43]. Equatorial scintillation is generated by plasma irregularities which can move eastwards at speeds between 50 and 150 m/s [43], [44].

A moving plasma in the ionosphere changes the ionospheric phase experienced by a target. Since the split-spectrum method is based on interferograms, it directly estimates the same ionospheric phase screen which is superimposed in the interferogram. An eventual motion of the ionosphere does not change the correction method. On the contrary, azimuth shifts are sensitive to the ionosphere motion. Supposing a constant drift in the orbit direction, the TEC variation (12) can be written as

$$\frac{dTEC(\eta)}{d\eta} = \rho_{TEC}\left(\frac{H_i}{H}v - v_{az}\right), \tag{18}$$

where v_{az} is the drift speed. The target shift becomes then

$$\Delta\eta_i = \frac{2vK(H_i - H\cdot v_{az}/v)}{cf_0K_aH}\Delta\rho_{TEC}. \tag{19}$$

An azimuthal ionospheric motion thus lowers the effective ionospheric height by the quantity $H\cdot v_{az}/v$. The inverse problem method should still be able to correctly combine the split-spectrum with the azimuth shifts, even if the estimated ionospheric height won't correspond to the physical one.

C. Forward Problem

Due to the moving window filtering effect of the synthetic aperture integration, the ionospheric phase screen observed in the interferogram is a smoothed version of the real ionosphere. Unless the ionosphere turbulence is that strong that it defocuses the images and lowers the coherence, there is no need to increase the ionospheric resolution using techniques as azimuth subbands or semifocusing [45], [46]. Moreover, the objective here is the estimation of the ionospheric phase screen that is superimposed on the ground signals in the interferogram and not the estimation of the *real* ionosphere. For this reason, neither the low-pass effects produced by the synthetic aperture nor by the interferogram multilooking are included in the forward problem modeling. For each observation data pixel, a line of the forward problem $\boldsymbol{G}$ is written. The line contains the transfer function that converts the model into the observation pixel.

1) Split-spectrum: The split-spectrum method data are a direct measure of the ionospheric phase screen, they just have to be filtered by an anti-aliasing filter prior to data subsampling. The transfer function is then relatively simple, it is obtained by interpolating the filter kernel to the model dimension. This way, the possibly general sampling distance of the model, as well as the correlation between data pixels, is taken into account.

2) Azimuth shifts: The azimuth shifts transfer function also contains the anti-aliasing filter, with the addition of the derivative operator. A target's azimuth shift depends on the linear variation of the ionosphere within the synthetic aperture. This is equivalent to low-pass filter the ionosphere with the synthetic aperture size and differentiate the result. As introduced above, we neglect the synthetic aperture low-pass filter and only consider the derivative. The transfer function is then the azimuth shifts anti-aliasing filtering kernel, interpolated

to the model dimensions and convolved with a derivative operator.

The latter can be realized by finite differentiation. A common way of computing the derivative operator coefficients is to assume to locally approximate the function to be differentiated by some polynomial. The derivative of the polynomial then approximates the derivative of the function. The higher the polynomial grade is, the better the approximation of the derivative is. If the signal is sufficiently oversampled the operator response is only important in the low-frequencies range, therefore also a short polynomial can be used.

To complete the azimuth shifts forward problem, a coefficient that converts the phase derivative (in radians per meter) to an azimuth shift (in meter) is required. The latter is derived from the relationship (17), which contains the unknown height of the ionosphere single layer. The ionospheric height scales the effect of the ionosphere derivative, therefore, it is an important parameter of the inverse problem. An iterative procedure is used to find the height that converts the shifts into the correct derivatives. The unknown height makes the system non-linear, therefore, the linear inverse problem is solved multiple times with different possible ionospheric heights, until the minimum mean square error between observed and recalculated data is found.

An azimuth offset, probably a timing error, is often present between PALSAR images. This offset adds an unwanted phase ramp to the inversion result, producing an error over long distances. The problem is solved by the split-spectrum data, which constrain large-scale variations. By including an offset for the azimuth shifts in the problem model unknowns and in the direct problem, it is thus possible to recover the timing error and avoid biases. The parameters vector becomes then

$$\boldsymbol{\theta} = \left[\theta(t_1,\eta_1)\ \ldots\ \theta(t_i,\eta_j)\ \ \Delta\eta_{\text{offset}}\right]^T, \tag{20}$$

where $\theta(t_i,\eta_j)$ are the ionospheric phase screen pixels and $\Delta\eta_{\text{offset}}$ is the azimuth offset. Consequently, the forward problem is

$$\boldsymbol{G} = \begin{bmatrix} \boldsymbol{G}_{\Delta\phi_{\text{iono}}} & \mathbf{0} \\ \dfrac{vH_i}{2\pi K_a H}\cdot\boldsymbol{G}_{\Delta\eta} & \mathbf{1} \end{bmatrix}, \tag{21}$$

where $\boldsymbol{G}_{\Delta\phi_{\text{iono}}}$ and $\boldsymbol{G}_{\Delta\eta}$ are respectively the transfer function of the split-spectrum method and azimuth shift.

D. Spectral Analysis

In order to show how the inverse problem uses the two information sources, the power spectra of the data, filtered by the inverse problem, and of the final output, are reported in Fig. 1. The solid line is the power spectrum model of the ionospheric phase screen that has to be recovered, a power law with outer scale. The horizontal line represents the noise of the split-spectrum data. The dash-dotted line is the output of the inverse problem when only the split-spectrum method data are used. Adding the azimuth shifts, the result becomes the dashed line. The crosses and the circles are, respectively, the split-spectrum and azimuth shifts data processed by the inverse problem. The dashed line represents the power spectrum of the sum of both data. It can be seen that, the split-spectrum data contributes to the longer wavelengths, whereas the azimuth shifts data are used for the medium scales. Therefore, thanks to the azimuth shifts, the measured signal bandwidth of the combined solution (dashed line) is wider than that of the single split-spectrum result (dash-dotted line).

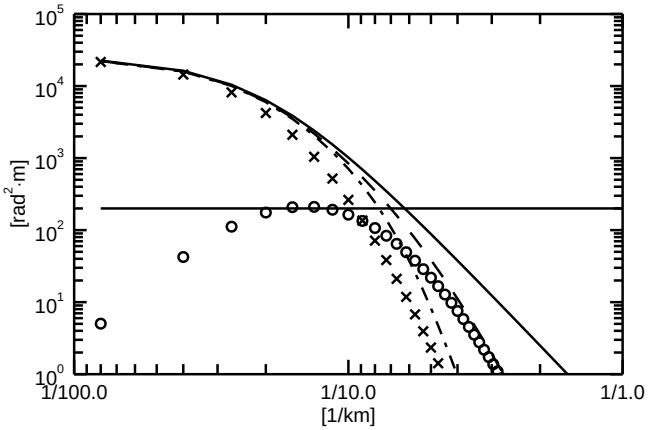

Fig. 1. Power spectral analysis of the inverse problem. The solid line is the power law model of the turbulent part of the ionospheric phase screen. The horizontal line is the split-spectrum method noise. The output of the inverse problem, when only the split-spectrum method data are used, is represented by the dash-dotted line. The dashed line is the power spectrum of the combined result, being composed by the split-spectrum and azimuth shifts data, represented respectively by the crosses and circles.

TABLE II
SCENES ACQUISITION INFORMATION

Example	Master	Slave	Path	Frame
Alaska	01/04/06	17/05/06	243	1410
Amazon	25/12/07	26/3/2008	91	7010

IV. APPLICATION EXAMPLES

A. Alaska Aurora Test Case

The Alaska test case is based on a pair of ALOS PALSAR images acquired in the northern part of Alaska during 2006. Acquisitions information are reported in Table II. The interferogram produced with these images shows the effects of strong and rapid fluctuations in the ionospheric electron density, caused by the aurora activity. The interferometric phase is shown in Fig. 2(a).

The strong variations produce large azimuth shifts, which can be measured and corrected with patch-based cross-correlation. A particular situation arises in this dataset, we suspect that ionosphere height variations are so large, that a single height for the whole scene is not appropriate, complicating the use of the measured shifts. Following the method presented in [47], multiple semi-focusing levels are used to extract the local ionospheric derivative, independently from the ionospheric height. The result is then converted back to azimuth shifts, assuming a fixed height, to be included in the inverse problem data. For non-aurora datasets, this preprocessing step shouldn't normally be required. Fig. 2(b) shows the estimated azimuth shifts.

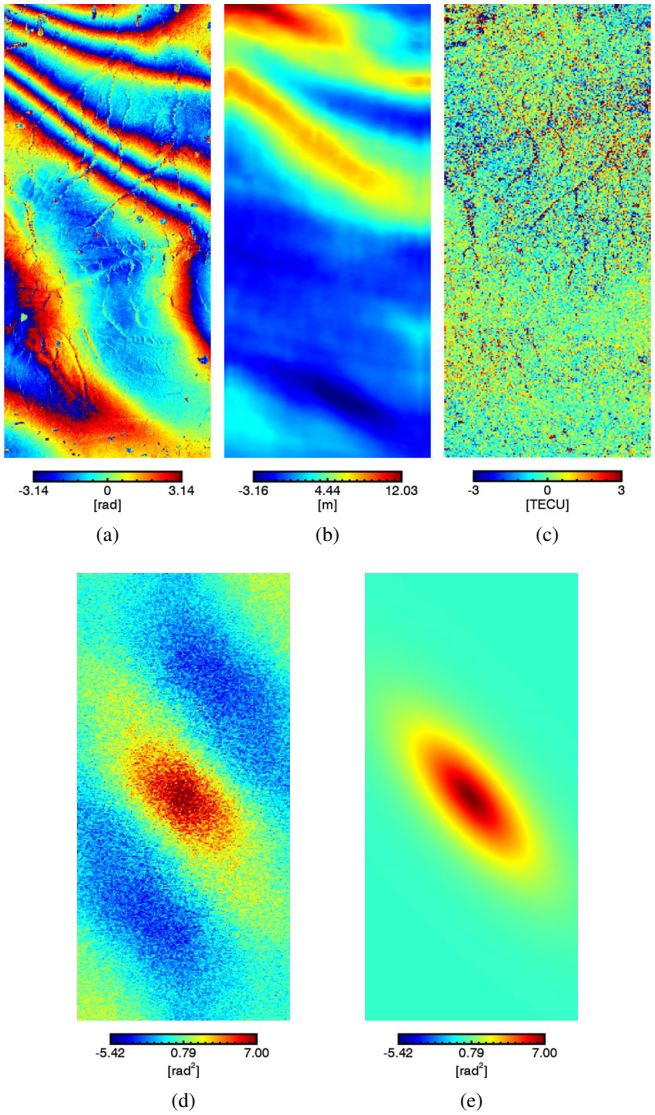

Fig. 2. Auroral ionospheric variations produce phase slopes, visible in the (a) interferogram, and (b) azimuth shifts. (c) Detrended raw estimates of the ionospheric phase screen obtained with the split-spectrum method. (d) Sample covariance of the detrended raw estimates. (e) Fitted model covariance. Azimuth length (vertical axis) is 66 km, range length is 28 km.

The detrended raw estimates of the split-spectrum method are shown in Fig. 2(c). The estimated covariance of the fluctuations, shown in Fig. 2(d), is fitted with a Matérn covariance function, shown in Fig. 2(e), to characterize the ionosphere turbulent part. Range, and azimuth variations of the measured covariance are plotted in black in Fig. 3(a) and 3(b). Alternatively, range and azimuth power spectral density of the residuals is plotted in Fig. 3(c) and (d). Two regimes can be clearly seen: at longer wavelengths the decreasing linear slope indicates a power law with outer scale distribution of phase irregularities, at shorter wavelengths the power density becomes flat due to the white estimation noise, masking small-scale ionospheric variations. The horizontal line is the mean split-spectrum method accuracy. The red line in Fig. 3 represents the fitted power law with outer scale model, and

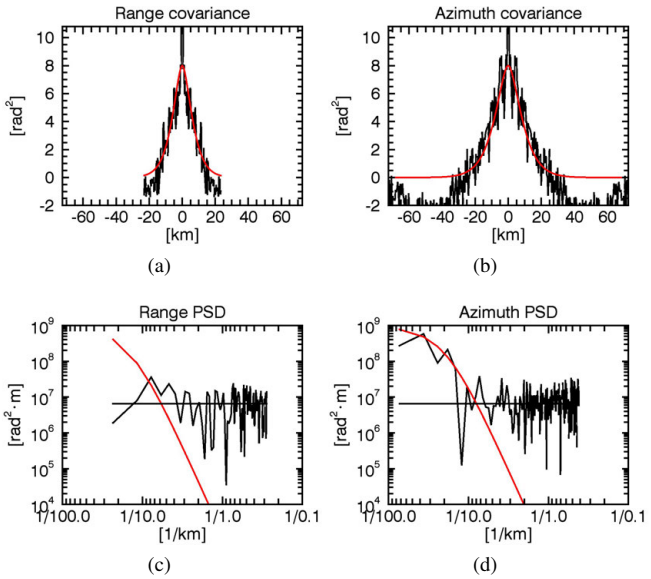

Fig. 3. Covariance (top) and power spectral density (bottom) of the detrended split-spectrum raw estimates. On the left is the range axis, and on the right the azimuth one. The red lines are the fitted turbulence model. The horizontal line in the power spectra is the theoretical mean split-spectrum method accuracy derived from the coherence.

the Matérn covariance function. The latter is used to fill the model covariance matrix of the inverse problem, regulating the smoothness of the inversion result. The estimated covariance and noise levels are also used to automatically determine the data downsampling factors. The negative covariance, which deviates from the Matérn model, is probably due to the presence of variations which does not present a turbulence regime, at least not within the size of the image.

The previous split-spectrum method results are shown for comparison in Fig. 4(a) and (b). The estimated ionospheric phase screen is in Fig. 4(a). The residual small-scale variations, which the split-spectrum method did not measure, alter the compensated interferogram, visible in Fig. 4(b). The result of the combined split-spectrum method and azimuth shifts is presented in Fig. 4(c). This ionospheric phase screen is smoother, and more similar to the original interferogram. The small-scale variations have been removed, as it can be seen from the compensated interferogram in Fig. 4(d).

B. Amazon Plasma Bubbles Test Case

Scintillation is the term given to amplitude, phase, polarization, and angle of arrival fluctuations of a radio signal. Scintillation effects are caused by randomly irregular electron density variations present along the radio wave propagation path. Plasma bubbles form after sunset in the equatorial area when the ionization of the atmosphere stops. The ions recombine, forming a lower density layer. This layer can rise through the more ionized layers above creating plasma bubbles. These structures are turbulent with irregular edges in the east-west direction, with scale sizes spanning from a few meters to a few kilometers, but extend along the magnetic field lines for hundreds of kilometers in a rod-like shape [43].

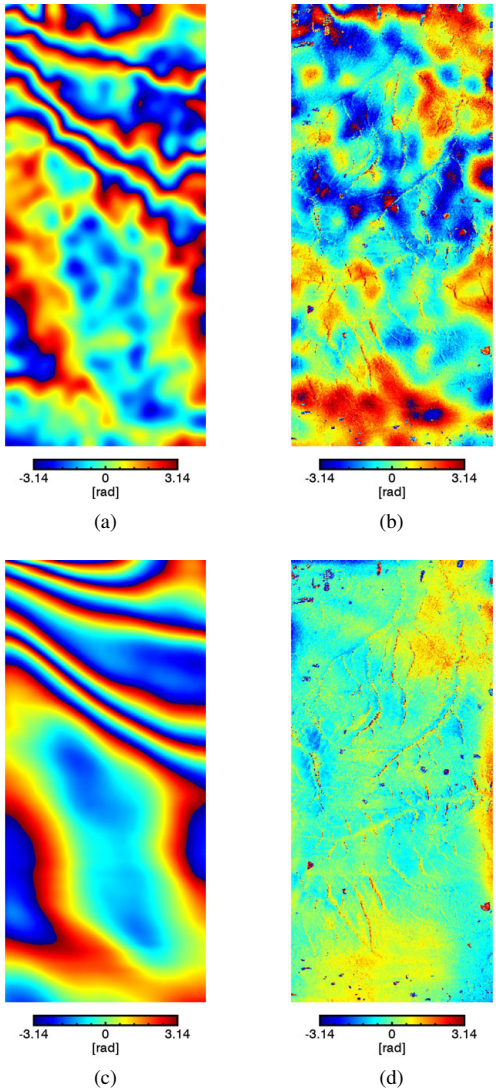

Fig. 4. On the left, the ionospheric phase screens, estimated with the split-spectrum method (top) and inverse problem (bottom). On the right, the respective compensated interferograms.

Plasma bubbles can produce fluctuations in the SAR image intensity and phase, originating ionospheric stripelike artifacts also called scintillation effects [2], [37]–[39], [48]–[50].

In this example, we use ascending ALOS PALSAR images acquired at around 10 PM local time over the Amazon region which present strong amplitude stripes. The interferogram of Fig. 5(a) shows a 600-km-long portion of the track, which also includes the images used in this example. The large-scale variation along azimuth has been successfully removed by the split-spectrum method, as it can be seen in Fig. 5(b). On the contrary, the turbulent range fluctuations which are due to the plasma bubbles cannot be measured by this method. The interferogram used in this example, corresponding to the bottom frame in the presented portion of the track, is shown again in Fig. 6(a). The slight orientation of the plasma bubbles with respect to the along track direction allows the fluctuations to also affect the SAR impulse response producing azimuth

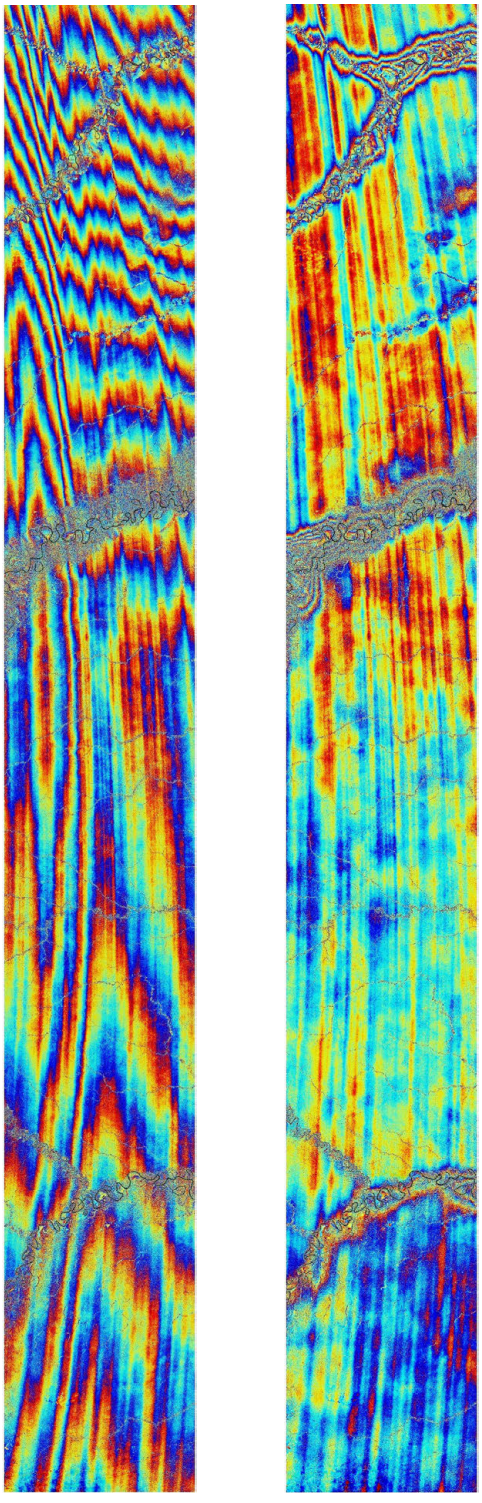

Fig. 5. (a) Interferogram over the Amazon region realized with 12 ALOS PALSAR image pairs. Plasma bubbles produces the turbulent variations in the range direction, a large-scale trend is responsible for the fringes in the azimuth direction (vertical axis). (b) Same interferogram compensated with the split-spectrum method, the large-scale variation has been removed whereas the turbulence is still present.

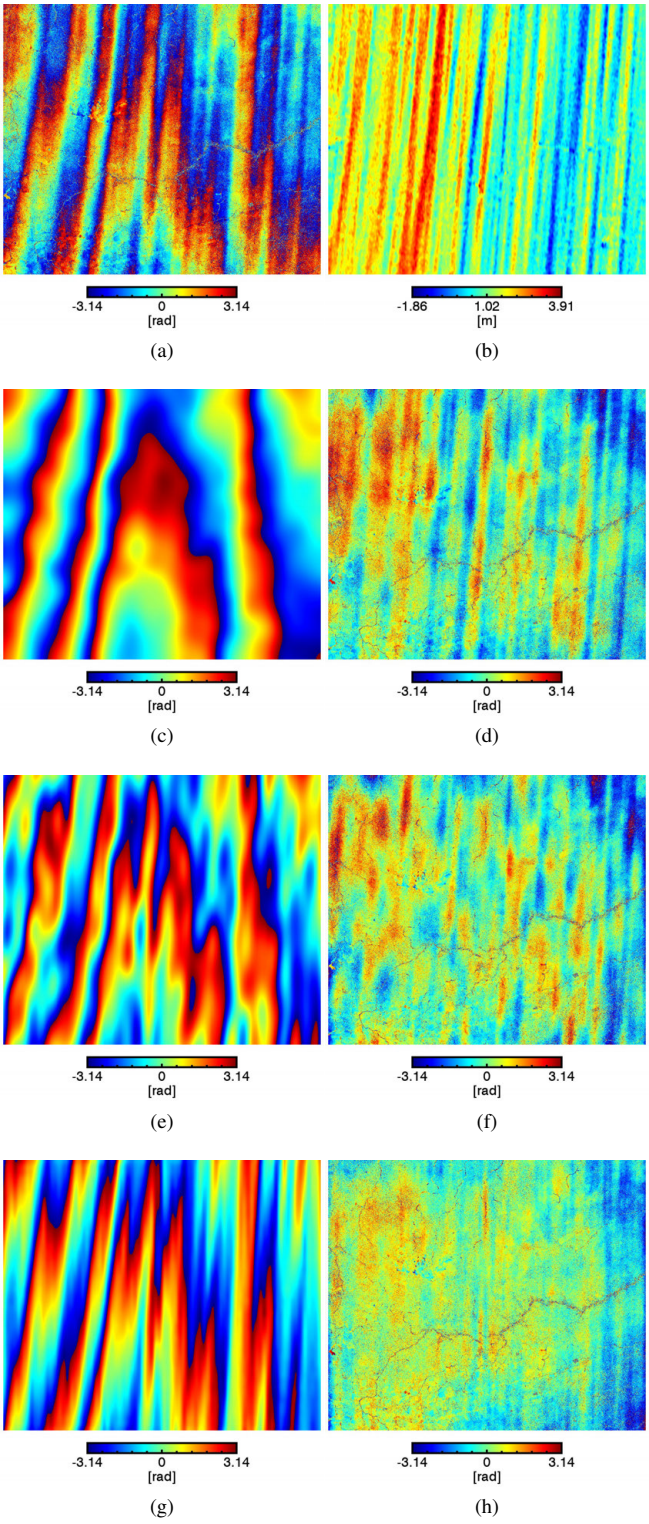

Fig. 6. (a) Interferogram of the scintillation test case, rapid range phase variations are due to the turbulent ionospheric state. (b) Azimuth shifts, measured with patch-based cross-correlation. Azimuth length is 59 km, ground range length is 66 km.

shifts. Fig. 6(b) shows the azimuth shifts, measured with patch-based cross correlation.

The split-spectrum method estimated ionospheric phase screen, and compensated interferogram, are presented respectively in Fig. 6(c), and (d). Here the estimates are filtered with an isotropic Gaussian window as in [20]. Fig. 6(e) and (f) shows respectively the phase screen and the compensated interferogram when applying the inverse problem method, but only to the split-spectrum data and not the azimuth shifts. This way, the inverse problem is used as an adapted anisotropic filter for the split-spectrum data. The result considerably improves when also the azimuth shifts are included, as it can be seen in Fig. 6(g) and 6(h).

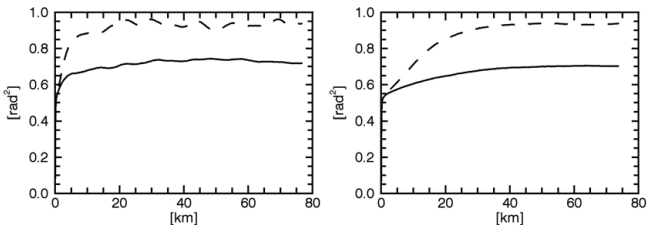

Fig. 7. (a) Range and (b) azimuth variogram of the compensated interferogram, using the split-spectrum method (dashed line) and the combined method (solid line).

The range and azimuth variogram of the compensated interferogram are reported in Fig. 7. The dashed line represent the split-spectrum method, the solid line the combination. It can be seen that the inverse problem result compensation reduces the variance of the compensated interferogram.

V. Conclusion

Information about the ionosphere can be extracted in various ways from SAR data. To improve the ionosphere estimation accuracy, the combination of different information sources has been suggested several times, and some attempts to implement it have been made. In this paper, a new method that combines data from various information sources using Bayesian inversion has been developed. To avoid arbitrary smoothing windows, it uses a data-based fractal model of turbulent ionospheric variations, leading to an adaptive anisotropic filtering. Large-scale ground displacements can as well be measured without biases by avoiding arbitrary trend removal from the interferometric phase, thus elevating InSAR methods to be a real alternative to GNSS measurements for large-scale deformation monitoring. The proposed concept also lays the basis for future developments such as estimation of the absolute ionosphere and along-track ground motion.

The combination of the split-spectrum method with ionosphere-induced mutual azimuth shifts has been tested. Azimuth shifts, being sensitive to local along-track gradients of the ionospheric electron density, can complement and improve the split-spectrum method, which estimates range and azimuth variations over long distances but lacks on precision on the small-scale range. The limit of this combination is the assumption of no azimuth ground motion. The extension to other data and methods could remove this limitation and further increase the accuracy. Faraday rotation measurements, for example, could be readily included if quad-polarized data

should be available. This work is also a first step towards the estimation of along-track ground motion in the presence of ionospheric disturbances, which requires an extremely precise reconstruction of the ionospheric phase screen, only reachable with the combination of various methods.

Two application examples were presented, one based on an aurora event and the second on equatorial scintillation. The combined results show how the proposed method improved the estimation and correction of the ionospheric phase screen, with respect to the single split-spectrum method. However, a thorough testing of various ground and ionospheric states is still necessary to evaluate the possible systematic use of the method in an operational processor.

APPENDIX A
SPLIT-SPECTRUM VERSUS FARADAY ROTATION METHODS PRECISION

The precision of the split-spectrum method is [20]:

$$\sigma_{\Delta\phi_{iono}} = \frac{3f_0}{4B}\sqrt{\frac{3}{N}}\frac{\sqrt{1-\gamma^2}}{\gamma}, \tag{22}$$

where f_0 is the carrier frequency, B is the full-band image bandwidth, N is the number of averaged samples, and γ is the interferometric covariance. The precision of the ionospheric phase derived from Faraday rotation angles, measured with the Bickel & Bates estimator, is [33]:

$$\sigma_{\Delta\phi_{iono}} = \frac{4\pi m f_0^2}{e\boldsymbol{B}\cdot\hat{\boldsymbol{\kappa}}}\sigma_{\Delta\Omega} \approx \frac{4\pi m f_0^2}{e\boldsymbol{B}\cdot\hat{\boldsymbol{\kappa}}}\frac{1}{4\sqrt{2N}}\frac{\sqrt{1-\gamma_P^2}}{\gamma_P}, \tag{23}$$

where $\Delta\Omega$ is the Faraday rotation angle, m is the electron mass, e the electron charge, $\boldsymbol{B}$ the magnetic field vector, $\hat{\boldsymbol{\kappa}}$ the propagation versor, and γ_P the polarimetric coherence. In [33], it is reported that the fraction in (23) ranges from about 2269, in polar regions, to 21024, in equatorial regions at about $\pm 5^\circ$ from the magnetic equator. At P-band this proportionality factor goes from 777 to 7200.

To compare the standard deviation of the two methods we assume an interferometric coherence of 0.5, a polarimetric coherence of 0.95, and equal number of averaged samples. For an L-band system with 14 MHz bandwidth, the Faraday rotation method standard deviation is, in polar regions, 1.5 times lower than the split-spectrum method's one, it becomes higher than the latter at about 40° latitude, and diverges at the magnetic equator. When the bandwidth is 28 MHz, the split-spectrum method is 1.3 to 12 times better than the Faraday rotation, respectively in polar and equatorial regions (at about $\pm 5^\circ$ from the magnetic equator). For the BIOMASS satellite, with 6 MHz bandwidth and carrier frequency at 435 MHz, the Faraday rotation method is, in polar regions, 3.6 times better than the split-spectrum method, they become similar at about 20° latitude from the magnetic equator, and the split-spectrum is then in equatorial regions 2.5 times better.

APPENDIX B
ANISOTROPIC POWER LOW AND MATÉRN FUNCTIONS

The Matérn function,

$$R(\boldsymbol{r}) = \frac{2^{3/2-\nu}}{\Gamma(\nu-1/2)}(k_0 r)^{\nu-1/2}K_{\nu-1/2}(k_0 r), \tag{24}$$

where $r^2 = r_x^2 + r_y^2$ (r_x and r_y are variables on two orthogonal axis) is circularly symmetrical. Its 2-D Fourier transform is the power law with outer scale function:

$$\Phi(\boldsymbol{k}) = \frac{\Gamma(\nu+1/2)}{\Gamma(\nu-1/2)}\frac{4\pi k_0^{2\nu-1}}{\left(k^2+k_0^2\right)^{\nu+1/2}}, \tag{25}$$

where $k^2 = k_x^2 + k_y^2$, with k_x and k_y being respectively the wavenumber associated with the variables r_x and r_y [51].

To add anisotropy we rotate the wavenumber domain by the angle α, and scale its axis by the ratios a and b. This yields the new term k, also used in (9):

$$\begin{aligned} k^2 &= \left(ak_x\cos\alpha + ak_y\sin\alpha\right)^2 + \left(-bk_x\sin\alpha + bk_y\cos\alpha\right)^2 \\ &= Ak_x^2 + Bk_xk_y + Ck_y^2, \end{aligned} \tag{26}$$

where

$$\begin{aligned} A &= a^2\cos^2(\alpha) + b^2\sin^2(\alpha), \\ B &= 2\cos^2(\alpha)\sin^2(\alpha)(a^2-b^2), \\ C &= a^2\sin^2(\alpha) + b^2\cos^2(\alpha). \end{aligned} \tag{27}$$

Consequently, the spatial domain is also scaled and rotated. With the scaling properties of the Fourier transform we obtain:

$$\begin{aligned} r^2 &= \left(\frac{x}{a}\cos\alpha + \frac{y}{a}\sin\alpha\right)^2 + \left(-\frac{x}{b}\sin\alpha + \frac{y}{b}\cos\alpha\right)^2 \\ &= \frac{Cr_x^2 - Br_xr_y + Ar_y^2}{AC - B^2/4}, \end{aligned} \tag{28}$$

which is used in (8). The axis scaling also changes the covariance function magnitude, which is divided by ab. The latter can be written as:

$$ab = \sqrt{AC - B^2/4} = 1/G. \tag{29}$$

To normalize the covariance (8), the factor G is moved to the power spectrum (9).

ACKNOWLEDGMENT

The authors would like to thank the anonymous reviewers, who offered suggestions that helped to improve the paper. The PALSAR data used in this study were provided by the Japanese Aerospace Exploration Agency under the ALOS RA-4 proposal PI1118.

REFERENCES

[1] F. Meyer, R. Bamler, N. Jakowski, and T. Fritz, "The Potential of Low-Frequency SAR Systems for Mapping Ionospheric TEC Distributions," *Geoscience and Remote Sensing Letters, IEEE*, vol. 3, no. 4, pp. 560–564, Oct 2006.

[2] D. Belcher, "Theoretical limits on SAR imposed by the ionosphere," *Radar, Sonar Navigation, IET*, vol. 2, no. 6, pp. 435–448, December 2008.

[3] F. Meyer, "A review of ionospheric effects in low-frequency SAR — Signals, correction methods, and performance requirements," in *Geoscience and Remote Sensing Symposium (IGARSS), 2010 IEEE International*, July 2010, pp. 29–32.

[4] U. Wegmüller, C. Werner, T. Strozzi, and A. Wiesmann, "Ionospheric Electron Concentration Effects on SAR and INSAR," in *2006 IEEE International Symposium on Geoscience and Remote Sensing*, July 2006, pp. 3731–3734.

[5] W. B. Gail, "Effect of Faraday rotation on polarimetric SAR," *IEEE transactions on aerospace and electronic systems*, vol. 34, no. 1, pp. 301–307, 1998.

[6] E. J. Rignot, "Effect of Faraday rotation on L-band interferometric and polarimetric synthetic-aperture radar data," *IEEE Transactions on Geoscience and Remote Sensing*, vol. 38, no. 1, pp. 383–390, 2000.

[7] P. A. Wright, S. Quegan, N. S. Wheadon, and C. D. Hall, "Faraday rotation effects on L-band spaceborne SAR data," *IEEE Transactions on Geoscience and Remote Sensing*, vol. 41, no. 12, pp. 2735–2744, 2003.

[8] A. Freeman and S. Saatchi, "On the detection of Faraday rotation in linearly polarized L-band SAR backscatter signatures," *Geoscience and Remote Sensing, IEEE Transactions on*, vol. 42, no. 8, pp. 1607–1616, Aug 2004.

[9] A. Freeman, "Calibration of linearly polarized polarimetric SAR data subject to Faraday rotation," *Geoscience and Remote Sensing, IEEE Transactions on*, vol. 42, no. 8, pp. 1617–1624, Aug 2004.

[10] R.-Y. Qi and Y.-Q. Jin, "Analysis of the effects of faraday rotation on spaceborne polarimetric sar observations at-band," *IEEE transactions on geoscience and remote sensing*, vol. 45, no. 5, pp. 1115–1122, 2007.

[11] F. Meyer and J. Nicoll, "Prediction, Detection, and Correction of Faraday Rotation in Full-Polarimetric L-Band SAR Data," *Geoscience and Remote Sensing, IEEE Transactions on*, vol. 46, no. 10, pp. 3076–3086, Oct 2008.

[12] J. B. Nicoll and F. J. Meyer, "Mapping the ionosphere using L-band SAR data," in *IGARSS 2008-2008 IEEE International Geoscience and Remote Sensing Symposium*, vol. 2. IEEE, 2008, pp. II–537.

[13] F. J. Meyer, J. Nicoll, and B. Bristow, "Mapping aurora activity with SAR - A case study," in *2009 IEEE International Geoscience and Remote Sensing Symposium*, vol. 4. IEEE, 2009, pp. IV–1.

[14] J. S. Kim and K. P. Papathanassiou, "Faraday rotation estimation performance analysis," *EUSAR 2010*, 2010.

[15] X. Pi, A. Freeman, B. Chapman, P. Rosen, and Z. Li, "Imaging ionospheric inhomogeneities using spaceborne synthetic aperture radar," *Journal of Geophysical Research: Space Physics*, vol. 116, no. A4, 2011.

[16] J. S. Kim, K. P. Papathanassiou, S. Quegan, and N. Rogers, "Estimation and correction of scintillation effects on spaceborne P-band SAR images," in *2012 IEEE International Geoscience and Remote Sensing Symposium*. IEEE, 2012, pp. 5101–5104.

[17] R. Brcic, A. Parizzi, M. Eineder, R. Bamler, and F. Meyer, "Estimation and compensation of ionospheric delay for SAR interferometry," in *Geoscience and Remote Sensing Symposium (IGARSS), 2010 IEEE International*, July 2010, pp. 2908–2911.

[18] P. Rosen, S. Hensley, and C. Chen, "Measurement and mitigation of the ionosphere in L-band Interferometric SAR data," in *Radar Conference, 2010 IEEE*, May 2010, pp. 1459–1463.

[19] R. Brcic, A. Parizzi, M. Eineder, R. Bamler, and F. Meyer, "Ionospheric effects in SAR interferometry: An analysis and comparison of methods for their estimation," in *Geoscience and Remote Sensing Symposium (IGARSS), 2011 IEEE International*, July 2011, pp. 1497–1500.

[20] G. Gomba, A. Parizzi, F. De Zan, M. Eineder, and R. Bamler, "Toward Operational Compensation of Ionospheric Effects in SAR Interferograms: The Split-Spectrum Method," *IEEE Transactions on Geoscience and Remote Sensing*, vol. 54, no. 3, pp. 1446–1461, March 2016.

[21] D. Raucoules and M. de Michele, "Assessing Ionospheric Influence on L-Band SAR Data: Implications on Coseismic Displacement Measurements of the 2008 Sichuan Earthquake," *IEEE Geoscience and Remote Sensing Letters*, vol. 7, no. 2, pp. 286–290, April 2010.

[22] J. S. Kim, A. Danklmayer, and K. Papathanassiou, "Correction of ionospheric distortions in low frequency interferometric SAR data," in *Geoscience and Remote Sensing Symposium (IGARSS), 2011 IEEE International*, July 2011, pp. 1505–1508.

[23] U. Wegmüller, T. Strozzi, and C. Werner, "Ionospheric path delay estimation using split-beam interferometry," in *2012 IEEE International Geoscience and Remote Sensing Symposium*, July 2012, pp. 3631–3634.

[24] J. Hu, Z. Li, L. Zhang, X. Ding, J. Zhu, Q. Sun, and W. Ding, "Correcting ionospheric effects and monitoring two-dimensional displacement fields with multiple-aperture InSAR technology with application to the Yushu earthquake," *Science China Earth Sciences*, vol. 55, no. 12, pp. 1961–1971, 2012.

[25] H. S. Jung, D. T. Lee, Z. Lu, and J. S. Won, "Ionospheric Correction of SAR Interferograms by Multiple-Aperture Interferometry," *IEEE Transactions on Geoscience and Remote Sensing*, vol. 51, no. 5, pp. 3191–3199, May 2013.

[26] A. C. Chen and H. A. Zebker, "Reducing Ionospheric Effects in InSAR Data Using Accurate Coregistration," *IEEE Transactions on Geoscience and Remote Sensing*, vol. 52, no. 1, pp. 60–70, Jan 2014.

[27] Z. Liu, H. S. Jung, and Z. Lu, "Joint Correction of Ionosphere Noise and Orbital Error in L-Band SAR Interferometry of Interseismic Deformation in Southern California," *IEEE Transactions on Geoscience and Remote Sensing*, vol. 52, no. 6, pp. 3421–3427, June 2014.

[28] J. S. Kim, K. P. Papathanassiou, R. Scheiber, and S. Quegan, "Correcting Distortion of Polarimetric SAR Data Induced by Ionospheric Scintillation," *IEEE Transactions on Geoscience and Remote Sensing*, vol. 53, no. 12, pp. 6319–6335, Dec 2015.

[29] H. S. Jung and W. J. Lee, "An Improvement of Ionospheric Phase Correction by Multiple-Aperture Interferometry," *IEEE Transactions on Geoscience and Remote Sensing*, vol. 53, no. 9, pp. 4952–4960, Sept 2015.

[30] B. Zhang, X. Ding, W. Zhu, C. Wang, L. Zhang, and Z. Liu, "Mitigating Ionospheric Artifacts in Coseismic Interferogram Based on Offset Field Derived From ALOS-PALSAR Data," *IEEE Journal of Selected Topics in Applied Earth Observations and Remote Sensing*, vol. PP, no. 99, pp. 1–10, 2016.

[31] F. J. Meyer, K. Papathanassiou, J. S. Kim, X. Pi, A. Freeman, K. Chotoo, K. Groves, and E. Jones, "Ionosar - collaborative research towards understanding and mitigating ionospheric effects in SAR," in *2012 IEEE International Geoscience and Remote Sensing Symposium*, July 2012, pp. 6039–6042.

[32] N. Wiener, *Extrapolation, Interpolation, and Smoothing of Stationary Time Series*. The MIT Press, 1964.

[33] J. Kim, "Development of Ionosphere Estimation Techniques for the Correction of SAR Data," Ph.D. dissertation, ETH Zürich, 2013.

[34] S. Kay, *Fundamentals of Statistical Signal Processing: Estimation theory*, ser. Fundamentals of Statistical Signal Processing. Prentice-Hall PTR, 1993.

[35] C. Rino, *The theory of scintillation with applications in remote sensing*. John Wiley & Sons, 2011.

[36] ——, "A power law phase screen model for ionospheric scintillation: 1. Weak scatter," *Radio Science*, vol. 14, no. 6, pp. 1135–1145, 1979.

[37] C. S. Carrano, K. M. Groves, and R. G. Caton, "Simulating the impacts of ionospheric scintillation on L band SAR image formation," *Radio Science*, vol. 47, no. 4, 2012.

[38] N. C. Rogers, S. Quegan, J. S. Kim, and K. P. Papathanassiou, "Impacts of Ionospheric Scintillation on the BIOMASS P-Band Satellite SAR," *IEEE Transactions on Geoscience and Remote Sensing*, vol. 52, no. 3, pp. 1856–1868, March 2014.

[39] F. J. Meyer, K. Chotoo, S. D. Chotoo, B. D. Huxtable, and C. S. Carrano, "The Influence of Equatorial Scintillation on L-Band SAR Image Quality and Phase," *IEEE Transactions on Geoscience and Remote Sensing*, vol. 54, no. 2, pp. 869–880, Feb 2016.

[40] C. Rino and E. Fremouw, "The angle dependence of singly scattered wavefields," *Journal of Atmospheric and Terrestrial Physics*, vol. 39, no. 8, pp. 859–868, 1977.

[41] P. Guttorp and T. Gneiting, "Studies in the history of probability and statistics XLIX On the Matérn correlation family," *Biometrika*, vol. 93, no. 4, pp. 989–995, 2006.

[42] S. Knospe and S. Jonsson, "Covariance Estimation for dInSAR Surface Deformation Measurements in the Presence of Anisotropic Atmospheric Noise," *IEEE Transactions on Geoscience and Remote Sensing*, vol. 48, no. 4, pp. 2057–2065, April 2010.

[43] K. Davies, *Ionospheric Radio*. IET, 1990.

[44] J. S. Kim and K. Papathanassiou, "On the separation of Dynamic Scattering and Ionospheric Effects in SAR data," in *ESA POLinSAR Workshop*, 2015.

[45] S. Tebaldini, A. M. Guarnieri, and F. Rocca, "Recovering time and space varying phase screens through SAR multi-squint differential interferometry," in *Synthetic Aperture Radar, 2012. EUSAR. 9th European Conference on*, April 2012, pp. 16–19.

[46] G. Gomba, M. Eineder, A. Parizzi, and R. Bamler, "High-resolution estimation of ionospheric phase screens through semi-focusing processing," in *2014 IEEE International Geoscience and Remote Sensing Symposium (IGARSS)*, July 2014, pp. 17–20.

[47] G. Gomba and F. De Zan, "Estimation of ionospheric height variations during an aurora event using multiple semi-focusing levels," in *2015 IEEE International Geoscience and Remote Sensing Symposium (IGARSS)*, July 2015, pp. 4065–4068.

[48] M. Shimada, Y. Muraki, and Y. Otsuka, "Discovery of anoumoulous stripes over the Amazon by the PALSAR onboard ALOS satellite," in *IGARSS 2008-2008 IEEE International Geoscience and Remote Sensing Symposium*, 2008.

[49] P. Bernhardt, T. Ainsworth, K. Groves, T. Beach, R. G. Caton, C. S. Carrano, C. M. Alcala, and D. D. Sponseller, "Detection of ionospheric structures with L-band synthetic aperture radars," in *IGARSS 2008-2008 IEEE International Geoscience and Remote Sensing Symposium*, vol. 2. IEEE, 2008, pp. II–395.

[50] D. P. Belcher and P. S. Cannon, "Amplitude scintillation effects on SAR," *IET Radar, Sonar & Navigation*, vol. 8, no. 6, pp. 658–666, 2014.
[51] C. E. Rasmussen, *Gaussian processes for machine learning*. The MIT press, 2006.

D

Gomba, G., Eineder, M., Parizzi, A., and Bamler, R. (2014). High-resolution estimation of ionospheric phase screens through semi-focusing processing. 2014 IEEE International Geoscience and Remote Sensing Symposium (IGARSS)

HIGH-RESOLUTION ESTIMATION OF IONOSPHERIC PHASE SCREENS THROUGH SEMI-FOCUSING PROCESSING

Giorgio Gomba, Michael Eineder, Alessandro Parizzi and Richard Bamler

Remote Sensing Technology Institute, German Aerospace Center (DLR), Wessling, Germany

ABSTRACT

Ionosphere irregularities along the synthetic aperture generate shifts and blurring that cause decorrelation. In this paper it is shown how, by partially focusing SAR images to the height of the ionosphere, it is possible to reduce the ionospheric azimuth effects and increase the coherence. This permits, even in case of turbulent ionosphere, to obtain better accuracies when separating the deformations phase from the ionospheric phase using the delta-k split-band interferometry method.

Index Terms— InSAR, SAR ionospheric effects, ionosphere estimation, ionosphere scintillation

1. INTRODUCTION

L-band remote sensing systems, like the future Tandem-L mission ([1]), are disrupted by the ionized upper part of the atmosphere called ionosphere. Ionospheric effects have to be estimated and corrected in order to fulfill the scientific requirements of the mission ([2]). This work concentrates on the effects that a ionosphere, which is unstable in the flight path direction, has on SAR images and interferograms. We then demonstrate a technique to eliminate these effects and produce high-resolution ionosphere estimates.

The ionosphere is a region of the upper atmosphere composed by gases that are ionized by the solar radiation. For this study we approximate the ionosphere by a thin layer at the altitude H_i of the peak of its vertical profile. The effects of the ionosphere on a SAR image are:

- phase advance and range delay,
- range defocus,
- azimuth shift,
- azimuth defocus.

Azimuth defocus happens in particular when the correlation length of the ionospheric variations along the flight path of the satellite is shorter than the synthetic aperture length. Ionospheric variations change the impulse response function lowering the coherence and thus the interferogram accuracy.

A method to reduce the effects of an unstable ionosphere, called multi-squint interferometry, is presented in [3], however, the resolution inside the ionosphere is limited by the system parameters and geometry. In [4], it is suggested to defocus SAR images to the ionospheric height prior to apply Faraday rotation estimation for measuring the ionosphere, to reduce the effects that ionosphere has on the impulse response function. In this work we demonstrate how, by partially focusing the images, it is actually possible to cancel or reduce the azimuth effects. The coherence is then increased and the estimation of the ionospheric and topographic phase becomes more accurate.

2. IONOSPHERE IN INTERFEROGRAMS

We neglect the range dimension to simplify the analysis. The geometry is represented in Figure 2 where $\psi(x)$ is the ionospheric phase screen, H is the height of the satellite orbit, H_i is the single layer model height, x is the ground coordinate and η the orbit coordinate.

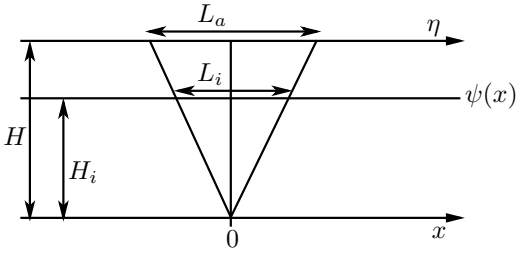

Fig. 1. System geometry, x is the ground coordinate and η is the satellite position. The ionosphere is modeled as a single layer so that $\psi(x)$ is the ionospheric phase screen.

When a single scatter is located in $x = 0$ an azimuth line of raw data collected by the satellite at the orbit position η can be written as

$$s_r(\eta) = a_0 e^{j\alpha_0} \operatorname{rect}\left(\frac{\eta}{L_a}\right) e^{j\pi K \eta^2} e^{j\psi\left(\eta \frac{H_i}{H}\right)}, \qquad (1)$$

where a_0 is the scatter reflectivity, L_a is the aperture length, $K = 2/\lambda R_0$ the azimuth chirp rate and $\psi(x)$ the ionospheric phase screen. The standard azimuth focusing is a convolution

with the conjugated chirp:

$$s_f(\eta) = \int s_r(u)\ \mathrm{rect}\left(\frac{\eta-u}{L_a}\right) e^{-j\pi K(\eta-u)^2}\, du$$
$$= \int\ \mathrm{rect}\left(\frac{u}{L_a}\right)\ \mathrm{rect}\left(\frac{t-u}{L_a}\right) e^{j\psi\left(u\frac{H_i}{H}\right)} e^{-j2\pi K\eta u}\, du. \tag{2}$$

We notice that if the ionosphere remains stable for $-L_i/2 < \eta < L_i/2$, where L_i is $L_a \cdot H_i/H$, the ionospheric term can be brought outside the integral. This suggests us to rewrite the ionosphere as: $\psi(\eta) = \psi_m + \psi_d \cdot \eta + (\psi(\eta) - \psi_m - \psi_d \cdot \eta) = \psi_m + \psi_d \cdot \eta + \psi_r(\eta)$, where ψ_m is the average value of the ionosphere inside the aperture length projected at the ionosphere height L_i and ψ_d is the average derivative of the ionosphere:

$$\psi_m = \frac{1}{L_i}\int\ \mathrm{rect}\left(\frac{\eta}{L_i}\right)\psi(\eta)\, d\eta,$$
$$\psi_d = \frac{1}{L_i}\int\ \mathrm{rect}\left(\frac{\eta}{L_i}\right)\left.\frac{d\psi(\eta')}{d\eta'}\right|_{\eta'=\eta} d\eta. \tag{3}$$

If $\psi_r(\eta)$ can be assumed negligible, Equation (2) becomes

$$s_f(\eta) = a_0 e^{j\alpha_0}\, e^{j\psi_m}\ \mathrm{sinc}\left(KL_a\left(\eta - \frac{KH_i}{f_0^2\cos(\theta_{inc})}\psi_d\right)\right), \tag{4}$$

while, if $\psi_r(\eta)$ becomes relevant the sinc function is blurred and the interferometric coherence drops. An accurate coregistration can corrects the shifts due to ψ_d, which also lower the coherence. If the ionosphere derivative is highly variable, however, it is possible that the shifts are not well estimated. Equation (4) shows how ψ_m is the phase measured by an interferogram, the average of the ionosphere contained in the aperture. The target shift along azimuth gives an estimate of the average derivative of the ionosphere inside the aperture. In conclusion, a standard interferogram only shows the azimuth filtered low-pass portion of the ionosphere, while the high-pass portion lower the interferogram quality.

3. PARTIAL FOCUSING

In this section we derive the result of a partial focusing and demonstrate how it can expose the ionospheric phase screen and cancel the azimuth effects. Cosider the raw data acquisition as:

$$s_r(\eta) = \int a(x)e^{j\alpha(x)}\cdot$$
$$\mathrm{rect}\left(\frac{\eta-x}{L_a}\right) e^{j\pi K(\eta-x)^2} e^{j\psi\left(\eta\frac{H_i}{H}+x\frac{H-H_i}{H}\right)}\, dx, \tag{5}$$

where $a(x)e^{j\alpha(x)}$ is the ground reflectivity and phase, representing distributed scatterers. The focusing is performed using the following modified chirp:

$$h_{sf}(\eta) = \ \mathrm{rect}\left(\frac{\eta}{L_a}\right)\exp\left(-j\pi KC\eta^2\right), \tag{6}$$

where C is a constant. The semi-focused data are thus

$$s_{sf}(\eta) = \int s_r(u)h_{sf}(\eta-u)\, du$$
$$= e^{j\pi KC\eta^2}\int a(x)e^{j\pi Kx^2}\cdot$$
$$\int\ \mathrm{rect}\left(\frac{u}{L_a}\right)\ \mathrm{rect}\left(\frac{x-u}{L_a}\right) e^{j\phi(u)\eta}\, du\ \ dx, \tag{7}$$

where $\phi(u)$ is a phase term containing the chirp phase terms and the ionosphere:

$$\phi(u) = -\pi K(C-1)\frac{u^2}{\eta} - 2\pi Ku\frac{x}{\eta} +$$
$$2\pi KCu + \frac{1}{\eta}\psi\left(u\frac{H_i}{H} + x\frac{H-H_i}{H}\right). \tag{8}$$

Equation (7), which contains an integral of an oscillating phase term $\phi(u)$, can be solved using the stationary phase method. The stationary phase point u_0 can be found by searching the value of u for which the phase derivative $\phi'(u)$ is zero:

$$\phi'(u) = -2\pi K(C-1)\frac{u}{\eta} - 2\pi K\frac{x}{\eta} + 2\pi KC + \psi'(...)\frac{H_i}{\eta H}. \tag{9}$$

We assume that the derivative of the ionospheric phase term ψ' does not change the position of u_0 and that it can be neglected. By choosing C equal to $H/(H-H_i)$ Equation (7) becomes:

$$s_{sf}(\eta) \approx e^{j\pi KC\eta^2}\int a(x)e^{j\alpha(x)}e^{j\pi Kx^2}\cdot$$
$$\mathrm{rect}\left(\frac{\eta-x}{L_a\frac{C-1}{C}}\right) e^{j\phi(u_0)\eta}e^{j\frac{\pi}{4}}\, dx$$
$$= e^{j\psi(\eta)}e^{j\frac{\pi}{4}}\int a(x)e^{j\alpha(x)}\ \mathrm{rect}\left(\frac{\eta-x}{L_i}\right)\cdot$$
$$e^{j\pi K\frac{H}{H_i}(\eta-x)^2}\, dx. \tag{10}$$

The ionospheric phase screen $e^{j\psi(\eta)}$ is now superimposed to the semi-focused data without being low-pass filtered and without to interfere with the impulse response function. The resolution of the semi-focused azimuth line of Equation (10) depends on the length of the aperture, projected at the ionosphere height. The gain factor of the focusing process is reduced because of the just partial focusing. Since this is counterbalanced by the increment of the resolution cell, the coherence does not change. The achievable accuracy of coregistration by cross-correlation also depends on the resolution cell,

leading to a less precise coregistration accuracy measured in meters. Nevertheless, the coherence degradation due to miscoregistration is proportional to the resolution cell, therefore, since the accuracy measured in fractions of resolution cell is the same, we do not expect a loss of coherence. On the contrary, since the impulse response function is no more modified by the ionospheric phase, all azimuth effects are canceled, leading to an increase of the coherence. The more turbulent the ionosphere was, the bigger the increase is, therefore, the semi-focusing processing is only useful when the images are severely degraded by a turbulent ionosphere. Techniques like Delta-k or Phase-Group Delay Difference ([5]) can then be applied to separate the two components, topographic and ionospheric, of the interferometric phase and to obtain a high-resolution estimation of the ionosphere.

Semi-focused images are in a sort of opposite plane with respect to focused images. The topographic phase, in fact, results low-pass filtered in semi-focused images because of the resolution decrease, while, to the ionospheric phase happens the opposite. Moreover, azimuth variations of the topographic phase generate shifts in semi-focused images like azimuth variations of the ionospheric phase do to focused images. A variation of half a cycle or more, inside the same resolution cell, reduces the coherence of semi-focused to zero. Therefore, the topographic and/or deformation phase has to be removed prior to defocusing. If an a priori knowledge of the ground phase cannot be obtained, an azimuth split-band processing of the semi-focused images could be implemented to avoid the coherence loss.

4. NUMERICAL SIMULATIONS

Simulations are used to test the effects of a turbulent ionosphere on InSAR and to test the presented algorithm. A ray tracing simulator with the parameters of the proposed mission Tandem-L is used to produce raw data azimuth lines using distributed targets as ground scene model. The turbulent ionospheric phase screen used in the simulations are produced by filtering white Gaussian noise with the power spectral density function ([6]):

$$\Psi(f) = \frac{T}{(f_0^2 + f^2)^{p/2}}, \qquad (11)$$

where T is a scaling constant, f_0 is related to the outer scale length l_0 and p is the spectral index. Typical parameters of the model for different test cases, considering strong and weak scintillation levels, have been generated using the Global Ionospheric Scintillation Model (GISM). In Figure 2 is shown an example of a generated phase screen in case of severe scintillation.

In the following are presented the results of the simulation done using the phase of Figure 2. In Figure 3 can be seen the coherence of focused data, represented with a black line, which is quite low due the azimuth shifts and blurring. The red line represents the coherence after the coregistration step. Since ionospheric azimuth effects are absent in semi-focused images, the coherence (blu line in Figure 3) is fully recovered.

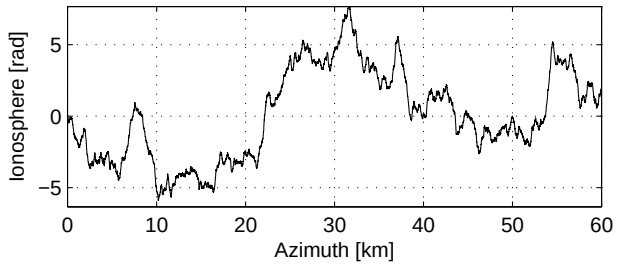

Fig. 2. Example of simulated ionospheric phase screen for strong scintillation condition.

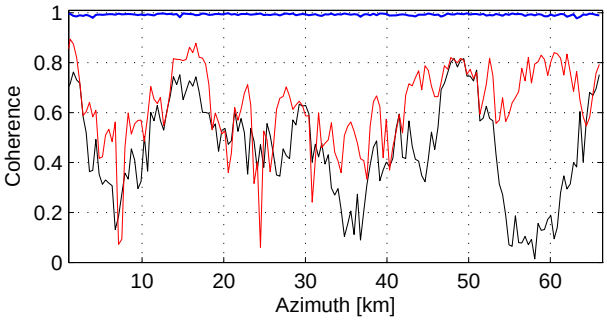

Fig. 3. Simulation example using the phase screen of Figure 2, in black the coherence of the focused data before coregistration and, in red, after coregistration. In blue the coherence of the semi-focused data.

Figure 4 shows the unwrapped interferogram from the focused and semi-focused data, along with the real and the low-pass filtered ionosphere. As expected, the interferogram is related to the low pass ionosphere, filtered by the aperture length. The interferogram from semi-focused, on the contrary, follows the true ionosphere.

5. REAL DATA EXAMPLE

A quad-pol PALSAR image pair is used to test the method on real data. The master image was acquired at 7:30 on April 1st 2007 and the slave on May 17th 2007. The coherence is quite low due to the vegetated terrain and due to a sudden change in the TEC level located in the top part of the image. The coherence, averaged along the range direction, is represented in black in Figure 5, while the coherence after the defocusing in blue. An improvement of the coherence can be seen in particular in areas where the ionosphere change was sudden and of high magnitude. This improvement is also visible comparing the two interferograms in Figure 6. The interferogram from semi-focused images, on the right, shows much more clearly

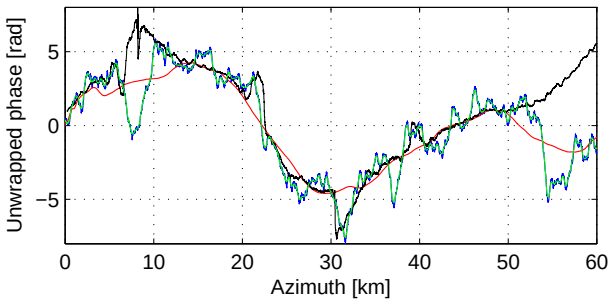

Fig. 4. Simulation example, interferogram of focused (black line) and semi-focused images (green line) along with ionosphere (blue line) and low-pass ionosphere (red line).

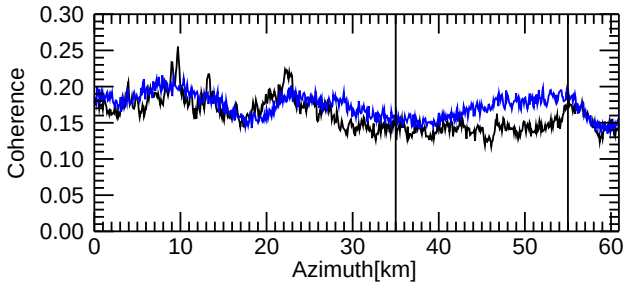

Fig. 5. Real data example. Black line: coherence of focused images pair. Blue line: coherence of semi-focused images. Inside the two vertical lines, the area where the ionosphere is steeper.

the fringes of the ionosphere steep slope.

6. CONCLUSION

The theoretical derivation of the semi-focusing technique, a simulation for a severe scintillation scenario and a real data example has been presented. It has been demonstrated that the semi-focusing can cancel azimuth effects and expose the true ionospheric phase screen. In case the images are disrupted by the electron density variations along the flight path, the semi-focusing is able to recover the coherence permitting a better estimation and removal of the ionosphere.

7. REFERENCES

[1] A. Moreira, G. Krieger, M. Younis, I. Hajnsek, K. Papathanassiou, M. Eineder, and F. De Zan, "Tandem-l: A mission proposal for monitoring dynamic earth processes," in *Geoscience and Remote Sensing Symposium (IGARSS), 2011 IEEE International*, july 2011, pp. 1385 –1388.

[2] M. Eineder, A. Friedrich, C. Minet, R. Bamler, F. Flerit, and I. Hajnsek, "Scientific requirements and feasibility on an l-band mission dedicated to measure surface deformation," in *Geoscience and Remote Sensing Symposium,2009 IEEE International,IGARSS 2009*, 2009, vol. 2, pp. II–789–II–792.

[3] S. Tebaldini, A. Monti Guarnieri, and F. Rocca, "Recovering time and space varying phase screens through sar multi-squint differential interferometry," in *Synthetic Aperture Radar, 2012. EUSAR. 9th European Conference on*, 2012, pp. 16–19.

[4] J.S. Kim, K.P. Papathanassiou, S. Quegan, and N. Rogers, "Estimation and correction of scintillation effects on spaceborne p-band sar images," in *Geoscience and Remote Sensing Symposium (IGARSS), 2012 IEEE International*, 2012, pp. 5101–5104.

[5] R. Brcic, A. Parizzi, M. Eineder, R. Bamler, and F. Meyer, "Estimation and compensation of ionospheric delay for sar interferometry," in *Geoscience and Remote Sensing Symposium (IGARSS), 2010 IEEE International*, 2010, pp. 2908–2911.

[6] C. L. Rino, "A power law phase screen model for ionospheric scintillation: 1. weak scatter," *Radio Science*, vol. 14, no. 6, pp. 1135–1145, 1979.

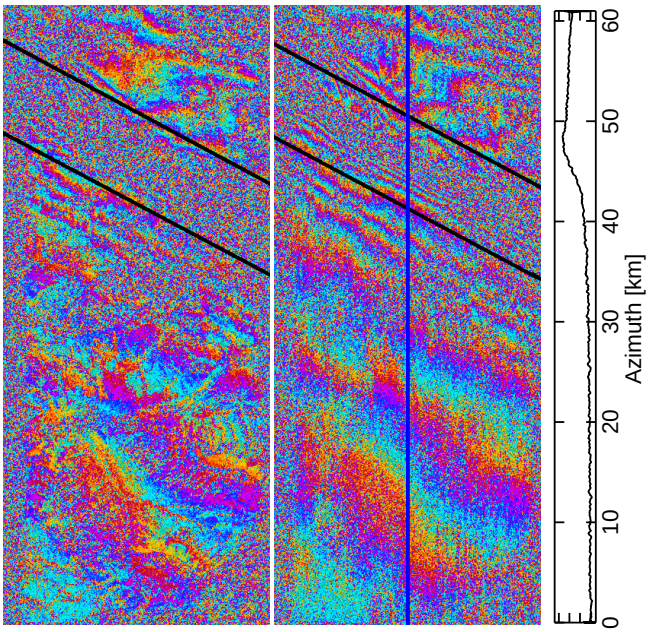

Fig. 6. Interferogram of focused images (left). Interferogram of semi-focused images (center). The black lines indicate the zone of the ionosphere TEC peak and steep slopes. On the right, the Faraday rotation calculated for the blue line zone, showing the ionosphere.

E

Gomba, G. and De Zan, F. (2015). Estimation of ionospheric height variations during an aurora event using multiple semi-focusing levels. 2015 IEEE International Geoscience and Remote Sensing Symposium (IGARSS)

ESTIMATION OF IONOSPHERIC HEIGHT VARIATIONS DURING AN AURORA EVENT USING MULTIPLE SEMI-FOCUSING LEVELS

Giorgio Gomba, Francesco De Zan

Remote Sensing Technology Institute, German Aerospace Center (DLR), Wessling, Germany

ABSTRACT

Many methods, to estimate the ionospheric effects on SAR images and interferograms, have been proposed and studied in the past years. However, depending on the conditions of the ionosphere, different methods can or should be applied. The effects that an aurora event has on SAR images and interferograms possibly have some differences with respect to the effects generated by a more normal ionospheric state. This work shows one of these differences, which is supposed to be a change in the ionosphere vertical profile, and propose and demonstrates a method to deal with it. This method improves the integrated-azimuth-shifts method, and permits to obtain a better estimate of the ionospheric phase screen.

Index Terms— InSAR, SAR ionospheric effects, ionosphere estimation, ionosphere scintillation

1. INTRODUCTION

The ionosphere is the portion of the Earth's upper atmosphere where ions and electrons are present with sufficient density to significantly affect the propagation of radio waves. Charged particles are created by the incoming solar radiation that ionizes atmospheric gases. Their concentration in the ionosphere varies with the altitude but has normally a peak between 300 and 400 km. The three-dimensional structure of the ionosphere is often approximated by an idealized thin layer, positioned at the barycenter of the electron density vertical profile. The magnitude of ionospheric effects depends on the slant total electron content (TEC), which is the total number of electrons integrated between the satellite and the target, along a tube of one square meter cross-section. The TEC can be related to the path delay and consequently to the phase observed in the interferogram

$$\phi_i = \frac{4\pi K}{c f_0} TEC, \tag{1}$$

where $K = 40.28$, f_0 is the carrier frequency and c the light speed in vacuum.

The aurora borealis is caused by interactions between the solar wind and the Earth's atmosphere. Charged particles, carried by the solar wind and accelerated by the interconnections between the magnetic field of the Earth and that of the Sun, are conducted downward toward the magnetic poles where they collide with the atmosphere, ionizing oxygen and nitrogen atoms. These ions emits radiation at various wavelengths, creating the characteristic colors of the aurora. In this complex ionospheric situation, the thin layer approximation with a fixed height proves itself to be not accurate enough to explain all effects seen in SAR images.

A solar wind stream hit the Earth on 31 March 2006 causing visible auroras all around the north polar region for almost three days. L-band ALOS PALSAR images were acquired above Alaska during April 1st and May 17th [1]. The ionospheric phase contribution can be estimated using the Faraday rotation technique [2] showing that the first image captured the aurora while the second image is ionosphere-free. By compensating the ionospheric phase screen, using the estimate from the Faraday rotation method, it can be shown that no visible tropospheric phase is present in the interferogram. Supposing therefore no other main contribution other than the ionosphere, the ionosphere derivative along the azimuth direction (Figure 2(b)) can be calculated by taking the derivative of the interferometric phase (Figure 2(a)).

2. AZIMUTH SHIFTS AND IONOSPHERE SPATIAL VARIATIONS

Variations of the ionosphere along the satellite flight path induce azimuth shifts in SAR images. A difference in these variations between different acquisitions becomes a differential shift between images and can be recovered by a precise coregistration. The relationship between the ionospheric phase derivative $\phi_i'(\eta)$ along the flight path

$$\phi_i'(\eta) = \left.\frac{d\phi_i(\bar{\eta})}{d\bar{\eta}}\right|_{\bar{\eta}=\eta}, \tag{2}$$

and the azimuth shift δ_{az}, is:

$$\delta_{az}(\eta) = \frac{K H_i}{f_0^2 \cos(\theta)} \cdot \phi_i'(\eta), \tag{3}$$

where θ is the incidence angle, $K = 40.28$, f_0 is the carrier frequency, H_i the height of the ionosphere single layer and η the azimuth spatial coordinate. Due to the azimuth length of the resolution cell at the height of the ionosphere (about

3 km), only a low-pass version of the real ionosphere actually contribute to modify the interferometric phase and the azimuth shifts. The *integrated azimuth shifts* method [3] estimates the ionospheric TEC by integrating the azimuth shifts and using Equation 3 to scale the result:

$$\hat{\phi}_i(\eta) = \frac{f_0^2 \cos(\theta)}{K H_i} \int_0^{\eta} \delta_{az}(\bar{\eta})\, d\bar{\eta} + C. \tag{4}$$

One drawback of this method is that the errors of the cross-correlation (coherent or incoherent), which is used to estimate the shifts, are also integrated. This may result in an increasing error in azimuth, which is a ramp in the compensated interferogram. One other problem is the recovery of range variations. Azimuth shifts are only sensible to ionospheric azimuth variations, the range component, which is the integration constants (the term C in Equation 4) of each azimuth line, is unknown. In this work, to solve this problem we simply add the interferogram range line, which corresponds to the integration starting line, to the integrated phase screen. This procedure works for our example but cannot be operationally applied. Since this is not the focus of this paper we leave the discussion of this problem for future improvements.

We see from Equation 3 that the height of the ionospheric single layer scales the ionosphere derivative and has therefore a big impact on the azimuth shifts. In order to correctly convert the azimuth shifts to the ionospheric phase screen using Equation 4, the ionosphere single layer height has to be known or estimated. Some ionospheric phase screens, which we generated using different ionospheric heights, are used to correct the original interferogram. In Figure 2(c) and 2(d) are presented the differences between the compensated and the original interferograms. As it can be seen from the residuals none of the generated phase screens is able to completely correct the original interferogram.

Inverting Equation 3 we estimate the derivative of the ionospheric phase in the azimuth direction using the azimuth shifts. The real derivative of Figure 2(b) should be equal to the estimated ionosphere derivative. Comparing Figure 2(b) with Figure 2(e) we see that they are not the same. Their difference, displayed in Figure 2(f), is not zero in the same area where the ionospheric phase rapidly changes. This suggests that the electron density is increasing and somehow changing, such that, also the barycenter of its three dimensional structure, which we call ionospheric height, is changed. If this is true, it would modify the scale factor that converts an ionospheric variation into an azimuth shift.

The result of the integral 4 will then only be correct if we use the real changing ionospheric height. Alternatively, another possibility would be to estimate the correct ionospheric phase screen derivative along the flight path $\hat{\phi}'_i(\eta)$ and integrate it,

$$\hat{\phi}_i(\eta) = \int_0^{\eta} \hat{\phi}'_i(\bar{\eta})\, d\bar{\eta} + C, \tag{5}$$

as it will be presented in the next section.

3. IONOSPHERE DERIVATIVE ESTIMATION USING SEMI-FOCUSING

The semi-focusing technique [4] consists in defocusing the images using a specific kernel for a specific defocusing height. The technique generates the raw data that would have been acquired from a satellite having an orbit height equal to the height used for the defocusing. If the height of the ionosphere and the one of the satellite are the same, the ionosphere is simply a phase screen and does not produce azimuth shift in the raw data. To estimate the ionosphere height we must find the defocusing height for which the shifts are zero. The relation between the shifts, as a function of the defocusing height H_f is:

$$\begin{aligned}\delta_{az}(\eta, H_f) &= \frac{K(H_i - H_f)}{f_0^2 \cos(\theta)} \cdot \phi'_i(\eta) \\ &= -\frac{K H_f}{f_0^2 \cos(\theta)} \cdot \phi'_i(\eta) + \frac{K H_i}{f_0^2 \cos(\theta)} \cdot \phi'_i(\eta). \end{aligned} \tag{6}$$

For each azimuth position $\bar{\eta}$ and for varying defocusing heights H_f, we fit a a first order polynomial to the azimuth shifts $\delta_{az}(\bar{\eta}, H_f)$. Considering Equation 6 we use the parameter of the fitted polynomial to obtain an estimate of the ionosphere derivative and height:

$$\hat{\phi}'_i(\bar{\eta}) = -b \cdot \frac{f_0^2 \cos(\theta)}{K}, \qquad \hat{H}_i = a \cdot \frac{f_0^2 \cos(\theta)}{K \hat{\phi}'_i(\bar{\eta})}, \tag{7}$$

where a and b are respectively the zero and first order parameters of the polynomial. After repeating this procedure for each azimuth and range position we obtain the ionosphere azimuth derivative and height for the whole image. The result is displayed in Figure 2(g). As seen from Equation 7, the ionospheric height estimate depends on the inverse of the derivative. Therefore, it can be insufficiently reliable due to noise amplification, if the ionosphere derivative is small. On the other hand, it can be seen from Figure 2(g) that the estimate of the ionosphere derivative is much more similar to the real derivative than the old estimate of Figure 2(e), and that the difference between the new estimate and the real derivative of Figure 2(h) is smaller than the old one too. Using Equation 5 on this new estimate we produce the phase screen of Figure 2(i), which subtracted from the original interferogram generates the residual of Figure 2(j).

4. CONCLUSION

Concluding, it seems that the supposition of a changing ionosphere barycenter height is true. The new residual, of Figure 2(j), is much smaller than the old ones, of Figures 2(c) and 2(d). This proves that the estimated ionosphere derivative is correct and that it is able to better compensate the ionospheric phase screen, with a great improvement with respect to the standard *integrated azimuth shifts* method.

5. REFERENCES

[1] F.J. Meyer, J. Nicoll, and B. Bristow, "Mapping aurora activity with sar - a case study," in *Geoscience and Remote Sensing Symposium,2009 IEEE International,IGARSS 2009*, July 2009, vol. 4, pp. IV–1–IV–4.

[2] A. Freeman, "Calibration of linearly polarized polarimetric sar data subject to faraday rotation," *Geoscience and Remote Sensing, IEEE Transactions on*, vol. 42, no. 8, pp. 1617–1624, Aug 2004.

[3] U. Wegmuller, C. Werner, T. Strozzi, and A. Wiesmann, "Ionospheric electron concentration effects on sar and insar," in *Geoscience and Remote Sensing Symposium, 2006. IGARSS 2006. IEEE International Conference on*, July 2006, pp. 3731–3734.

[4] G. Gomba, M. Eineder, A. Parizzi, and R. Bamler, "High-resolution estimation of ionospheric phase screens through semi-focusing processing," in *Geoscience and Remote Sensing Symposium (IGARSS), 2014 IEEE International*, July 2014, pp. 17–20.

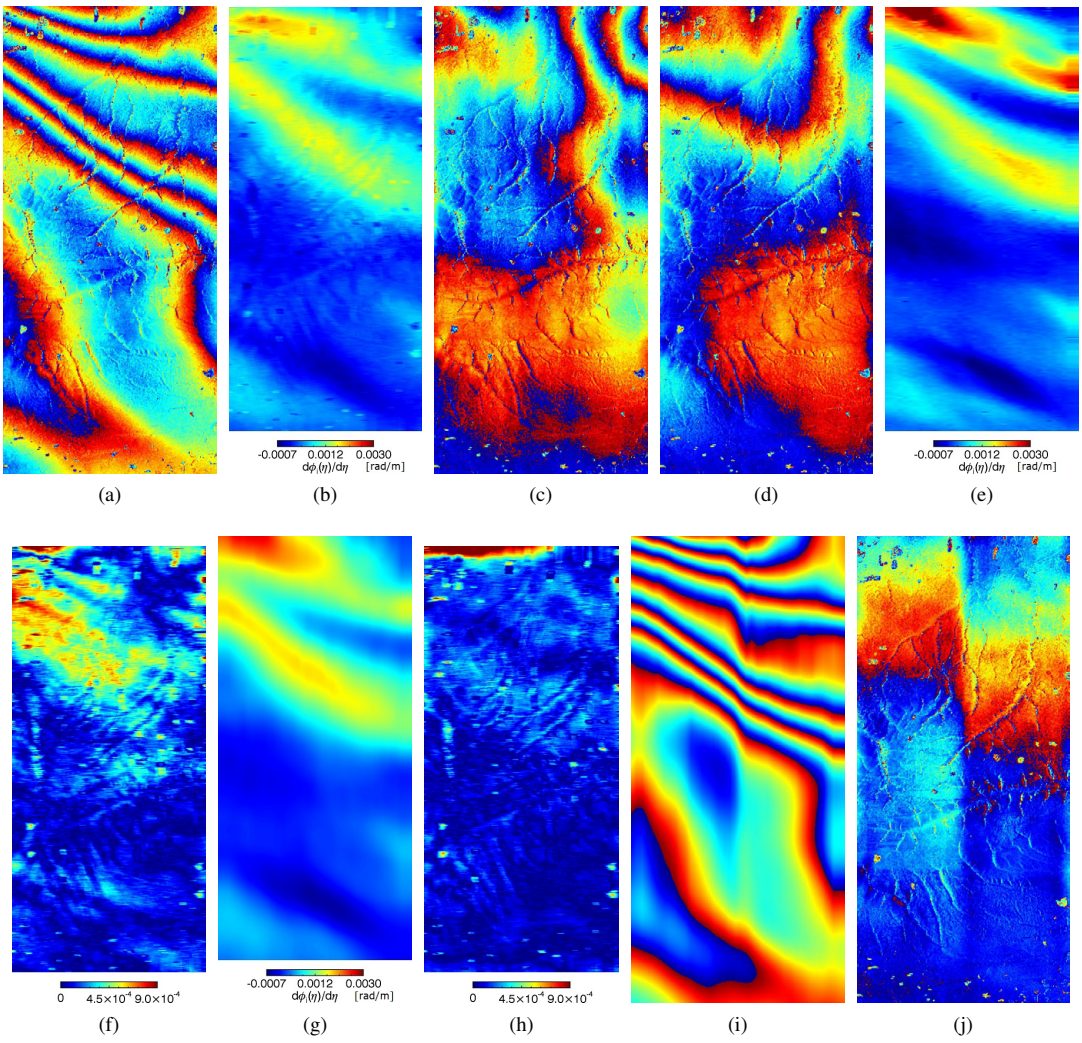

Fig. 1. The aurora test-case: (a) is the original interferogram, (b) is the ionosphere derivative; (c) is the ionosphere-compensated interferogram with a supposed ionospheric height of 200 km, (d) with a height of 300 km; (e) and (g) are respectively the ionosphere derivative estimated using the azimuth shifts and using the semi-focusing method, (e) and (h) are their differences with the real derivative (b); (i) is the height of the ionosphere; (j) and (k) are respectively the generated ionospheric phase screen and the compensated interferogram.

Bibliography

Afraimovich, E., Terekhov, A., Udodov, M. Y., and Fridman, S. (1992). Refraction distortions of transionospheric radio signals caused by changes in a regular ionosphere and by travelling ionospheric disturbances. *Journal of atmospheric and terrestrial physics*, 54(7):1013–1020.

Bamler, R. and Eineder, M. (1996). ScanSAR processing using standard high precision SAR algorithms. *IEEE Transactions on Geoscience and Remote Sensing*, 34(1):212–218.

Bamler, R. and Eineder, M. (2005). Accuracy of differential shift estimation by correlation and split-bandwidth interferometry for wideband and delta-k SAR systems. *Geoscience and Remote Sensing Letters, IEEE*, 2(2):151–155.

Belcher, D. (2008). Theoretical limits on SAR imposed by the ionosphere. *Radar, Sonar Navigation, IET*, 2(6):435–448.

Belcher, D. and Rogers, N. (2009). Theory and simulation of ionospheric effects on synthetic aperture radar. *IET radar, sonar & navigation*, 3(5):541–551.

Belcher, D. P. and Cannon, P. S. (2013). Ionospheric effects on synthetic aperture radar (SAR) clutter statistics. *IET Radar, Sonar & Navigation*, 7(9):1004–1011.

Belcher, D. P. and Cannon, P. S. (2014). Amplitude scintillation effects on SAR. *IET Radar, Sonar & Navigation*, 8(6):658–666.

Bernhardt, P., Ainsworth, T., Groves, K., Beach, T., Caton, R. G., Carrano, C. S., Alcala, C. M., and Sponseller, D. D. (2008). Detection of ionospheric structures with L-band synthetic aperture radars. In *IGARSS 2008-2008 IEEE International Geoscience and Remote Sensing Symposium*, volume 2, pages II–395. IEEE.

Brcic, R., Eineder, M., and Bamler, R. (2009). Interferometric absolute phase determination with TerraSAR-X wideband SAR data. In *Radar Conference, 2009 IEEE*, pages 1–6.

Brcic, R., Parizzi, A., Eineder, M., Bamler, R., and Meyer, F. (2010). Estimation and compensation of ionospheric delay for SAR interferometry. In *Geoscience and Remote Sensing Symposium (IGARSS), 2010 IEEE International*, pages 2908–2911.

Brcic, R., Parizzi, A., Eineder, M., Bamler, R., and Meyer, F. (2011). Ionospheric effects in SAR interferometry: An analysis and comparison of methods for their estimation. In *Geoscience and Remote Sensing Symposium (IGARSS), 2011 IEEE International*, pages 1497–1500.

Carrano, C. S., Groves, K. M., and Caton, R. G. (2010). A phase screen simulator for predicting the impact of small-scale ionospheric structure on SAR image formation and interferometry. In *IGARSS*, pages 162–165.

Carrano, C. S., Groves, K. M., and Caton, R. G. (2012). Simulating the impacts of ionospheric scintillation on L band SAR image formation. *Radio Science*, 47(4).

Chapin, E., Chan, S. F., Chapman, B. D., Chen, C. W., Martin, J. M., Michel, T. R., Muellerschoen, R. J., Pi, X., and Rosen, P. A. (2006). Impact of the ionosphere on an L-band space based radar. In *2006 IEEE Conference on Radar*, pages 8–pp. IEEE.

Chen, A. C. and Zebker, H. A. (2014). Reducing Ionospheric Effects in InSAR Data Using Accurate Coregistration. *IEEE Transactions on Geoscience and Remote Sensing*, 52(1):60–70.

Cong, X. (2014). *SAR Interferometry for Volcano Monitoring: 3D-PSI Analysis and Mitigation of Atmospheric Refractivity*. PhD thesis, Munich, Technische Universität München.

Cumming, I. and Wong, F. (1964). *Digital processing of synthetic aperture radar data*. Artech House remote sensing library.

Davies, K. (1990). *Ionospheric Radio*. IET.

De Zan, F. (2014). Accuracy of Incoherent Speckle Tracking for Circular Gaussian Signals. *IEEE Geoscience and Remote Sensing Letters*, 11(1):264–267.

De Zan, F., Prats-Iraola, P., and Rodriguez-Cassola, M. (2015). On the Dependence of Delta-k Efficiency on Multilooking. *Geoscience and Remote Sensing Letters, IEEE*, PP(99):1–5.

De Zan, F., Prats-Iraola, P., Scheiber, R., and Rucci, A. (2014). Interferometry with TOPS: coregistration and azimuth shifts. In *EUSAR 2014; 10th European Conference on Synthetic Aperture Radar; Proceedings of*, pages 1–4.

Ding, F., Wan, W., Liu, L., Afraimovich, E., Voeykov, S., and Perevalova, N. (2008). A statistical study of large-scale traveling ionospheric disturbances observed by GPS TEC during major magnetic storms over the years 2003-2005. *Journal of Geophysical Research: Space Physics (1978-2012)*, 113(A3).

Feng, G., Li, Z., Shan, X., Zhang, L., Zhang, G., and Zhu, J. (2015). Geodetic model of the 2015 April 25 M w 7.8 Gorkha Nepal Earthquake and M w 7.3 aftershock estimated from InSAR and GPS data. *Geophysical Journal International*, 203(2):896–900.

Fitzgerald, T. J. (1997). Ionospheric effects on synthetic aperture radar at VHF. In *Radar Conference, 1997., IEEE National*, pages 237–239.

Freeman, A. (2004). Calibration of linearly polarized polarimetric SAR data subject to Faraday rotation. *Geoscience and Remote Sensing, IEEE Transactions on*, 42(8):1617–1624.

Freeman, A. and Saatchi, S. (2004). On the detection of Faraday rotation in linearly polarized L-band SAR backscatter signatures. *Geoscience and Remote Sensing, IEEE Transactions on*, 42(8):1607–1616.

Gail, W. B. (1998). Effect of Faraday rotation on polarimetric SAR. *IEEE transactions on aerospace and electronic systems*, 34(1):301–307.

Gatelli, F., Monti Guarnieri, A., Parizzi, F., Pasquali, P., Prati, C., and Rocca, F. (1994). The wavenumber shift in SAR interferometry. *Geoscience and Remote Sensing, IEEE Transactions on*, 32(4):855–865.

Gilman, M., Smith, E., and Tsynkov, S. (2013). Reduction of ionospheric distortions for spaceborne synthetic aperture radar with the help of image registration. *Inverse Problems*, 29(5):054005.

Gomba, G. and De Zan, F. (2015). Estimation of ionospheric height variations during an aurora event using multiple semi-focusing levels. In *2015 IEEE International Geoscience and Remote Sensing Symposium (IGARSS)*, pages 4065–4068.

Gomba, G. and De Zan, F. (2016 submitted). Bayesian Data Combination for the Estimation of Ionospheric Effects in SAR Interferograms. *IEEE Transactions on Geoscience and Remote Sensing*.

Gomba, G., Eineder, M., Parizzi, A., and Bamler, R. (2014). High-resolution estimation of ionospheric phase screens through semi-focusing processing. In *2014 IEEE International Geoscience and Remote Sensing Symposium (IGARSS)*, pages 17–20.

Gomba, G., González, F. R., and Zan, F. D. (2017). Ionospheric Phase Screen Compensation for the Sentinel-1 TOPS and ALOS-2 ScanSAR Modes. *IEEE Transactions on Geoscience and Remote Sensing*, 55(1):223–235.

Gomba, G., Parizzi, A., De Zan, F., Eineder, M., and Bamler, R. (2016). Toward Operational Compensation of Ionospheric Effects in SAR Interferograms: The Split-Spectrum Method. *IEEE Transactions on Geoscience and Remote Sensing*, 54(3):1446–1461.

Grandin, R., Vallée, M., Satriano, C., Lacassin, R., Klinger, Y., Simoes, M., and Bollinger, L. (2015). Rupture process of the Mw= 7.9 2015 Gorkha earthquake (Nepal): insights into Himalayan megathrust segmentation. *Geophysical Research Letters*, 42(20):8373–8382.

Guttorp, P. and Gneiting, T. (2006). Studies in the history of probability and statistics XLIX On the Matérn correlation family. *Biometrika*, 93(4):989–995.

Hernández-Pajares, M., Juan, J., Sanz, J., Orus, R., Garcia-Rigo, A., Feltens, J., Komjathy, A., Schaer, S., and Krankowski, A. (2009). The IGS VTEC maps: a reliable source of ionospheric information since 1998. *Journal of Geodesy*, 83(3-4):263–275.

Hocke, K. and Schlegel, K. (1996). A review of atmospheric gravity waves and travelling ionospheric disturbances: 1982-1995. In *Annales Geophysicae*, page 917.

Hu, J., Li, Z., Zhang, L., Ding, X., Zhu, J., Sun, Q., and Ding, W. (2012). Correcting ionospheric effects and monitoring two-dimensional displacement fields with multiple-aperture InSAR technology with application to the Yushu earthquake. *Science China Earth Sciences*, 55(12):1961–1971.

Ishimaru, A., Kuga, Y., Liu, J., Kim, Y., and Freeman, T. (1999). Ionospheric effects on synthetic aperture radar at 100 MHz to 2 GHz. *Radio Science*, 34(1):257–268.

Jakowski, N., Mayer, C., Hoque, M. M., and Wilken, V. (2011). Total electron content models and their use in ionosphere monitoring. *Radio Science*, 46(6).

Jung, H. S., Lee, D. T., Lu, Z., and Won, J. S. (2013). Ionospheric Correction of SAR Interferograms by Multiple-Aperture Interferometry. *IEEE Transactions on Geoscience and Remote Sensing*, 51(5):3191–3199.

Jung, H. S. and Lee, W. J. (2015). An Improvement of Ionospheric Phase Correction by Multiple-Aperture Interferometry. *IEEE Transactions on Geoscience and Remote Sensing*, 53(9):4952–4960.

Kay, S. (1993). *Fundamentals of Statistical Signal Processing: Estimation theory*. Fundamentals of Statistical Signal Processing. Prentice-Hall PTR.

Kelley, M. (2012). *The Earth's Ionosphere: Plasma Physics and Electrodynamics*. International geophysics series. Elsevier Science.

Kim, J. (2013). *Development of Ionosphere Estimation Techniques for the Correction of SAR Data*. PhD thesis, ETH Zürich.

Kim, J. S., Danklmayer, A., and Papathanassiou, K. (2011). Correction of ionospheric distortions in low frequency interferometric SAR data. In *Geoscience and Remote Sensing Symposium (IGARSS), 2011 IEEE International*, pages 1505–1508.

Kim, J. S. and Papathanassiou, K. (2015). On the separation of Dynamic Scattering and Ionospheric Effects in SAR data. In *ESA POLinSAR Workshop*.

Kim, J. S. and Papathanassiou, K. P. (2010). Faraday rotation estimation performance analysis. *EUSAR 2010*.

Kim, J. S., Papathanassiou, K. P., Quegan, S., and Rogers, N. (2012). Estimation and correction of scintillation effects on spaceborne P-band SAR images. In *2012 IEEE International Geoscience and Remote Sensing Symposium*, pages 5101–5104. IEEE.

Kim, J. S., Papathanassiou, K. P., Scheiber, R., and Quegan, S. (2015). Correcting Distortion of Polarimetric SAR Data Induced by Ionospheric Scintillation. *IEEE Transactions on Geoscience and Remote Sensing*, 53(12):6319–6335.

Knospe, S. and Jonsson, S. (2010). Covariance Estimation for dInSAR Surface Deformation Measurements in the Presence of Anisotropic Atmospheric Noise. *IEEE Transactions on Geoscience and Remote Sensing*, 48(4):2057–2065.

Lindsey, E. O., Natsuaki, R., Xu, X., Shimada, M., Hashimoto, M., Melgar, D., and Sandwell, D. T. (2015). Line-of-sight displacement from ALOS-2 interferometry: Mw 7.8 Gorkha Earthquake and Mw 7.3 aftershock. *Geophysical Research Letters*, 42(16):6655–6661.

Liu, J., Kuga, Y., Ishimaru, A., Pi, X., and Freeman, A. (2003). Ionospheric effects on SAR imaging: A numerical study. *IEEE Transactions on Geoscience and Remote Sensing*, 41(5):939–947.

Liu, Z., Jung, H. S., and Lu, Z. (2014). Joint Correction of Ionosphere Noise and Orbital Error in L-Band SAR Interferometry of Interseismic Deformation in Southern California. *IEEE Transactions on Geoscience and Remote Sensing*, 52(6):3421–3427.

Mannix, C. R., Belcher, D. P., Cannon, P. S., and Angling, M. J. (2016). Using GNSS signals as a proxy for SAR signals: Correcting ionospheric defocusing. *Radio Science*.

Meyer, F. (2010). A review of ionospheric effects in low-frequency SAR — Signals, correction methods, and performance requirements. In *Geoscience and Remote Sensing Symposium (IGARSS), 2010 IEEE International*, pages 29–32.

Meyer, F. (2011). Performance Requirements for Ionospheric Correction of Low-Frequency SAR Data. *Geoscience and Remote Sensing, IEEE Transactions on*, 49(10):3694–3702.

Meyer, F., Bamler, R., Jakowski, N., and Fritz, T. (2006). The Potential of Low-Frequency SAR Systems for Mapping Ionospheric TEC Distributions. *Geoscience and Remote Sensing Letters, IEEE*, 3(4):560–564.

Meyer, F. and Nicoll, J. (2008). Prediction, Detection, and Correction of Faraday Rotation in Full-Polarimetric L-Band SAR Data. *Geoscience and Remote Sensing, IEEE Transactions on*, 46(10):3076–3086.

Meyer, F. J., Chotoo, K., Chotoo, S. D., Huxtable, B. D., and Carrano, C. S. (2016). The Influence of Equatorial Scintillation on L-Band SAR Image Quality and Phase. *IEEE Transactions on Geoscience and Remote Sensing*, 54(2):869–880.

Meyer, F. J., Nicoll, J., and Bristow, B. (2009). Mapping aurora activity with SAR - A case study. In *2009 IEEE International Geoscience and Remote Sensing Symposium*, volume 4, pages IV–1. IEEE.

Meyer, F. J., Papathanassiou, K., Kim, J. S., Pi, X., Freeman, A., Chotoo, K., Groves, K., and Jones, E. (2012). Ionosar - collaborative research towards understanding and mitigating ionospheric effects in SAR. In *2012 IEEE International Geoscience and Remote Sensing Symposium*, pages 6039–6042.

Meyer, F. J. and Watkins, B. (2011). A statistical model of ionospheric signals in low-frequency SAR data. In *Geoscience and Remote Sensing Symposium (IGARSS), 2011 IEEE International*, pages 1493–1496. IEEE.

Moffett, R. and Quegan, S. (1983). The mid-latitude trough in the electron concentration of the ionospheric F-layer: a review of observations and modelling. *Journal of Atmospheric and Terrestrial Physics*, 45(5):315–343.

Nagler, T., Rott, H., Hetzenecker, M., Wuite, J., and Potin, P. (2015). The Sentinel-1 Mission: New Opportunities for Ice Sheet Observations. *Remote Sensing*, 7(7):9371–9389.

Nicoll, J. B. and Meyer, F. J. (2008). Mapping the ionosphere using L-band SAR data. In *IGARSS 2008-2008 IEEE International Geoscience and Remote Sensing Symposium*, volume 2, pages II–537. IEEE.

Otsuka, Y., Suzuki, K., Nakagawa, S., Nishioka, M., Shiokawa, K., and Tsugawa, T. (2013). GPS observations of medium-scale traveling ionospheric disturbances over Europe. In *Annales Geophysicae*, pages 163–172. Copernicus GmbH.

Pi, X., Freeman, A., Chapman, B., Rosen, P., and Li, Z. (2011). Imaging ionospheric inhomogeneities using spaceborne synthetic aperture radar. *Journal of Geophysical Research: Space Physics*, 116(A4).

Prats, P., Marotti, L., Wollstadt, S., and Scheiber, R. (2010). TOPS Interferometry with TerraSAR-X. In *Synthetic Aperture Radar (EUSAR), 2010 8th European Conference on*, pages 1–4.

Prats-Iraola, P., Scheiber, R., Rodriguez-Cassola, M., Mittermayer, J., Wollstadt, S., De Zan, F., Bräutigam, B., Schwerdt, M., Reigber, A., and Moreira, A. (2014). On the Processing of Very High Resolution Spaceborne SAR Data. *IEEE Transactions on Geoscience and Remote Sensing*, 52(10):6003–6016.

Qi, R.-Y. and Jin, Y.-Q. (2007). Analysis of the effects of faraday rotation on spaceborne polarimetric sar observations at-band. *IEEE transactions on geoscience and remote sensing*, 45(5):1115–1122.

Quegan, S. and Lamont, J. (1986). Ionospheric and tropospheric effects on synthetic aperture radar performance. *International Journal of Remote Sensing*, 7(4):525–539.

Rasmussen, C. E. (2006). *Gaussian processes for machine learning*. The MIT press.

Raucoules, D. and de Michele, M. (2010). Assessing Ionospheric Influence on L-Band SAR Data: Implications on Coseismic Displacement Measurements of the 2008 Sichuan Earthquake. *IEEE Geoscience and Remote Sensing Letters*, 7(2):286–290.

Rignot, E. J. (2000). Effect of Faraday rotation on L-band interferometric and polarimetric synthetic-aperture radar data. *IEEE Transactions on Geoscience and Remote Sensing*, 38(1):383–390.

Rino, C. (1979). A power law phase screen model for ionospheric scintillation: 1. Weak scatter. *Radio Science*, 14(6):1135–1145.

Rino, C. (2011). *The theory of scintillation with applications in remote sensing*. John Wiley & Sons.

Rino, C. and Fremouw, E. (1977). The angle dependence of singly scattered wavefields. *Journal of Atmospheric and Terrestrial Physics*, 39(8):859–868.

Rogers, N. C., Quegan, S., Kim, J. S., and Papathanassiou, K. P. (2014). Impacts of Ionospheric Scintillation on the BIOMASS P-Band Satellite SAR. *IEEE Transactions on Geoscience and Remote Sensing*, 52(3):1856–1868.

Rosen, P., Hensley, S., and Chen, C. (2010). Measurement and mitigation of the ionosphere in L-band Interferometric SAR data. In *Radar Conference, 2010 IEEE*, pages 1459–1463.

Seymour, M. and Cumming, I. (1994). Maximum likelihood estimation for SAR interferometry. In *Geoscience and Remote Sensing Symposium, 1994. IGARSS'94. Surface and Atmospheric Remote Sensing: Technologies, Data Analysis and Interpretation., International*, volume 4, pages 2272–2275. IEEE.

Shen, Z.-K., Sun, J., Zhang, P., Wan, Y., Wang, M., Bürgmann, R., Zeng, Y., Gan, W., Liao, H., and Wang, Q. (2009). Slip maxima at fault junctions and rupturing of barriers during the 2008 Wenchuan earthquake. *Nature Geoscience*, 2(10):718–724.

Shimada, M., Muraki, Y., and Otsuka, Y. (2008). Discovery of anoumoulous stripes over the Amazon by the PALSAR onboard ALOS satellite. In *IGARSS 2008-2008 IEEE International Geoscience and Remote Sensing Symposium*.

Tebaldini, S., Guarnieri, A. M., and Rocca, F. (2012). Recovering time and space varying phase screens through SAR multi-squint differential interferometry. In *Synthetic Aperture Radar, 2012. EUSAR. 9th European Conference on*, pages 16–19.

Teshebaeva, K., Sudhaus, H., Echtler, H., Schurr, B., and Roessner, S. (2014). Strain partitioning at the eastern Pamir-Alai revealed through SAR data analysis of the 2008 Nura earthquake. *Geophysical Journal International*.

Tsunoda, R. T. (1988). High-latitude F region irregularities: A review and synthesis. *Reviews of Geophysics*, 26(4):719–760.

Wang, K. and Fialko, Y. (2015). Slip model of the 2015 Mw 7.8 Gorkha (Nepal) earthquake from inversions of ALOS-2 and GPS data. *Geophysical Research Letters*, 42(18):7452–7458.

WDC-SILSO (2016). WDC-SILSO, Royal Observatory of Belgium, Brussels.

Wegmüller, U., Strozzi, T., and Werner, C. (2012). Ionospheric path delay estimation using split-beam interferometry. In *2012 IEEE International Geoscience and Remote Sensing Symposium*, pages 3631–3634.

Wegmüller, U., Werner, C., Strozzi, T., and Wiesmann, A. (2006). Ionospheric Electron Concentration Effects on SAR and INSAR. In *2006 IEEE International Symposium on Geoscience and Remote Sensing*, pages 3731–3734.

Wiener, N. (1964). *Extrapolation, Interpolation, and Smoothing of Stationary Time Series*. The MIT Press.

Wright, P. A., Quegan, S., Wheadon, N. S., and Hall, C. D. (2003). Faraday rotation effects on L-band spaceborne SAR data. *IEEE Transactions on Geoscience and Remote Sensing*, 41(12):2735–2744.

Xu, Z.-W., Wu, J., and Wu, Z.-S. (2004). A survey of ionospheric effects on space-based radar. *Waves in Random Media*, 14:189.

Xu, Z. W., Wu, J., and Wu, Z. S. (2008). Potential Effects of the Ionosphere on Space-Based SAR Imaging. *IEEE Transactions on Antennas and Propagation*, 56(7):1968–1975.

Yagüe-Martínez, N., Prats-Iraola, P., González, F. R., Brcic, R., Shau, R., Geudtner, D., Eineder, M., and Bamler, R. (2016). Interferometric Processing of Sentinel-1 TOPS Data. *IEEE Transactions on Geoscience and Remote Sensing*, 54(4):2220–2234.

Yeh, K. and Liu, C. (1972). Theory of ionosphere waves. *Academic Press*.

Zhang, B., Ding, X., Zhu, W., Wang, C., Zhang, L., and Liu, Z. (2016). Mitigating Ionospheric Artifacts in Coseismic Interferogram Based on Offset Field Derived From ALOS-PALSAR Data. *IEEE Journal of Selected Topics in Applied Earth Observations and Remote Sensing*, PP(99):1–10.

Zolesi, B. and Cander, L. R. (2014). *Ionospheric prediction and forecasting*. Springer.